

Improving driver comfort in commercial vehicles : modeling and control of a low-power active cabin suspension system

Citation for published version (APA):

Evers, W. J. E. (2010). *Improving driver comfort in commercial vehicles : modeling and control of a low-power active cabin suspension system*. [Phd Thesis 1 (Research TU/e / Graduation TU/e), Mechanical Engineering]. Technische Universiteit Eindhoven. <https://doi.org/10.6100/IR673075>

DOI:

[10.6100/IR673075](https://doi.org/10.6100/IR673075)

Document status and date:

Published: 01/01/2010

Document Version:

Publisher's PDF, also known as Version of Record (includes final page, issue and volume numbers)

Please check the document version of this publication:

- A submitted manuscript is the version of the article upon submission and before peer-review. There can be important differences between the submitted version and the official published version of record. People interested in the research are advised to contact the author for the final version of the publication, or visit the DOI to the publisher's website.
- The final author version and the galley proof are versions of the publication after peer review.
- The final published version features the final layout of the paper including the volume, issue and page numbers.

[Link to publication](#)

General rights

Copyright and moral rights for the publications made accessible in the public portal are retained by the authors and/or other copyright owners and it is a condition of accessing publications that users recognise and abide by the legal requirements associated with these rights.

- Users may download and print one copy of any publication from the public portal for the purpose of private study or research.
- You may not further distribute the material or use it for any profit-making activity or commercial gain
- You may freely distribute the URL identifying the publication in the public portal.

If the publication is distributed under the terms of Article 25fa of the Dutch Copyright Act, indicated by the "Taverne" license above, please follow below link for the End User Agreement:

www.tue.nl/taverne

Take down policy

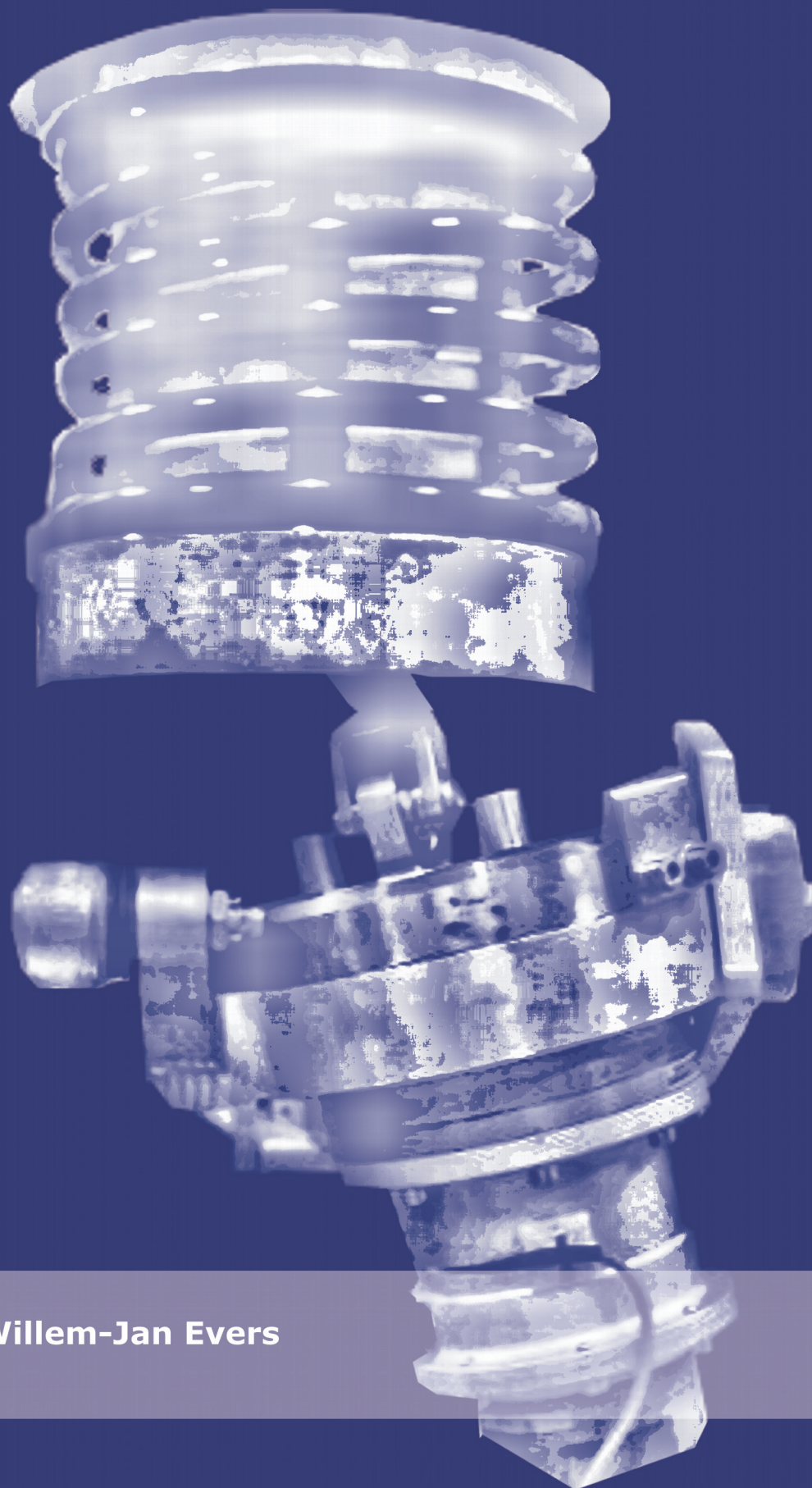
If you believe that this document breaches copyright please contact us at:

openaccess@tue.nl

providing details and we will investigate your claim.

Improving driver comfort in commercial vehicles

Modeling and control of a low-power active cabin suspension system



Willem-Jan Evers

**Improving driver comfort in
commercial vehicles**
**Modeling and control of a low-power active
cabin suspension system**



The research reported in this thesis is part of the research program of the Dutch Institute of Systems and Control (DISC). The author has successfully completed the educational program of the Graduate School DISC.



This research is supported by TNO Automotive, Helmond, The Netherlands.

Improving driver comfort in commercial vehicles: Modeling and control of a low-power active cabin suspension system by Willem-Jan Evers – Eindhoven: Technische Universiteit Eindhoven, 2010 – Proefschrift.

A catalogue record is available from the Eindhoven University of Technology Library.
ISBN: 978-90-386-2225-5.

This thesis was prepared with the L^AT_EX 2_ε documentation system.
Reproduction: Ipskamp Drukkers B.V., Enschede, The Netherlands.

Copyright ©2010 by W.J.E. Evers. All rights reserved.

**Improving driver comfort in
commercial vehicles**
**Modeling and control of a low-power active
cabin suspension system**

PROEFSCHRIFT

ter verkrijging van de graad van doctor
aan de Technische Universiteit Eindhoven,
op gezag van de rector magnificus, prof.dr.ir. C.J. van Duijn,
voor een commissie aangewezen door het College voor Promoties
in het openbaar te verdedigen
op donderdag 20 mei 2010 om 16.00 uur

door

Wilhelmus Johannes Everardus Evers

geboren te Tilburg

Dit proefschrift is goedgekeurd door de promotor:

prof.dr. H. Nijmeijer

Copromotor:

dr.ir. I.J.M. Besselink

To my beloved parents

Samenstelling promotiecommissie:

prof.dr.ir. D.H. van Campen	(voorzitter)
prof.dr. H. Nijmeijer	(promotor)
dr.ir. I.J.M. Besselink	(copromotor)
prof. D.J.N. Limebeer DSc PhD, Oxford, England	(lid kerncommissie)
prof.dr. E.A. Lomonova MSc	(lid kerncommissie)
prof.dr.ir. D.J. Rixen, TU Delft	(lid kerncommissie)
prof.dr.ir. P.P.J. van den Bosch	
ir. A.C.M. van der Knaap, DAF Trucks N.V.	

Contents

1	Introduction	1
1.1	From the diary of a trucker	1
1.2	A brief history of commercial vehicle suspensions	2
1.3	Enhancing cabin comfort: recent developments	4
1.4	Suspension performance criteria	7
1.4.1	Comfort	7
1.4.2	Handling and attitude behavior	11
1.4.3	Energy	12
1.4.4	Durability	12
1.5	Problem statement and objectives	12
1.6	Contributions	13
1.7	Outline and publications	14
2	Tractor semi-trailer simulation model	15
2.1	Introduction	15
2.2	Model hierarchy	17
2.2.1	Driver module	18
2.2.2	Tractor module	18
2.2.3	Semi-trailer module	21
2.2.4	External influences	21
2.3	Model parameters	22
2.4	Modal analysis	23
2.5	The test vehicle	23
2.6	Time-domain validation	25
2.6.1	Accelerating	26
2.6.2	Braking	28
2.6.3	Road obstacles	31
2.6.4	Double lane change	35
2.7	Frequency-domain validation	37
2.8	Conclusions	42

3	Reduced order models and frequency domain validation	43
3.1	Introduction	43
3.2	Reduced order models	44
3.2.1	Data-based or first-principles?	44
3.2.2	Road models	45
3.2.3	Quarter truck heave model	46
3.2.4	Half truck roll model	49
3.2.5	Half truck pitch-heave model	51
3.3	Model validation using asynchronous measurements	56
3.3.1	Background	56
3.3.2	Problem description	57
3.3.3	Preliminaries	58
3.3.4	Assumptions	60
3.3.5	Approach	62
3.3.6	Example	64
3.4	Model validation	67
3.4.1	Quarter truck heave model	67
3.4.2	Half truck roll model	69
3.4.3	Half truck pitch-heave model	71
3.4.4	Tractor semi-trailer model (continued)	74
3.5	Conclusion	80
4	The search for a low-power active suspension concept	83
4.1	Introduction	83
4.2	Active vehicle suspensions	84
4.2.1	Hydraulic active suspension systems	84
4.2.2	Electrical active suspension systems	85
4.3	Variable geometry actuator	87
4.3.1	Concept analysis	87
4.3.2	Variable geometry active suspension	89
4.4	Active suspension comparison	91
4.4.1	Reference systems	92
4.4.2	Suspension performance and control	94
4.4.3	Evaluation	95
4.5	Conclusion	97
5	The electromechanical low-power active suspension	99
5.1	Introduction	99
5.2	eLPAS design and parameter optimization	100
5.2.1	Geometric design	100
5.2.2	Parameter optimization	104
5.3	Simulation model	108
5.3.1	Actuator model	108

5.3.2	Electric motor model	108
5.3.3	Friction model	109
5.3.4	Actuator limitations	110
5.4	Controller design	111
5.4.1	Electric motor control	111
5.4.2	Angle control	112
5.4.3	Force control	113
5.4.4	Actuator power consumption	113
5.5	Experimental validation	114
5.5.1	The prototype	115
5.5.2	Steady-state validation	116
5.5.3	Dynamic validation	118
5.6	Conclusions	122
6	Optimal vertical cabin control	123
6.1	Introduction	123
6.2	One DOF quarter car optimal control	125
6.2.1	Background	126
6.2.2	Effect of the ISO comfort weighting	128
6.3	Quarter truck LQ(G) cabin controller design	130
6.3.1	Quarter truck control problem	131
6.3.2	Quarter truck optimal control solution	133
6.3.3	Quarter truck output feedback	135
6.3.4	Quarter truck state estimation	138
6.4	Quarter truck road dependent control	142
6.4.1	Reformulation of the control problem	142
6.4.2	LQ optimal control without passive suspension elements	143
6.4.3	LQ optimal control with passive suspension elements	145
6.5	Conclusions	146
7	Modal control of an active cabin suspension	149
7.1	Introduction	149
7.2	Input-output decoupling	151
7.2.1	Roll and pitch-heave	154
7.2.2	Roll, pitch and heave	156
7.3	Roll control	157
7.3.1	Roll control problem	157
7.3.2	LQ optimal roll control solution	160
7.3.3	State estimation	163
7.3.4	Roll disturbance compensation	165
7.4	Pitch-heave control	168
7.4.1	Pitch-heave control problem	168
7.4.2	Pitch-heave optimal solution	172

7.4.3	State estimation for pitch-heave control	174
7.4.4	Disturbance compensation	175
7.5	Full vehicle modal controller evaluation	177
7.5.1	Implementation	178
7.5.2	Road obstacles	179
7.5.3	Comfort evaluation	180
7.5.4	Braking	182
7.5.5	Double lane change	183
7.5.6	Acceleration	186
7.6	Conclusion	186
8	Conclusions and recommendations	187
8.1	Vehicle models and validation	187
8.1.1	Conclusions	187
8.1.2	Recommendations	188
8.2	The variable geometry actuator	189
8.2.1	Conclusions	189
8.2.2	Recommendations	190
8.3	Cabin control	190
8.3.1	Conclusions	190
8.3.2	Recommendations	192
A	Model specification	193
A.1	44-DOF tractor semi-trailer model	193
A.2	2-mass quarter car heave model	193
A.3	4-mass quarter truck heave model	193
A.4	4-mass quarter truck roll model	193
A.5	9-DOF pitch-heave model	196
B	Control invariant points	203
	Bibliography	213
	Summary	215
	Samenvatting	217
	Acknowledgements	219
	Curriculum Vitae	221

Chapter 1

Introduction

1.1 From the diary of a trucker

Truckers are a rare breed of people. They are extremely important for the economies of many nations as they give meaning to the word *trade* - but not everyone is cut out to be one. Truckers transport goods, between cities, regions, or countries; and doing so requires them to spend many hours a day on the road. Long distance truckers are even forced to spend many nights sleeping in their vehicles.

Technically, a vehicle that carries the cargo or load itself, without a trailer, is called a truck. A vehicle which pulls the load in a trailer is called a tractor. However, the tractor-trailer combination is again called heavy-duty truck. To distinguish between these vehicles and railway trucks, the term commercial vehicle is sometimes used.

The intense usage of commercial vehicles, places some stringent durability and comfort demands. Each year, during the summer holidays, scores of people leave the Netherlands by car in the general direction of France, Italy and Spain. While the majority reaches their destination - exhausted from the long ride - a few percent experiences car failure. Some truckers on the other hand make this journey day in day out. They have to be able to rely on- and live in their vehicles.

Durability is the most important design aspect: if the vehicle fails, the cost of transportation rises. Consequently, each component of modern day commercial vehicles is designed such that it does not fail during the nominal life-span of the vehicle. Herein, the nominal life-span ranges from approximately 350.000 km for short distance- up to 1.600.000 km for long distance vehicles, Liebrechts (2007). Note that this is considerably more than that of passenger cars, which is one of the reasons they are commercially viable.

The other aspect that makes trucks commercially viable is the gross weight they can transport. A fully loaded tractor semi-trailer can weight up to 40.000 kg. With a (commercial) load of 27 tons, this gives a load to vehicle weight ratio of 0.675, Liebrechts (2007). In comparison, a typical passenger car can reach about 0.33 when fully loaded. However, typically this ratio is below 0.1. So, commercial vehicles are clearly optimized to make money. Herein, the optimization constraints (like vehicle

dimensions) are mainly determined by legislation.

A life on the road is not always without risks. There is a relatively large number of fatalities in traffic accidents with commercial vehicles. For example, in the Netherlands there are approximately 150.000 trucks versus more than seven million passenger cars. Nevertheless, when looking at traffic fatalities in the period 1999 to 2001, one in six was caused by accidents with truck involvement. This is one of the reasons that many truck manufacturers are investigating the use of electronic systems to further enhance the safety of their vehicles, Schilperoord (2007).

Driving a 40 ton vehicle requires a massive engine and gearbox. To provide room for these, the cabin is located relatively high above the road. Consequently, the driver position is less than optimal for good ride, Gillespie (1985). Due to the high position, cabin pitch and roll result in considerable longitudinal and lateral motion. To make things worse, (vertical) road vibrations as well as shocks from the trailer can further heighten the feeling of discomfort.

Driver comfort, which is related to the acceleration levels of the cabin, has been one of the main engineering topics ever since the first commercial vehicles emerged. However, as a result of the long days on the road, exposed to many sources of vibration, truckers are still the most common occupation seen in a chiropractic office (second most common are nurses). Their complaints are typically a mixture of muscle and/or lower back pains, Phillips (2009). So, from the point of view of the driver, a further improvement of cabin comfort is clearly required.

Moreover, the impact of driver discomfort in commercial vehicles on the economy is huge. It reduces performance and is also the leading cause of industrial disability for persons under 45 years of age, accounting for 20% of all work injuries. The total cost per year for the United States is estimated at 90 billion dollar, Deprez et al. (2005). For these reasons, the European parliament is working on directives to restrict the effect of whole-body vibration. One of the results is Machinery Directive 98/392/EEC and its amendments of 1996, which forces manufacturers of mobile machinery to reduce the influence of noise and vibration to the lowest possible level, by taking into account all available technical developments, Donati (2002).

1.2 A brief history of commercial vehicle suspensions

The first trucks and passenger cars emerged almost at the same time, at the end of the 19th century. Both types of vehicle have evolved according to different criteria ever since. While passenger cars and busses were designed to transport passengers at a high level of personal comfort, the truck has evolved along the lines of a highly efficient, durable machine for transport of goods, Gillespie (1985).

The fact that driver comfort is not the main evolutionary criteria does not mean that it is not taken into consideration. On the contrary driver comfort, as well as the

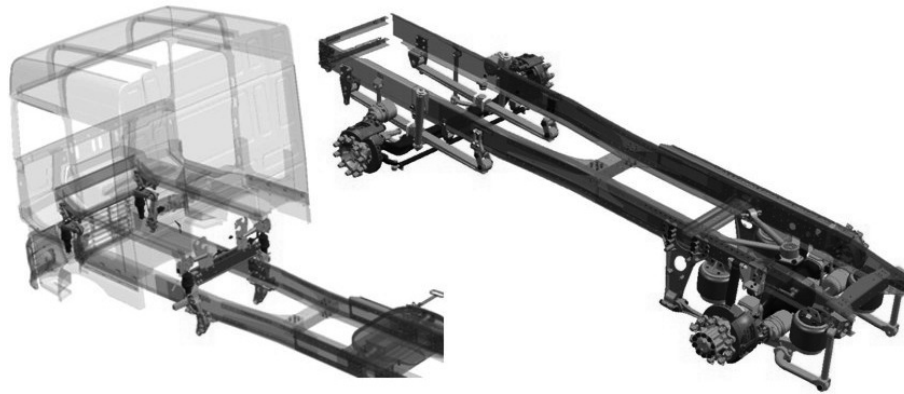


Figure 1.1: Schematic representation of a secondary (left) and primary (right) tractor suspension, Liebrechts (2007).

cabin dynamics when braking, accelerating or steering (attitude behavior), have been significantly enhanced over the years. The first commercial vehicles had relatively small solid rubber tyres and no suspension worth mentioning. Pneumatic tyres emerged in the 1920's, reducing the vibrations to the cargo and increasing driver comfort.

In the years after, driver comfort was slowly enhanced by variations in the suspension between the axle and the chassis (primary suspension, see Figure 1.1). As a consequence of the high loads, the only option in those days was a leaf spring design. Various designs for front and rear axle configurations with leaf springs can be found in Gillespie (1985).

In the 1950's the first sleeper cabs emerged, as drivers were more often forced to spend the night in the vehicles. Still, it wasn't until the 1960's that changes were being made in the trucks secondary suspension. Till then, the cabins were welded to the chassis, resulting in a relatively uncomfortable ride. Especially considering that the roads in those days were of poorer quality than what we are used to today. Consequently, the use of rubber suspension mounts between the chassis and cabin was quite an improvement. Moreover, in the same period the first tilt cab's emerged, which are still the standard today, as they greatly facilitate drive-line inspection.

A major drawback of the more comfortable secondary suspension, was the poorer cabin attitude behavior. Ideally, from a handling point of view, the cabin follows the motions of the chassis perfectly. However, due to the lower stiffness of the secondary suspension, the cabin had a yaw delay and increased roll when steering, as well as an increased pitch motion when braking or accelerating. The roll and yaw problems were "solved" by means of a very stiff roll stabilizer in the years to come. However, the rigid connection through the roll stabilizer is again a source of discomfort for the driver.

In the 1970's and 1980's the secondary suspension evolved further with various steel- and air sprung designs. Furthermore, air sprung suspensions were also becoming more common in the primary suspension (especially for the driving axle). Looking at modern day trucks, it can be seen that this trend is still continuing. There are both leaf sprung and air sprung primary suspensions, as well as steel sprung and air sprung

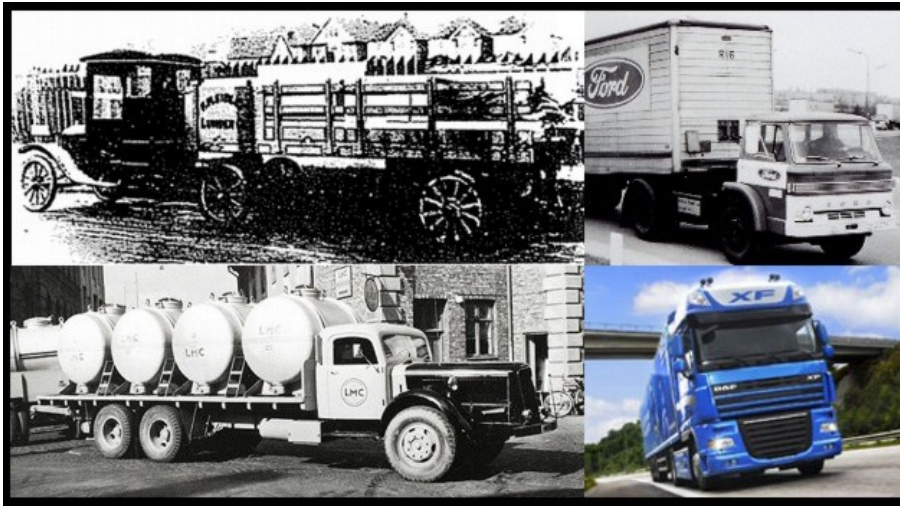


Figure 1.2: Some tractor semi-trailer designs through the years. *Ford* tractor with *Fruehauf* semi-trailer from 1911 (top left), Gillespie (1985). *Volvo* from the 1940's (bottom left), Volvo (2009). A *Ford* continental from the 1970's (top right), Ford (2009) and a modern day *DAF XF* (bottom right), DAF (2009).

cabin suspensions. Since the early years, the cabin seats have also greatly evolved. Currently, air sprung seats are the standard on heavy-duty trucks.

So, looking back at history (Figure 1.2), enhancing driver comfort has been a constant engineering effort of many truck manufacturers. Particularly important steps were the air sprung tyre, air sprung primary suspension, air sprung secondary suspension and air sprung driver seat. However, the last big step in comfort enhancement dates back quite a few years. So, what will be the next one? Or is this the best we can do?

1.3 Enhancing cabin comfort: recent developments

In the previous section it is mentioned that trucks and cars evolved following different lines. Driver and passenger comfort has been more important for cars than for trucks. So, when looking to enhance truck cabin comfort, it is natural to first study recent developments in passenger cars.

Suspension systems can be roughly divided into three types: active, semi-active and passive suspensions. Passive spring-damper suspensions dominate the market. In passive suspension design the choice of the suspension stiffness is mainly determined by the type of vehicle, as there is a trade-off between comfort and handling behavior. In luxury saloon cars, where comfort is important, the stiffness is relatively low. On the other hand, in sport cars where handling is important, the stiffness is higher resulting in a less comfortable ride. Although, it may be possible to further enhance passive suspension performance using nonlinear stiffness and damping characteristics, and/or interconnection (Zhang et al. (2010)); the overall potential for passive suspensions is limited.

Active and semi-active suspensions are more promising. Herein, active suspensions have the ability to add energy to the suspension system, where semi-active systems only control the rate of energy dissipation. Consequently, fully active suspensions can give the greatest comfort increase, but this comes at the cost of a high energy demand. The trade-off between semi-active and active suspensions is that of power consumption versus performance. In Fischer and Isermann (2004), an overview is given of the expected suspension performance and energy demand for passenger cars. Herein, it is said that semi-active suspensions may give a comfort gain of 20-30%, at a cost of approximately 50 W. On the other hand, active suspensions are expected to give more than 30% comfort gain, but at a cost of 1-7 kW. Due to the high energy requirements of active suspensions, many modern day car manufacturers choose to upgrade their suspensions with semi-active designs.

As a consequence of the promising results using semi-active passenger car suspensions, the *Eindhoven University of Technology* and several companies including *DAF*, started a project called *CASCOV* in 1992. The goal of the project was the development of a semi-active rear-axle suspension for heavy-duty vehicles. In Muijderman (1997), a semi-active control strategy is developed and the differences between two-state and continuous variable semi-active dampers are evaluated in simulation. Herein, the observer design of Huisman (1994) is used to construct a preview controller. The control strategy is evaluated in Vissers (1997) on an experimental truck. However, the results are rather disappointing, as the controller proved highly sensitive to measurement and reconstruction errors.

Despite these early setbacks, it is expected that it will not be long till semi-active suspension designs are adopted by truck manufacturers. In the 2008 paper by *Scania* and *KTH*, Holen (2008), it is shown that a substantial performance increase can also be obtained for heavy-duty vehicles using modally distributed semi-active damping in the secondary suspension. Especially the influence of the bounce and pitch modes is reported to diminish.

For enhancement of driver comfort in heavy-duty vehicles, optimization of the secondary suspension is preferable. The goal of the primary suspension is to carry the immense load, protect the cargo from shocks, minimize road damage and at the same time provide good handling behavior. Consequently, there is little lenience towards driver comfort in the design. Not even if the suspension includes (semi-) active devices. The sole task of the secondary suspension, on the other hand, is to enhance driver comfort and optimize attitude behavior. Therefore, the logical place for a (semi-) active suspension, when aiming for comfort and attitude enhancement, is the secondary suspension. Even more so, considering the fact that the power consumption is related to the weight of the suspended mass.

Power consumption is a very important topic for commercial vehicles. This inspired a group of Japanese researchers to investigate the concept of a self-powered truck cabin suspension. The concept was first presented in 1999, Nakano et al. (1999) and in 2004 an actuator design followed, Nakano and Suda (2004). It is proposed to use an energy

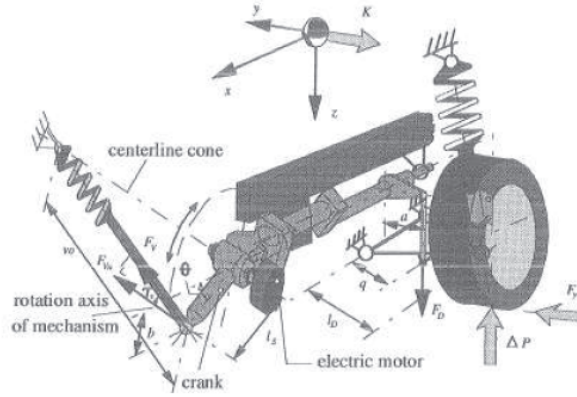


Figure 1.3: The Delft Active Suspension (DAS), Venhovens and van der Knaap (1995).

regenerative damper in the primary suspension. The acquired energy can then be used to enhance the performance of the active secondary suspension. Simulations with a half truck model demonstrate the feasibility of this idea. The “screw-type” actuator design has been patented by *Toyota* for the European market, H. Inoue and Kondo (2007).

The variable geometry actuator is another active alternative with a power consumption that is potentially lower than that of conventional active designs. The first concept was presented in 1995 as the *Delft Active Suspension*, Venhovens and van der Knaap (1995), see Figure 1.3. The basic idea behind the concept is based on a wishbone which has a spring (under pretension) connected to one end. The sprung mass is connected to the other end, and a rotary joint is placed in the middle. By changing the distance or orientation of the spring with respect to the joint, the force on the suspended mass is changed (equilibrium of moments). This change of position, the variation of geometry, can be realized with relatively little energy when the spring force is perpendicular to the direction of motion. Feasibility of the *Delft Active Suspension* has been demonstrated on a (real) passenger car.

An exploratory study, in association with *Daimler*, with respect to the effectiveness of active secondary suspensions is presented in Graf et al. (2008). Herein, it is claimed that huge comfort enhancements are obtainable - up to 78% - using a modal control strategy. However, cabin attitude behavior, suspension travel, actuator characteristics and power consumption are not taken into account. Still, despite the fact that further research is clearly needed, these results are promising.

The need for more research activity on the areas of secondary suspension design and controllable suspensions for heavy vehicles is also stressed in Cole (2001). Furthermore, it is mentioned that the topics of ride discomfort- and ride/suspension performance criteria also require more attention. In most studies, performance is evaluated under conditions of constant speed and straight-line travel, omitting the important attitude aspect.

1.4 Suspension performance criteria

The main task of a suspension is to limit the influence of the “noisy” environment to the suspended mass, in other words to limit the transmissibility. In a vehicle setting, this is closely related to the comfort of the driver. However, the suspension also influences the handling or attitude behavior. As a result, there is a trade-off between comfort, handling, and suspension travel.

Ride comfort and handling or attitude behavior are not the only active suspension design criteria. In Cole (2001) seven are specified: ride; suspension working space; energy consumption; infrastructure damage; rollover stability; yaw stability; and braking and traction. As the focus of this thesis lies on the cabin suspension, the last three are not considered. Furthermore, suspension working space can also be seen as a design constraint, instead of a design criteria.

Commercial vehicles are optimized to minimize the cost per transported kilogram, Fancher and Winkler (2007). Consequently, minimization of the energy consumption is very important. Cost is also at the basis of the last criterion. The suspension is a safety critical part of the vehicle. If it fails the costs will rise, so durability is key. Each of the mentioned suspension criteria (comfort, handling, energy and durability) is shortly discussed in the next subsections.

1.4.1 Comfort

Driver (dis-)comfort is a subjective matter which differs from one individual to another. Several objective measures have been developed over the years. However, it is difficult to distinguish the small differences that test drivers perceive, Strandemar (2005). Therefore, these measures should only be used to augment the findings of the drivers and possibly gain some additional insight.

Standards

At present there are two standard methods to predict driver discomfort in vehicles. The first is BS 6841 (1987), which was posed as a reaction to the ISO standard ISO 2631(1985). The latter was revisited in ISO 2631-1 (1997), so that the two are now quite similar. Both methods are based on the root-mean-square (rms) value of the frequency weighted accelerations. Difference is made between sitting, standing and lying positions, but in this thesis only the sitting position is considered. The frequency weighting at the backrest of the seat according to the ISO standard is given in Figure 1.4.

Clearly, there is a large difference in (dis)comfort experience for the different disturbance directions. In vertical (heave) direction, disturbances between 4-8 Hz are considered to be relatively uncomfortable. On the other hand, for the longitudinal and lateral direction 0.7-2 Hz disturbances are weighted more heavily. Furthermore, for the rotational directions the disturbances between 0.5-1 Hz result in the relatively highest

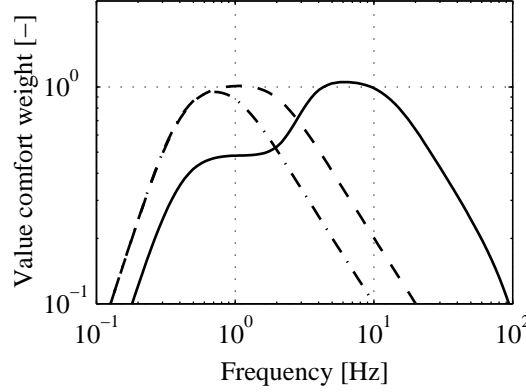


Figure 1.4: ISO 2631(1997) comfort weighting. Vertical direction (solid); longitudinal and lateral direction (dashed); roll, pitch, yaw direction (dash-dotted).

level of discomfort. Moreover, it is also mentioned that vertical vibrations, and possibly also rotational vibrations, below 0.5 Hz may result in motion sickness. Following ISO 2631-1 (1997), the level of comfort can be determined by calculating the point total vibration value

$$a_v = \sqrt{k_x^2 a_{wx}^2 + k_y^2 a_{wy}^2 + k_z^2 a_{wz}^2 + k_\theta^2 a_{w\theta}^2 + k_\phi^2 a_{w\phi}^2 + k_\xi^2 a_{w\psi}^2}, \quad (1.1)$$

where a_{wi} are the rms frequency weighted accelerations

$$a_{wi} = \sqrt{\frac{1}{T} \int_0^T a_{wi}^2(t) dt}, \quad (1.2)$$

$a_{wi}(t)$ the instantaneous frequency weighted accelerations of the driver seat surface, and $i \in [x, y, z, \theta, \phi, \psi]$ are the longitudinal-, lateral-, and horizontal directions, rotation around y (pitch), x (roll) and z (yaw) respectively. Furthermore, $k_i : k_x = k_y = k_z = 1$, $k_\phi = 0.63$, $k_\theta = 0.4$, $k_\psi = 0.2$ are multiplying factors, and T is the total time period. If the weighted value in one direction is less than 25% of the total value it may be omitted. Furthermore, when more than one point is measured, the different point total vibration values can be summed in a way identical to that done in (1.1) to obtain the total vibration value.

The total vibration value (1.1), sometimes called Ride Comfort Index (RCI), does not always suffice to predict driver discomfort. The RCI is known to underestimate the importance of incidental shocks. An indication whether this is the case is given by the crest-factor, which is defined as the modulus of the maximum instantaneous peak value of the frequency weighted acceleration signal to its rms value. For vibrations with crest factors below 9 it is said that the RCI-method can be applied. If this is not the case the fourth power vibration dose method, which is also included in ISO 2631-1 (1997), may give better results:

$$VDV_{total} = \left\{ \sum_i \int_0^T (k_i a_{wi}(t))^4 dt \right\}^{\frac{1}{4}}. \quad (1.3)$$

The Vibration Dose Value (VDV) is time dependent as the time period during which vibrations are experienced also influences the sense of discomfort.

Ride comfort for commercial vehicles

A discussion on ride comfort for commercial vehicles and the means to enhance this is given in, Jiang et al. (2001). Herein it is mentioned that the tyre and primary suspension parameters are determined by the vehicle configuration and as such cannot be compromised to enhance the ride comfort. So, the variables that remain are seat suspension stiffness and damping and cabin suspension stiffness and damping.

According to Jiang et al. (2001), a good computer simulation model for comfort analysis requires the following modules:

- A vehicle module, which describes the dynamic behavior;
- A road profile input module, which supplies the road excitation;
- A seat and driver body module.

Herein, it is important that the vehicle model incorporates a flexible chassis model to accurately simulate vibrations above 5.6 Hz. The general idea seems to be that adding more detail automatically leads to a better prediction. However, no proof is provided that driver comfort can be accurately predicted when adopting these recommendations.

Highly detailed models may limit the physical understanding and even lead to a false sense of accuracy. For suspension design it is important to understand the main aspects of the vehicle that may limit the ride quality. Herein, the models should be kept as simple as possible, while still covering the main effects. In general, the required complexity depends on the intended use. For example, when optimizing seat geometry, Verver (2004), highly complex seat and driver models are required. On the other hand, when designing suspension controllers, a much lower model complexity is desirable. For that reason and the fact that there is no available measurement data for validation, the seat and driver body module are omitted in this thesis.

Comments on the standards and alternative methods

An individual with a long history in the field of ride comfort analysis is M.J. Griffin. In Griffin (2007), an overview is given of his findings and a number of suggestions are given to enhance the standards. The main points are summarized below.

Firstly, the standards assume that a doubling of vibration magnitude has the same discomfort effect for all frequencies, which is not the case in practice. Moreover, the standards do not give precise information on comfort thresholds, i.e., the minimum vibration magnitudes which can be sensed. This would be essential information for suspension optimization studies like considered in this thesis.

Secondly, the frequency weightings in the standards are not optimal for very-low-magnitude vibration. In those cases the weightings vary less as a function of frequency.

Moreover, the predicted discomfort due to roll and pitch vibrations at frequencies below 0.4 Hz is unreliable.

Thirdly, the standards do not consider the influence of relative motion between different vibration sources. However, such motions can result in discomfort, especially concerning motion between the seat and feet. Furthermore, at frequencies below 2 Hz, phase differences between the different directions of motion may also influence discomfort.

Finally, time dependency is not included in the standards. It is expected that the time-dependent effects vary as a function of frequency and direction. Consequently it will be difficult to include these in a single measure. Experimental studies indicate that there is (very roughly) a fourth-power relationship between acceleration magnitude and duration. Consequently, the root-mean-quad (rmq) value seems more appropriate for comfort prediction

$$rmq(a_{wi}) = \left\{ \frac{1}{T} \int_0^T (a_{wi}(t))^4 dt \right\}^{\frac{1}{4}}, \quad (1.4)$$

as it gives more relative weight to shocks. However, like the rms value it does not increase with duration, while vehicle vibration tends to become more unacceptable for increasing time periods. For that reason, Griffin (2007), recommends the use of the vibration dose value (VDV) given in (1.3), as “there is no evidence that there is any measure with a higher level of accuracy.”

Another interesting alternative is given in Strandemar (2005). It is suggested that the driver comfort perception can be predicted more accurately using a so-called ride diagram. Herein, a difference is made between mean-square stationary (MS_{stat}) and transient (MS_{trans}) accelerations, and both are plotted as a function of the vehicle velocity. An example is given in Figure 1.5. In the figure the ride diagram for two different cabin suspension settings is depicted. According to the test drivers the most comfortable cabin setting is the one represented by the solid grey line.

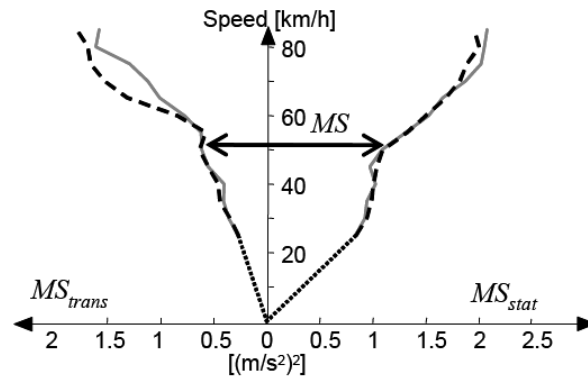


Figure 1.5: Ride diagram, based on measurements from a *Scania* tractor semi-trailer combination with two different cabin suspension settings, Strandemar (2005).

The main difficulty lies in relating the ride diagram to the perceived level of discomfort. The transient effects appear to have a relatively large influence on the ride

comfort evaluation. However, there also seems to be a correlation between the opinions of the test drivers and the shape of the ride diagram. In the example of Figure 1.5, the test drivers indicated that the highest level of discomfort is generated by both cabs around 60 km/h, where the increase in mean square accelerations is the highest. More research is required to properly evaluate this approach, especially when considering very large vehicle modifications as would be the case when evaluating (semi-) active suspension designs.

Ride comfort prediction in this thesis

Following the recommendations of ISO 2631-1 (1997), the comfort prediction in this thesis is based on the rms value of the ISO weighted accelerations (1.1) and, when crest factors are above 9, the vibration dose value (1.3). However, it is evident that the topic of comfort prediction for heavy road vehicles still contains a lot of open questions.

1.4.2 Handling and attitude behavior

Vehicle handling behavior is, like ride comfort, a subjective notion that differs from one driver to another. It signifies the response of the vehicle to driver steering, braking and accelerating. Typically it is desirable to have a minimal time- or phase-delay between driver input and vehicle response. Moreover, the vehicle response should be predictable, so (strong) nonlinearities are undesirable.

From a suspension perspective, the handling behavior of a vehicle is often evaluated using the dynamic tyre load, see for example Muijderman (1997); Venhovens (1993). However, the attitude behavior - the cabin heave, roll, pitch, yaw response as a result of driver steering, braking and accelerating - is often omitted. The influence of the secondary suspension design on the dynamic tyre loads is relatively small. Therefore, only the attitude behavior is evaluated in this thesis. Herein, the vehicle yaw-response should ideally show a linear relation with the steer input, Williams and Haddad (1995).

When braking or accelerating in a modern day truck, the cabin shows significant pitch and heave motion. The ideal response, is expected to depend on the preferences of the driver. When the longitudinal accelerations are sufficient for the driver to assess what is happening, all pitch and heave motions can be fully suppressed; making the cabin a stabilized vehicle command platform. Alternatively, if the driver desires more feedback, the heave and pitch response of the cabin should mimic that of the chassis.

One of the main problems with the commercial vehicles of today is the threat of roll-over. As such, the ideal cabin roll response when cornering is a difficult issue. Some drivers might argue that all cabin roll should be compensated for optimal vehicle control and overview. Others find the roll feeling to be essential for safety. As mentioned in Sampson and Cebon (2003), one of the problems that cause trucks to roll-over lies in the fact that truck drivers have no feel for the dynamics of the trailer(s). Active cabin suspension systems have the potential to increase the interaction.

In literature there is quite some work on roll-over analysis and prevention, see for example Acarman and Özgüner (2006). One way to lower the risk of roll-over, is the use of power consuming (hydraulic) actuators that tilt the trailer(s), Miede and Cebon (2005). However, as long as the driver is not notified of the roll condition of the trailer the danger of roll-over remains. The *Electronic Stability Program (ESP)*, Van Zanten (2000), is an alternative that does inform the driver. It identifies dangerous situations and gives an automated braking response when roll-over is imminent.

Desired attitude behavior in this thesis

In this thesis, the attitude behavior is defined as the driver induced cabin yaw, roll, pitch and heave, when braking, accelerating or steering. It is assumed that the ideal cabin yaw, roll and pitch response under these conditions mimics the driver induced (low frequent) chassis motions. This way, the driver has optimal feedback of the vehicle's dynamics.

1.4.3 Energy

Users of commercial vehicles, i.e., the transporting industry, have the desire to transport a maximum amount of load at the lowest possible cost. Therefore, every single design is optimized when it comes to weight, volume, durability, and production/operation cost.

In this thesis only the energy consumption of the various active elements is evaluated. Energy neutral (see Nakano et al. (1999); Nakano and Suda (2004) and Kawamoto et al. (2008)) or energy optimal control may be desirable from an economic point of view, but there will be a trade-off with the suspension performance in terms of comfort and attitude behavior.

1.4.4 Durability

The topic of durability evaluation is very important, but also complex, see for example Dressler et al. (2008); Baek et al. (2008) and Howe et al. (2004). Therefore, the durability of the active suspension designs is not considered in this thesis. However, before any type of active suspension can be employed in a commercial vehicle, such an analysis will be required.

1.5 Problem statement and objectives

Improving cabin comfort has been an engineering challenge ever since the first commercial vehicles were designed. Currently, the options for further enhancement using passive suspension devices are limited. However, several semi-active and active alternatives are available. Herein, the latter offers the biggest performance gains, both with respect to cabin comfort and attitude behavior, but also requires the most development.

In this thesis the focus lies on active suspensions. More specifically, the following problem is addressed:

In which manner, using a low-power active secondary suspension, is it possible to further enhance the cabin comfort and attitude behavior of commercial vehicles?

In view of this problem, the research objectives are defined as:

1. Develop and validate a tractor semi-trailer model, which is suitable for comfort and attitude studies;
2. Develop a model for a new design variable geometry actuator and use it to evaluate the actuator's characteristics;
3. Design a cabin controller, for the tractor semi-trailer model equipped with variable geometry active suspension, that significantly enhances cabin comfort and attitude behavior at a low energy cost.

1.6 Contributions

This research offers the following novel contributions:

1. A frequency domain model validation method for asynchronous repeated experiments with uncertain inputs, [Chapter 3];
2. Several experimentally validated tractor semi-trailer models, including a 44-DOF modular *Matlab SimMechanics* model, which is suitable for comfort and attitude studies, [Chapters 2 and 3];
3. An experimentally validated model with (local) control strategy for a new actuator design, the *electromechanical Low-Power Active Suspension (eLPAS)*, and an analysis of its characteristics, [Chapter 5];
4. A detailed analysis of the characteristics of the optimal vertical cabin control strategy, using Linear Quadratic Gaussian (LQG) control for a quarter truck model with *eLPAS* energy characteristics, [Chapter 6];
5. A low-power roll-pitch-heave cabin control strategy for the tractor semi-trailer system with *eLPAS*, that enhances both cabin comfort and attitude behavior under certain conditions. Furthermore, the limitations of the used linear controller design techniques are illustrated and insight is provided in the remaining challenges, [Chapter 7].

1.7 Outline and publications

The outline of this thesis is as follows. In Chapter 2, a modular 44-DOF tractor semi-trailer model is developed and validated in the time domain using experimental data. The model is based on work published in Evers et al. (2009b); Spijkers (2008), augmented with the insights detailed in Houben (2008) and Pinxteren (2009). Some additional tools are required to validate the model for the comfort relevant frequencies up to 20 Hz, which are developed in Chapter 3. In addition, reduced order models are developed and validated for analysis and controller design purposes. Some of these results have been presented in Evers et al. (2010b) and Evers et al. (2010a).

In Chapter 4, an overview is given of known suspension concepts. Several are lined-up and evaluated using a validated 4-DOF quarter vehicle model and skyhook control strategy. It is shown that the variable geometry actuator concept may provide the best performance. This result has been published in Evers et al. (2008a). The concept is further optimized in Chapter 5. The new *eLPAS* design is modeled, analyzed and evaluated experimentally. A part of these findings can be found in Evers et al. (2008b). Furthermore, in Sampaio (2009) and van der Sanden (2008) the possibilities for alternative actuator designs are further explored.

The topic of cabin controller design is addressed in more detail in Chapter 6, where the optimal control strategy is determined for the 4-DOF quarter vehicle model with *eLPAS* energy characteristics. Based on these insights, and using the other validated models, a roll-pitch-heave cabin control strategy is developed and evaluated in Chapter 7. Some of the early results have been presented in Evers et al. (2009a). Chapter 8 ends with the conclusions and recommendations.

Chapter 2

Tractor semi-trailer simulation model

2.1 Introduction

To study the problem as stated in the previous chapter a reliable tractor semi-trailer model is needed, which is suitable for comfort analysis and evaluation purposes. The model needs to be flexible, in the sense that design changes can be easily implemented and evaluated. Herein, design changes can be related to both changes in the simulated hardware components as to changes in the chosen control strategies. Furthermore, the model should (ideally) be able to describe the vehicle response for all imaginable feasible driving situations.

Multi-body modeling of commercial vehicles is not a new subject. General purpose software packages like *Adams*, *SIMPACK* and *LMS Virtual.Lab* have already been used for many years to study the dynamic behavior of commercial vehicles, and to investigate the effect of design changes. Although the models, created with these packages, can be quite complex, they typically lack the accuracy required for durability studies. That is where finite element models come in to play. Detailed tractor semi-trailer finite element models can contain over a million degrees of freedom. A large number of these generally lie in the flexible chassis, which is the part that interconnects the main truck components.

So, for durability studies a high level of complexity is necessary for sufficiently accurate results. According to Jiang et al. (2001), this complexity is also necessary for the evaluation of driver comfort. However, no proof is provided that reduced order models cannot give reasonable results, nor is it completely clear which dynamics are - and which are not - relevant. This is an important question, as limited complexity models generally simulated faster, which is beneficial for concept analysis and controller design. Furthermore, considering the many possible vehicle combinations, uncertainties in loading conditions, etc; complex models may actually give a false sense of accuracy.

In the last decade more dedicated software packages like *TruckSim*, and *veDYNA* have been developed. These packages include complete models of various types of

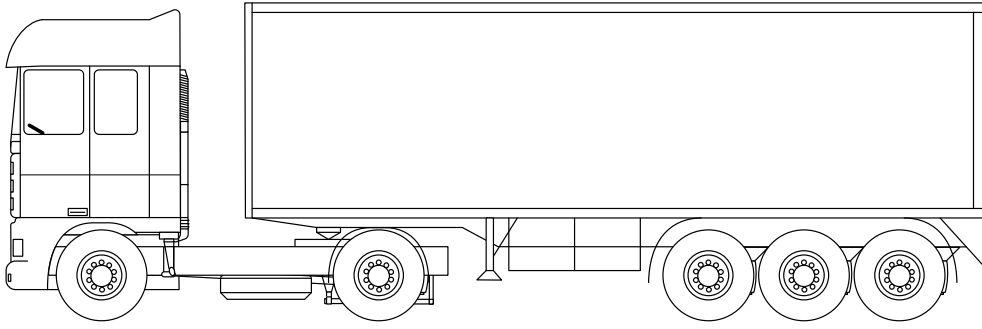


Figure 2.1: Tractor semi-trailer.

trucks which can be used for simulation and analysis of various events. One particularly interesting package is *Dymola/Modelica VDL* (see for example Philipson et al. (2008)), which has a modular hierarchy. Herein, the included module library can be used to easily create or reconfigure vehicle models. This is desirable given the wide variety of possible truck configurations (see Gillespie and Karamihas (2000)).

For the interaction with control software, these packages typically have the option to export the model. As such, the model can be loaded in, for example, MATLAB/*Simulink*. Alternatively, the use of two different software programs (with possible conversion issues) can be circumvented by using the multi-body toolbox of MATLAB/*Simulink*, *SimMechanics*. It has the advantage that it can interact with any level of controller developed in *Simulink* and that it allows a modular hierarchy. The main drawback however is the poor default visualization. This is especially bothersome when more complex systems are evaluated. Still, when using the MATLAB *Virtual Reality toolbox* the visualization can be acceptable, as is illustrated by Besselink (2006).

No matter which software package is used to construct a model, the last step of the procedure is the model validation. This last step is critical as it quantifies the accuracy of the model in its range of application. It is used to specify the overall quality of the model. Unfortunately, reports of the experimental validation of vehicle models developed with any of the packages mentioned above are scarce in the open literature.

In this chapter a modular vehicle model is presented for a tractor semi-trailer, as is schematically depicted in Figure 2.1. This configuration with a two axle tractor and a three axle semi-trailer is the most common layout on the European roads. The model is constructed in MATLAB/*Simulink* using the *SimMechanics* toolbox and is validated using a wide range of measurements, obtained with a DAF XF95 tractor semi-trailer. It is shown that even though the used model has some major simplifications of reality, among which a tractor chassis with only a single flexible mode, the simulation results give a fairly good real world representation. Overall, the model is considered to be suitable for the comfort and attitude evaluation of active suspension systems.

The chapter is structured as follows. First, an overview is given of the truck model hierarchy and the various component modules. Then, using the developed modules, the tractor semi-trailer simulation model is assembled and validated in the time-domain.

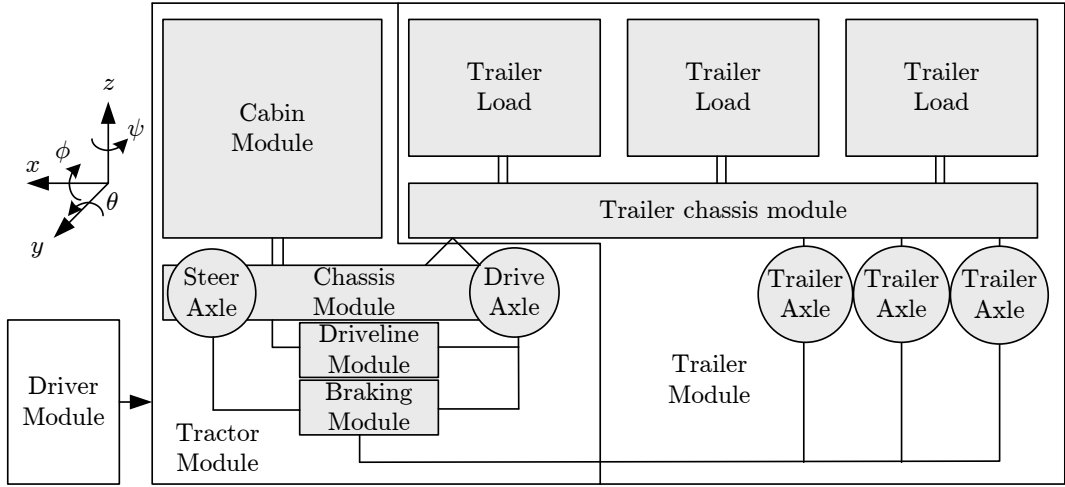


Figure 2.2: Model structure, connection of the modules.

Finally, the subject of frequency-domain validation is addressed.

2.2 Model hierarchy

The MATLAB/*SimMechanics* model is structured in a way that resembles the physical appearance of a truck. The chassis modules serve as the backbone for the model, to which the other modules can be connected. This way, the effect of using for example an additional trailer or a different drive-line can be verified more easily. The model hierarchy, for the tractor semi-trailer combination under consideration, is depicted in Figure 2.2. There are three main modules: the driver module; tractor module; and the trailer module. Herein, the last two consist of several other (sub)-modules.

The axis definition is also given in Figure 2.2. Herein, x represents the longitudinal, y the lateral, and z the vertical direction. Furthermore, the rotations ϕ , θ , ψ are called roll, pitch and yaw respectively. This axis definition is adopted throughout this thesis for the various vehicle models.

All the modules have their own parameters embedded and each module has its own coordinate system. As such, it is only required to specify the global position of the origin of this frame in its initial condition. All other components within the module are specified with respect to this coordinate system. The modules are interconnected with a single connection (rigid constraint). The complete model has 44 degrees of freedom (DOF) and is schematically depicted in Figure 2.3. Herein, the diamonds represent suspension elements. A more detailed view of the model is given in the Appendix, Figure A.1. The different modules are shortly discussed in the following sections.

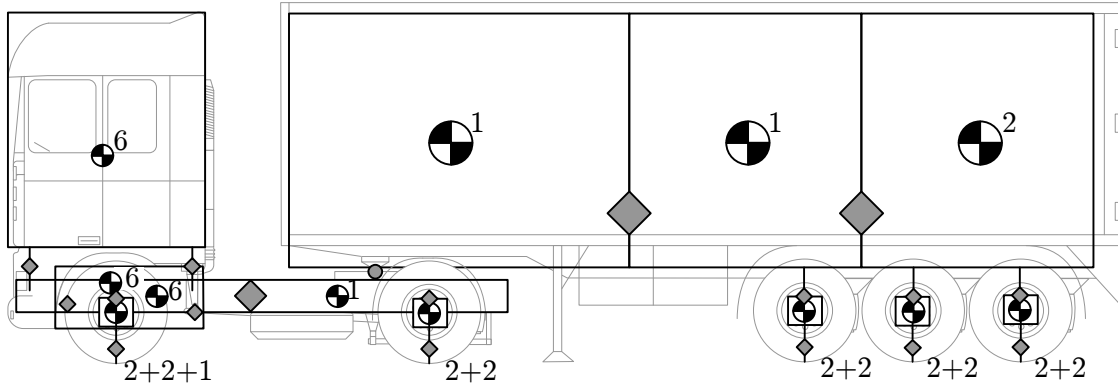


Figure 2.3: Schematic representation of the 44 DOF model.

2.2.1 Driver module

Modeling a driver and his or her driving behavior is complicated as driving styles are very personal. Furthermore, as remarked in Muijderman (1997), it also depends on the type of vehicle that is being driven. The driver influences the vehicle with the throttle, brakes, steering wheel and gear-shift, depending on the desired velocity and trajectory.

The driver module includes these driver inputs in a simplified way. There is a cruise controller, which outputs the throttle input as a function of the difference between the actual- and desired velocity (proportional-integral feedback). Herein, the desired velocity can be either specified manually, or it can be based on measurements. In case of the latter, the measured velocity is filtered with a 1 Hz second order butterworth filter, to limit the influence of measurement noise.

When the vehicle needs to decelerate, the cruise controller gives a zero value for the throttle input and the braking controller is enabled. The braking controller specifies the brake input as a function of the desired deceleration (feed forward) and the difference between the desired- and actual velocity (proportional feedback). Herein, the desired velocity and acceleration can be either specified manually, or it can be based on the chassis velocity and acceleration measurements, filtered with a 1 Hz and 2 Hz second order butterworth filter respectively.

Finally, the steering wheel angle can also be specified manually, or based on measurements data. As the measurement noise on this signal is relatively low, no significant filtering is necessary. However, to mimic the limitations of the driver a 20 Hz first order low-pass filter is implemented.

2.2.2 Tractor module

The tractor module consists of a chassis module, a cabin module, steer axle, drive axle, drive-line module, and braking module. Each of these is shortly discussed.

Cabin module

The cabin is modeled as a rigid body. In vertical direction, there are spring-damper combinations at each of the cabin corners. In lateral direction, it is fixed with rubber bushings with stiffness and damping at the front and dampers at the rear. All of the vertical suspension elements are modeled with bump-stops and a pre-load is also included to start simulations from an equilibrium. Furthermore, a leveling controller is implemented for pitch and heave, to cope with load changes. The leveling force is given by

$$\begin{aligned} F_{front} &= I_{front} \int_0^t (z_s^{FL} + z_s^{FR}) d\tau \\ F_{rear} &= I_{rear} \int_0^t (z_s^{RL} + z_s^{RR}) d\tau, \end{aligned} \tag{2.1}$$

where I_{front} , I_{rear} are control gains and z_s^{FL} , z_s^{FR} , z_s^{RL} , z_s^{RR} are the cabin suspension displacements at the front left, front right, right left and rear right respectively. However, no switching logic is included to handle the special case of cornering and/or braking maneuvers.

Chassis module

The chassis module consists of two lumped masses which are connected through a revolute joint with a torsion stiffness. As a result, the dynamically important torsion mode of the chassis is included in the model. This way of modeling the chassis flexibility is also used in for example *TruckSim*. The front mass is connected to the cabin module, the steering axle module and the drive-line module. The rear mass is connected to the driving axle module and the semi-trailer module. Naturally, this 7 DOF chassis model does not cover the complex flexible nature of the real chassis, but as will be shown later it gives a reasonable approximation.

Steering axle module

The front axle is modeled as a lumped mass which is connected vertically to the chassis using two linear springs (no bump-stops) and two nonlinear dampers which are parameterized using lookup tables. As a result, the axle has only two degrees of freedom (z, ϕ) with respect to the tractor chassis. Herein, the roll stabilizer is modeled as a (z, ϕ) -joint with rotational stiffness, which is located in the roll center.

A wheel hub is connected at each end of the front axle through a revolute joint with ψ freedom. The angle at these joints is determined by the steering system. For reasons of simplicity it is chosen to prescribe the steering angle as a multiplication of the steering wheel angle and the steering ratio. As such, the *Ackerman* geometry is not modeled, which will result in some inaccuracy for larger steering angles. Moreover, flexibility of the steering column, friction effects and play are all not included.

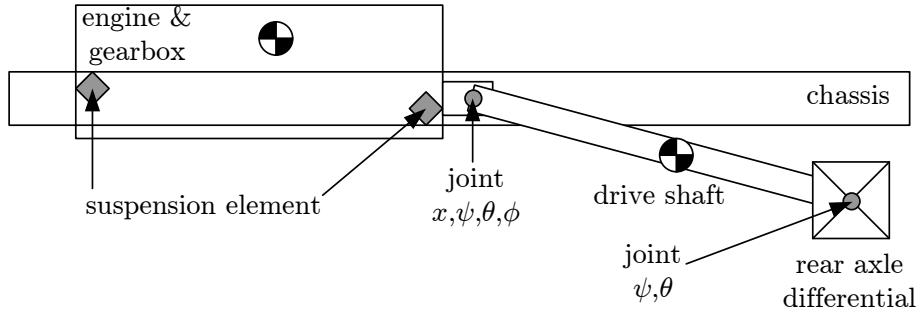


Figure 2.4: Drive-line model, side-view.

Each of the wheel hubs is connected using a revolute joint (ϕ rotation) to one of the front tyres. These tyres are modeled using the *TNO Delft Tyre* model, see Besselink (2006) and Pacejka (2002). The brakes can generate a braking moment that is applied on the revolute joints. These braking moments are computed in the braking module.

Braking module

The braking system consists of the brake and the pneumatic connections to all the braking disks on each of the wheels. In practice there may be a time-delay between the time of braking (application of brake pedal) and the time of clamping. Moreover, the driver also has the option to brake using the engine and/or a retarder.

The braking module is a simplification of the real world conditions. No retarders, load-dependent brake force distribution, or time delays are taken into account. The system generates the braking moment on each of the wheels as a linear function of the normalized driver braking input (brake pedal inclination).

Drive axle module

The driving axle module greatly resembles the steering axle module. However, there are three differences between both modules. Firstly, the wheels are not connected to the steering system. Secondly, there are four wheels, two at either side of the axle. Finally, the wheels are actuated by the drive-line.

Drive-line module

The engine and gearbox are lumped in one mass that is connected with four bushings to the chassis, see Figure 2.4. The mass is connected through a joint with four degrees of freedom (x, θ, ϕ, ψ) to the drive shaft. When accelerating (aggressively) with a tractor semi-trailer, the chassis will twist as a result of the engine torque and the chassis flexibility. To simulate this behavior, the joint is actuated in roll (ϕ) direction by the engine torque coming from the gearbox. The engine torque is computed with a lookup table using the angular wheel velocity and throttle as inputs.

Drive-line dynamics are not included in this model. Even though these may have a profound influence during certain maneuvers, see Dortland (2009); Zalm et al. (2008). Nevertheless, in steady-state the engine does generate a (realistic) torque on the chassis. The drive-shaft is connected through a joint with two degrees of freedom (θ, ψ) to the driving axle. As a result, the driving axle will not actually drive the wheels in θ direction. Instead, the driving moment is computed from the applied drive-shaft torque and the final drive ratio. This moment is directly applied to each of the wheels.

2.2.3 Semi-trailer module

The semi-trailer and its load have a very significant influence on the dynamics of the vehicle. Furthermore, it is important to note that the vehicle dynamics with liquid cargo differ substantially from those with solid cargo, see for example Acarman and Özgüner (2006). For this module a standard semi-trailer is considered. It consists of a flexible ladder-like chassis, three axles, and six tyres. Furthermore, it is carrying a maximum weight of stone bricks.

The flexible chassis is modeled as three masses which are connected with joints that allow torsion along the longitudinal axis. At each of these joints, a spring stiffness is added to mimic the chassis torsion stiffness. Rigidly connected to each of these chassis blocks (at a certain height above the frame) is a cargo block with a certain mass. Furthermore, the mid chassis mass is connected to one axle and the rear to two. The front trailer chassis mass is connected to the chassis module with the fifth wheel: a joint that allows pitch (θ) and yaw (ψ) rotation.

2.2.4 External influences

Apart from the driver inputs, the vehicle is influenced by two main external influences. First, there is the road profile, which is specified in the road profile file, that is included in the tyre software. The file consists of a table that specifies the road height as a function of the traveled distance.

Secondly, there are the aerodynamic forces, which act on the vehicle. From these, the one acting on the cabin has the largest influence, and is included in the model. The aerodynamic forces in $[x, y, z]$ direction, acting on the center of gravity of the cabin, are modeled as

$$\underline{F}_{aero} = \frac{1}{2} \rho A C_d [v_{air,x}^2, v_{air,y}^2, v_{air,z}^2]^T, \quad (2.2)$$

with ρ the air density, A the frontal surface, C_d the drag coefficient and $v_{air,x,y,z}$ the relative air velocity in longitudinal, lateral and vertical direction. Note, that although the values of C_d and A are in reality different for these directions, Ahmed et al. (1985), the same values are used in this model. Given the relatively stiff cabin roll-stabilizer, the lateral aerodynamic force is not expected to significantly influence the cabin dynamics for the case of the passive suspension. However, it may become a factor when studying suspension modifications.

Table 2.1: Axle weights in kg, measured and 44-DOF tractor semi-trailer model.

	No trailer		With trailer	
	Measured	Model	Measured	Model
Front	5230	5233	6860	6856
Rear	2250	2247	12680	12712
Trailer front			7250	7146
Trailer mid			7080	7055
Trailer rear			6700	6801
Total mass	7480	7480	40570	40570

The aerodynamic forces acting on the trailer are not taken into account. The aerodynamic effects are mainly visible during high speed maneuvers, wind bursts and heavy braking. As the relative air velocity is not measured, the cabin velocity is used as approximation: $\underline{v}_{air} = -\underline{v}_{cab}$.

2.3 Model parameters

The simulation model uses a large number of parameters, see Appendix A.1. All of these have a physical interpretation and some can be measured directly on the test vehicle. However, locations of the centers of gravity, the inertias, the torsional stiffness of the various chassis elements and the orientation of the suspension elements, are all more difficult to determine. Most of these have been estimated based on physical insight, information from the manufacturer, literature, and tuning.

The location of the longitudinal position of the various masses, for example, are tuned based on the weight measurements of the vehicle with and without trailer, see Table 2.1. First, the measurement without trailer is used for the positioning of the center of gravity of the chassis and the determination of the total mass of the tractor. Next, the measurement with trailer is used to determine the location of the center of gravity of the trailer.

Considering the axle loads, as given in Table 2.1, it can be seen that the loads obtained with the model are close to the measurements for the solo tractor. However, for the case with trailer, the front and rear trailer axle masses are approximately 100 kg (2%) off. This might be an indication that the trailer was slightly pitched during the measurements or that the position of the trailer axles is not modeled entirely correct. Still, the mismatch is relatively small and it is not expected to significantly influence the modeled dynamics.

2.4 Modal analysis

The dynamic behaviour of the tractor semi-trailer model can be split in a symmetric and anti-symmetric part. These two have virtually no correlation to each other, providing a good way to split up excitation, modes and response, Liebrechts (2007). The undamped eigenfrequencies of the model, and their corresponding eigen-modes are given in Table 2.2 (left). These have been determined using the linearization of the model at standstill. Herein, it should be noted that it is currently far from easy to obtain the modes of a *SimMechanics* model. For some modes a range is given, which indicates that multiple modes with a similar shape are within that frequency range.

Furthermore, in Liebrechts (2007) a list of the dominant eigen modes is also given for this type of vehicle, which has been determined with a more detailed finite element model. These modes are given in Table 2.2 (right). Given the complex shape of the modes, it is difficult to compare the results. For example, in the 44-DOF model there is a mode around 7.7 Hz in which the rear of the engine moves in lateral direction. Consequently, this mode could also have been labeled engine yaw-mode. There is no guarantee that this mode has actually the same shape as the engine lateral mode at 7.3 Hz mentioned in Liebrechts (2007). To give such a guarantee, it would have been necessary to determine and compare the shape of the eigenvectors of each mode of the two models, which is a rather complicated task.

2.5 The test vehicle

The truck under investigation is a DAF XF 95, air-sprung tractor semi-trailer, see Figure 2.5. It is owned by *TNO Automotive*, and the tractor has been equipped with a number of additional sensors for the purpose of model validation. Sensor data, at a 200 Hz sample-rate, is available from:

- 8 vertical acceleration sensors, above and below the cabin suspension;
- 4 vertical acceleration sensors, on the axles;
- x,y,z acceleration sensors and yaw velocity center of gravity chassis;
- x,y,z acceleration sensors at the front center of the cabin;
- roll, pitch and yaw velocity at the front center of the cabin;
- 8 displacement sensors, wheel and cabin suspension.

At standstill, the displacement sensors have a measurement noise root-mean-square (rms) value of approximately 1 mm; the rotational velocities are distorted with measurement noise with a rms value of 0.025 deg/s; and the acceleration measurements

Table 2.2: Vibration modes of a tractor semi-trailer model.

44-DOF model		Liebregts (2007)	
Symmetric modes	Freq. [Hz]		Freq. [Hz]
Cabin pitch	0.9		
Cabin bounce	0.9 – 1.5		
Cabin bounce + pitch	1.3	Cabin bounce + pitch	1.2 – 1.3
Trailer bounce	1.6	Trailer bounce	1.6
Tractor bounce	2.3	Tractor bounce	2.1
		Tractor pitch	2.8
Engine pitch	6.9	Engine pitch	7.6
Front axle bounce	10.4	Front axle bounce	10.6
Drive axle bounce	10.5	Drive axle bounce	10.4
Trailer axles bounce	11.7	Trailer axles bounce	12
Chassis + engine pitch	13.5		
Engine longitudinal	15.4		
Cabin top pitch	22.4		
Anti-symmetric modes	Freq. [Hz]		Freq. [Hz]
Cabin roll	1.4 – 1.6	Cabin roll	1.5
Trailer roll	2.4 – 2.8	Trailer roll	2.3
Cabin yaw	7.5	Cabin yaw	5.3
		Tractor torsion	6.5
Engine + front chassis roll	7.3		
Engine lateral rear	7.7	Engine lateral	7.3
		Trailer torsion	8.5
		Frame bending	8.8
Engine yaw	11.3	Engine yaw	10.2
Front axle roll	12.4	Front axle roll	11.2
		Fuel tank	11.5
Drive axle roll	11.1	Drive axle roll	12.4
		Battery carrier	12.7
Engine + cabin roll	16.2		
Trailer axles roll	16.4 – 16.9		
Chassis front roll + lateral	23.8		

have a measurement noise rms of 0.1 m/s^2 , see Spijkers (2008) for more details. Furthermore, the sensors near the center of gravity of the chassis (accelerations and yaw velocity) are the original vehicle sensors and are filtered onboard.

As the semi-trailer was not available for instrumentation, and the focus of the validation lies on the tractor (cabin) modeling, no additional sensors have been added to the trailer. For the validation, the measurements (real world and simulated) are filtered with a causal, anti-causal second order butterworth filter with a cut-off frequency of 45 Hz. This is approximately three times the highest frequency of interest for this model.



Figure 2.5: Tractor semi-trailer experimental vehicle.

Moreover, the simulated accelerations are obtained using a sensor model that includes the influence of gravity.

2.6 Time-domain validation

An extensive amount of measurement data has been obtained from a variety of tests with the test vehicle. Each test has been executed a number of times (trials). An overview of the tests is given in Table 2.3. All of these are performed with the tractor semi-trailer combination, unless stated otherwise. Note that some of the tests are performed for a number of initial velocities. For example, for the one-sided pyramid test there were five different initial velocities and three trials for each, making a total of fifteen experiments. On the other hand, for the comfort measurements there are: 4 experiments on smooth asphalt, 12 experiments on wavy asphalt, 12 experiments on concrete slabs, 12 experiments on a clinker brick road, and a single experiment on a Belgian blocks road. Furthermore, this set of 41 experiments was performed for the both the case with and without trailer. So, this makes a total of 82 experiments.

Given the large number of experiments and sensors, model validation is not a simple task. In this section, the main results from the time-domain comparison between the model and measurements are given. Herein, the data of the acceleration, braking, one-sided pyramid obstacle, and double lane-change are used to visually evaluate the quality of the model. The measurement data from the 82 comfort oriented tests is used for frequency domain validation in the next section.

Table 2.3: Overview of the performed tests.

Test	Init. velocity [km/h]	Trials	Remarks
Longitudinal		(18)	
Max accelerating	0	5	flat road
Max accelerating	0	5	6% road grade
Normal braking	60	5	approx. -1.5 m/s^2
Max braking	60	3	approx. -5 m/s^2
Road obstacles		(25)	
One-sided pyramid	[5, 7.5, 10, 12.5, 15]	3	Figure 2.14 (left)
One-sided step-down	5	5	Figure 2.21 (left)
One-sided threshold	5	5	Figure 2.21 (right)
Lateral		(16)	
Steady-state cornering	45	2	Left and right corner
Double lane change	[40, 60]	[3, 4]	
Step steer	[40, 50]	[2, 3]	
Comfort (straight)		(82)	
Smooth asphalt	[60, 80]	2	With and without trailer
Wavy asphalt	[60, 80]	6	With and without trailer
Concrete slabs	[60, 80]	6	With and without trailer
Clinker brick road	[40, 50]	6	With and without trailer
Belgian blocks road	40	1	With and without trailer

2.6.1 Accelerating

The first test under evaluation is an acceleration test on a flat surface. Herein, the driver starts from standstill, quickly accelerates up to approximately 9 km/h, without letting the wheels spin, and then presses the clutch. The test is performed in first gear. The effect of gear shifts is not evaluated, as those dynamics are not included in the model.

The vehicle's longitudinal velocity is given in Figure 2.6 (left). It can be seen that there is a sudden jump in the measured velocity at $t = 2.3$ seconds. This is a result of the fact that the CAN-bus output is zero for very low velocities. Furthermore, the oscillation of the measured velocity, after $t = 2.3$ seconds, is most likely caused by drive-line flexibilities, Dortland (2009).

This drive-line oscillation has a significant influence on the pitch dynamics of the cabin, see Figure 2.6 (right). So, in this respect the accuracy of the model is somewhat limited. Still, the overall trend of the simulation does resemble that of the measurements.

The longitudinal acceleration of the cabin and chassis are shown in Figure 2.7. Apart from the noise, the simulated and measured accelerations are quite similar. Still, there are two points of interest. Firstly, in simulation, the vehicle starts to move forward smoothly at $t = 1.8$ seconds. The test vehicle starts a little bit later, and there

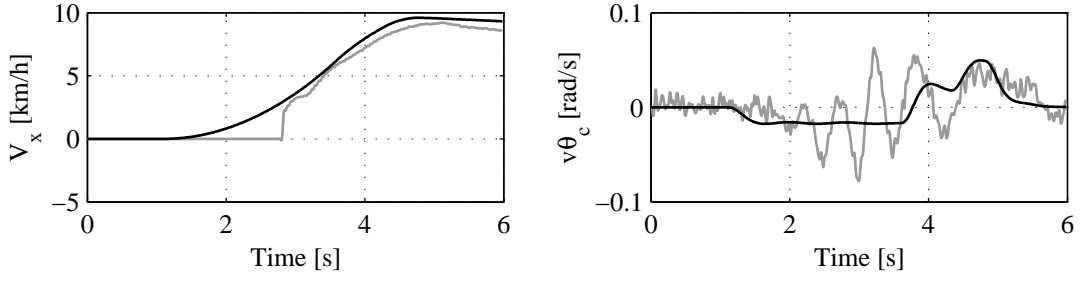


Figure 2.6: Acceleration test. Vehicle longitudinal velocity (left) and cabin pitch velocity (right); measured (grey) and simulated (black).

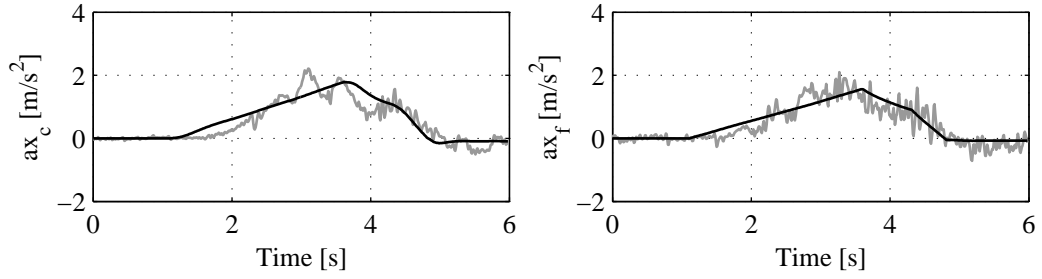


Figure 2.7: Acceleration test. Longitudinal accelerations cabin front center (left) and chassis center of gravity (right); measured (grey) and simulated (black).

is also a bit more oscillation in the acceleration signals, which is probably related to the drive-line elasticity. Secondly, at $t = 3$ seconds the measured cabin accelerations rise significantly more than those modeled. It is possible that this is the result of the excitation of one of the cabin pitch modes, as peaks like these have also been observed in some of the other trials of this test.

The comparison of primary suspension displacements, given in Figure 2.8, shows a good correlation. It can be seen that the relative displacement at the front left suspension has the largest difference between measurement and simulation. This is mainly the result of the velocity jump at $t = 2.3$ seconds, see Figure 2.6(left). The step input, which is given to the engine during the test, seems to be smoothed too much in simulation. Furthermore, note the difference between the front left and right displacement magnitudes. The left suspension travels almost twice as much as the one on the right side of the vehicle. This is the result of chassis torsion, which is included in the model.

When looking at the relative displacements of the secondary suspension, see Figure 2.9, a similar trend is visible. However, in this case the rear left suspension displacement is too large in simulation, even though the rear right displacement matches quite well. This is expected to be the effect of chassis torsion between the two cabin mounts, which is not included in the simulation model.

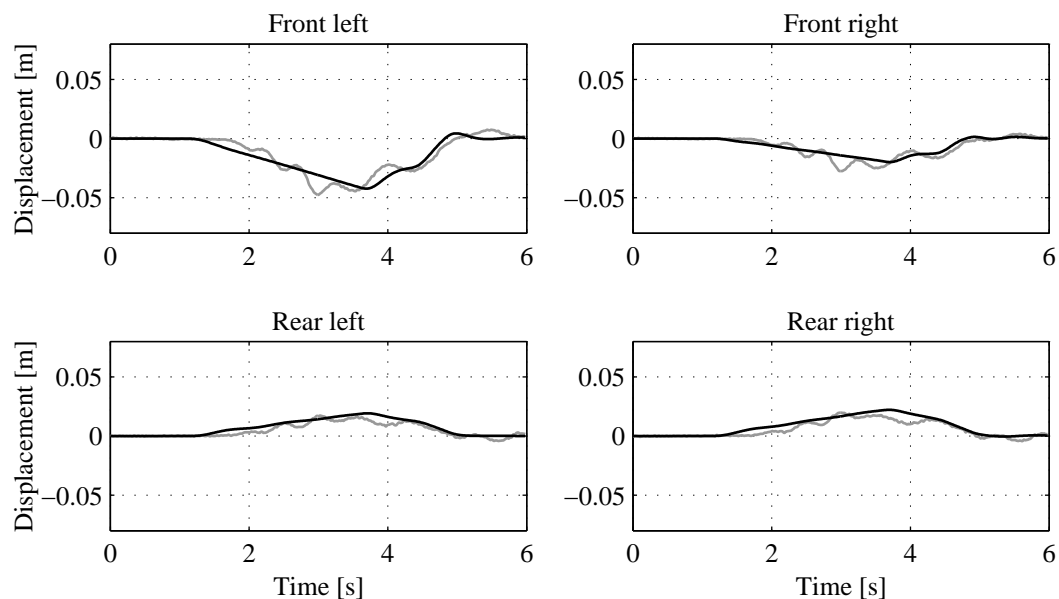


Figure 2.8: Acceleration test. Primary suspension displacements, measured (solid) and simulated (grey). Positive displacements correspond to compression.

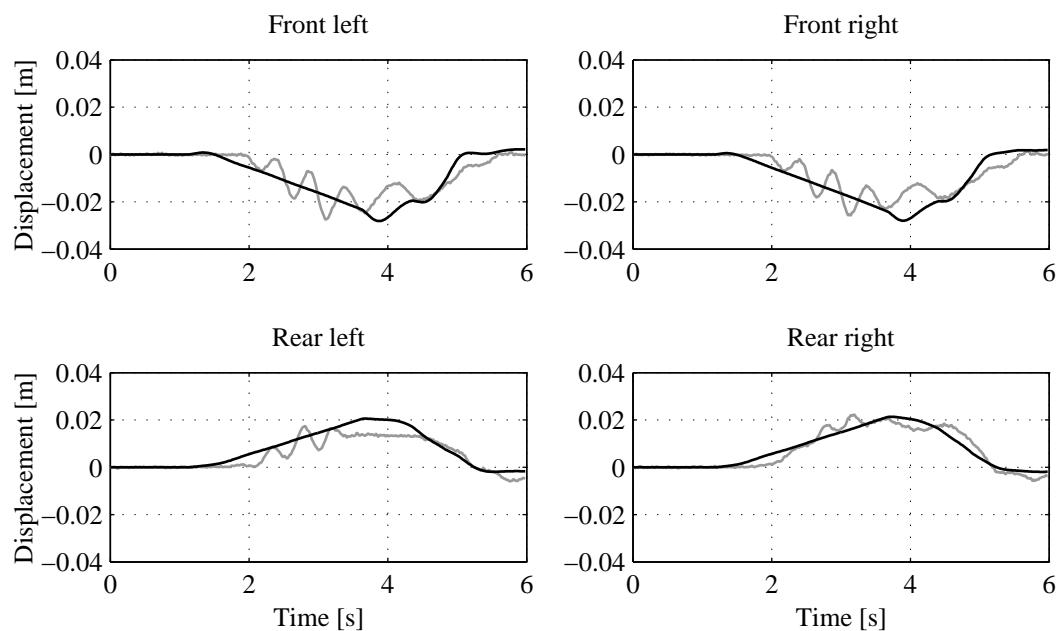


Figure 2.9: Acceleration test. Secondary suspension displacements, measured (solid) and simulated (grey). Positive displacements correspond to compression.

2.6.2 Braking

In this section the simulated braking response of the truck is compared to that of a real vehicle. The test driver was asked to drive on a straight road at 60 km/h and brake aggressively, with a constant brake pedal position, in an attempt to mimic

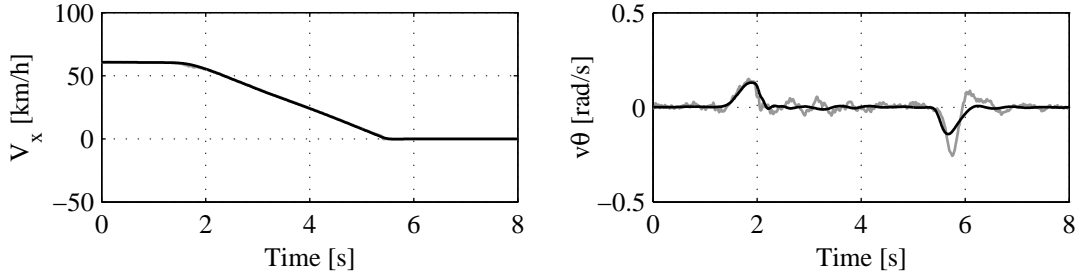


Figure 2.10: Braking test. Vehicle longitudinal velocity (left) and cabin pitch velocity (right); measured (grey) and simulated (black).

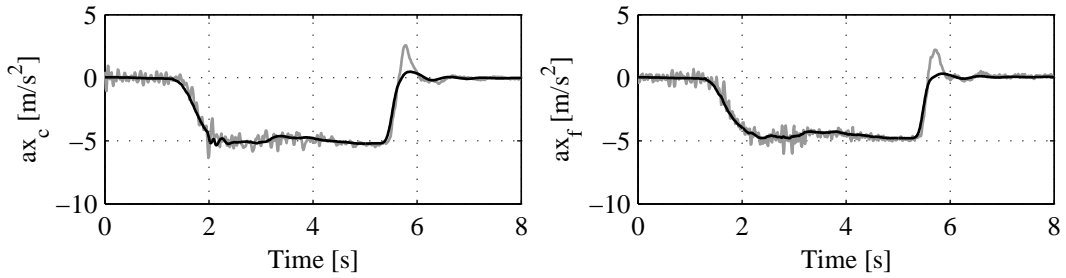


Figure 2.11: Braking test. Longitudinal accelerations cabin front center (left) and chassis center of gravity (right); measured (black) and simulated (grey).

an emergency stop. The longitudinal velocity of the vehicle is shown in Figure 2.10 (left). Clearly, the braking controller effectively minimizes the difference between the measured and simulated velocity profiles.

From the cabin pitch velocity, Figure 2.10 (right), it is possible to identify the two spikes of forward (at $t = 1.9$ seconds) and backward pitching (at $t = 5.8$ seconds). The first spike is predicted very well with the simulation model, whereas the mismatch at the second spike is substantially larger. Furthermore, after pitching forward the measurements also show an 1.6 Hz oscillation, which is not visible in the simulation.

When comparing the measured and simulated longitudinal accelerations at the chassis and the cabin, Figure 2.11, a profound mismatch is again visible between simulation and measurement around $t = 5.8$ seconds. The measurements show relatively large acceleration spikes when the vehicle comes to a complete standstill. This is mainly caused by friction effects in the brakes, which is not accurately modeled. To prevent this effect from occurring, truck drivers normally lift the brake prior to coming to a full stop.

When comparing the responses of the primary suspension displacements, see Figure 2.12, a small mismatch at the front and rear suspension is visible. Here, the mass distribution and height of the center of gravity of the trailer is expected to play a role. As a result, the trailer chassis pitches a little too much in simulation.

The response of the secondary suspension, see Figure 2.13, shows a similar result. However, here the simulated displacements are slightly lower than those measured.

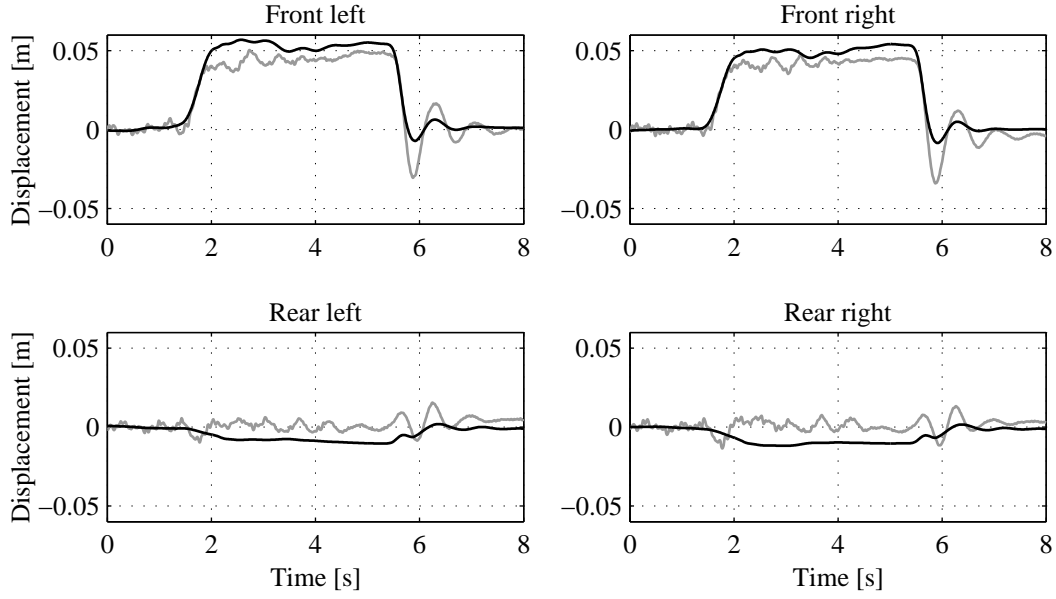


Figure 2.12: Braking test. Primary suspension displacements, measured (grey) and simulated (solid). Positive displacements correspond to compression.

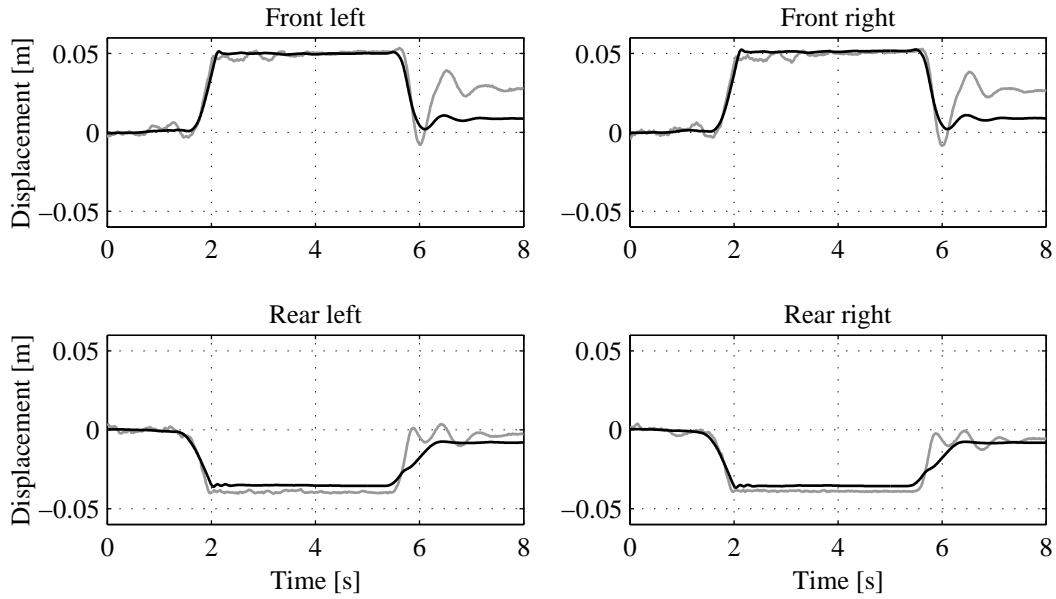


Figure 2.13: Braking test. Secondary suspension displacements, measured (grey) and simulated (solid). Positive displacements correspond to compression.

Furthermore, there is something else that deserves attention. For $t > 5.8$ seconds there is a profound difference in the front displacements. It can be seen that the truck cabin remains in a pitched position for quite a while after coming to a standstill. This is the result of the significant decrease in the aerodynamic force, which is also included in the model. However, what causes the mismatch at the front suspension is unclear. It

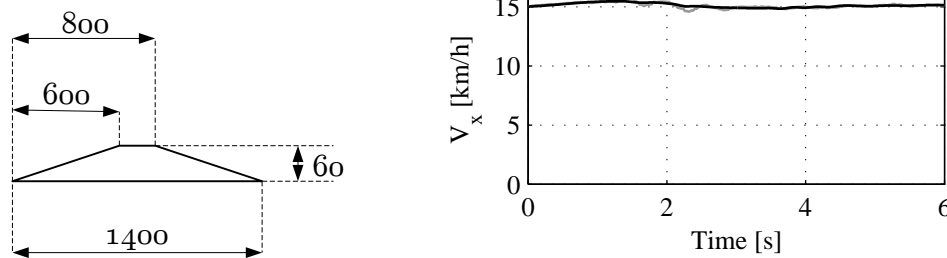


Figure 2.14: One-sided pyramid. Road input, with dimensions in millimeters (left) and longitudinal velocity (right); measured (grey) and simulated (black).

might be an indication that the vertical component of the aerodynamic force is also of influence.

2.6.3 Road obstacles

Next, the response to a discrete event is considered. A single representative experiment is selected from the wide range of available tests. The event under consideration is a trapezium-shaped road profile disturbance as given in Figure 2.14 (left), applied to the right side of the vehicle, and crossed with a nearly constant longitudinal velocity of 15 km/h, see Figure 2.14 (right). The front axle crosses the obstacle in the interval [1.15, 1.55] seconds, and the drive axle in the interval [2.1, 2.5] seconds.

In Figure 2.15 it can be seen that the axle accelerations, although correct in phase, show a magnitude mismatch between measurements and simulations. This might be an indication that either the nonlinear axle damping is not modeled accurately, or that the adopted tyre model is relatively inaccurate. Furthermore, when looking at the primary suspension deflections, given in Figure 2.16, it can be also seen that there notable mismatch.

Figures 2.17 and 2.18 show the chassis and cabin accelerations, measured above and below the cabin suspension elements, respectively. Despite the mismatch of the axle accelerations, the acceleration spikes induced by the obstacle can be predicted very accurately for both the chassis and the cabin. The largest difference is in the interval [2.1, 2.5] seconds, in which the drive axle crosses the obstacle.

The angular velocities measured in the front of the cabin also show a good match, see Figure 2.19. The largest mismatch lies again in the interval where the drive axle crosses the obstacle. In this interval, the simulated cabin pitch velocity is smaller than measured value. The reason for this mismatch is unclear, but it is only observed for the one-sided pyramid trials, not for the step-down and threshold tests.

When looking at the secondary suspension displacements, it can be seen that the differences between the measured and simulated response (Figure 2.20) show a similar picture. The response of the front axle crossing the obstacle is covered very well by the model. However, when the drive axle crosses the obstacle a mismatch is visible.

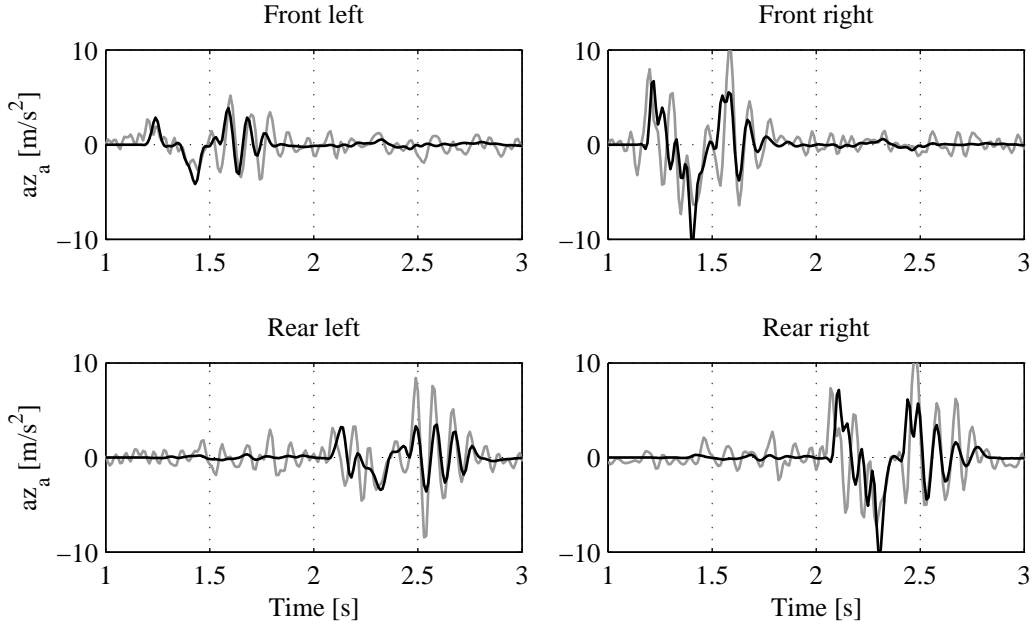


Figure 2.15: One-sided pyramid. Vertical accelerations tractor axles; measured (grey) and simulated (black).

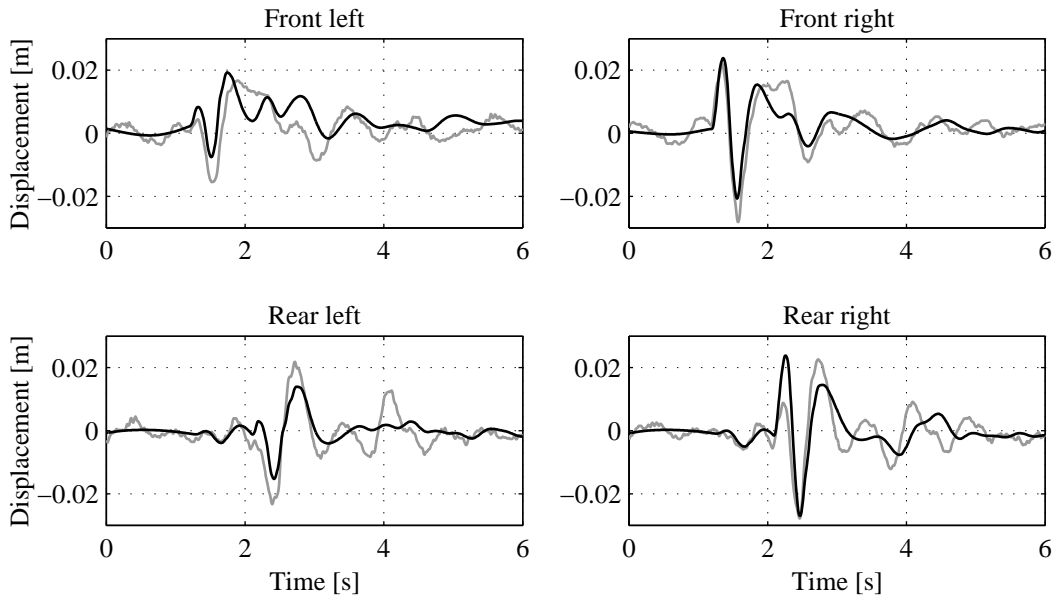


Figure 2.16: One-sided pyramid. Primary suspension displacements; measured (grey) and simulated (black). Positive displacements correspond to compression.

Although, the mismatch can partly be contributed to the flexible chassis, it is expected that other factors also play a role.

The measurements at other velocities and using other road profiles show similar pictures, with one notable difference. For this obstacle, the simulated axle accelerations

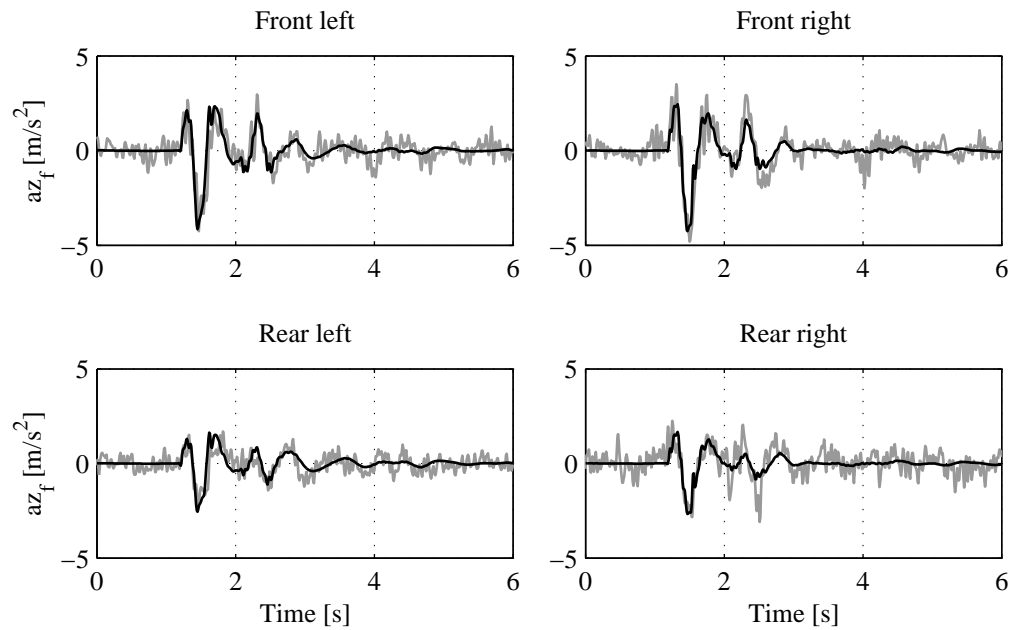


Figure 2.17: One-sided pyramid. Vertical accelerations chassis below cabin suspension elements; measured (grey) and simulated (black).

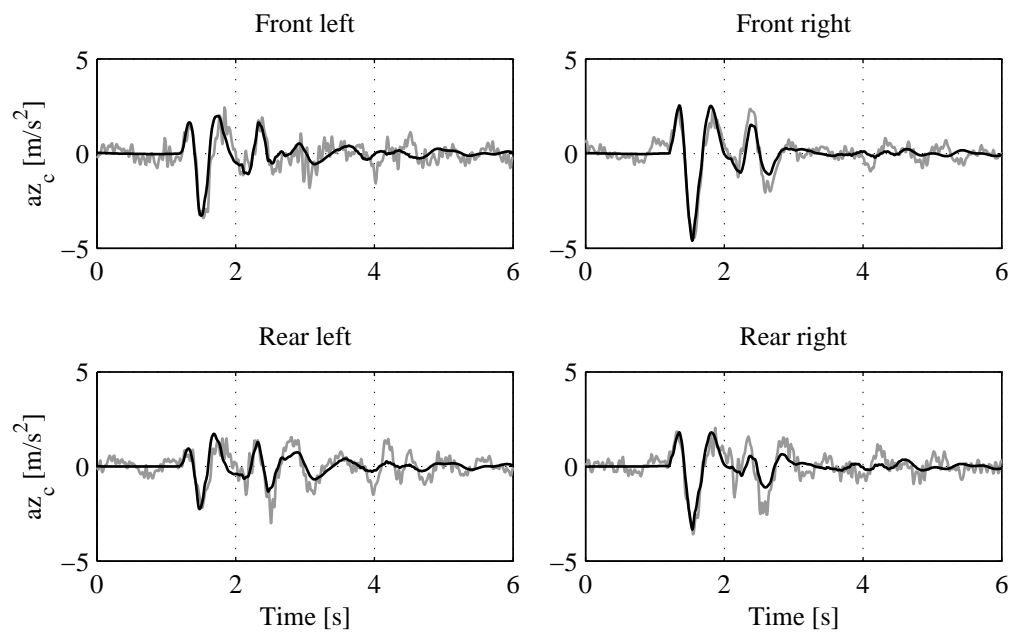


Figure 2.18: One-sided pyramid. Vertical accelerations cabin above suspension elements; measured (grey) and simulated (black).

are lower than those measured. However, for the step-down and threshold tests, which have sharper edges (see Figure 2.21), the simulated axle accelerations are significantly larger than those measured. The mismatch in these tests is probably caused by friction effects in the suspension, which are not included in the model to reduce simulation

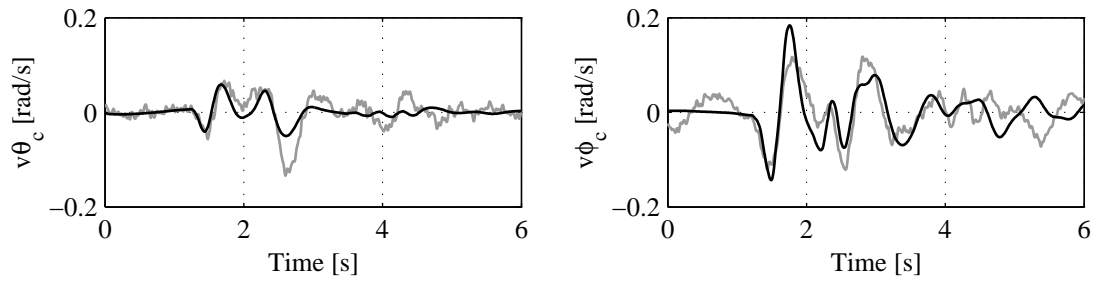


Figure 2.19: One-sided pyramid. Pitch- (left) and roll angular velocities cabin (right); measured (grey) and simulated (black).

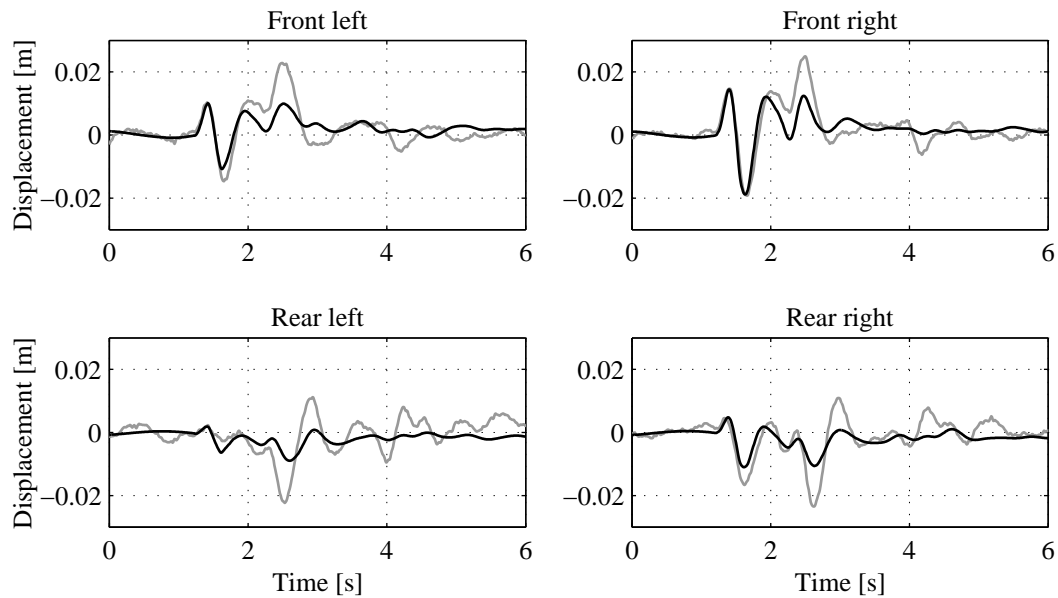


Figure 2.20: One-sided pyramid. Secondary suspension displacements; measured (grey) and simulated (black). Positive displacements correspond to compression.

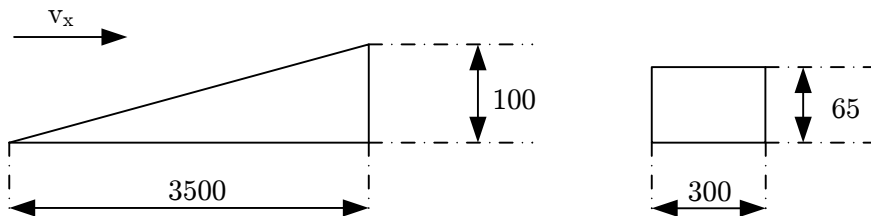


Figure 2.21: Road obstacles with dimensions in millimeter: step-down (left) and threshold (right).

time. Still, given the accurate prediction of the frame and cabin acceleration levels, this acceleration mismatch is not expected to be of major consequence for comfort evaluation.

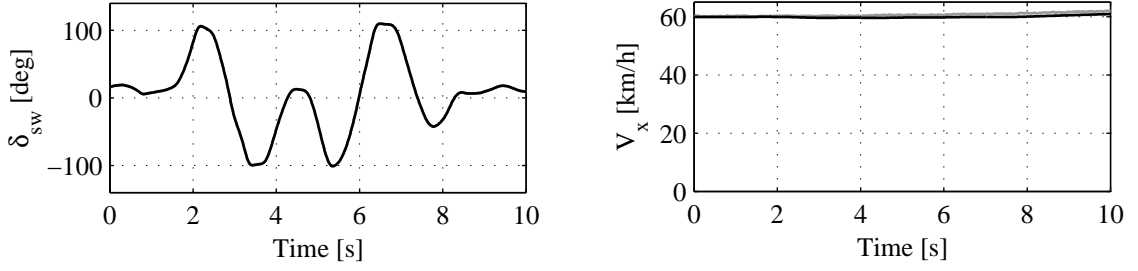


Figure 2.22: Double lane change. Driver steering angle (left) and longitudinal velocity (right); measured (grey) and simulated (black).

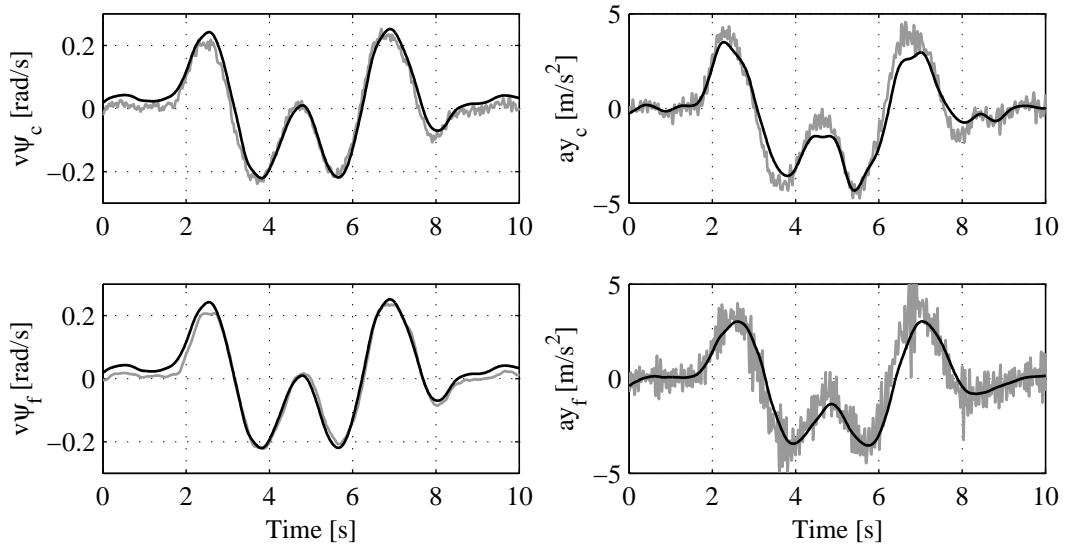


Figure 2.23: Double lane change. Yaw-rate (left) and lateral accelerations (right) of cabin front center (top) and chassis center of gravity (bottom); measured (grey) and simulated (black).

2.6.4 Double lane change

One of the standard tests for vehicle handling is the double lane change. Herein, the driver starts with a constant velocity on a straight road. At a certain point he or she quickly steers the vehicle to a parallel lane and subsequently back to the original lane. The measured steering wheel angle for this maneuver is used as input for the model, see Figure 2.22 (left). Furthermore, the vehicle's longitudinal velocity is kept nearly constant around 60 km/h, see Figure 2.22 (right).

As a consequence of the steering, the vehicle will yaw. The yaw-rate of the chassis and cabin is given in Figure 2.23 (left). Clearly, the simulated and measured response match well. The minor delay in the chassis measurement is a results of the onboard filtering as discussed in Section 2.5, which is not included in the simulation.

The execution of this maneuver results in high lateral accelerations on the vehicle. These accelerations, measured and simulated both at the chassis center of gravity and the front center of the cabin are given in Figure 2.23. It can be seen, that the main

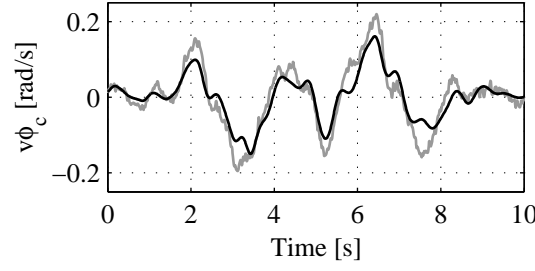


Figure 2.24: Double lane change. Roll velocity cabin; measured (grey) and simulated (black).

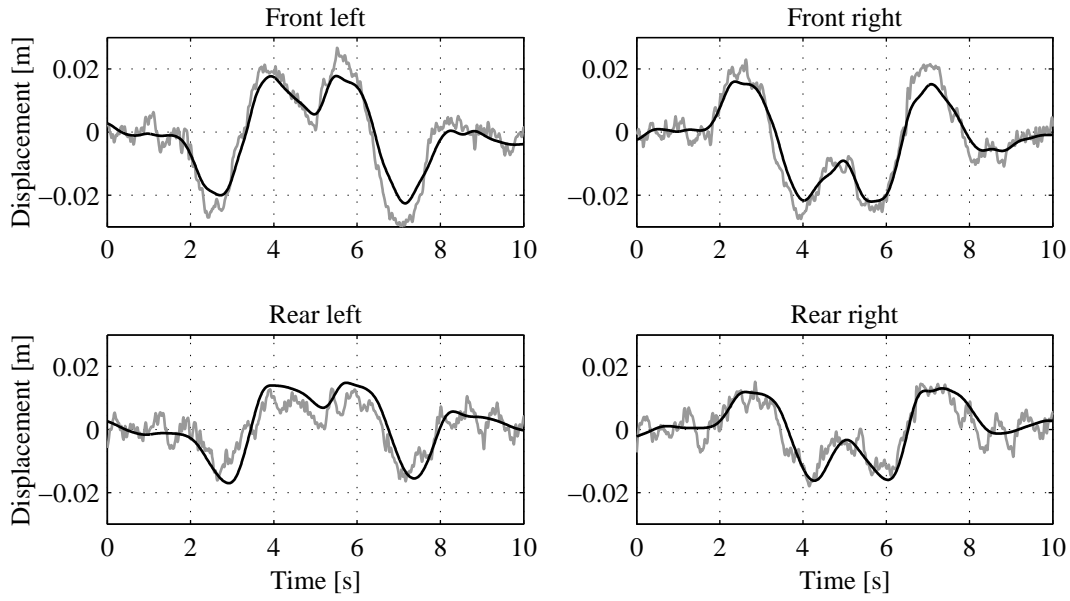


Figure 2.25: Double lane change. Primary suspension displacements; measured (grey) and simulated (black). Positive displacements correspond to compression.

trend of the response matches well. However, there is a small difference in maximum values. Furthermore, it can be seen that the noise level on the chassis measurement is substantially higher than that of the cabin measurement. The power spectral density of the chassis acceleration showed a peak around 28 Hz, indicating that the noise mainly originates from the engine (running at 1700 rpm).

The roll velocity of the cabin, measured and simulated, is shown in Figure 2.24. Again, the main trends match, but there remains a difference in maximum values.

When comparing the responses of the primary and secondary suspension, Figures 2.25 and 2.26 respectively, a more significant mismatch is visible at the rear of the cabin. The roll stabilizer at the front of the vehicle minimizes roll between the front of the cabin and the chassis. However, at the rear the relatively flexible chassis twists. This effect is not included in the model.

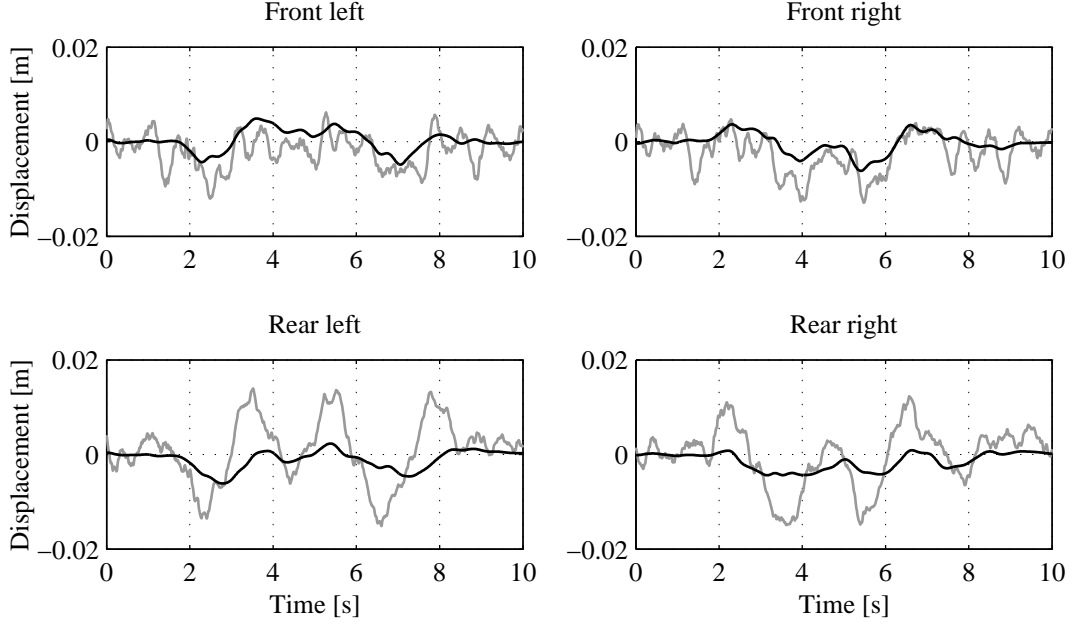


Figure 2.26: Double lane change. Secondary suspension displacements; measured (grey) and simulated (black). Positive displacements correspond to compression.

2.7 Frequency-domain validation

As the presented tractor semi-trailer model is intended for comfort evaluation, it is important to know its accuracy in the comfort relevant frequency range up to approximately 20 Hz, ISO 2631-1 (1997).

As can be seen in Table 2.3, of the 141 performed tests 82 are comfort oriented. Test drivers, normally evaluate the vehicle comfort by extensive driving tests on different types of roads, with different velocities. This is due to the nonlinear properties of the vehicle: it may be comfortable at one velocity and/or one particular road, but uncomfortable at another. For the simulation model, two different road profiles are currently available. The first is from a typical highway road, and the second from a (very bumpy) Belgian blocks road. As the first is expected to be more representative for the normal driving conditions, it is chosen for the following validation process.

In order to give a fair comparison between simulation and measurements, it is necessary to evaluate both under the same conditions. This means that the vehicle velocity (wheel-base filtering) and road roughness need to be identical. However, the exact road profile for each of the tests is unknown. Therefore, it is chosen to use the power spectral density (PSD) of the vertical (az_a^f)- and roll acceleration of the front axle ($a\phi_a^f$) as measures. These are determined as

$$\begin{aligned} az_a^f &= \frac{1}{2} (az_a^{fl} + az_a^{fr}) \\ a\phi_a^f &= \frac{1}{b_{af}^s} (az_a^{fl} - az_a^{fr}), \end{aligned} \quad (2.3)$$

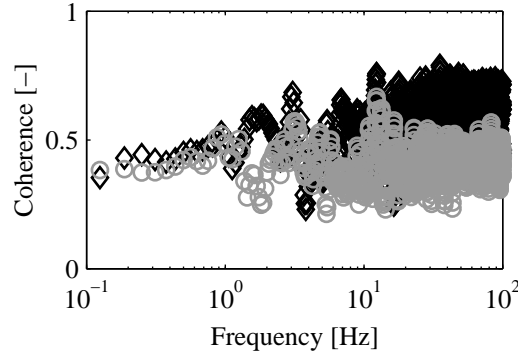


Figure 2.27: Coherence front axle vertical- and roll acceleration: measurements (grey circles) and simulation (black diamonds).

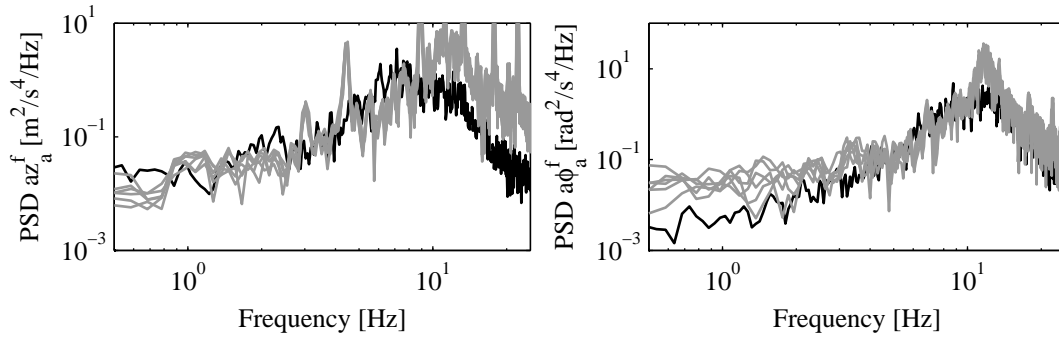


Figure 2.28: Power spectral density front axle vertical- (left) and roll accelerations (right); 6 trials on brick slabs at 80 km/h, measurements (grey) and asphalt road simulations at 80 km/h (black).

with b_{af}^s the distance between the sensors, and az_a^{fl}, az_a^{fr} the front left- and front right vertical axle accelerations, respectively. The vertical- and roll front axle acceleration can be considered to be uncorrelated, see Figure 2.27.

For each of the tests, the PSD's of the vertical and roll front axle acceleration have been determined, and these have been compared with the PSD's obtained from the simulation model on the highway road at 80 km/h. It is assumed, that the test which shows the highest level of similarity with the simulation data also has the closest matching road conditions. This is the case for the trials on the brick slabs, of which the front axle PSD's are depicted in Figure 2.28 by the grey lines. Up to approximately 10 Hz, the PSD's of the front axle acceleration are relatively close to the PSD's of the simulated signals, given by the black line. Furthermore, the PSD's of the various trials are relatively close, indicating a good repeatability on this type of road.

For the frequency domain validation of the other signals, there are basically two options. The first is to look at the PSD's of each of these signals. However, the mismatch between the measured and simulated road profile, which is visible in Figure 2.28, will also result in a mismatch between all the other measured and simulated signals. Alternatively, the transfer function estimate can be determined for each signal,

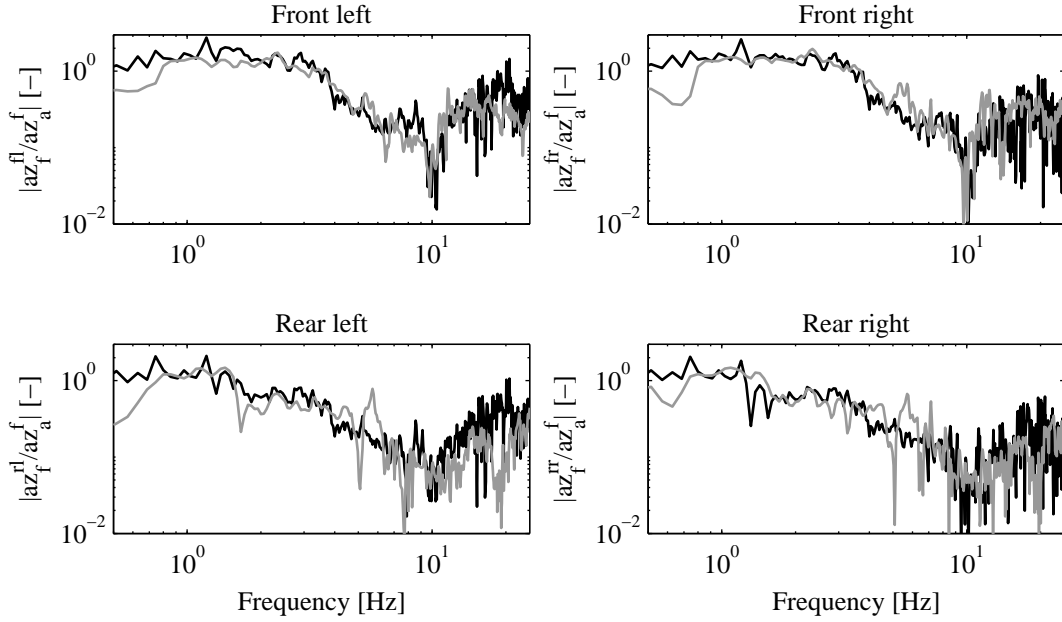


Figure 2.29: Bode magnitude plots. Chassis accelerations as function of the front axle vertical accelerations; based on measurements (grey) and simulations (black).

taking either of the axle accelerations as an input. This way, the road profile mismatch has a more limited influence, and the results can be evaluated more easily, using for example bode plots. However, for low signal-to-noise ratios the results may be biased.

This last approach is adopted for the following validation. The various trials are used to average the estimate and reduce the influence of measurement noise. Hereto, the chosen time interval for all trials is of the same length. Furthermore, to minimize the effect of signal leakage a Hamming window is applied, with a length equal to half of the 18 second time interval. The main observations are shortly discussed.

The bode magnitude plot of the chassis accelerations as function of the front axle vertical accelerations, under the chosen conditions, is given in Figure 2.29. It can be seen that the trend of the simulations and experiments match quite well at the front. However, at the rear there are many small spikes and dips that differ. At this point, it remains unclear which are a result of (measurement) noise, and which are the effect of the modeling mismatch. Furthermore, the same question applies to the low-frequency mismatch, given the relatively low input levels, see Figure 2.28 (left).

The transfer function from the front axle vertical accelerations to the cabin accelerations, see Figure 2.30, shows a similar picture. There seems to be a significant mismatch around 3 and 6 Hz at the rear of the cabin. Looking back at Table 2.2, the 3 Hz mismatch may be related to one of the trailer modes. The 6 Hz mismatch on the other hand may be a result of the engine modeling. Alternatively, it could also be related to one (or more) of the flexible modes of the chassis. Furthermore, the dip around 1.5 Hz which is covered quite well by the model, is expected to be related to one of the cabin modes.

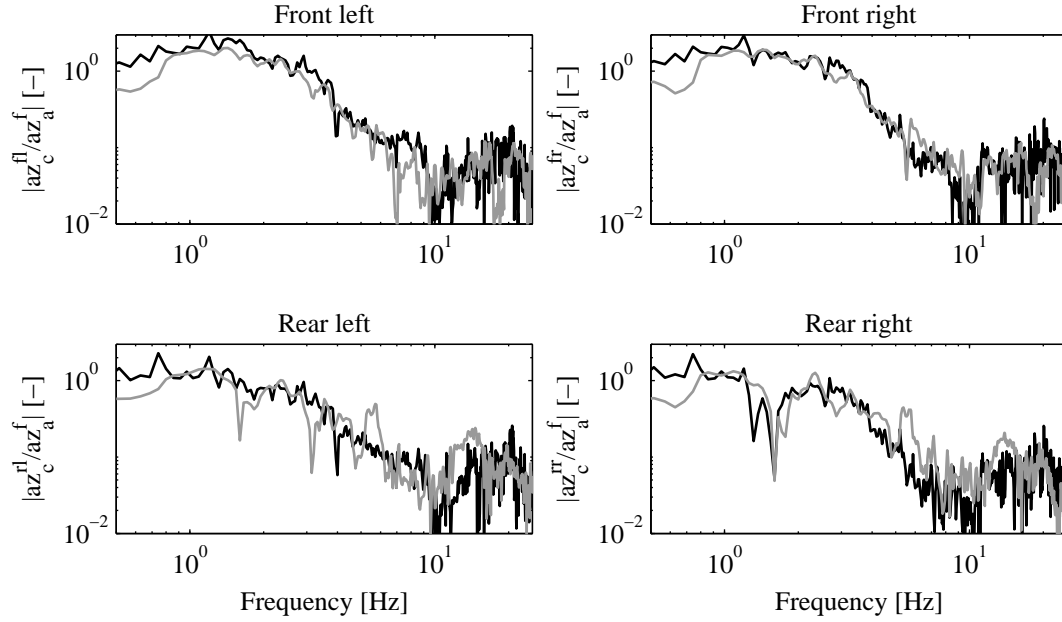


Figure 2.30: Bode magnitude plots. Cabin accelerations displacements as function of the front axle vertical accelerations; based on measurements (grey) and simulations (black).

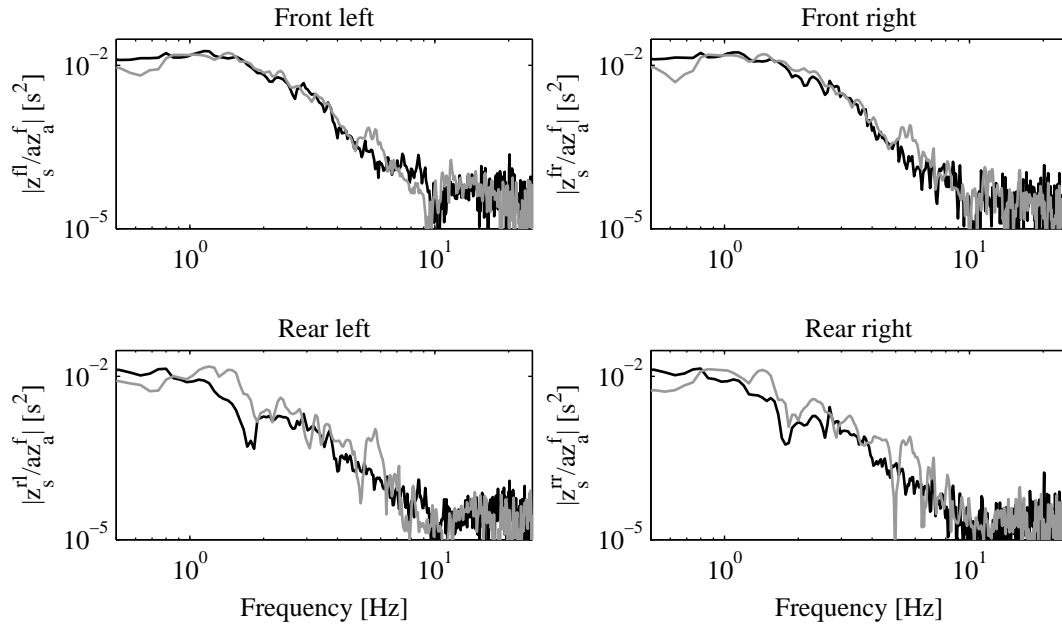


Figure 2.31: Bode magnitude plots. Secondary suspension displacements as function of the front axle vertical accelerations; based on measurements (grey) and simulations (black).

The transfer function to the primary suspension displacement match almost perfectly. The only discrepancies are at low frequency, where the signal-to-noise ratio is questionable. The secondary suspension displacements on the other hand, see Figure 2.31 show a larger mismatch. Especially at the rear, there is a significant difference

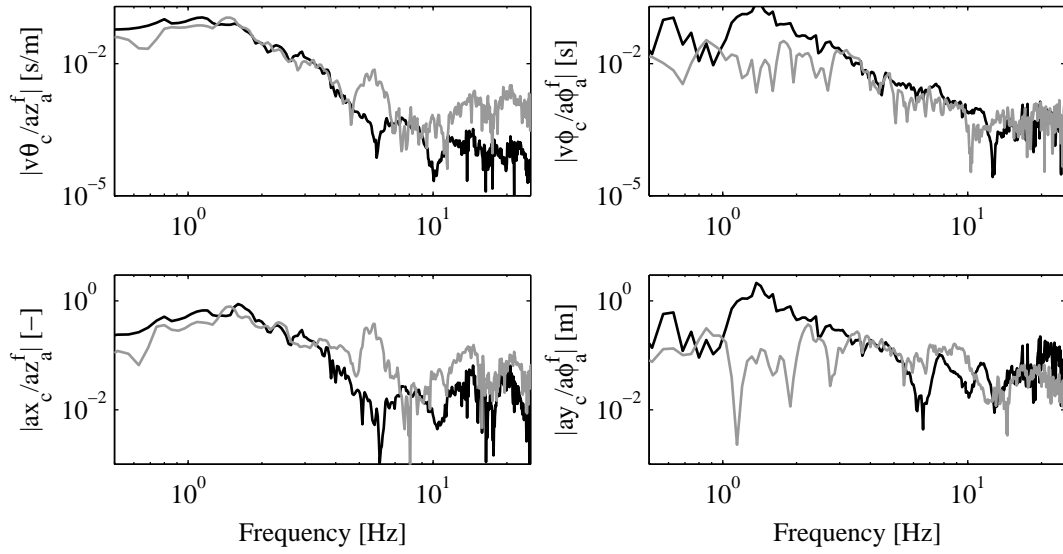


Figure 2.32: Bode magnitude plots. Cabin pitch velocity (top left) and, longitudinal acceleration (bottom left) as function of the front axle vertical accelerations; cabin roll velocity (top right) and, lateral acceleration (bottom right) as function of the front axle roll accelerations; based on measurements (grey) and simulations (black).

Table 2.4: Overview validation results.

	Acc.	Brake ¹	Pyramid ²	DLC	FRF
$\dot{\theta}_c$	—	±	+		± ⁵
\ddot{x}_c	±	+			± ⁵
\ddot{x}_f	+	+			
$\dot{\phi}_c$			±	±	— ⁴
$\dot{\psi}_c$			±	+	
\ddot{y}_c			+	+	— ⁴
\ddot{y}_f			±	+	
\ddot{z}_c			+		+ ³
\ddot{z}_f			+		+ ³
\ddot{z}_a			—		
z_s	±	±	±	— ³	± ³
z_p	±	±	±	±	+

1: Poor results when coming to a standstill

2: Poor results when drive axle crosses obstacle

3: Poorer results at the rear

4: Low input levels may give wrong impression

5: Large mismatch for frequencies above 4 Hz.

between the measurements and simulations. This may be the effect of chassis flexibility.

The mismatch between 5-6 Hz is most apparent in the bode magnitude plots of the front axle vertical acceleration to the cabin pitch velocity and longitudinal acceleration,

see Figure 2.32 (left). Furthermore, these two transfer functions seem to be modeled less accurately above approximately 4 Hz.

Finally, as the vehicle roll and lateral acceleration are expected to be influenced mainly by the front axle roll acceleration, these frequency response functions are given in Figure 2.32 (right). From these plots, there appears to be a major mismatch between measurements and simulations at the lower frequencies, where it is actually important for the model to be accurate for comfort evaluation. However, looking back at the PSD of the axle roll acceleration, given in Figure 2.28, it can be seen that the accelerations levels are very low at those frequencies. Consequently, it is expected that the model is more accurate than indicated by this plot.

Overall, the simulation model seems to give a good representation of the experimentally determined frequency response functions. For all the mentioned differences, it is unclear which part is a result of modeling errors and which of (measurement) noise. So, for a more precise validation, a method is required to separate these error sources.

2.8 Conclusions

In this chapter a simulation model of a tractor semi-trailer combination is presented. It can be used to evaluate the dynamic behavior of the vehicle for a wide range of driving conditions. Due to its modular design the evaluation can be performed for a range of vehicle combinations. Furthermore, as it is constructed in *SimMechanics* which is the multi-body toolbox of *MATLAB/Simulink*, the model can also be used conveniently for the design and control of active components. Especially this last feature may prove very valuable for further developments in this field.

For the validation of the model, measurements of a large variety of tests on a real tractor semi-trailer combination are available. The following have been considered: an acceleration test, a braking test, driving over a pyramid-shaped road obstacle, a double lane change (DLC), and comfort tests which are used to evaluate several frequency response functions (FRF). The results of the comparison between measurements and simulations are given in Table 2.4. Herein, the model quality is labeled as good (+), reasonably accurate (\pm), or poor ($-$). There are a few points of attention.

First of all, the rear axle accelerations show a significant mismatch in the majority of the road obstacle tests. Secondly, the deflections of the rear cabin suspension during the double lane change also show a large mismatch. Thirdly, a static offset was noticed in the front cabin suspension at the end of the brake test. Finally, although a more precise frequency domain validation method is required to separate modeling errors from noise and bias induced errors, there seems to be a significant mismatch above 4 Hz for the transfers to the longitudinal- and pitch cabin acceleration.

Nevertheless, the model is deemed suitable for the comfort and attitude evaluation of active cabin suspension systems. Still, for controller design, the model is too complex. For that reason, reduced order models and an improved frequency-domain validation method are considered in more detail in the next chapter.

Chapter 3

Reduced order models and frequency domain validation

3.1 Introduction

For the design of an active cabin suspension, two types of models are required. On the one-hand, for evaluation purposes, there needs to be a generic tractor semi-trailer model, which covers a variety of driving conditions with a sufficiently high level of accuracy. The model, as presented in the previous chapter, may suffice for this aspect. On the other hand, reduced order models are needed for the purpose of controller design. These models should have a significantly lower complexity, but may also have a lower level of accuracy. Still, they need to cover the main dynamic effects.

Relatively little is known in literature about the design of secondary- and controllable suspensions for commercial vehicles, Cole (2001). To improve the understanding of these complex systems, reliable models are essential. In Jiang et al. (2001) and Gillespie and Karamihas (2000) an overview is given of various models, but the subject of model validation is not addressed. This despite the fact that it is a vital step in any modeling procedure. Consequently, the reliability/quality of the models remains unclear.

Model validation in an automotive context is difficult given the unknown road input, low signal-to-noise ratios for certain frequency ranges, and forward velocity variations which result in asynchronous characteristics for repeated tests. Conventional approaches, see for example the previous chapter, do not distinguish between measurement and model uncertainty, leading to conservatism in the quantification of the model quality. There is a wide range of literature available on the identification of models with noise contributions on both inputs and outputs, Söderström (2007). However, there is no objective, non-conservative, and practically implementable model validation approach available, that can be used to validate vehicle models subjected to uncertain/unknown, asynchronous inputs, with low signal-to-noise ratios. Given the desire for reliable vehicle models, there is a need for a suitable validation approach.

The main contributions of this chapter consist of a 4 degrees of freedom (DOF)

quarter truck heave model, a 4 DOF roll model, and a 9 DOF half truck pitch-heave model, which have been experimentally validated and may be used for the design and control of an active cabin suspension. Moreover, the tractor semi-trailer model of the previous chapter is again validated in the comfort relevant frequency range. The validation is done using a new approach, which is suited for asynchronous repeated measurements with noise contributions on both inputs and outputs. This validation approach is also considered to be an important result. It separates noise- and model uncertainty, and is optimistic in the sense, that the quality of the model is determined based on the reliable (part of the) measurements only.

The outline of this chapter is as follows. First, in Section 3.2, a reduced order heave-, roll-, and pitch-heave model are presented, which are intended for controller design. In Section 3.3, the validation methodology is presented. This methodology is used in Section 3.4 to evaluate the quality of the various models.

3.2 Reduced order models

Vehicle models are probably the most important tool available to suspension designers. They are not only used for suspension (controller) design and parameter optimization but the more advanced models are also suitable for detailed comfort analysis and durability studies. When using modern day controller design techniques like LQG or H_∞ , the controller has at least the same level of complexity as the plant model, (Skogestad and Postlethwaite, 2005, Chapter 11). So, when using the highly complex models that are available in the automotive world, the resulting controllers may be too complex for practical implementation. That is why reduced order models are needed.

Following the classification given in Hrovat (1997), vehicle models can be roughly divided in three classes: 1. quarter vehicle; 2. half vehicle; and 3. full vehicle models. In this section three reduced order models are presented: a 4 DOF quarter truck heave model, a 4 DOF half truck roll model, and a 9 DOF half truck pitch-heave model. All these models are based on the detailed tractor semi-trailer model as presented in the previous chapter. The simplified models can be used for the analysis of the roll, pitch and heave dynamics of the vehicle, as well as for the design of low order controllers for these modes.

3.2.1 Data-based or first-principles?

When aiming at the development of reduced order models, the question arises what type of model or reduction technique to use. If a high order state-space model is available, (balanced) truncation, (balanced) residualisation or optimal Hankel norm approximation can be used to obtain reduced order models (Skogestad and Postlethwaite, 2005, Chapter 11). However, linearizing the 44 DOF tractor semi-trailer *SimMechanics* model, obtaining a state-space realization, and finding the physical interpretation of the state components is far from easy.

As there is a large amount of measurement data, it might also be possible to obtain accurate low order data-based (“black-box”) models. This is the field of system identification, which is thoroughly discussed in Pintelon and Schoukens (2001); Nelles (2001). Alternatively, it is possible to derive (“white-box”) models based on first-principles modeling, see for example Huston (1995); Wouw (2005), which do not require measurements. Furthermore, a combination of the last two techniques can be used to obtain so-called “grey-box” models, where the parameters of a first-principles model are identified using experimental data.

The problem with data-based vehicle models lies mostly in the experimental requirements. For identification purposes it is necessary to have known inputs, which are tested independently, exciting the system at all (relevant) frequencies. All noise sources potentially add to the model uncertainty, so a high signal-to-noise ratio is desirable. In other words, when considering the vehicle-road dynamics, the road induced accelerations need to be significantly larger than the accelerations induced by unknown disturbances and measurement noise. However, in the automotive world this is typically not the case. Road inputs are not known (exactly), signal-to-noise ratios are low in certain frequency ranges, and the model properties are velocity dependent (wheel-base filtering). For this reason, the reduced order models are developed using first-principles techniques and the parameters of the 44 DOF model.

3.2.2 Road models

As vehicles drive on roads, a vehicle model also requires a model of the road. There is a wide range of literature available on the topic of road modeling. The standard model (Gillespie (1985); ISO 8608 (1995)) gives the power spectral density (PSD) of the road displacement as

$$S_z(\Omega) = S_z(\Omega_0) \left(\frac{\Omega}{\Omega_0} \right)^n, \quad (3.1)$$

with $\Omega = 1/\lambda = f/V$ the spatial frequency, λ the wavelength, f the frequency in Hz, V the vehicle velocity, $\Omega_0 = 0.1 \text{ m}^{-1}$ and $n = -2$. As is mentioned in Hrovat (1997), this implies that the ground velocity can be modeled as a white noise disturbance, which is convenient when applying standard LQG optimization techniques.

From (3.1) it follows that the road PSD has a -2 slope on log-log scale irrespective of the road type. Changing the road type or vehicle velocity results in a vertical or horizontal shift of the characteristic. A more accurate model is given in Verros et al. (2005), where a difference is made between short and long wavelengths. However, the increase in model complexity versus the gain in accuracy may not be attractive from a control point of view.

When modeling vehicle roll, it is important to consider the coherence between the left and right track, Cole (2001). At low spatial frequencies, the roll input from a road is much lower in its relative magnitude than that of the vertical input. However, the relative roll input magnitude grows with increasing spatial frequency, Gillespie (1985).

Consequently, roll is more of an issue at low vehicle velocities and not so much at typical highway speeds. Furthermore, according to Liebrechts (2007), the symmetric and anti-symmetric road inputs are uncorrelated and can be regarded as two independent inputs to the axles.

3.2.3 Quarter truck heave model

The quarter vehicle model is the most often used model when it comes to suspension design studies. For passenger cars there is a subdivision in 1 and 2 DOF models, Hrovat (1997). Herein, the 2 DOF model is known for its good description of the vertical dynamics. Especially the inclusion of the control-invariant-point at the wheel hop resonance is important, as it implies strong limitations on the achievable performance, Karnopp (2008).

The 2 DOF model can also be used to model the vertical dynamics of trucks, Gillespie (1985); Huisman (1994). However, in that case, with the chassis, engine and cabin lumped into a single mass, the model is less accurate. In Cole (2001) it is demonstrated that the 2 DOF model cannot be used for stiffness optimization under changing payload conditions. So, given the inaccuracy of the 2 DOF model, the question arises whether it is possible to model the vertical truck dynamics using a (simple) generalized model.

According to Gillespie and Karamihas (2000) it is not possible to model the vertical truck dynamics using only one quarter vehicle model. Therefore, three different nonlinear quarter vehicle models are suggested when focussing on the dynamic tyre forces: one for the steer axle; one for the drive axle with leaf spring; and one for the drive axle with air spring. It is indicated that the inclusion of suspension friction is essential. However, in this thesis the focus lies on the secondary suspension. As such, it is unclear whether or not a generalized quarter vehicle model exists that predicts the cabin dynamics sufficiently accurate.

One of the key differences between passenger cars and trucks - from a suspension point of view - is the amount of body modes. Even though the frequencies and shape of the modes (see Table 2.2 and Gillespie (1985); Elmadany et al. (1979)) may differ between trucks, they generally have over 30 modes below 20 Hz, so in the relevant region for comfort studies. It is unlikely that all are equally important for suspension design, but it remains unclear which dominate the dynamic response.

Focussing on the front of the vehicle, the main bodies are the cabin, engine, chassis and axle. This motivates the use of a 4 DOF quarter truck model for the vertical dynamics. The model is schematically represented in Figure 3.1. Herein, the diamonds represent suspension elements and the actuator force F_{act} is included to facilitate the active suspension design studies in the following chapters.

The equations of motion for the quarter truck heave model are given by

$$M_z \ddot{\underline{x}}_z + D_z \dot{\underline{x}}_z + K_z \underline{x}_z = \underline{f}_z(F_{act}) + \underline{g}_z(\underline{w}_z), \quad (3.2)$$

where $\underline{x}_z = [z_a, z_e, z_f, z_c]^T$ are the vertical position of the axle, engine, chassis and cabin

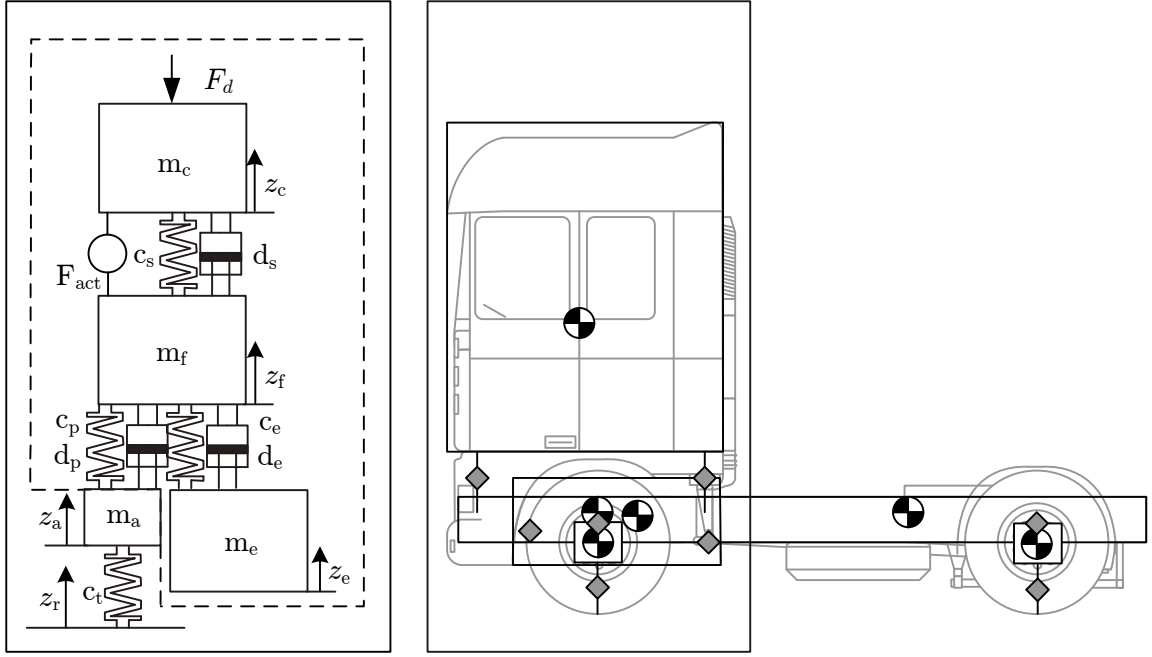


Figure 3.1: Quarter truck 4 DOF heave model, schematic representation. The part of the model which is validated for road induced vibrations is given in the dashed box.

respectively. The vector of manipulated inputs is given by $\underline{f}_z(F_{act}) = [0, 0, -F_{act}, F_{act}]^T$, where F_{act} is the actuator force, and

$$M_z = \begin{bmatrix} m_a & 0 & 0 & 0 \\ 0 & m_e & 0 & 0 \\ 0 & 0 & m_f & 0 \\ 0 & 0 & 0 & m_c \end{bmatrix}, \quad \underline{g}_z(\underline{w}_z) = \begin{bmatrix} c_t z_r \\ 0 \\ 0 \\ -F_d \end{bmatrix} \quad (3.3)$$

$$D_z = \begin{bmatrix} d_p & 0 & -d_p & 0 \\ 0 & d_e & -d_e & 0 \\ -d_p & -d_e & d_e + d_p + d_s & -d_s \\ 0 & 0 & -d_s & d_s \end{bmatrix} \quad (3.4)$$

$$K_z = \begin{bmatrix} c_p + c_t & 0 & -c_p & 0 \\ 0 & c_e & -c_e & 0 \\ -c_p & -c_e & c_e + c_p + c_s & -c_s \\ 0 & 0 & -c_s & c_s \end{bmatrix}. \quad (3.5)$$

Herein, $\underline{g}_z(\underline{w}_z)$ is a vector with unknown external disturbances $\underline{w}_z = [z_r, F_d]^T$, consisting of the vertical road displacement and disturbance force. Furthermore, m_i, d_i, c_i represent the mass, damping and stiffness elements respectively. The parameters for this model are obtained from the 44 DOF tractor semi-trailer model as described in the previous chapter and are given in Appendix A.3. The undamped eigen-frequencies of the 4-DOF model are found to be: 1.1 Hz cabin bounce; 2.2 Hz engine and chassis

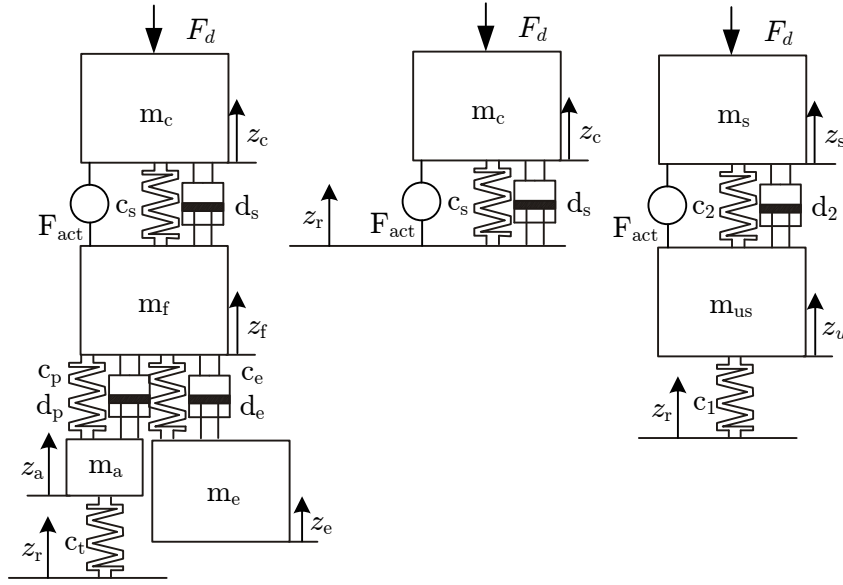


Figure 3.2: Quarter vehicle models: 4 DOF (left), 1 DOF (mid), and 2 DOF (right).

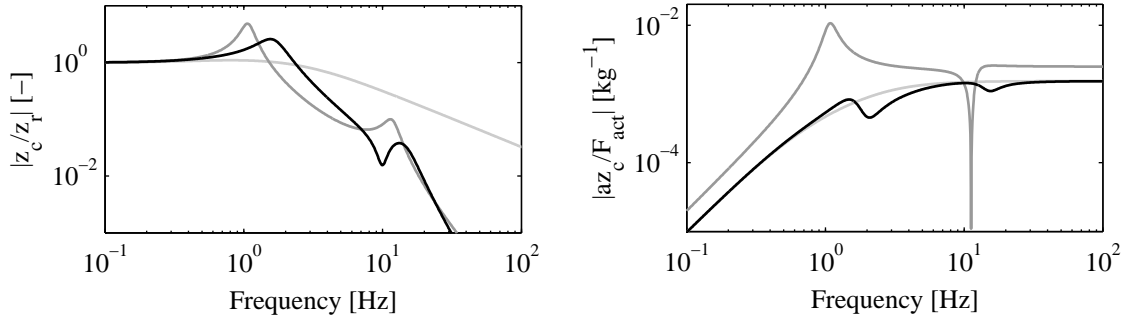


Figure 3.3: Quarter vehicle models, 1 DOF (light-grey), 2 DOF (grey), and 4 DOF (black): open-loop transmissibility (left); and open-loop plant, i.e., cabin acceleration resulting from an actuator force (right).

bounce (in phase); 10.4 Hz axle bounce; and 15.7 Hz engine and chassis bounce mode (counter phase), see also Figure (3.1).

Given the available literature on 2 DOF models, it is interesting to investigate the differences between the 4 DOF quarter truck model, a 2 DOF quarter car model as is parameterized in Appendix A.2, and a 1 DOF cabin model. The latter uses the secondary suspension parameters of the 4 DOF model and assumes that both the frame, engine and axle follow the road perfectly. The three models are depicted in Figure 3.2.

When studying the transfer function from road to cabin/suspended mass position, given in Figure 3.3 (left), it is clear that adding masses significantly changes the dynamic properties of the system. While the 1 DOF model shows the influence of the cabin suspension, namely a reduced transmissibility above the 1.1 Hz resonance frequency, it does not include the resonances resulting from the chassis, engine and axle.

The eigen frequencies of the 2 DOF model differ somewhat from those of the 4 DOF model due to the fact the parameters for the truck and passenger car are different. Still, apart from the anti-resonance at 10 Hz, there is a certain similarity.

A different picture becomes visible, when studying the effect of the actuator force on the cabin/suspended mass acceleration, see Figure 3.3 (right). The 2 DOF quarter car model has a control invariant point around the 10 Hz wheel hop resonance. However, both the 1 and 4 DOF truck models do not have this limitation. A generalized proof is provided in Appendix B.

So, the quarter truck heave model shows some essential differences in comparison to the quarter car dynamics. Not only are the design criteria different, as road holding is less of an issue when designing the cabin suspension, the truck dynamics also include more (anti-) resonances below 20 Hz. Moreover, while primary suspension design is constraint around the wheel hop resonance due to the occurrence of a control invariant point, no such limitation exists for secondary suspensions.

3.2.4 Half truck roll model

For the analysis in the roll direction, the tractor semi-trailer (heavy-duty truck) representation as is depicted in Figure 3.4 (left) is considered. Herein, S_p , S_e , and S_c are the primary-, engine-, and cabin suspension elements respectively. Furthermore, c_f represents the chassis roll stiffness, and F_t , F_{pr} , F_{air} , F_5 respectively represent the tyre forces, rear primary suspension forces, aerodynamic forces, and forces induced by the trailer.

Assumption 3.2.1. *The depicted elements in Figure 3.4 (left) determine the main cabin roll dynamics.*

Despite the fact that the chassis flexibility is not always taken along in literature, this can be seen as a classic assumption.

Assumption 3.2.2. *There is no interaction between the roll and pitch-heave dynamics.*

Although the symmetric and anti-symmetric road inputs can be considered to be decoupled Liebrechts (2007), there may in practice be a correlation between the roll and heave dynamics. Still, this (unconventional) assumption is adopted for reasons of simplicity.

Under these assumptions, the roll behavior of the front of the tractor can be modeled using the 4 DOF truck roll model, as is depicted in Figure 3.4 (right). Herein, M_d is the roll moment induced by the aerodynamic disturbance forces F_{air} and lateral acceleration when cornering, M_{act} is the actuator moment acting on both the cabin and chassis, J_i is an inertia, c_i a (torsion) stiffness, d_i a damping coefficient and ϕ_i an absolute roll angle. Furthermore, $i = a, f, c, e$, where a denotes the axle, f the front chassis, c the cabin and e the engine. Note that this model does not include the rear axle, rear chassis and trailer dynamics.

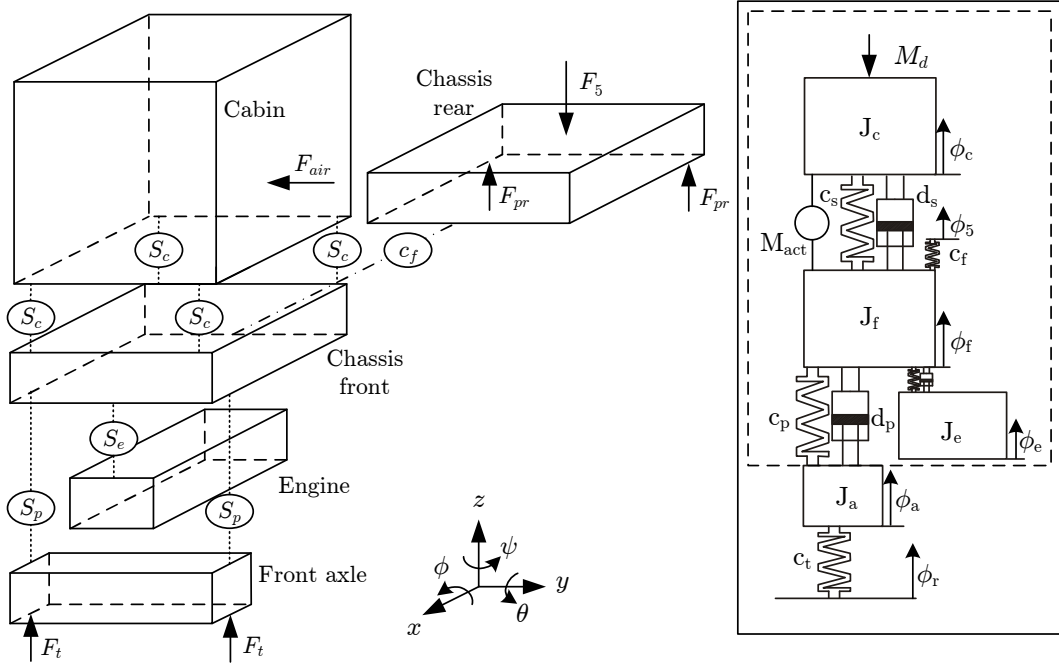


Figure 3.4: Half truck 4-DOF roll model, schematic representation. The part of the model which is validated for road induced vibrations is given in the dashed box.

The equations of motion for the quarter truck roll model, corresponding to Figure 3.4 (right), are given by

$$M_\phi \ddot{\underline{x}}_\phi + D_\phi \dot{\underline{x}}_\phi + K_\phi \underline{x}_\phi = \underline{f}_\phi(M_{act}) + \underline{g}_\phi(\underline{w}_\phi), \quad (3.6)$$

where $\underline{x}_\phi = [\phi_a, \phi_e, \phi_f, \phi_c]^T$, the manipulated inputs are given by $\underline{f}(M_{act}) = [0, 0, -M_{act}, M_{act}]^T$, and

$$M_\phi = \begin{bmatrix} J_a & 0 & 0 & 0 \\ 0 & J_e & 0 & 0 \\ 0 & 0 & J_f & 0 \\ 0 & 0 & 0 & J_c \end{bmatrix}, \quad \underline{g}_\phi(\underline{x}_\phi) = \begin{bmatrix} c_t^\phi \phi_r \\ 0 \\ c_f^\phi \phi_5 \\ -M_d \end{bmatrix} \quad (3.7)$$

$$D_\phi = \begin{bmatrix} d_p^\phi & 0 & -d_p^\phi & 0 \\ 0 & d_e^\phi & -d_e^\phi & 0 \\ -d_p^\phi & -d_e^\phi & d_e^\phi + d_p^\phi + d_s^\phi & -d_s^\phi \\ 0 & 0 & -d_s^\phi & d_s^\phi \end{bmatrix} \quad (3.8)$$

$$K_\phi = \begin{bmatrix} c_p^\phi + c_t^\phi & 0 & -c_p^\phi & 0 \\ 0 & c_e^\phi & -c_e^\phi & 0 \\ -c_p^\phi & -c_e^\phi & c_e^\phi + c_p^\phi + c_s^\phi + c_f^\phi & -c_s^\phi \\ 0 & 0 & -c_s^\phi & c_s^\phi - m_c g r_c \end{bmatrix}. \quad (3.9)$$

Herein, $\underline{g}_\phi(\underline{w}_\phi)$ is a vector with external disturbances $\underline{w}_\phi = [\phi_r, \phi_5, M_d]^T$, consisting of the road roll angle, rear chassis roll angle and disturbance moment. Furthermore, r_c

is the height of the cabin center of gravity with respect to the roll center of the cabin suspension.

Assumption 3.2.3. *The chassis, engine and axle effective stiffness reduction caused by gravity is assumed negligible.*

It can be seen in (3.9), that for larger values of r_c the effective cabin roll stiffness is reduced by gravity. A similar effect also influences the engine, chassis and axle dynamics. However, given the relatively high roll stiffness in those components, Assumption 3.2.3 is expected to hold.

The parameters for this model are obtained from the 44 DOF tractor semi-trailer model as described in the previous chapter, and are given in the Appendix, Table A.8. The undamped eigen-frequencies of the 4-DOF model are found to be: 1.7 Hz vehicle roll; 6.7 Hz engine roll; 12.9 Hz axle roll; and 18.5 Hz chassis roll mode.

3.2.5 Half truck pitch-heave model

The pitch and heave motion of a truck are coupled due to the nature of the road excitations. Therefore, it makes sense to combine the pitch and heave motion in one model. Doing so, it may be possible to model the heave motion more accurate than when using the quarter truck model.

An additional benefit of pitch-heave models is the inclusion of the wheelbase filtering effect, see for example Zuo and Nayfeh (2007). This is a velocity dependent effect resulting from the fact that the rear wheels “see” the same road profile as the front wheels apart for a certain time-delay. As a result of wheelbase filtering, locations between the front and rear axle have a reduced transmissibility at certain frequencies. These frequencies are velocity dependent, and have a significant influence on the pitching dynamics of the cabin. Therefore, it is necessary to evaluate a suspension at various velocities when the model includes this effect, Cole (2001).

In literature a range of half truck models is used for various purposes. In Huisman (1994), the feasibility of an active primary suspension is investigated. Hereto, a 4 DOF half truck model is used for controller and observer design and a 6 DOF nonlinear half truck model for the evaluation. It is claimed that the differences, between the results with a 2 DOF quarter car and 4 DOF half truck internal control model, are marginal. However, as only the primary suspension is considered these findings cannot be generalized to this research without further study.

There are also models that do include the cabin suspension. A 6 DOF tractor model is given in Nakano et al. (1999) and in Ksiazek and Luczko (2007) an 8 DOF half tractor semi-trailer model is used for suspension optimization. As the 6 DOF model does not include the dynamics of the semi-trailer, it is expected to be less accurate. The 8 DOF model on the other hand does include the dynamics of the semi-trailer, but herein the cabin front and rear suspension are lumped. Consequently, neither model is considered to be a suitable reduced order representation of the 44 DOF model as given in the previous chapter. Furthermore, both models have not been experimentally validated.

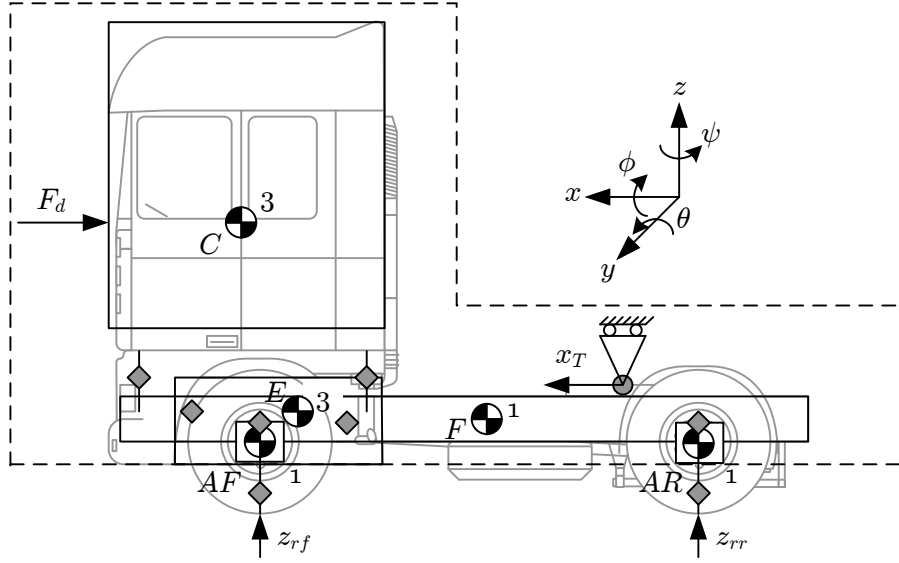


Figure 3.5: Half truck pitch-heave model.

Given the need for a reduced order half truck pitch-heave model, which accurately describes the cabin pitch and heave dynamics and is suited for controller design, the 9 DOF model as is schematically represented in Figures 3.5 and A.4 is proposed. It is based on several assumptions.

Assumption 3.2.4. *The trailer hitch point does not move in vertical direction with respect to the chosen inertial reference frame (\vec{e}_O) and the longitudinal motion x_t is fully determined by an unknown input.*

This assumption is the main difference between this and more classic models. In the case of a tractor with fully loaded semi-trailer, this assumption is expected to be valid. However, when the weight of the trailer is reduced, it may result in additional model uncertainty.

Assumption 3.2.5. *The cabin and axle suspension forces work along the principal directions of the inertial frame.*

Assumption 3.2.6. *the engine suspension mounts are located at the same height as the chassis center of gravity.*

These last two assumptions are added for reasons of simplicity and are not expected to add significant model uncertainty.

Assumption 3.2.7. *The aerodynamic disturbances are assumed to be unknown and are represented by the force F_d , which acts on the cabin.*

Under these assumptions, the equations of motion can be determined as given in the appendix (A.1). After linearization around the steady-state equilibrium conditions

$\underline{x}_h = \dot{\underline{x}}_h = \ddot{\underline{x}}_h = 0$, these can be written as

$$M_h \ddot{\underline{x}}_h + D_h \dot{\underline{x}}_h + K_h \underline{x}_h = \underline{f}_h(\underline{F}_{act}) + \underline{g}_h(\underline{w}_h), \quad (3.10)$$

with the generalized coordinates $\underline{x}_h = [z_{af}, z_{ar}, \theta_f, x_e, z_e, \theta_e, x_c, z_c, \theta_c]^T$, z_{af}, z_{ar} the vertical displacement of the front and rear axle respectively, θ_f the chassis orientation, x_e, z_e, θ_e the longitudinal displacement, vertical displacement and orientation of the engine, and x_c, z_c, θ_c the longitudinal displacement, vertical displacement and orientation of the cabin. The manipulated inputs $\underline{F}_{act} = [F_{act}^F, F_{act}^R]^T$ and unknown disturbances $\underline{w}_h = [z_{rf}, z_{rr}, x_T, \dot{x}_T, F_d]^T$, influence the system as

$$\underline{f}_h(\underline{F}_{act}) = \begin{bmatrix} 0 \\ 0 \\ F_{act}^F(l_{f5} + l_{am}) + F_{act}^R(l_{f5} + l_{am} - l_{cf} - l_{cr}) \\ 0 \\ 0 \\ 0 \\ 0 \\ F_{act}^F + F_{act}^R \\ F_{act}^R l_{cr} - F_{act}^F l_{cf} \end{bmatrix}, \quad (3.11)$$

$$\underline{g}_h(\underline{w}_h) = \begin{bmatrix} c_{tf} z_{rf} \\ c_{tr} z_{rr} \\ (c_{ef}^x + c_{er}^x + c_{sf}^x) z_{f5} x_T + (d_{ef}^x + d_{er}^x + d_{sf}^x) z_{f5} \dot{x}_T \\ (c_{ef}^x + c_{er}^x) x_T + (d_{ef}^x + d_{er}^x) \dot{x}_T \\ 0 \\ 0 \\ -F_d + c_{sf}^x x_T + d_{sf}^x \dot{x}_T \\ 0 \\ -c_{sf}^x z_{cf} x_T - d_{sf}^x z_{cf} \dot{x}_T \end{bmatrix}. \quad (3.12)$$

The off-diagonal components of the mass-matrix are all zero and the diagonal elements are given by

$$\text{diag}(M_h) = [m_{af}, m_{ar}, J_f^*, m_e, m_e, J_e, m_c, m_c, J_c], \quad (3.13)$$

where J_f^* is the chassis inertia when rotating around the trailer hitch-point. The

damping and stiffness matrix are respectively given by

$$D_h = \begin{bmatrix} d_{pf} & 0 & D_{31} & 0 & 0 & 0 & 0 & 0 & 0 \\ 0 & d_{pr} & D_{32} & 0 & 0 & 0 & 0 & 0 & 0 \\ D_{31} & D_{32} & D_{33} & D_{34} & D_{35} & D_{36} & D_{37} & D_{38} & D_{39} \\ 0 & 0 & D_{34} & d_{ef}^x + d_{er}^x & 0 & 0 & 0 & 0 & 0 \\ 0 & 0 & D_{35} & 0 & d_{ef}^z + d_{er}^z & D_{56} & 0 & 0 & 0 \\ 0 & 0 & D_{36} & 0 & D_{56} & D_{66} & 0 & 0 & 0 \\ 0 & 0 & D_{37} & 0 & 0 & 0 & d_{sf}^x & 0 & -d_{sf}^x z_{cf} \\ 0 & 0 & D_{38} & 0 & 0 & 0 & 0 & d_{sf}^z + d_{sr}^z & D_{89} \\ 0 & 0 & D_{39} & 0 & 0 & 0 & -d_{sf}^x z_{cf} & D_{89} & D_{99} \end{bmatrix}, \quad (3.14)$$

$$K_h = \begin{bmatrix} c_{tf} + c_{pf} & 0 & K_{31} & 0 & 0 & 0 & 0 & 0 & 0 \\ 0 & c_{tr} + c_{pr} & K_{32} & 0 & 0 & 0 & 0 & 0 & 0 \\ K_{31} & K_{32} & K_{33} & K_{34} & K_{35} & K_{36} & K_{37} & K_{38} & K_{39} \\ 0 & 0 & K_{34} & c_{ef}^x + c_{er}^x & 0 & 0 & 0 & 0 & 0 \\ 0 & 0 & K_{35} & 0 & c_{ef}^z + c_{er}^z & K_{56} & 0 & 0 & 0 \\ 0 & 0 & K_{36} & 0 & K_{56} & K_{66} & 0 & 0 & 0 \\ 0 & 0 & K_{37} & 0 & 0 & 0 & c_{sf}^x & 0 & -c_{sf}^x z_{cf} \\ 0 & 0 & K_{38} & 0 & 0 & 0 & 0 & c_{sf}^z + c_{sr}^z & K_{89} \\ 0 & 0 & K_{39} & 0 & 0 & 0 & -c_{sf}^x z_{cf} & K_{89} & K_{99} \end{bmatrix}. \quad (3.15)$$

Herein,

$$\begin{array}{l|l} D_{31} = d_{pf} l_{f5} & K_{31} = c_{pf} l_{f5} \\ D_{32} = d_{pr} (l_{f5} - l_{wb}) & K_{32} = c_{pr} (l_{f5} - l_{wb}) \\ D_{33} = d_{pf} l_{f5}^2 + d_{pr} (l_{f5} - l_{wb})^2 + & K_{33} = c_{pf} l_{f5}^2 + c_{pr} (l_{f5} - l_{wb})^2 + \\ d_{ef}^z (l_{f5} + l_{am} - l_{em} + l_{ef})^2 + & c_{ef}^z (l_{f5} + l_{am} - l_{em} + l_{ef})^2 + \\ d_{er}^z (l_{f5} + l_{am} - l_{em} - l_{er})^2 + & c_{er}^z (l_{f5} + l_{am} - l_{em} - l_{er})^2 + \\ d_{sf}^z (l_{f5} + l_{am})^2 + d_{sr}^z (l_{f5} + l_{am} - & c_{sf}^z (l_{f5} + l_{am})^2 + c_{sr}^z (l_{f5} + l_{am} - \\ l_{cf} - l_{cr})^2 & l_{cf} - l_{cr})^2 + z_{f5} (F_{cf}^0 + F_{cr}^0 + F_{ef}^0 + \\ & F_{er}^0 - F_{af}^0 - F_{ar}^0) + m_f g z_{f5} \\ D_{34} = (d_{ef}^x + d_{er}^x) z_{f5} & K_{34} = (c_{ef}^x + c_{er}^x) z_{f5} \\ D_{35} = d_{ef}^z (l_{f5} + l_{am} - l_{em} + l_{ef}) + & K_{35} = c_{ef}^z (l_{f5} + l_{am} - l_{em} + l_{ef}) + \\ d_{er}^z (l_{f5} + l_{am} - l_{em} - l_{er}) & c_{er}^z (l_{f5} + l_{am} - l_{em} - l_{er}) \\ D_{36} = d_{er}^z l_{er} (l_{f5} + l_{am} - l_{em} - l_{er}) - & K_{36} = c_{er}^z l_{er} (l_{f5} + l_{am} - l_{em} - l_{er}) - \\ d_{ef}^z l_{ef} (l_{f5} + l_{am} - l_{em} + l_{ef}) & c_{ef}^z l_{ef} (l_{f5} + l_{am} - l_{em} + l_{ef}) \\ D_{37} = d_{sf}^x z_{f5} & K_{37} = c_{sf}^x z_{f5} \end{array}$$

$$\begin{array}{lcl}
D_{38} & = d_{sf}^z(l_{f5}+l_{am})+d_{sr}^z(l_{f5}+l_{am}-l_{cf}-l_{cr}) & K_{38} = c_{sf}^z(l_{f5}+l_{am})+c_{sr}^z(l_{f5}+l_{am}-l_{cf}-l_{cr}) \\
D_{39} & = d_{sr}^z l_{cr}(l_{f5}+l_{am}-l_{cf}-l_{cr})-d_{sf}^x z_{f5} z_{cf}-c_{sf}^z l_{cf}(l_{f5}+l_{am}) & K_{39} = c_{sr}^z l_{cr}(l_{f5}+l_{am}-l_{cf}-l_{cr})-c_{sf}^x z_{f5} z_{cf}-c_{sf}^z l_{cf}(l_{f5}+l_{am}) \\
D_{56} & = d_{er}^z l_{er}-d_{ef}^z l_{ef} & K_{56} = c_{er}^z l_{er}-c_{ef}^z l_{ef} \\
D_{66} & = d_{ef}^z l_{ef}^2+d_{er}^z l_{er}^2+d_{ef}^x z_{ef}^2+d_{er}^x z_{er}^2 & K_{66} = c_{ef}^z l_{ef}^2+c_{er}^z l_{er}^2+c_{ef}^x z_{ef}^2+c_{er}^x z_{er}^2-F_{ef}^0 z_{ef}-F_{er}^0 z_{er} \\
D_{89} & = d_{sr}^z l_{cr}-d_{sf}^z l_{cf} & K_{89} = c_{sr}^z l_{cr}-c_{sf}^z l_{cf} \\
D_{99} & = d_{sf}^x z_{cf}^2+d_{sf}^z l_{cf}^2+d_{sr}^z l_{cr}^2 & K_{99} = c_{sf}^x z_{cf}^2+c_{sf}^z l_{cf}^2+c_{sr}^z l_{cr}^2-z_{cf} F_{cf}^0-z_{cr} F_{cr}^0.
\end{array}$$

The cabin and engine pre-loads can be calculated from the equilibrium conditions,

$$\begin{aligned}
F_{cf}^0 &= m_c g \left(1 + \frac{l_{cf}}{l_{cr}}\right)^{-1} = 3495 \text{ N} \\
F_{cr}^0 &= F_{cf}^0 \frac{l_{cf}}{l_{cr}} = 2882 \text{ N} \\
F_{ef}^0 &= m_e g \left(1 + \frac{l_{ef}}{l_{er}}\right)^{-1} = 2479 \text{ N} \\
F_{er}^0 &= F_{ef}^0 \frac{l_{ef}}{l_{er}} = 6276 \text{ N},
\end{aligned} \tag{3.16}$$

with $g = 9.81 \text{ [m/s}^2\text{]}$ the gravity constant. Furthermore, as the tyre loads of the tractor are known from measurements (see Table 2.1),

$$m_{tot}g = F_{tf}^0 + F_{tr}^0, \tag{3.17}$$

where the total tractor mass m_{tot} is known. With this knowledge the pre-loads of the primary suspension and tyres can also be determined as

$$\begin{aligned}
F_{af}^0 &= l_{wb}^{-1}(F_{cf}^0(l_{f5}+l_{am})+F_{ef}^0(l_{f5}+l_{am}-l_{em}+l_{ef})+m_f g(l_{f5}-l_{fm}) \\
&\quad +F_{er}^0(l_{f5}+l_{am}-l_{em}-l_{er})+g(l_{wb}-l_{f5})(m_{tot}-m_{af}-m_{ar})) = 30090 \text{ N} \\
F_{tf}^0 &= m_{af}g + F_{af}^0 = 33524 \text{ N} \\
F_{ar}^0 &= (m_{tot}-m_{ar})g - F_{tf}^0 = 56370 \text{ N} \\
F_{tr}^0 &= m_{tot}g - F_{tf}^0 = 62452 \text{ N}.
\end{aligned} \tag{3.18}$$

The parameters for this model are obtained from the 44 DOF tractor semi-trailer model as described in the previous chapter, and are given in Appendix A.5. The undamped eigen-frequencies of the 9 DOF model are found to be: 0.9 Hz cabin pitch; 1.1 Hz cabin heave; 2.1 Hz engine and cabin heave; 7.8 Hz engine pitch; 10.1 Hz rear axle heave; 10.4 Hz front axle heave; 13.5 Hz engine longitudinal; 15.1 Hz engine heave and pitch; 22.3 Hz cabin longitudinal and pitch. With these parameters, the weights beneath the front and rear axle are found to be 6835 and 12732 kg respectively, which is close to the measured values given in Table 2.1.

3.3 Model validation using asynchronous measurements

In the previous section, several reduced order models are presented which provide relations between the various disturbances and the resulting cabin accelerations. The parameters of these models are based on the 44 DOF model which has been validated in the time-domain and to some extent in the frequency-domain. However, the quality of the models in the comfort relevant frequency range remains unclear. There is a wide range of measurement data available from comfort measurements with a real tractor semi-trailer configuration, see Table 2.3, which may be used for model validation. The only problem lies in the fact that the measurement conditions are not ideal as the signal-to-noise ratios are low for certain frequencies and the repetitions are not synchronous. So, conventional validation approaches are not suited. Therefore, a model validation approach is needed which is tailored to cope with these conditions.

In this section, a new model validation method is presented which is suited for asynchronous repeated measurement data with noise on inputs and outputs and low signal-to-noise ratios. First, some background information is provided and the model validation problem is specified. After this, the method is discussed and illustrated using a SISO simulation example.

3.3.1 Background

The model validation problem amounts to deciding whether a set of experimental input-output data could have been produced by the model for some choice of unmodeled dynamics, initial condition, and measurement noise satisfying the given bounds, Poolla et al. (1994). It is, strictly speaking, not actually possible to validate a model. It is only possible to say whether or not a model is not invalidated given a certain set of measurement data. This does not mean that the model is in fact a correct description of the physical system, since future measurements may invalidate it, Smith and Doyle (1992).

Model validation can be done in the frequency-domain, Smith and Doyle (1992); Mazzaro and Sznaier (2004); Smith and Dullerud (1996), and time-domain, Poolla et al. (1994). In model validation for robust control, it is important to consider both model uncertainty and noise influences. A mismatch between model and measurements can be the consequence of either, leading to a trade-off situation. However, the influence of model uncertainty, when designing a robust controller, Skogestad and Postlethwaite (2005); Zhou et al. (1996), differs from that of noise. If the model uncertainty is underestimated, the designed controller may potentially destabilize the true system. Alternatively, if the model uncertainty is overestimated, Ozay and Sznaier (2007), the resulting robust controller will be conservative.

The trade-off between model and noise uncertainty, results in an ill-posed deterministic validation problem. Therefore, an enhanced (frequency-domain) approach is

proposed in Oomen and Bosgra (2008, 2009). By using repeated experiments, a deterministic, non-parametric disturbance model is constructed. The measurement data that cannot be explained by the combination of the nominal model and non-parametric disturbance model is attributed to model uncertainty. The resulting validation-based uncertainty model is optimistic in the sense that experiments with a poor signal-to-noise ratio do not result in an overly conservative uncertainty model. However, when the noise reduces to zero, it is shown that the estimated model uncertainty converges to the true systematic modeling error. Consequently, it is expected to be worthwhile to investigate possible adaptations of this approach which include the case of uncertain/unknown, asynchronous repeated inputs, with low signal-to-noise ratios.

3.3.2 Problem description

The reduced order models, as described in the previous section, are intended for the design of a (robust) controller for an active truck cabin suspension. As driver comfort will be a design criterium, the models need to be reasonably accurate up to approximately 20 Hz, see ISO 2631-1 (1997). However, the question remains how to check this.

Three of the different tests, as described in Table 2.3, are available for the validation. In the first test, the vehicle drives in a straight line at 60 or 80 km/h over undulating (wavy) asphalt. In the second test, it travels at 60 or 80 km/h over brick slabs. In the third test, the vehicle drives with a velocity of 40 or 50 km/h over a brick road. For each of the tests, at each of the velocities, six trials of 16 seconds in length are available for the case with-, and without trailer. So, in total 72 experiments are available for the validation. The other comfort tests are not deemed suitable as there are not enough different trials to get a reliable noise model.

While the road disturbance input has the same power magnitude for all the trials of one test, at one velocity and with a certain loading condition, the timing is different. So, the repetitions are asynchronous with respect to each other,

$$\begin{aligned} |\underline{v}_r^1(\omega_i)| - |\underline{v}_r^k(\omega_i)| &= 0 \\ \angle(\underline{v}_r^1(\omega_i)) - \angle(\underline{v}_r^k(\omega_i)) &\in [0, 2\pi] \text{ rad}, \end{aligned} \quad (3.19)$$

with $\underline{v}_r^j(\omega_i)$ the Discrete Fourier Transform (DFT) of $\underline{v}_r^j(t)$, $\angle(\underline{v}_r^j(\omega_i))$ the phase of $\underline{v}_r^j(\omega_i)$, test-trial number $k \in [1, \dots, 6]$ and $\omega_i \in \Omega$ a member of a discrete frequency grid. This is a result of (minor) differences in the vehicle velocity, the position of the vehicle on the test track, etcetera. Consequently, averaging the measurements - in an attempt to minimize the influence of noise - will not give good results.

The (relevant) measurements are given in Section 2.5. These are distorted by noise, where the magnitude of the noise may be larger than that of the true signal. This signal-to-noise ratio of a measured signal x_m is defined as

$$SNR(x_m(\omega_i)) = \frac{|x_t(\omega_i)|}{|v_x(\omega_i)|}, \quad (3.20)$$

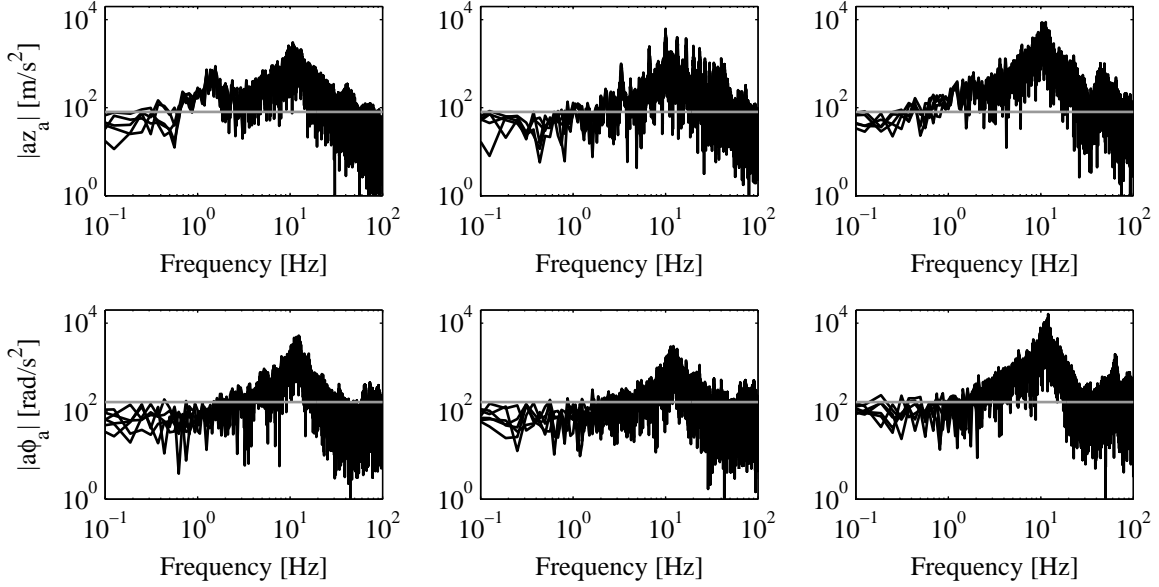


Figure 3.6: Discrete-time Fourier transform axle vertical (top) and roll (bottom) acceleration measurements. Six repetitions on: undulating asphalt at 60 km/h (left); brick slabs at 60 km/h (mid); and brick road at 40 km/h (right). Input tolerances are represented by the grey lines.

where the true value of the signal $x_t(\omega_i)$ is unknown and the measurement $x_m(\omega_i) = x_t(\omega_i) + v_x(\omega_i)$ is distorted by measurement noise $v_x(\omega_i)$ of which the value is also unknown. Consequently, the signal-to-noise ratio of the measurements is difficult to determine exactly. However, it can be approximated if an estimation of the noise standard deviation σ_x is available.

The absolute value of the discrete-time Fourier transform of the axle roll and heave acceleration, for the three different tests at their lowest velocities, is given in Figure 3.6. The frequency content is approximately similar for all three tests, although there is some difference in magnitude. Furthermore, the input intensity, and overall signal-to-noise ratio, below 1 Hz and above 30 Hz is relatively low. The chosen input tolerance $\tau_u = 6.9\sigma_u$, which will be discussed in the next section, is represented by the grey line. When the velocities increase, the inputs characteristics shift upwards.

The problem is to find a non-conservative uncertainty model (quality label), with which the reduced order models are not invalidated given the asynchronous repeated measurements of the three different tests. Herein, the input measurements are distorted by noise, signal-to-noise ratios are low for certain frequencies and all the disturbances $\underline{f}(\underline{x})$ are unknown for the described tests.

3.3.3 Preliminaries

There are a few topics that require special attention, as they will be at the basis of the proposed method.

Validation-based uncertainty modeling

The model validation decision problem consists of verifying whether there exists a noise V and model uncertainty Δ_u realization, such that the measurements lie within the set of possible model realizations. Or in other words, decide whether the model can account for all the previously observed input-output behavior, Smith and Doyle (1992); Poolla et al. (1994). When determining the non-conservative validation-based model uncertainty, the minimum model uncertainty is chosen such that the model is validated for the given data. This is called the *Model Validation Optimization Problem* in Davis (1995); Oomen and Bosgra (2009).

Using the measurements as given in the previous section, it is difficult to solve the model validation decision problem. Still, the validation data can be used to approximate the minimal model uncertainty not invalidating the parametric model. Hereto, the approach is adopted to identify a set of linear nonparametric system and disturbance models for each of the test conditions, and to compare these to the parametric model. This process of model uncertainty quantification from validation data is also called model validation in this thesis.

Confidence intervals of a complex normal distribution

Given the signal $v_y = V_0 e$, where $e \in l_2$ is a sequence of independent, identically distributed random variables with zero mean, unit variance, and bounded moments of all orders, and $V_0 \in \mathcal{RH}_\infty$. Then, for $N \rightarrow \infty$, the Discrete Fourier Transform (DFT) of v_y converges to a complex normal distribution $\mathcal{N}_c(0, C_{v_y}(\omega_i))$, see Oomen and Bosgra (2008) or (Pintelon and Schoukens, 2001, Chapter 14) for the formal definitions.

Furthermore, given the signal $z = z_r + jz_i$, which is complex normally distributed with variance C_z , there is a probability $\alpha \in [0, 1]$ that

$$z_r^2 + z_i^2 < \frac{1}{2} C_z(\omega_i) \chi_{2,1-\alpha}^2. \quad (3.21)$$

The upper bound of the 99.5 percent confidence interval is then given by

$$|\bar{Z}(\omega_i)| = 2.3 \sqrt{C_z(\omega_i)}. \quad (3.22)$$

Errors-in-variables estimators

The model with uncertain inputs and outputs is known in literature as an *errors-in-variables* model. From Guillaume et al. (1992) it is known that for synchronous measurements, the error-in-variables estimator

$$\hat{H}_{EV}(\omega_i) = \frac{\text{ave}(y_m(\omega_i))}{\text{ave}(u_m(\omega_i))}, \quad (3.23)$$

with $y_m(\omega_i)$, $u_m(\omega_i)$ the DFT of the measured outputs and inputs respectively and *ave* the average over all trials, can be regarded as most optimal as it is consistent,

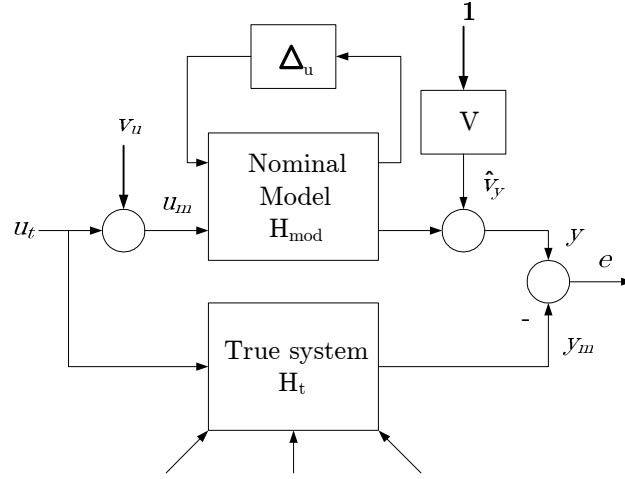


Figure 3.7: Errors-in-variables model, placed within the validation setup presented in Oomen and Bosgra (2009).

efficient and unbiased. On the other hand, for asynchronous measurements, arithmetic averaging

$$\hat{H}_{ari}(\omega_i) = \text{ave}((H_m)(\omega_i)), \quad (3.24)$$

with the empirical transfer function estimate

$$H_m(\omega_i) = \frac{y_m(\omega_i)}{u_m(\omega_i)} = H_t(\omega_i) \frac{1 + v_y(\omega_i)/y_t(\omega_i)}{1 + v_u(\omega_i)/u_t(\omega_i)}, \quad (3.25)$$

gives good results, and can be assumed to be complex normally distributed for input signal-to-noise ratios above 6 dB. In the case of arithmetic averaging, the estimation bias is given by

$$B(\omega_i) = \mathcal{E}(H_m(\omega_i)) - H_t(\omega_i) = -H_t(\omega_i) e^{-\frac{|u_t(\omega_i)|^2}{C_u(\omega_i)}}, \quad (3.26)$$

with $C_u(\omega_i)$ the variance of the true input u_t at frequency ω_i .

3.3.4 Assumptions

The validation approach, which is proposed next, hinges on several assumptions. Consider the *errors-in-variables* model Söderström (2007), placed in the validation setup as presented in Oomen and Bosgra (2009), depicted in Figure 3.7.

There is a true system H_t which is excited by n_u true inputs u_t and n_y the true outputs y_t . The system may also be excited by various other uncorrelated disturbances. There is measurement data from n_e tests, and n_r repetitions for each test. The true inputs and outputs are unknown, but measurements of the inputs u_m and outputs y_m are available which are distorted with measurement noise,

$$\begin{aligned} u_m(t) &= u_t(t) + v_u(t) \\ y_m(t) &= y_t(t) + v_y(t). \end{aligned} \quad (3.27)$$

Assumption 3.3.1. *It is assumed that the input and output noise are:*

- a. zero mean, Gaussian distributed in the time-domain and complex normal distributed in the frequency-domain;*
- b. internally uncorrelated and independent of each other;*
- c. independent of u_t and y_t (no feedback).*

When each of the outputs is measured with a dedicated sensor and the measurement noise dominates the other noise sources, this assumption is expected to hold.

Assumption 3.3.2. *The input spectrum of each repetition of one test is identical and the variance σ_u^2 of the input measurement noise is frequency independent. Furthermore, all frequency domain realizations of the input lie within a 99.5% confidence interval, i.e., $[-2.3\sigma_u, 2.3\sigma_u]$ of the true value.*

This assumption is expected to be reasonable, given (3.22).

Assumption 3.3.3. *For the determination of the empirical transfer function estimate, it is assumed that the influence of leakage effects, see (Pintelon and Schoukens, 2001, Sections 2.22, 2.23 and 2.6), is negligible.*

In practice, when dealing with random excitations, the leakage error decreases with an increasing number of data. Using a Hanning window the leakage effects can be decreased further, although it may introduce a bias error.

Assumption 3.3.4. *For input signal-to-noise ratios below 6 dB, all uncertainty is the result of the poor measurements. So, in that case the differences between model and estimation cannot be contributed to model uncertainty.*

For the noise variance estimation the empirical transfer function estimate of each input-output combination needs to have a complex normal distribution. For input signal-to-noise ratios below 6 dB this will not be the case unconditionally as the variance may grow to infinity Heath (2003); Guillaume et al. (1992). So, although this assumption may lead to optimistic results in some cases, it is required to avoid under-estimation of the noise variance.

Assumption 3.3.5. *For input signal-to-noise ratios above 6 dB, the estimation bias is assumed to be negligible.*

From evaluation of (3.26) it is known that the bias equals $\bar{B} = 0.018H_t$ at a signal-to-noise ratio of 6 dB, which is considered to be negligible.

Assumption 3.3.6. *The inputs u_t are uncorrelated.*

This assumption is needed as the proposed method is based on single input - single output identification. However, depending on the model and measurement conditions, this may not always be the case.

3.3.5 Approach

The following validation approach is proposed to determine the minimum model uncertainty not invalidating the model for the given measurement data.

1. Define inputs u_m and outputs y_m and a discrete frequency grid Θ on which the transfer functions need to be validated.

2. For each test e and each input-output combination k , determine $H_{m,e}^k$ (3.25) for each repetition and use these to determine the mean transfer function estimate \hat{H}_e^k (3.24) for $\omega_i \in \Theta$.

3. Determine, for each test and each input-output combination, a deterministic disturbance model with upper bound $\bar{V}_e^k(\omega_i)$ of the noise variance and maximum bias $\bar{B}_e^k(\omega_i)$. The variance estimate of the empirical transfer function estimates, under the assumptions of Section 3.3.4, is for a certain test, input-output combination, and frequency given by

$$\hat{C}_H^{e,k}(\omega_i) = \frac{1}{n_r - 1} \sum_{r=1}^{n_r} \left((H_{m,e}^{k,r}(\omega_i) - \hat{H}_e^k(\omega_i))(H_{m,e}^{k,r}(\omega_i) - \hat{H}_e^k(\omega_i))^* \right), \quad (3.28)$$

where $(.)^*$ is the conjugate operator. Using (3.22), a 99.5 percent confidence interval for the noise is given by

$$|\bar{V}_e^k(\omega_i)| = 2.3 \sqrt{\hat{C}_H^{e,k}(\omega_i)} \quad (3.29)$$

An alternative way to determine the noise variance is by doing an experiment where the vehicle is at standstill and to compute the variance of the measured signals Hakvoort and van den Hof (1997). However, for the tractor semi-trailer system, the noise level is expected to change for different velocities and driving conditions.

Under Assumption 3.3.5, the bias estimate equals zero for signal-to-noise ratios above 6 dB. For signal-to-noise ratios below 6 dB, Assumption 3.3.4 specifies that the combination of bias and noise variance equals the full error between model and measurements. Herein, for a signal-to-noise ratio of 6 dB, it holds that

$$\frac{|u_t(\omega_i)|}{|v_u|} = 2, \quad (3.30)$$

From Assumptions 3.3.1 and 3.3.2 it follows, that the upper bound on the measurement noise is given by $|\bar{v}_u| = 2.3\sigma_u$. Consequently, the maximum measured input for a signal-to-noise ratio of 6 dB is given by

$$|\bar{u}_m(\omega_i)| = |\bar{u}_t(\omega_i)| + 2.3\sigma_u = 6.9\sigma_u, \quad (3.31)$$

where σ_u is the frequency independent standard deviation of the input noise.

For all $|\bar{u}_m(\omega_i)| < 6.9\sigma_u$ the signal-to-noise ratio may be below 6 dB. Herein σ_u needs to be estimated based on physical insight, measurement data, and the sensor

specifications. Consequently, the upper bound on the bias estimate for a certain trial is given by

$$\begin{aligned} |\bar{B}_e^{k,r}(\omega_i)| &= |H_{mod}^{k,r}(\omega_i) - \hat{H}_e^{k,r}(\omega_i)| \quad \forall |u_m^{e,r}(\omega_i)| < \tau_u \\ |\bar{B}_e^{k,r}(\omega_i)| &= 0 \quad \forall |u_m^{e,r}(\omega_i)| \geq \tau_u, \end{aligned} \quad (3.32)$$

where the input tolerance is given by

$$\tau_u = 6.9\sigma_u. \quad (3.33)$$

The upper bound on the bias estimate for all trials is given by

$$|\bar{B}_e^k(\omega_i)| = \max(|\bar{B}_e^{k,1}(\omega_i)|, \dots, |\bar{B}_e^{k,n_r}(\omega_i)|). \quad (3.34)$$

4. Determine the minimum model uncertainty $\|\Delta_u^k\|_\infty < \gamma_k(\omega_i)$ for each input-output combination not invalidating the model. Hereto, first determine for each test

$$\|W_k(\omega_i)\Delta_{u,e}^k(\omega_i)\|_\infty = \max(|H_{mod}^k(\omega_i) - \hat{H}_e^k(\omega_i)| - |\bar{V}_e^k| - |\bar{B}_e^k|, 0), \quad (3.35)$$

with $W_k(\omega_i)$ a weighting filter that is included to relate to robust control literature dealing with parametric overbounds, Skogestad and Postlethwaite (2005), in which the combination of W and γ model the uncertainty. For our case of a nonparametric overbound, the weighting may be set to 1.

When $\|W_k(\omega_i)\Delta_{u,e}^k\|_\infty$ is determined for each test, the minimum model uncertainty not invalidating the model for the k^{th} input-output combination $\gamma_k > \|\Delta_u^k\|_\infty$ is given for each frequency by

$$\gamma_k(\omega_i) = \max(\|\Delta_{u,1}^k(\omega_i)\|_\infty, \dots, \|\Delta_{u,n_e}^k(\omega_i)\|_\infty). \quad (3.36)$$

Herein, the model is not invalidated if a $\Delta_u^k(\omega_i) \in \mathcal{RH}_\infty$, $\|\Delta_u^k(\omega_i)\|_\infty < \gamma_k(\omega_i)$ exists for each k . A proof that this holds, on a discrete frequency grid, is based on a Nevanlinna-Pick interpolation result, and provided in Oomen and Bosgra (2008).

The concept is depicted in Figure 3.8. Herein, the mean transfer function estimate \hat{H} and the modeled transfer function estimate H_{mod} are depicted in the complex-plane for a certain frequency ω_i . The circle around \hat{H} represents the interval within which the true-system should lie, based on the 99.5% confidence interval of the noise variance in combination with the estimated bias B . The distance between the edge of this circle and H_{mod} equals the minimum model uncertainty for this one specific frequency and test.

Note that $\|\Delta_u^k\|_\infty < \gamma_k(\omega_i)$ is a non-conservative, non-parametric overbound on the systematic modeling error (measure for the model quality), which is useful for model evaluation and robustness analysis. However, for robust controller synthesis a parametric overbound is typically required. Consequently, the question remains how to obtain a good parametric overbound from the non-parametric one. This topic is not further addressed in this thesis.

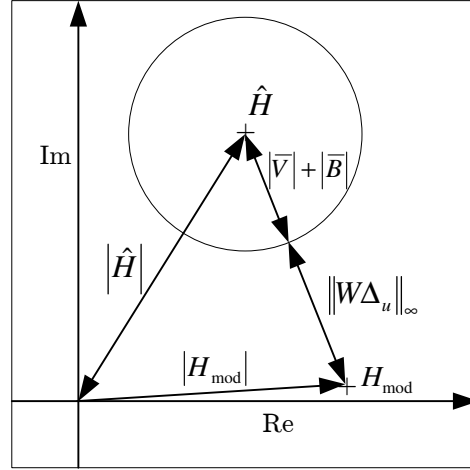


Figure 3.8: Minimum model uncertainty determination for a certain frequency.

3.3.6 Example

To illustrate the proposed validation approach, consider the following (SISO) example. The true system H_t is given by

$$H_t = \frac{4\pi}{s + 4\pi}, \quad (3.37)$$

and a model of the system is given by

$$H_{mod} = \frac{2\pi}{s + 2\pi}. \quad (3.38)$$

Assume it is possible to exactly identify the true system ($|\bar{V}| = |\bar{B}| = 0$). Choosing $W(\omega_i) = 1$ for all frequencies, it is then possible to determine the minimum model uncertainty using (3.35, 3.36), see Figure 3.9 (left). The maximum over all frequencies of the minimum model uncertainty not invalidating the model equals $\max(\gamma(\omega_i)) = 0.33$ at $\omega_i = 1.4$ Hz, which is a 57% deviation with respect to the model at that frequency. It should be noted that the relative model uncertainty increases at higher frequencies. In the remainder of this chapter the maximum absolute model uncertainty is chosen as the main measure for the model quality, as that gives more useful information when comparing models.

The model uncertainty can be translated to a phase and gain uncertainty on the nominal model. Computation of the gain uncertainty is straightforward

$$\delta_{H,mag}(\omega) = |W(\omega_i)|\gamma(\omega_i), \quad (3.39)$$

and the phase uncertainty (in rad) can be obtained using goniometric relations

$$\begin{aligned} \delta_{H,phase}(\omega_i) &= \min \left(\sin^{-1} \left(\frac{|W(\omega_i)|\gamma(\omega_i)}{|H_{mod}(\omega_i)|} \right), \pi \right), \\ &\quad \text{if } |W(\omega_i)|\gamma(\omega_i) \leq |H_{mod}(\omega_i)| \\ &= 2\pi, \text{ if } |W(\omega_i)|\gamma(\omega_i) > |H_{mod}(\omega_i)|. \end{aligned} \quad (3.40)$$

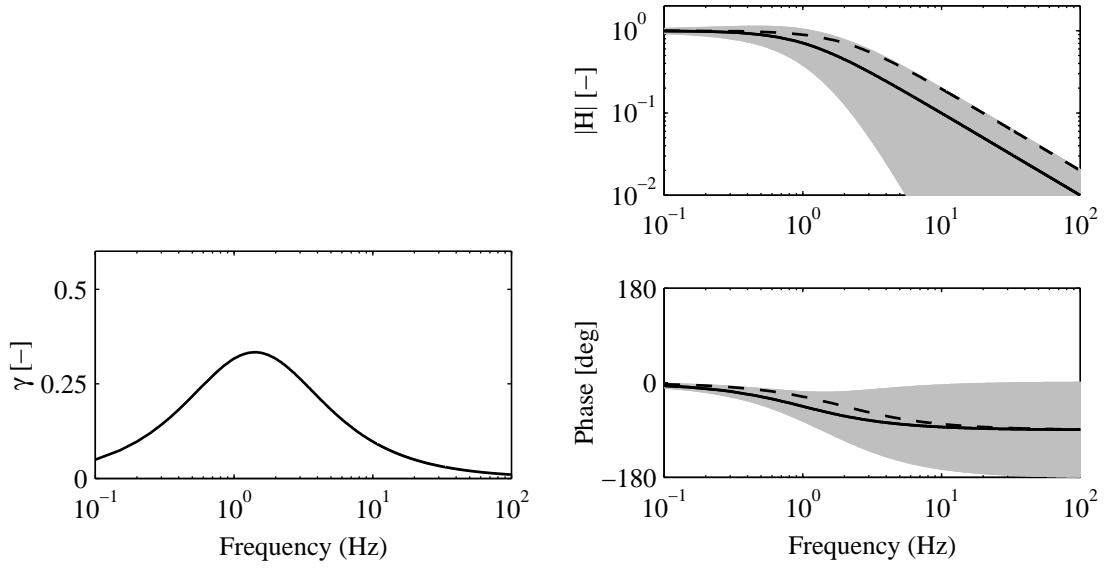


Figure 3.9: Example using idealized conditions. Frequency dependent model uncertainty (left); and bode plot (right) of the nominal model (black), true system (dashed), and uncertainty region (grey).

When doing so for the example system, the nominal model with uncertainty bounds as given in Figure 3.9 (right) is found. As a consequence of the circular uncertainty model, there is a relatively large phase uncertainty at higher frequencies, even though the modeled phase is in fact quite accurate.

In practice the true system will not be known exactly. Lets assume that measurement data is provided from two different tests, and that each is repeated six times. In the first test the true input for repetition r is given by

$$u_t^r = 0.3 \sin(2\pi t + \phi_r) + \sin(20\pi + \phi_r), \quad (3.41)$$

where ϕ_r is a constant, which differs for each repetition. Consequently, the measurements are asynchronous. In the second test, the input is generated by selecting values from a zero mean uniform random distribution (white noise), with a standard deviation of 5, that has been filtered with a 5 Hz first order low-pass filter. Furthermore, a new input set is generated for each repetition, so the data are again asynchronous. In the simulations the input and output time-domain signals are distorted by noise with a root-mean-square (rms) value of 0.1. The simulation time is 20 seconds and a sample frequency of 200 Hz is used.

The input tolerance is chosen as $\tau_u = 50$. The minimum model uncertainty not invalidating the model, using only the first numerical experiment, is given in Figure 3.10 (left). Clearly, the first test gives an indication that there is model uncertainty at the input frequencies of 1 and 10 Hz. Moreover, the poor signal-to-noise ratio at the other frequencies does not result in an overly conservative model uncertainty estimate. The maximum γ of 0.28 at $\omega_i = 1$ Hz, which corresponds to a 40% deviation from the model at that frequency, is reasonably close to the true maximum. However,

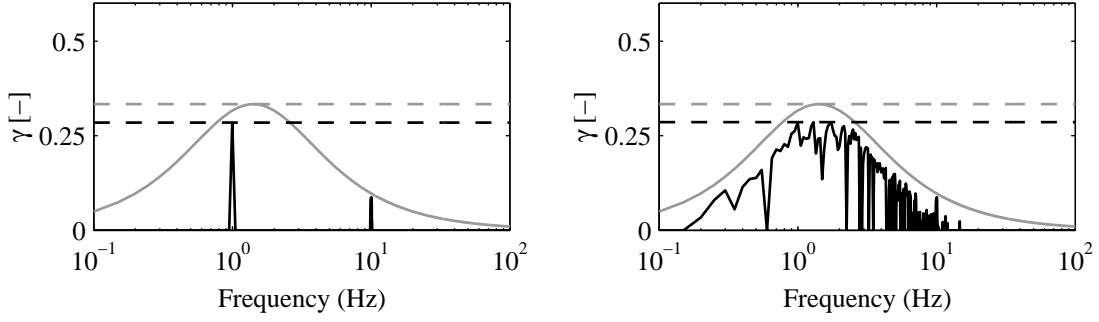


Figure 3.10: Example using only the first numerical experiment (left) or using both (right): frequency dependent maximum singular value model uncertainty (black) and the true value (grey). The peak minimum model uncertainty γ is given by the dashed lines.

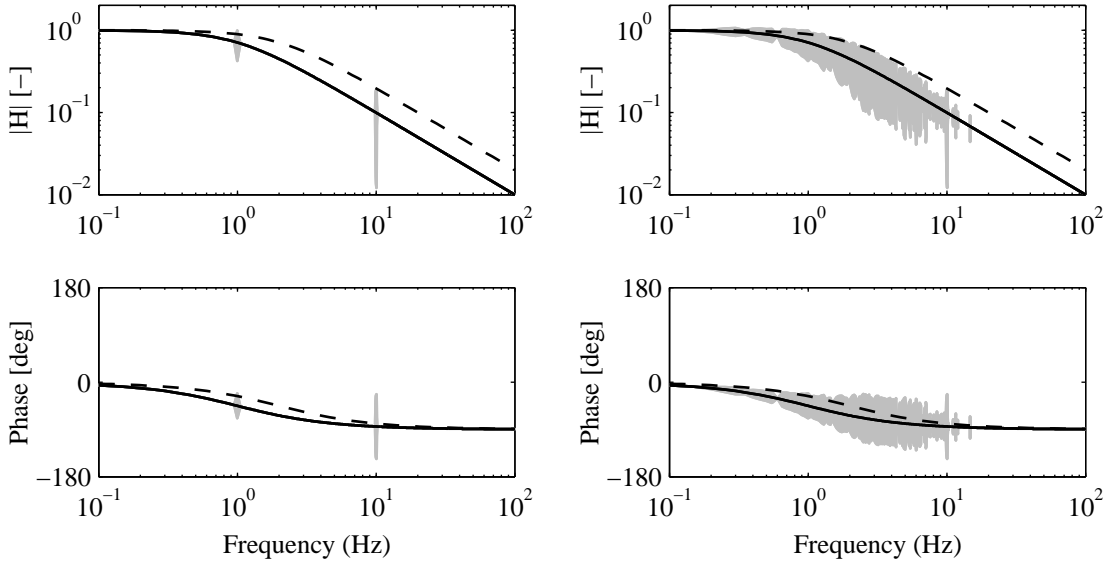


Figure 3.11: Example using only the first test (left) or using both (right). Bode plot: nominal model (black); true system (dashed); and model uncertainty (grey).

the determined value is still slightly optimistic as the signal-to-noise ratio does not equal infinity. When also using the second numerical experiment, the minimum model uncertainty for the low frequency region increases, Figure 3.10 (right). In this case, $\max(\gamma) = 0.29$ (47%) at $\omega_i = 1.3$ Hz.

The resulting transfer functions are given in Figure 3.11. The large uncertainty at 10 Hz originates from the first numerical experiment and the uncertainty at the remaining frequencies from the second. Clearly, the found model uncertainty using these two numerical experiments is contained by the true uncertainty as is given in Figure 3.9. Even though there are only six repetitions - more would give a more reliable noise model - the proposed validation reliably reveals the model deficiencies.

3.4 Model validation

In this section, the proposed model validation approach is applied to the three reduced order models and the 44 DOF tractor semi-trailer model. The disturbance force or moment (F_d , M_d) is assumed to be zero as there is no steering, braking, accelerating, or passing traffic; $\dot{x}_T = x_T = 0$; and $F_{act} = M_{act} = 0$ as the experimental vehicle does not have an active suspension. Furthermore, for the roll model it is assumed that the roll of the rear chassis ϕ_5 is an independent zero mean Gaussian distributed (white noise) disturbance, given the high inertia of the trailer. The transfer function from the road inputs \underline{v}_r to each of the measured outputs \underline{y} cannot be determined from the provided experimental data. However, it is possible to determine the transfer functions from the front axle roll and heave acceleration ($\ddot{\phi}_{af}$, \ddot{z}_{af}) to each of the other measurements. Likewise, the modeled transfer functions can be determined as

$$\begin{aligned} H_{y_i/\ddot{\phi}_{af}} &= H_{y_i/\phi_r} H_{\ddot{\phi}_{af}/\phi_r}^{-1} \\ H_{y_i/\ddot{z}_{af}} &= H_{y_i/z_r} H_{\ddot{z}_{af}/z_r}^{-1}. \end{aligned} \quad (3.42)$$

So, using the data of these tests it is possible to determine the quality of a part of the reduced order models, as depicted in the dashed box in Figure 3.1, 3.4 and 3.5, for road induced vibration.

3.4.1 Quarter truck heave model

For the validation of the quarter truck heave model (3.2), with the parameters as given in Table A.7, and the measurement data as discussed in Section 3.3.2, the tolerance is chosen as $\tau = 80$. The maximum of the minimum model uncertainty not invalidating the model, over the full frequency grid for the four outputs

$$\underline{y} = [\ddot{z}_f, \ddot{z}_c, z_p, z_s]^T, \quad (3.43)$$

with $z_p = z_f - z_a$ and $z_s = z_c - z_f$, is found to be

$$\max(\gamma_{1,2,3,4}(\omega)) = [0.63, 0.93, 0.01, 0.01]. \quad (3.44)$$

at [1.8, 1.6, 1.3, 1.0] Hz respectively, which corresponds to a deviation with respect to the model at those frequencies of [33%, 46%, 85%, 100%]. The largest model uncertainty lies near the cabin bounce mode (1.2 Hz).

The transfer function from the axle- to the chassis acceleration is given in Figure 3.12 (left). It can be seen that there is a significant variation between the various measured transfer functions. Note that these are in fact the averaged transfer functions over the 6 trials of each of the tests. The variation is not (completely) the result of noise. The different velocities, and differences between the case with and without trailer, influence the system dynamics leading to model uncertainty. The transfer to the cabin acceleration, as is given in Figure 3.12 (right), shows a similar picture. The

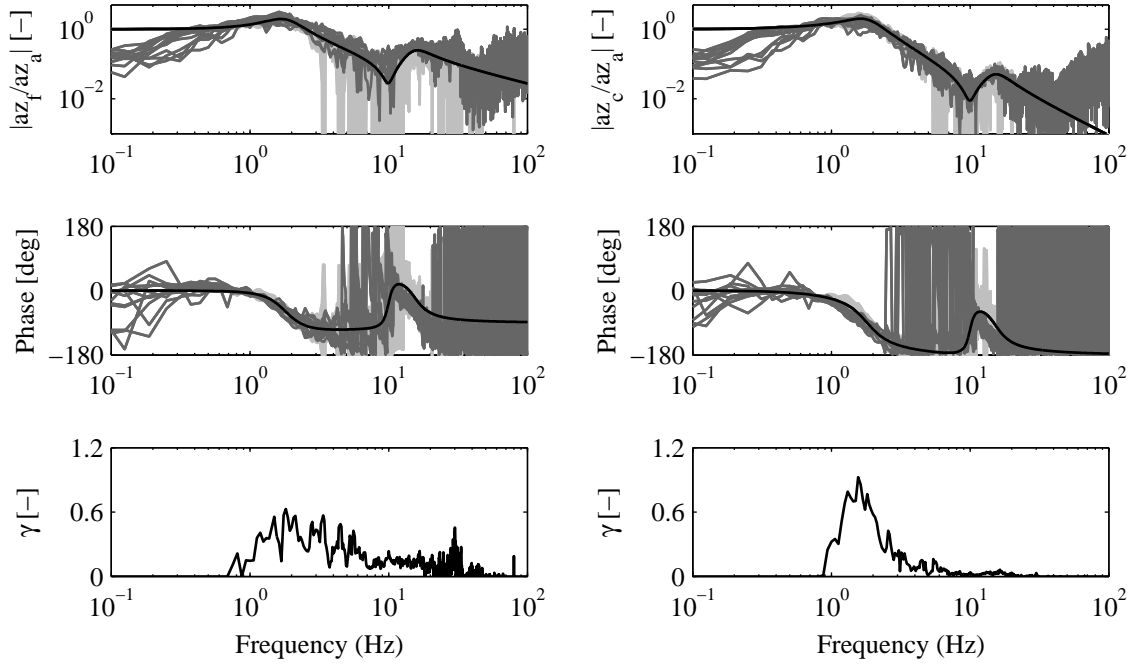


Figure 3.12: Four-mass heave model, transfer axle vertical acceleration to vertical chassis- (left) and cabin acceleration (right): nominal model (black); mean transfer function estimates (dark grey); and model uncertainty (light grey). Minimum model uncertainty not invalidating the model (bottom).

large mismatch around the cabin heave mode dominates the uncertainty plot. The difference below 1 Hz is mainly contributed to noise effects and the poor signal-to-noise ratio.

When looking at the transfer function of the axle acceleration to the primary suspension displacement, see Figure 3.13 (left), the accuracy is remarkable. This, despite the fact that the model is linear, and that friction effects in the suspension are not included in the model. Furthermore, the variations between the measured transfer functions is relatively small in the region 2 – 10 Hz, indicating that the influence of noise and nonlinearities is small in this region, for this transfer, under these conditions. The main model uncertainty is located around the cabin resonance frequency (1.2 Hz).

Finally, when considering the transfer function to the secondary suspension displacement, as is given in Figure 3.13 (left), it can be seen that the variation between the measured transfer functions is larger than is the case for the primary suspension displacement. Overall, the absolute value of the modeled transfer lies below the averaged measurements. This may be an indication that the used cabin stiffness is chosen too high.

Now, the question arises whether or not it would be a good idea to fine tune the cabin stiffness based on these results. As the value of the cabin stiffness is based on that of the 44 DOF model, it was decided not to change it. Otherwise, the stiffness parameter of the 44 DOF model would also have to be changed to keep the physical interpretation of the parameter. In that case, the time-domain validation procedure of

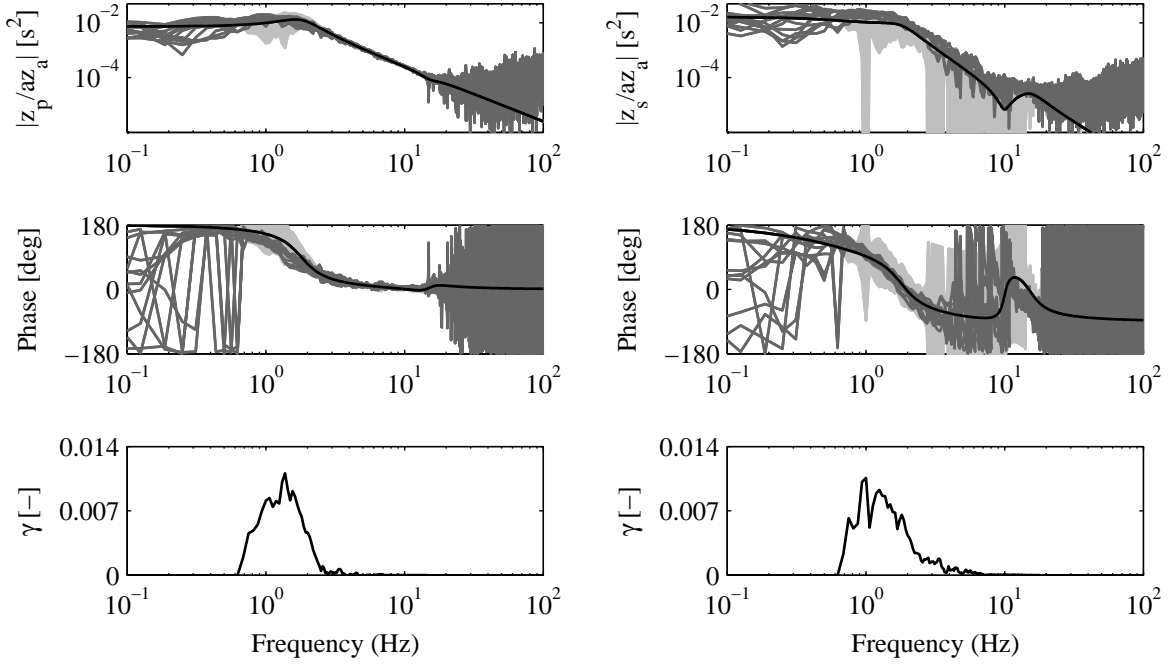


Figure 3.13: Four-mass heave model, transfer axle vertical acceleration to primary (left) and secondary (right) suspension displacement: nominal model (black); mean transfer function estimates (dark grey); and model uncertainty (light grey). Minimum model uncertainty not invalidating the model (bottom).

the previous chapter would have to be done again.

Furthermore, tuning parameters is part of the identification procedure while validation is used to evaluate the predictive properties (quality) of the model. As such, the most robust way to check the model quality is by separating identification and model validation by validating with an independent set of measurement data, (Pintelon and Schoukens, 2001, Chapter 11.4).

Overall, it can be concluded that the quarter truck heave model gives a fair description of the vertical dynamics of the front of the vehicle for the comfort relevant frequency range. The largest model uncertainty lies around the cabin resonance frequency, which needs to be taken into account when using this model for suspension design.

3.4.2 Half truck roll model

The second model that is validated is the half truck roll model (3.6), with the parameters as given in Table A.8. The proposed validation approach is applied with input tolerance $\tau = 160$, as the roll axle acceleration is distorted by a larger amount of measurement noise than the vertical axle acceleration, see Figure 3.6. The maximum of the minimum model uncertainty not invalidating the model, over the full frequency grid for the four outputs

$$\underline{y} = [\ddot{\phi}_f, \ddot{\phi}_c, \phi_p, \phi_s]^T, \quad (3.45)$$

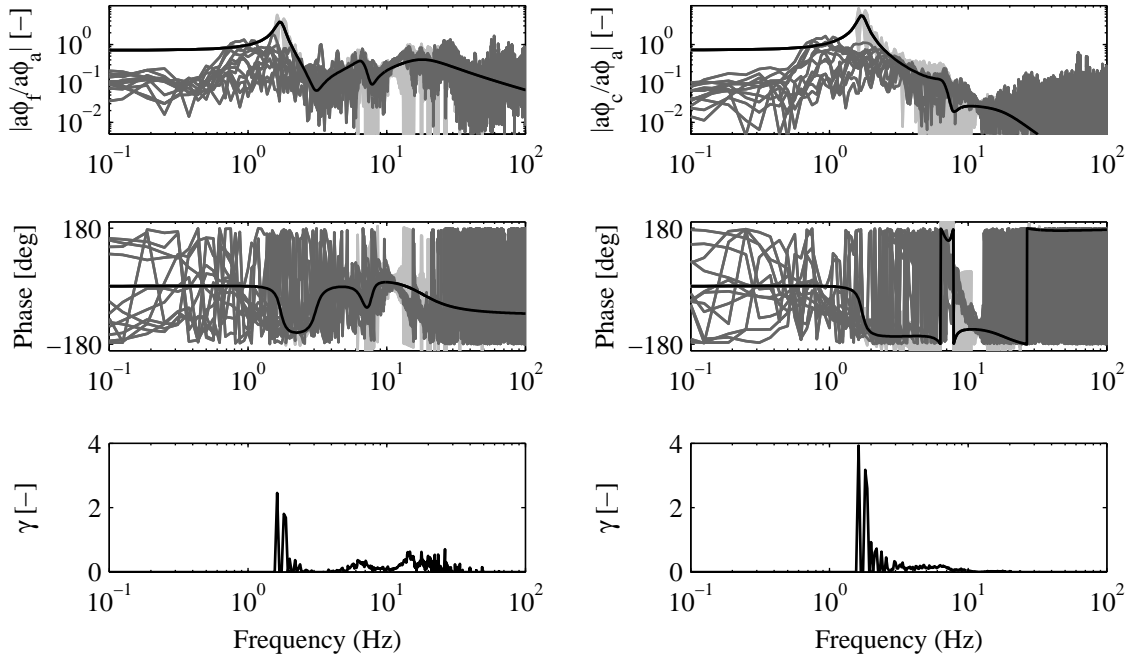


Figure 3.14: Four-mass roll model, transfer axle roll acceleration to chassis (left) and cabin (right) roll acceleration: nominal model (black); mean transfer function estimates (dark grey); and model uncertainty (light grey). Minimum model uncertainty not invalidating the model (bottom).

with $\phi_p = \phi_f - \phi_a$ and $\phi_s = \phi_c - \phi_f$, is found to be

$$\max(\gamma_{1,2,3,4}(\omega)) = [2.46, 3.93, 0.02, 0.01]. \quad (3.46)$$

at 1.6 Hz, which corresponds to a relative mismatch of [76%, 87%, 89%, 88%] with respect to the model. So, the largest model uncertainty lies near the vehicle roll mode (1.7 Hz). This can also be seen when looking at the transfer function from the axle roll acceleration to the chassis front roll acceleration, as is given in Figure 3.14 (left). The vehicle mode appears to be damped significantly more in practice. On the other hand, in the region 2–20 Hz the model gives a good representation of the measured dynamics. The differences between the model and measurements below 1 Hz are attributed to the noise.

The transfer from the axle roll acceleration to the cabin roll acceleration, as is given in Figure 3.14 (right), shows a similar picture. The mismatch at the 1.7 Hz resonance is mainly attributed to model uncertainty. The model uncertainty in the region of 3–10 Hz is more or less of a constant magnitude. Furthermore, there is a relatively large spread between the measured transfer functions in this region which is not completely the result of noise effects.

Finally, the transfer functions from the axle roll acceleration to the primary and secondary suspension displacements are given in Figure 3.15. Herein, it can be seen that the transfer to the primary suspension displacement is modeled relatively accurately. The main source of model uncertainty lies at low frequencies, and originates from the

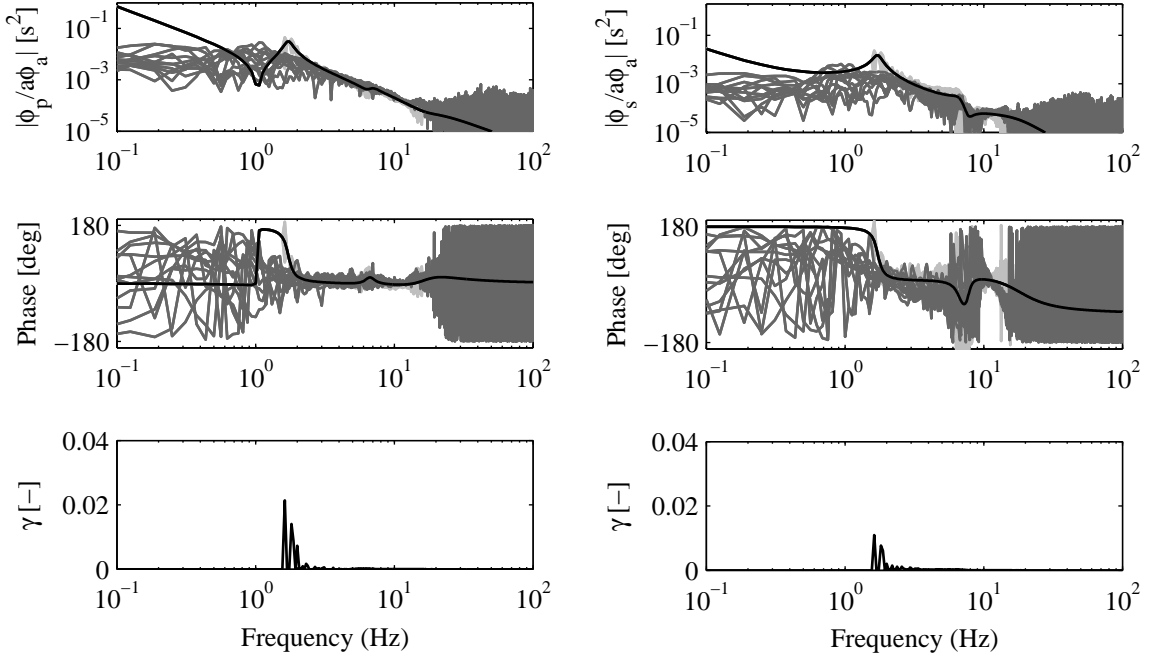


Figure 3.15: Four-mass roll model, transfer axle roll acceleration to primary (left) and secondary (right) suspension displacement, using tuned parameters: nominal model (black); mean transfer function estimates (dark grey); and model uncertainty (light grey). Minimum model uncertainty not invalidating the model (bottom).

assumption that the rear chassis roll equals zero, which is not the case in practice. The transfer function to the secondary suspension shows again the most uncertainty around the cabin resonance frequency.

Overall, the half truck roll model gives a fair representation of the measured road vibration characteristics of the real tractor semi-trailer system under different driving conditions. However, the significant model uncertainty around the cabin resonance frequency might be problematic when using this model for controller design purposes.

3.4.3 Half truck pitch-heave model

Validation of the 9 DOF pitch-heave model, as is schematically depicted in Figures 3.5, A.4 and parameterized in Appendix A.5, is slightly more complicated than is the case for the previously described roll and heave models. Again the transmissibility from road to each of the measured outputs cannot be determined experimentally. Similar to the case for the roll and heave quarter truck models, it is possible to determine the transfer from the front axle acceleration to each of the outputs, and use these transfer functions to validate the model for road induced vibrations. However, the reason that validation of the pitch-heave model is more difficult lies in the fact that the front z_{rf} and rear tyre displacement z_{rr} are correlated, while the validation procedure requires uncorrelated disturbance and input signals.

When taking into account that the front and rear road displacement are correlated

$$z_{rr}(t) = z_{rf}(t - \tau_w), \quad (3.47)$$

which has the frequency-domain equivalent ((Franklin et al., 1994, Chapter 5))

$$z_{rr}(\omega) = z_{rf}(\omega)e^{-j\omega\tau_w}, \quad (3.48)$$

with $\tau_w = l_{wb}/\dot{x}_{ar}$ and \dot{x}_{ar} the vehicle longitudinal velocity in m/s, it is possible to substitute z_{rr} . In this case,

$$\begin{aligned} y_i &= H_{y_i/z_{rf}} z_{rf} + H_{y_i/z_{rr}} z_{rr} \\ y_i &= H_{y_i/z_{rf}} z_{rf} + H_{y_i/z_{rr}} e^{-j\omega\tau_w} z_{rf} \\ &= \bar{H}_{y_i/z_{rf}} z_{rf}, \end{aligned} \quad (3.49)$$

with $\bar{H}_{y_i/z_{rf}} = H_{y_i/z_{rf}} + H_{y_i/z_{rr}} e^{-j\omega\tau_w}$. Likewise, the transfer function to the front axle acceleration can be written as $\bar{H}_{\ddot{z}_{fa}/z_{rf}} = H_{\ddot{z}_{fa}/z_{rf}} + H_{\ddot{z}_{fa}/z_{rr}} e^{-j\omega\tau_w}$. The part of the model that can be validated is given by the transfer functions

$$\bar{H}_{y_i/\ddot{z}_{fa}} = \bar{H}_{y_i/z_{rf}} \bar{H}_{\ddot{z}_{fa}/z_{rf}}^{-1}. \quad (3.50)$$

Clearly, the modeled transfer functions are velocity dependent. Consequently, lumping all tests for validation, as is done in the previous two subsections, will result in a conservative uncertainty model. For this reason, the validation procedure is performed for two different velocities (60 and 80 km/h), using the model and experimental data that are valid for each of these velocities. Moreover, as the model is not valid for the case without trailer, due to the assumption on the vertical movement of the hitch-point, the measurements without trailer (see Table 2.3) are not used. This way, using the same input tolerance as for the quarter truck heave model ($\tau = 80$), the maximum of the minimum model uncertainty not invalidating the model, over the full frequency grid for the nine outputs

$$\underline{y}_{hp} = [\ddot{z}_f, \ddot{\theta}_f, \ddot{x}_c, \ddot{z}_c, \ddot{\theta}_c, z_{pf}, z_{pr}, z_{sf}, z_{sr}]^T, \quad (3.51)$$

is found to be

$$\max(\gamma_{1-9}(\omega)) = [0.85, 0.71, 0.73, 0.45, 0.62, 8.10^{-3}, 0.06, 7.10^{-3}, 0.015], \quad (3.52)$$

at [1.7, 1.4, 1.4, 2.1, 1.4, 1.6, 0.6, 1.4, 1.4] Hz, when driving at 80 km/h. This is equivalent to a relative uncertainty with respect to the model magnitude at those frequencies of [39%, 127%, 187%, 56%, 122%, 50%, 97%, 46%, 245%]. The results are (slightly) different when driving at 60 km/h:

$$\max(\gamma_{1-9}(\omega)) = [0.85, 0.60, 0.52, 0.38, 0.37, 7.10^{-3}, 0.05, 9.10^{-3}, 0.01], \quad (3.53)$$

at [1.6, 1.6, 1.4, 1.9, 1.4, 1.5, 0.7, 0.8, 0.8] Hz, which is equivalent to a relative mismatch of [37%, 116%, 134%, 37%, 74%, 42%, 100%, 44%, 190%]. So, the modeled

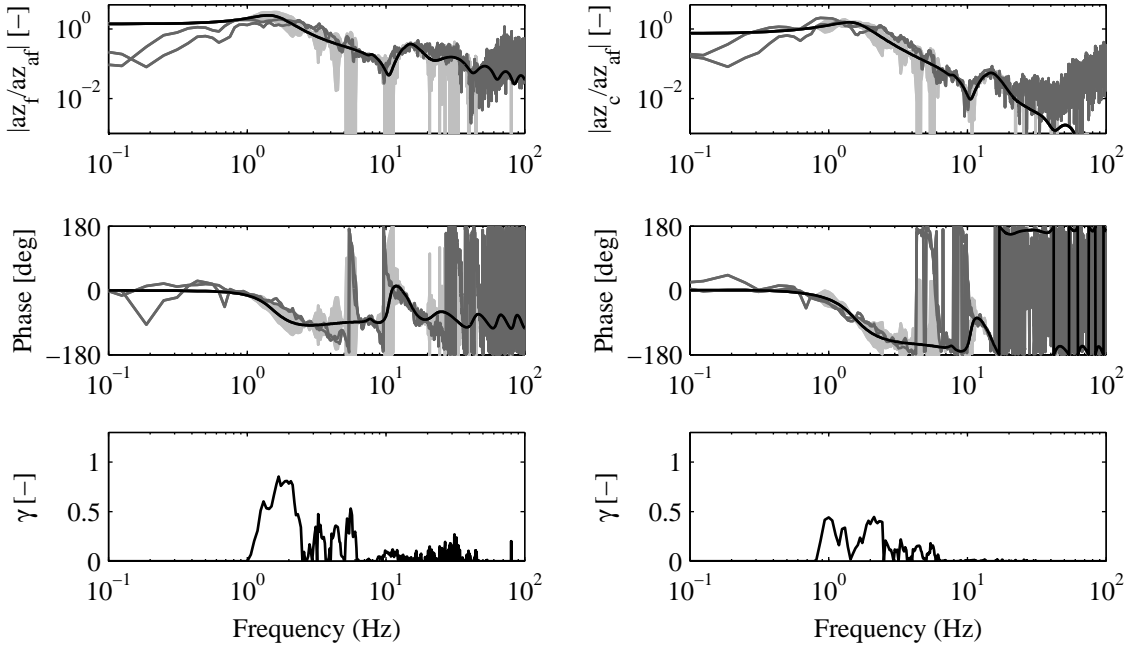


Figure 3.16: Pitch-heave model at 80 km/h, transfer front axle vertical acceleration to vertical chassis- (left) and cabin acceleration (right): nominal model (black); mean transfer function estimates (dark grey); and model uncertainty (light grey).

transfer functions, the measured transfer functions, and the model uncertainty are all velocity dependent.

The transfer from the front axle vertical acceleration to the vertical chassis acceleration at 80 km/h is given in Figure 3.16 (left). Around 2 Hz it reaches the value of 0.85, which is higher than was the case for the quarter truck heave model (0.66). This is related to the fact that the cabin heave mode lies at a lower frequency in the pitch-heave model. However, the uncertainty of the transfer to the vertical cabin acceleration is considerably lower, 0.45 versus 1.16 for the quarter truck model. For both transfer functions, the model gives a relatively accurate representation of the experimental data up to 20 Hz.

The inclusion of the cabin pitch motion is one of the main advantages of this model over the simpler quarter truck heave model. However, as can be seen in Figure 3.17, the model is not that accurate. At 3 and 6 Hz there are resonances in the measurements, which are not included in the model. Still, up to approximately 5 Hz, the main trend of the model and measurements is identical.

The transfer function to the longitudinal cabin acceleration, as is given in Figure 3.18 (left) shows a similar picture. The dynamics at 60 km/h (right) are slightly different, which serves to illustrate the velocity dependency.

When looking at the transfer functions to the primary suspension displacement, as is given in Figure 3.19, it can be seen that the model is considerably more accurate for the front than for the rear dynamics. The uncertainty at the rear originates from

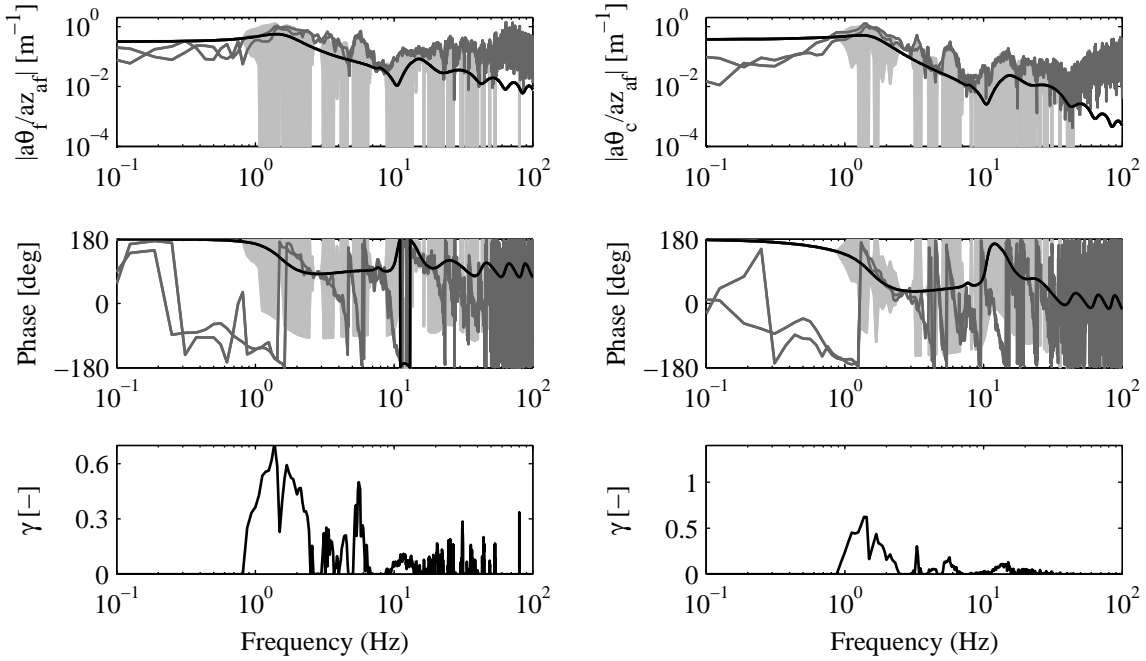


Figure 3.17: Pitch-heave model at 80 km/h, transfer front axle vertical acceleration to chassis (left) and cabin pitch acceleration (right): nominal model (black); mean transfer function estimates (dark grey); and model uncertainty (light grey).

a phase mismatch in combination with a magnitude mismatch below 1 Hz. Both are expected to be the result of the constraint on the trailer hitch point vertical movement.

The transfer function to the secondary suspension displacement (Figure 3.20) shows a similar picture. So, overall the half truck pitch-heave model gives a reasonably accurate representation of the measured vehicle dynamics in the comfort relevant frequency ranges. The most significant uncertainty lies near the cabin resonances (1 – 2 Hz) and, for the rear suspension displacements, in the frequency region below 1 Hz. Furthermore, there is a noticeable mismatch for the pitch dynamics above 5 Hz, although the influenced when designing cabin controllers may be less severe due to the low ISO pitch weighting at those frequencies, see ISO 2631-1 (1997).

3.4.4 Tractor semi-trailer model (continued)

In the previous chapter a comparison is given between the different transfer functions of the 44 DOF tractor semi-trailer model and the measurement data. In this section, the model validation is completed by distinguishing between noise and structural errors, using the approach as presented in the previous section. Similar to the case of the pitch-heave model, the validation is performed at two different velocities: 60 and 80 km/h.

As the model is nonlinear, the transfer functions of the model are determined using a simulation of 60 seconds on the highway road described in section 2.7 and Figure

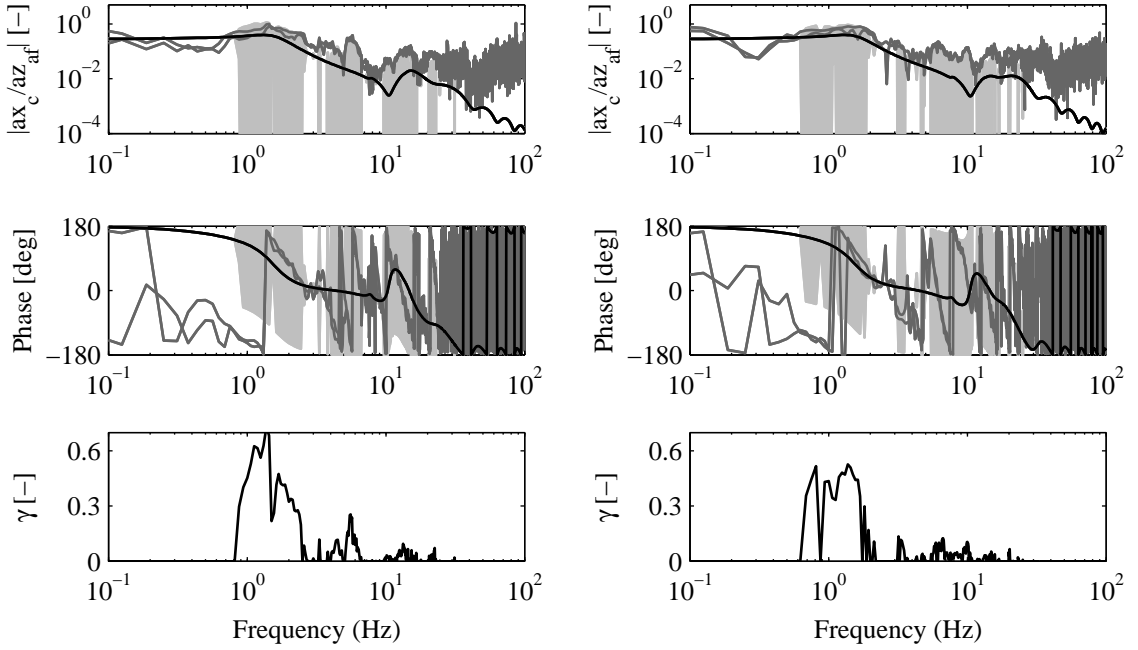


Figure 3.18: Pitch-heave model at 80 km/h (left) and 60 km/h (right), transfer front axle vertical acceleration to cabin longitudinal acceleration: nominal model (black); mean transfer function estimates (dark grey); and model uncertainty (light grey).

2.28. The vertical- and roll acceleration of the middle of the front axle are taken as inputs, which can be considered to be uncorrelated (Figure 2.27).

Using the same input tolerance as for the heave, pitch-heave and roll model, the maximum of the minimum model uncertainty not invalidating the model, over the full frequency grid for the eighteen outputs

$$\underline{y}_{44} = [\ddot{x}_f, \ddot{y}_f, \ddot{z}_f, \ddot{\theta}_f, \ddot{\phi}_f, \ddot{x}_c, \ddot{y}_c, \ddot{z}_c, \ddot{\theta}_c, \ddot{\phi}_c, z_{pf}, z_{pr}, z_{sf}, z_{sr}, \phi_{pf}, \phi_{pr}, \phi_{sf}, \phi_{sr}]^T, \quad (3.54)$$

and two inputs $[\ddot{z}_{fa}, \ddot{\phi}_{fa}]$ is obtained. The most interesting differences are shortly discussed.

When considering the transfer functions from the front axle heave acceleration to the cabin vertical acceleration, as is given in Figure 3.21 (left), it can be seen that the model describes the measured dynamics with a high level of accuracy. The 44 DOF model is in this respect more accurate than the 4 DOF heave model, but slightly less accurate than the 9 DOF pitch-heave model. The two reduced order models do not describe the influence of the front axle roll acceleration on the cabin vertical acceleration. However, as can be seen in Figure 3.21 (right), the influence of this transfer to the overall response is very significant. Moreover, the tractor semi-trailer model has a relatively large level of uncertainty for this transfer in the region of 2 – 4 Hz, which may be related to the modeling of the trailer roll modes.

The transfer functions to the cabin pitch acceleration, as depicted in Figure 3.22, also show a large influence of both inputs. But in this case, the model accurately

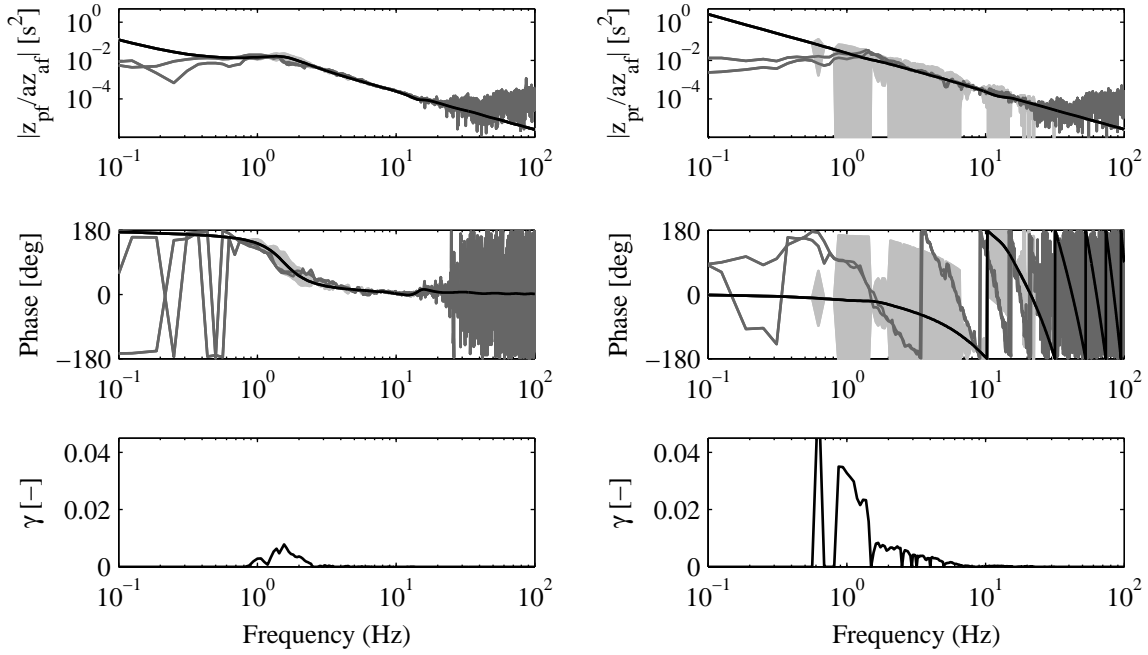


Figure 3.19: Pitch-heave model at 80 km/h, transfer front axle vertical acceleration to front (left) and rear (right) primary suspension displacement: nominal model (black); mean transfer function estimates (dark grey); and model uncertainty (light grey).

describes the dynamics in the comfort relevant frequency range. The transfer from the vertical front axle acceleration is more accurate than the pitch-heave model, although both models have a similar level of inaccuracy above 5 Hz. This is mainly the result of chassis bending which is not included in these models.

As can be seen in Figure 3.23 (right), the transfer from the front axle roll acceleration to the lateral cabin acceleration is modeled relatively well. However, the transfer from the front axle vertical acceleration shows a larger mismatch in the region 1-2 Hz. The transfer functions to the cabin roll acceleration Figure 3.24 show similar results.

Finally, when considering the transfer functions to the rear secondary suspension displacements as given in Figure 3.25, it can be seen that the model is relatively accurate in comparison to the pitch-heave model. Moreover, the relation between these inputs and the other suspension displacements is modeled equally well.

Overall it can be concluded that the 44 DOF tractor semi-trailer model has a relatively high level of accuracy in the comfort relevant frequency ranges. The only exceptions are the transfer from the front axle vertical acceleration to the cabin lateral acceleration and the transfer from the front axle roll acceleration to the cabin vertical acceleration. Herein, some correlation between the inputs may be affecting the results. Still, even though the model does not give a perfect representation of these two transfer functions, the trends show a reasonable match. As such, it is assumed that the 44 DOF model is sufficiently accurate for the comfort evaluation of the (active) suspension designs in this thesis.

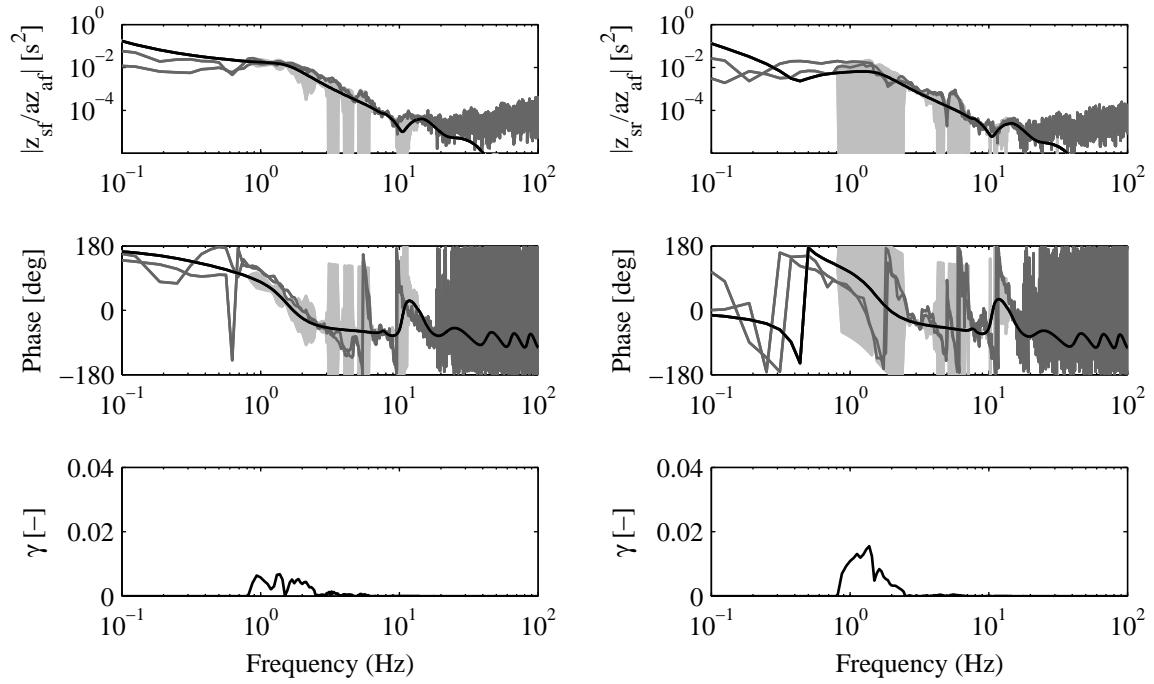


Figure 3.20: Pitch-heave model at 80 km/h, transfer front axle vertical acceleration to front (left) and rear (right) secondary suspension displacement: nominal model (black); mean transfer function estimates (dark grey); and model uncertainty (light grey).

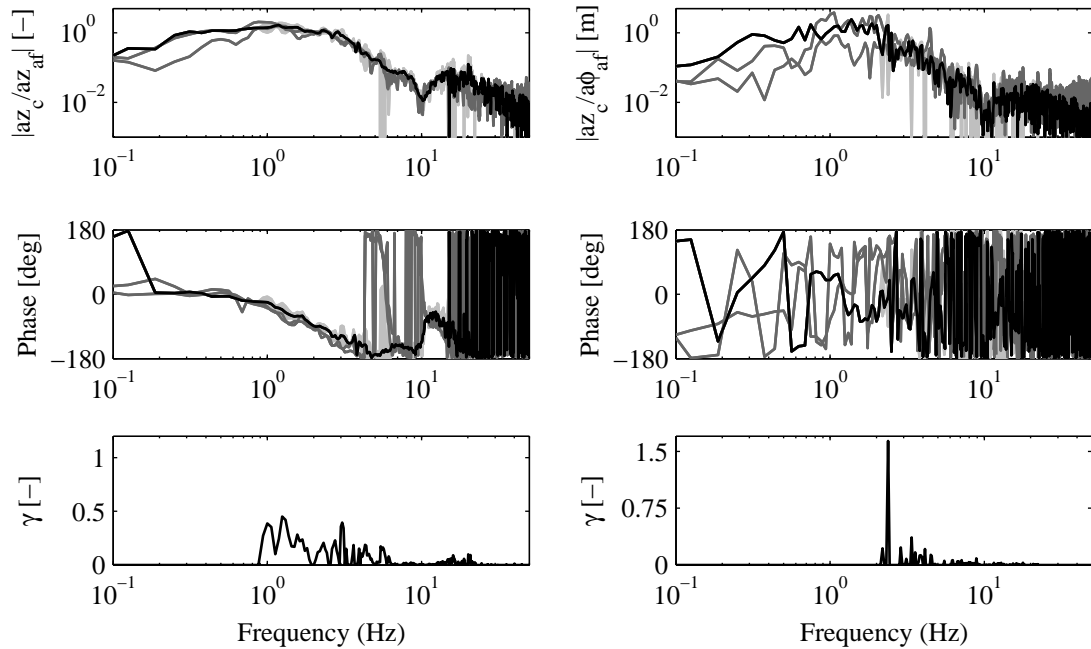


Figure 3.21: Tractor semi-trailer model at 80 km/h, transfer front axle vertical (left) and roll (right) acceleration to cabin vertical acceleration: nominal model (black); mean transfer function estimates (dark grey); and model uncertainty (light grey).

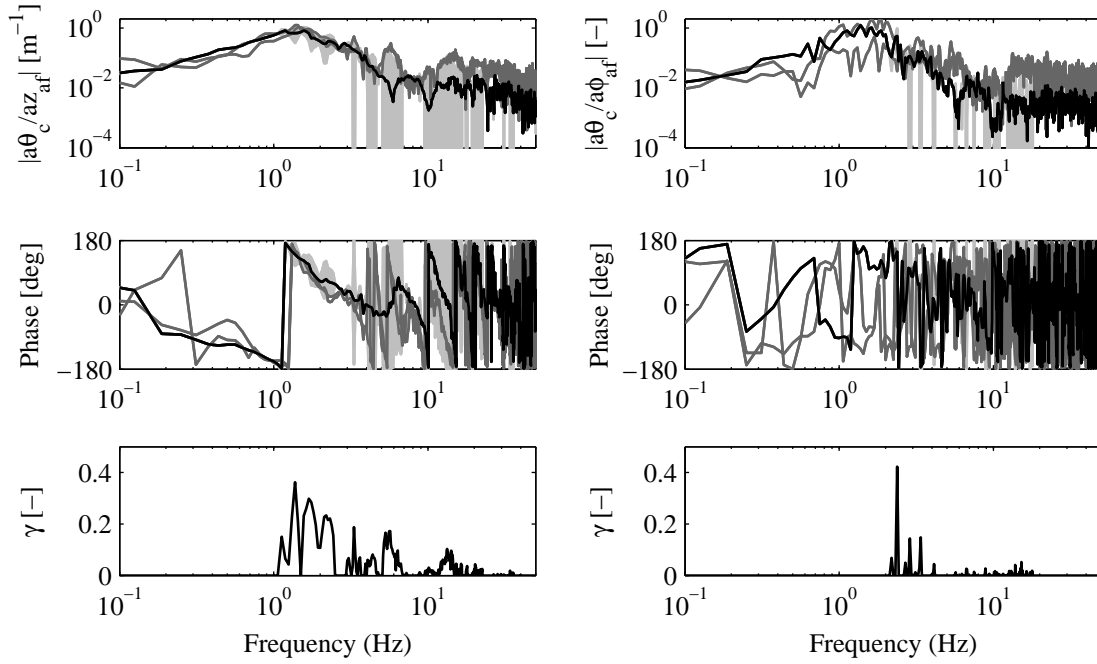


Figure 3.22: Tractor semi-trailer model at 80 km/h, transfer front axle vertical (left) and roll (right) acceleration to cabin pitch acceleration: nominal model (black); mean transfer function estimates (dark grey); and model uncertainty (light grey).

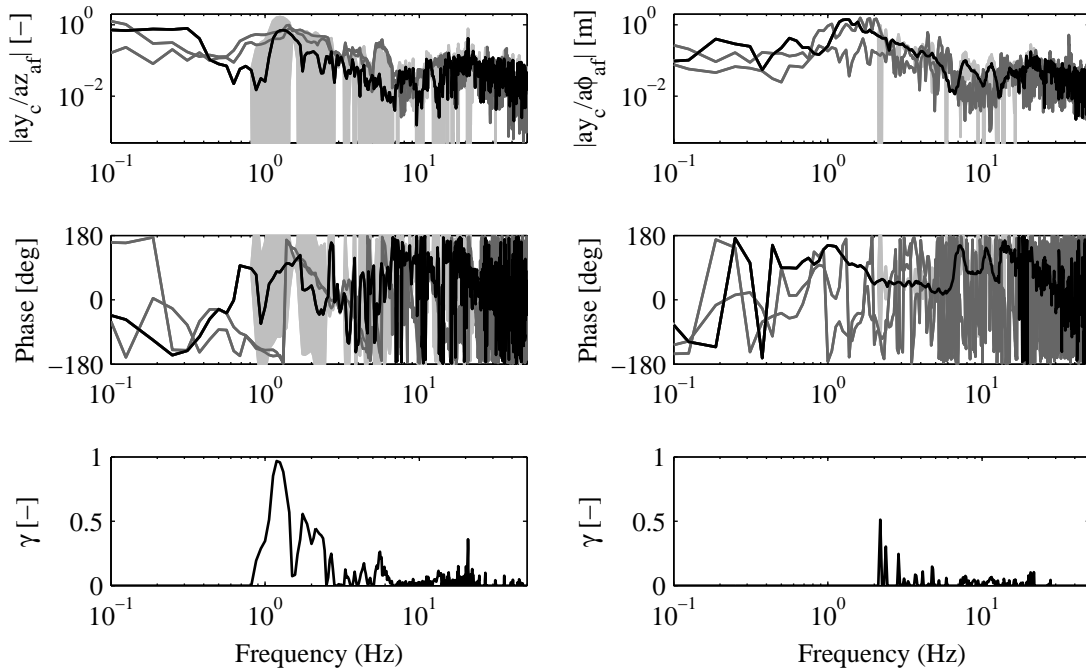


Figure 3.23: Tractor semi-trailer model at 80 km/h, transfer front axle vertical (left) and roll (right) acceleration to cabin lateral acceleration: nominal model (black); mean transfer function estimates (dark grey); and model uncertainty (light grey).

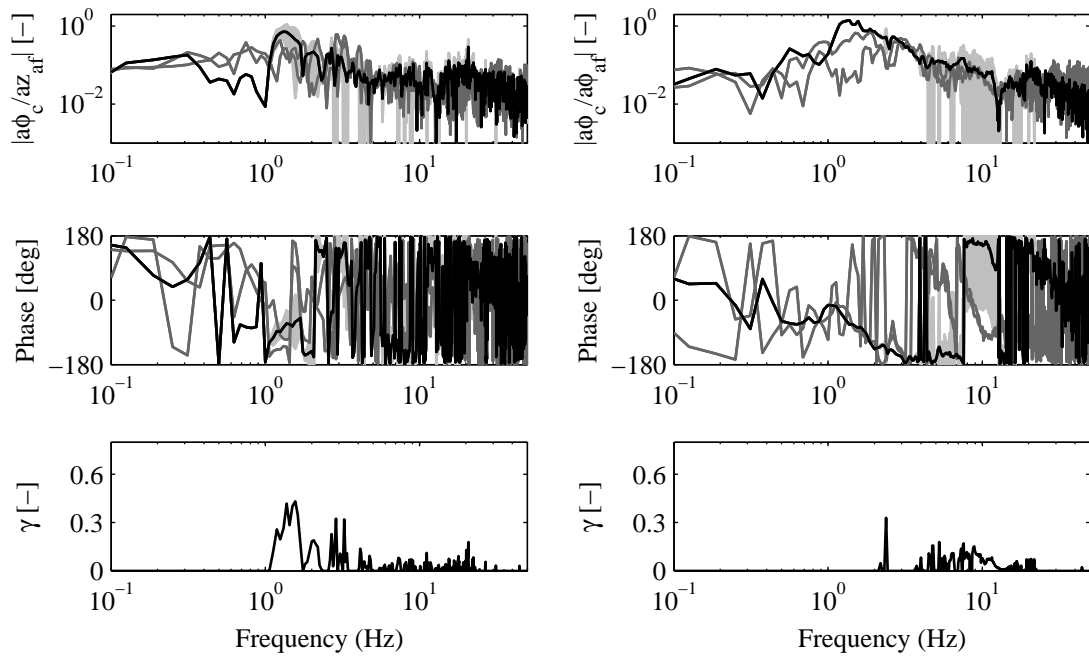


Figure 3.24: Tractor semi-trailer model at 80 km/h, transfer front axle vertical (left) and roll (right) acceleration to cabin roll acceleration: nominal model (black); mean transfer function estimates (dark grey); and model uncertainty (light grey).

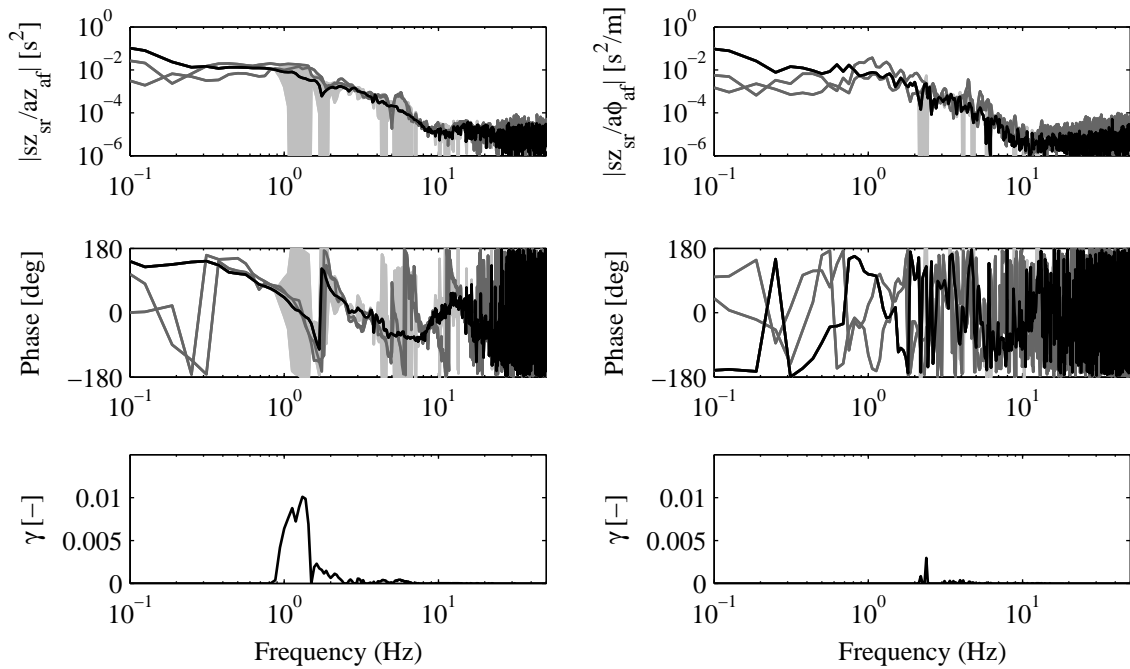


Figure 3.25: Tractor semi-trailer model at 80 km/h, transfer front axle vertical (left) and roll (right) acceleration to rear secondary suspension displacement: nominal model (black); mean transfer function estimates (dark grey); and model uncertainty (light grey).

3.5 Conclusion

In this chapter a 4 degrees of freedom (DOF) quarter truck heave model, a 4 DOF roll model, and a 9 DOF half truck pitch-heave model are presented for the purpose of active cabin suspension design. To validate their accuracy in the comfort relevant frequency range, as well as that of the 44 DOF tractor semi-trailer model presented in the previous chapter, a new model validation technique is proposed. The technique is suited for asynchronous repeated measurements with noise contributions on both inputs and outputs and separates noise- and model uncertainty.

The validation procedure basically consists of a comparison of the modeled and measured transfer functions from the front vertical/roll axle acceleration to the various outputs. As a result, the transfer function from the (unknown) road input to each of the axle accelerations is not validated. Moreover, it is important to note that there is a difference between, for example, the transfer function from the road input to the vertical cabin acceleration and that from the vertical front axle acceleration to the vertical cabin acceleration. The first will have a larger magnitude around the front axle resonance frequency (around 10 – 11 Hz), as can be seen when comparing Figures 3.3 and 3.12.

An overview of the validation results is given in Table 3.1. Herein, for each of the models, the maximum of the minimum model uncertainty not invalidating the model over the chosen frequency grid is given for each of the transfers. The inputs are the front axle vertical and roll acceleration and the outputs are given in the first column. As the 9 and 44 DOF models are velocity dependent, the models are validated once at 60 and once at 80 km/h. Furthermore, as these two models are not valid for the case without semi-trailer, only the measurements with semi-trailer are used for the validation. For the 4 DOF heave and roll models on the other hand, all the comfort measurements given in Table 2.3 with 6 trials are used.

Overall, the 44 DOF model provides the highest level of accuracy and is expected to be suitable for comfort evaluation. However, the high level of complexity might be problematic for controller design studies. For that purpose, the reduced order models have been developed. Although they cover only a part of the vehicle, the 4 DOF heave and 9 DOF pitch-heave model also have a relatively high level of accuracy in the comfort relevant frequency ranges. The 4 DOF roll model on the other hand, is significantly less accurate around the vehicle resonance frequency at 1.7 Hz. Still, as the 44 DOF model does cover this frequency with a high level of accuracy and the 4 DOF roll model is relatively accurate for the other frequencies, it may be possible to use the roll model for controller design as long as the 44 DOF model is used for the controller evaluation.

There are three remaining points that need to be addressed. First of all, it can be argued that 6 trials is too low to get a reliable noise variance estimate, see Oomen and Bosgra (2009). As a result, the determined model uncertainty may still be conservative. Secondly, the proposed validation approach hinges on several restrictive assumptions

Table 3.1: Validation results. Maximum model uncertainty at 80(60) km/h.

	\ddot{z}_{af}			$\ddot{\phi}_{af}$	
	heave	9 DOF	44 DOF	roll	44 DOF
\ddot{x}_f	0.63	0.85 (0.85)	0.23 (0.30)	2.46	0.09 (0.07)
\ddot{y}_f			0.23 (0.30)		0.37 (0.08)
\ddot{z}_f			0.50 (0.79)		2.30 (0.21)
$\ddot{\theta}_f$			0.47 (0.39)		0.69 (0.09)
$\ddot{\phi}_f$			1.82 (0.87)		0.81 (0.71)
\ddot{x}_c	0.93	0.73 (0.52)	0.47 (0.21)	3.93	0.32 (0.04)
\ddot{y}_c			0.97 (0.80)		0.51 (0.16)
\ddot{z}_c			0.45 (0.52)		1.64 (0.16)
$\ddot{\theta}_c$			0.36 (0.21)		0.42 (0.06)
$\ddot{\phi}_c$			0.43 (0.56)		0.33 (0.17)
z_{pf}	0.01	8.10^{-3} (7.10^{-3})	6.10^{-3} (5.10^{-3})		6.10^{-3} (1.10^{-3})
z_{pr}		0.06 (0.05)	0.02 (0.01)		8.10^{-3} (1.10^{-3})
z_{sf}	0.01	7.10^{-3} (9.10^{-3})	4.10^{-3} (6.10^{-3})		9.10^{-3} (1.10^{-3})
z_{sr}		0.02 (0.01)	0.01 (6.10^{-3})		3.10^{-3} (1.10^{-3})
ϕ_{pf}			4.10^{-3} (5.10^{-3})	0.02	2.10^{-4} (5.10^{-4})
ϕ_{pr}			5.10^{-3} (6.10^{-3})	0.01	1.10^{-3} (3.10^{-4})
ϕ_{sf}			1.10^{-3} (1.10^{-3})		2.10^{-4} (1.10^{-4})
ϕ_{sr}			3.10^{-3} (3.10^{-3})		8.10^{-4} (1.10^{-3})

which may not always hold, and is limited to single input - single output systems. Thirdly, the bias estimation method is relatively crude. As such, there is plenty of opportunity to further develop and enhance this approach. Nevertheless, the validation approach as presented has already proven to be very useful.

The validated reduced order models in combination with the validated 44 DOF tractor semi-trailer model are a part of the set of tools needed in the following chapters.

Chapter 4

The search for a low-power active suspension concept

4.1 Introduction

In the previous chapters various validated vehicle models are presented, which can be used for suspension design and comfort evaluation. Parameter optimization, Besselink and van Asperen (1994), and innovative designs, see for example Cao et al. (2008), have brought us to the boundaries of the achievable passive suspension performance. Still, better cabin comfort and attitude behavior is desired. Furthermore, while air suspensions can be used for load leveling, they are too slow to actively improve driver comfort, Ballo (2001). Therefore, it is interesting to study the semi-active and active alternatives.

Active suspensions have the ability to add energy to the suspension system, where semi-active systems only control the rate of energy dissipation. For the attitude behavior, i.e., the cabin dynamics when accelerating, braking or cornering; varying the rate of energy dissipation may not be sufficient, as the cabin will still roll and pitch significantly under these conditions. Therefore, the focus in this thesis lies on the active suspensions, which are expected to give the best performance. However, it comes at the cost of a high energy demand, Fischer and Isermann (2004). And this is a problem.

Even though enhancing driver comfort and cabin attitude behavior is very important, the overall cost is not allowed to increase (much). Commercial vehicles have to be as efficient as possible, with the highest possible durability, at the lowest possible cost. So, a relatively low power consumption is a necessary condition for the feasibility of any active cabin suspension design.

The need for a low power active cabin suspension is also addressed in Nakano et al. (1999) and Nakano and Suda (2004). Herein, a “screw-like” actuator concept is proposed, which can be placed in both the primary and secondary suspension. In the primary suspension it functions as energy regenerative damper, and the regenerated energy is used to actively control the secondary suspension. This controller is chosen such that the overall suspension is energy neutral, to minimize the operational cost.

Naturally, this idea of an energy neutral active suspension is very attractive.

The design of controllable secondary suspensions is, according to Cole (2001), a topic that needs more study. The small amount of research papers on this topic serves as a good illustration. There are fundamental questions - like: *What is a good suspension configuration? What type of actuator gives the best performance? And how should the suspension be optimally controlled?* - that all still need to be addressed.

In this chapter, a conceptual analysis is given of various active suspension configurations and actuator types. The aim is to select one concept for the development of an active cabin suspension for commercial vehicles. It is shown, that under idealized conditions, the variable geometry active suspension concept and parallel active configuration give the best performance at the lowest energy cost. Furthermore, energy regenerative actuators have the preference over non-regenerative systems. Configurations where the actuator carries the load are typically undesirable. Moreover, it is shown that the results for the variable geometry active suspension and parallel active suspension concepts strongly depend on the chosen controller and suspension parametrization. If the reference force variations are kept small enough, the variable geometry actuator is expected to be very energy efficient. Therefore this concept is selected for further study.

This chapter is structured as follows. First a survey is given of active suspension concepts in Section 2, followed by an analysis of one particularly interesting suspension device: the variable geometry actuator. The performance of this actuator, placed in the 4 DOF quarter truck heave model (Chapter 3), is compared to several reference systems in Section 4.

4.2 Active vehicle suspensions

Active vehicle suspensions can be classified in different ways. One way is by looking at the place of the actuators with respect to the passive (spring and damper) elements: parallel; in series; or embedded - as is the case with the variable geometry actuator, Venhovens and van der Knaap (1995). Another way is by focussing on the type of actuator that is used: hydraulic or electrical.

4.2.1 Hydraulic active suspension systems

The first commercially available car with a (low bandwidth) active suspension was the *Citroën Traction Avant* (1954). It has the *Hydropneumatic* suspension system, which was invented and developed by *Citroën*, applied to the rear axle. Its successor, the *Citroën DS* (1955) was the first commercially available car with both front and rear active suspensions.

The *hydropneumatic* suspension consists of several nitrogen filled spheres (which act as springs), of which the pressure is controlled using an hydraulic system. In most designs, the hydraulic system is also used for other functions like braking, power

steering, etc. Despite the high system complexity, which presents some maintenance issues, it has been adopted by *Rolls-Royce*, *Mercedes-Benz*, *Peugeot* and *Berliet trucks*.

The *hydropneumatic* suspension further evolved to the *Hydractive* and *Active*. These have additional functionality, in the form of adaptive control of ride height and spring stiffness. The suspension adapts, depending on the loads, driving velocity, steer velocity and modus (sport or normal). However, the *Hydractive* and *Active* are more designed for handling than comfort, Carbibles (2007).

Many of the vehicle suspension control algorithms in literature assume some kind of force actuator capable of tracking a reference. As is mentioned in Chantranuwathana and Peng (1999), “actuators that can push/pull the vehicle sprung mass at frequencies up to several Hz are extremely bulky and expensive. At this level of force actuation, hydraulic actuators remain to be one of the most viable choices due to their high power to weight ratio. However, they are highly nonlinear and their force generation capability is closely coupled with the vehicle body motion.”

The *Lotus* formula 1 team pioneered with the development of high bandwidth electro-hydraulic active suspension systems in the early 1980s, Wright and Williams (1984). They developed a modal control algorithm which softens the vehicle in heave, but gives a rigid response in pitch and roll. It proved enormously successful and triggered a wide interest in active suspension design, Williams and Haddad (1995). However in the end, company conclusions were mostly negative, as a result of the high power consumption and overall cost of the systems, Sharp (1998).

Another example of an active hydraulic suspension (in an automotive context) is the *DaimlerChrysler Active Body Control system*, Heißing and Ersoy (2007). At each corner of the vehicle, it consists of an hydraulic actuator placed in series with a coil spring and a passive shock absorber. Using this configuration, the influence of high frequent environmental vibrations on the actuator is limited, and vehicle motions up to approximately 5 Hz can be controlled.

Iveco studied the possibilities of an active hydraulic cabin suspension in the early 1990’s, Wiesmeijer and Uffelmann (1991); Uffelmann and Wiesmeijer (1992). Suspension specifications have been determined from experimental measurement data obtained using a vehicle with a passive suspension. It is mentioned that the oscillatory power beyond 12 is relatively small, which allows a restriction on the required bandwidth of the active suspension. Furthermore, a cascade controller has been developed and implemented on an experimental test vehicle. It is claimed that a significant comfort increase can be obtained, although the performance above 5 Hz is “not yet satisfactory”. The power consumption, on the other hand, is considerable, with a maximum of approximately 16 kW.

4.2.2 Electrical active suspension systems

Recently, the *Bose Corporation* presented a project they have been working on for over 24 years, Jones (2005). It is called the *Bose suspension* and consists of four linear

electro-magnetic actuators. These actuators are packaged such that they can replace the passive suspension of any passenger car. *Bose* claims to have mathematically validated that the use of electro-magnetic actuators will give better performance than any hydraulic or variable spring/damper system, Bose (2007).

The *Bose suspension* is not the first linear electro-magnetic suspension. A company called *Aura systems* developed a similar linear electro-magnetic suspension system around 1991. It looked similar to the *Bose* actuators and had the same limitation that it could not carry the dead weight of the vehicle, Carbibles (2007).

There are very few electro-magnetic actuators available that can be used in an active suspension setting. The high loads and high level of vibrations impose some high demands. In Encică (2008) a new design methodology is proposed, which can be used to develop electro-magnetic actuators, given a set of constraints. It is successfully demonstrated with the design and experimental validation of an active suspension, which has the passive characteristics of a spring and is capable of actively mitigating vibrations. Especially the fact that it *can* passively carry the dead weight of the vehicle makes this design very interesting. However, packaging of the device is still an issue.

An alternative brushless tubular permanent magnet actuator design, called the *Eindhoven Active Suspension System*, is presented in Gysen et al. (2009). It works in parallel with a mechanical spring. Using optimization, a topology is derived which meets the packaging specifications for implementation in a BMW 530. The achievable bandwidth is in excess of 50 Hz and it can work both in generator and actuator mode. For the final design it is shown, by means of simulations and quarter-car experiments, that the passive vehicle roll can be significantly reduced. However, another cooling solution needs to be adopted to prevent thermal overloading when tracking reference forces with a high root-mean-square (rms) value (≥ 1000 N).

The *Delft Active Suspension*, Venhovens and van der Knaap (1995); Van der Knaap (1989); Van der Knaap and Pacejka (1993); Venhovens et al. (1992), is an alternative electromechanical suspension. It was designed, built and tested in the period 1989 – 1995, and has in theory a very low power consumption. This is a result of the special geometric choices that were made for the actuator design. By varying lengths of a wishbone construction, which are realized perpendicular to the main suspension force, a wide range of actuator forces can be obtained - under idealized conditions - without consuming any energy. Furthermore, the *Delft Active Suspension* is also capable of carrying the static weight of the vehicle.

However, practical implementation, Van der Knaap et al. (1994), showed that the power consumption is still significant, with an average of around 500 W and peaks up to 2.5 kW under worst-case conditions. Friction and electric losses are assumed to be the main causes. Furthermore, the reduction of the root-mean-square (rms) accelerations (about 10%) is relatively low, and mainly concentrated around the dominant sprung mass oscillation mode. The subjective ratings of the ride comfort improvement, on the other hand, are much higher. In Hrovat (1997), it is stated that despite these shortcomings of the practical realization: “the concept is expected to have significant practical

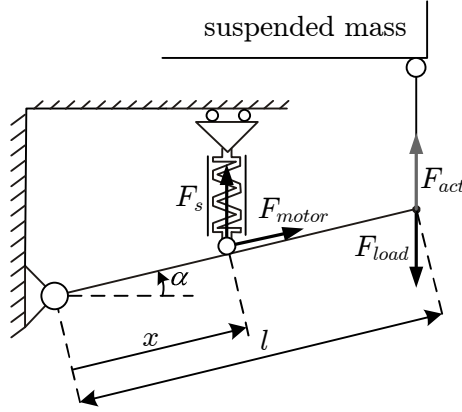


Figure 4.1: Kinematics of the variable geometry force actuator concept.

ride improvement potential, which may be materialized through further developments and design changes.”

In Sharp (1998); Watanabe and Sharp (1999), the actuator concept of the *Delft Active Suspension* is called *Variable Geometry Actuator*. It is written that: “knowledge of *Variable Geometry Actuator* systems is currently far from complete... All matters of detailed design are open, so that much research and development effort is needed to get the most out of the design.” With this in mind, the concept is studied in more detail in the next section.

4.3 Variable geometry actuator

In this section the power requirements of the variable geometry actuator concept in its simplest form - placed within a suspension setting - are analyzed. Before doing so, the steady-state characteristics are evaluated first.

4.3.1 Concept analysis

The concept of the variable geometry actuator is illustrated in Figure 4.1. Consider a wishbone with inertia J_w and length l , which can be rotated over an angle α . Furthermore, attached to this wishbone at a variable distance x from the revolute joint is a spring with mass m_s , pre-tension F_s^0 and stiffness c_a . The spring position can be manipulated with the motor force F_{motor} . At the end of the wishbone, there is a connection to the suspended mass. The weight of this mass gives rise to a force F_{load} , which acts on the wishbone. The equations of motion for this system are given by

$$\begin{aligned} J_w \ddot{\alpha} &= (F_s x - F_{load} l) \cos \alpha \\ m_s \ddot{x} &= F_{motor} + F_s \sin \alpha, \end{aligned} \quad (4.1)$$

where the spring force F_s is given by

$$F_s = F_s^0 - c_a x \sin \alpha. \quad (4.2)$$

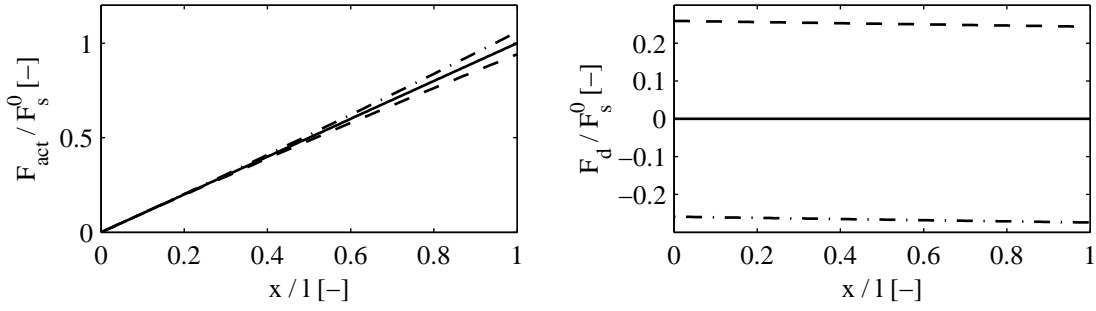


Figure 4.2: Dimensionless actuator force (left) and disturbance force (right) of the 2D concept, for $\alpha = 0$ degrees (solid), $\alpha = -15$ degrees (dash-dotted) and $\alpha = 15$ degrees (dashed).

Table 4.1: Parameters variable geometry active suspension concept

parameter	value	unit
c_a	10000	N/m
F_s^0	6573	N
l	0.15	m

The force at the end of the wishbone is called the actuator force F_{act} . It can be changed by varying x . Under equilibrium conditions ($\ddot{\alpha} = 0$, $\ddot{x} = 0$) the actuator force is given by

$$F_{act} = \frac{x}{l} F_s. \quad (4.3)$$

When the angle α is zero, any variation in x does not change the length of the spring and can thus be executed with relatively low power consumption. Only the inertia and friction effects have to be overcome by the (electric) motor. However, under normal working conditions α will vary. For any nonzero α an additional control force is required to maintain a certain position x . This is a result of the spring force component that works parallel to the wishbone. This force component, the disturbance force (F_d), is given by

$$F_d = F_s \sin \alpha, \quad (4.4)$$

which, under steady-state conditions, is perfectly compensated by the control force: $F_{motor} = -F_d$. The normalized actuator force and normalized disturbance force are shown in Figure 4.2 for various angles of the wishbone (α), using the parameters as given in Table 4.1.

The nonlinear relationship between x , α and the disturbance- and actuator force is clearly visible. For larger x the actuator force variation as a function of α increases quadratically. This effect can be seen as the stiffness of the actuator. More precisely, the effective stiffness of the actuator c_{eff} is defined as the actuator force variation

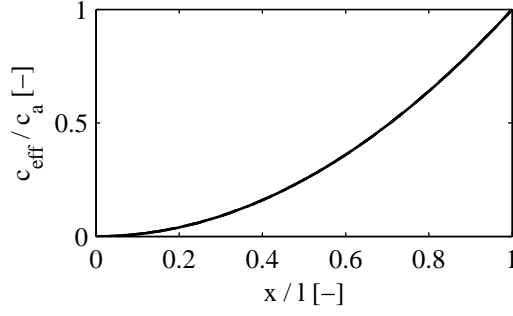


Figure 4.3: Dimensionless effective actuator stiffness at the end of the wishbone of the 2D concept.

resulting from a small vertical displacement at the end of the wishbone. It is given by

$$\begin{aligned}
 c_{eff} &= -\frac{\partial \alpha}{\partial (l \sin \alpha)} \frac{\partial F_{act}}{\partial \alpha} \\
 &= -\frac{1}{l \cos \alpha} \frac{\partial F_{act}}{\partial \alpha} \\
 &= \frac{1}{l \cos \alpha} \frac{\partial \left(\frac{x}{l} (c_a x \sin \alpha) \right)}{\partial \alpha} \\
 &= c_a \frac{x^2}{l^2}.
 \end{aligned} \tag{4.5}$$

For this simple concept the effective stiffness, see Figure 4.3, does not vary as a function of α . However, the nonlinearity of the effective stiffness with respect to x may be problematic for some applications.

4.3.2 Variable geometry active suspension

A schematic representation of the variable geometry active suspension concept, placed within the 4-DOF quarter truck heave model of the previous chapter, is given in Figure 4.4. As the body with mass m_c represents half the cabin, two variable geometry actuators are included in this model.

For the passive suspension, the cabin suspension stiffness equals c_c . For the variable geometry active suspension on the other hand, the passive stiffness equals c_c^* , which is chosen such that the active- and passive suspension system have the same stiffness under equilibrium conditions ($\ddot{z}_r = \ddot{z}_f = \ddot{z}_e = \ddot{z}_c = 0$).

Again consider the equations of motion for the passive system, as is given in (3.2), where $\underline{x}_z = [z_a, z_e, z_f, z_c]^T$.

Assumption 4.3.1. *The inertia of the wishbone J_w , the mass of the spring m_s and the influence of all friction effects are negligible.*

Under Assumption 4.3.1, the only difference between the passive and the active

with F_{act}^{ref} the reference actuator force. It should be noted that using (4.8), there will be a difference between the reference (F_{act}^{ref}) and realized actuator force F_{act} :

$$F_{act} = F_{act}^{ref} \left(1 - \frac{F_{act}^{ref}}{(F_s^0)^2} c_a l \sin \alpha \right). \quad (4.9)$$

This is a consequence of the fact that the effective stiffness of the actuator is not compensated. When the actuator stiffness is sufficiently small or optimized (see Chapter 5), this will not be problematic.

Assumption 4.3.3. *All angles (α) are small. Consequently, the following approximations may be used*

$$\begin{aligned} \cos \alpha &= 1 \\ \sin \alpha &= \alpha \\ \sin^2 \alpha &= 0. \end{aligned} \quad (4.10)$$

Combining (4.7) and (4.8) under Assumptions 4.3.2 and 4.3.3, gives

$$P_{act} = -2\dot{F}_{act}^{ref}(z_c - z_f). \quad (4.11)$$

This result is quite remarkable as it differs fundamentally from the (idealized) power requirements of a “conventional” active suspension

$$P_{conv} = 2F_{act}^{ref}(\dot{z}_c - \dot{z}_f). \quad (4.12)$$

For the latter, slow control actions which require a high actuator force - like carrying the static weight of the vehicle - may consume a significant amount of energy. The variable geometry actuator on the other hand, requires relatively little energy when the variations of the reference force are slow. Consequently, from an energy perspective, it is highly desirable to minimize the rate of change of the reference force as fast changes may result in power spikes.

4.4 Active suspension comparison

In this section, the performance and energy requirements of the 4-DOF heave model with variable geometry active suspension are compared to those of several reference systems. For the comparison, which is based on simulation results only, it is assumed that the mechanical energy output of the various actuators provides a good representation of the differences in power consumption of the actual systems. Of course, this is disputable for the hydraulic actuator, as the pump may also consume energy when no force is generated. Still, with this in mind, much can be learned from this simplified representation.

First the reference systems are given, followed by the performance and evaluation criteria and the used control approach.

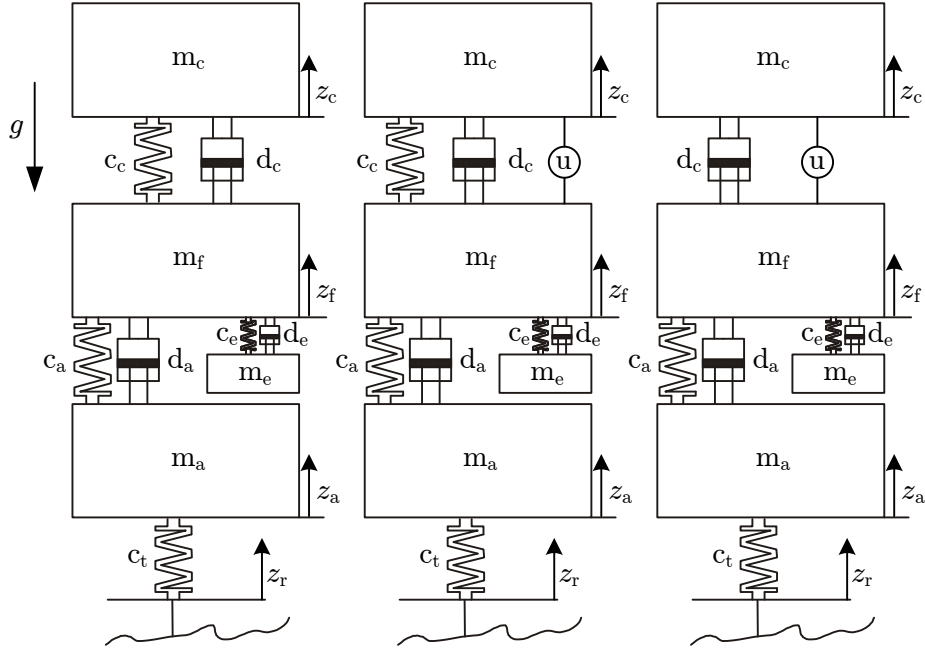


Figure 4.5: Reference suspension systems: *passive* (left); *parallel active* (mid); and *loaded active* (right).

4.4.1 Reference systems

There are three reference systems, see Figure 4.5, each consisting of a 4-DOF heave model. The difference between the three lies in the placing of, and the load carried by, the actuator.

The first reference system is the passive suspension system, see Figure 4.5 (left), which does not have any active devices. This is the system as is discussed and validated in Chapter 3.

The second reference system is the so-called *parallel active* configuration. Herein, an idealized actuator (no bandwidth limitations) is placed in parallel to the existing suspension, see Figure 4.5 (mid). An important property of this setup, is the fact that the passive spring still carries the nominal weight of the suspended mass. So, in the absence of perturbations, the actuator force (u) equals zero.

The parallel active suspension is evaluated with two different actuator types: a hydraulic and an electro-mechanical version. The latter is assumed to be a conservative system, i.e., it can regenerate energy with a 100% efficiency, where the first is not. Consequently, the energy required by the electric actuator is given by

$$P_{mech}^{electric} = u(\dot{z}_c - \dot{z}_f), \quad (4.13)$$

and that required by the hydraulic actuator by

$$\begin{aligned} P_{mech}^{hydraulic} &= u(\dot{z}_c - \dot{z}_f), \text{ if } u(\dot{z}_c - \dot{z}_f) > 0 \\ &= 0, \text{ if } u(\dot{z}_c - \dot{z}_f) \leq 0. \end{aligned} \quad (4.14)$$

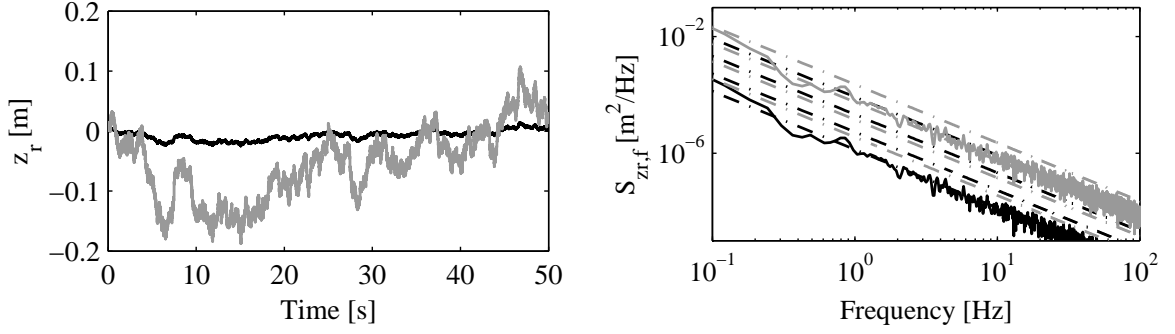


Figure 4.6: Stochastic road input, used for the evaluation of the different suspension settings. Left: absolute road height z_r as a function of time. Right: Power Spectral Density of the absolute road height z_r solid and (A,B,C,D) road roughness levels (dash-dotted). A-class road at 30 km/h (black), and C-class road at 80 km/h (grey).

The last reference system is the *loaded active* configuration, see Figure 4.5 (right). Herein, an idealized actuator is placed in parallel with the passive damper, but there is no passive spring to carry the load of the suspended mass. This configuration is typical for hydraulic suspensions, as the actuator and spring are typically placed in series to avoid high frequent discomfort. In this case, the power requirements are again given by (4.13) and (4.14). However, the actuator force includes an additional $m_c g$, which will result in larger maximum power values.

The systems are evaluated using two different ISO random road inputs, ISO 8608 (1995). The first mimics the road vibrations from an A-class (very good) ISO road, when driving at 30 km/h. The second is a model of the vibrations coming from a C-class (average) ISO road, when driving at 80 km/h. Exactly the same road input, see Figure 4.6 (left), is used for all simulations.

The power spectral density of both inputs is represented by the solid lines in Figure 4.6 (right). Furthermore, the dotted lines represent the different road classification levels, ranging from A to D. These classification levels have been computed by taking the displacement power spectral density

$$S_{zr}(n) = S_{zr}(n_0) \left(\frac{n}{n_0} \right)^{-2}, \quad (4.15)$$

with $n_0 = 0.1 \text{ m}^{-1}$ and $S_{zr}(n_0)$ a constant depending on the road roughness. In ISO 8608 (1995) it is given that the geometric mean of $S_{zr}(n_0)$ equals $[16, 64, 256, 1024] \cdot 10^{-6}$ for [A,B,C,D]-class roads. Assuming a constant velocity V , the power spectral density is then given by

$$S_{zr,f}(f) = \frac{1}{V} S_{zr} \left(\frac{f}{V} \right), \quad (4.16)$$

where f is the frequency in hertz, Besselink (2008).

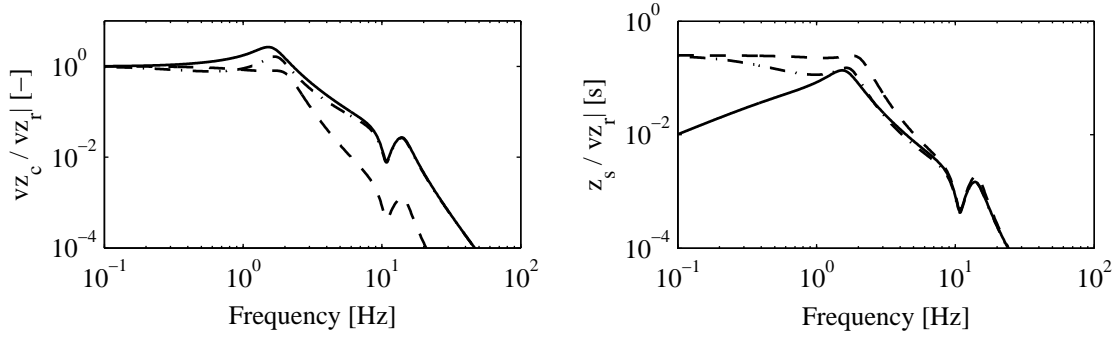


Figure 4.7: Bode magnitude relations 4-DOF heave model, from vertical road velocity to cabin velocity (left) and cabin suspension displacement (right). Passive suspension (solid); active suspension with nominal passive damping (dash-dotted); and active suspension with reduced passive damping (dashed).

4.4.2 Suspension performance and control

When driving in a vehicle, environmental vibrations may result in a feeling of discomfort. The level of discomfort is related to the root-mean-square (rms) value of the (ISO) frequency weighted suspended mass accelerations, ISO 2631-1 (1997). However, as a first indication, the rms and maximum value of the suspended mass accelerations can also be used. This last approach is adopted here for simplicity.

A suspension requires working space. The more working space, the higher the maximum suspension travel, and the more it can potentially reduce hazardous vibrations. However, in practical applications, the available suspension travel is always limited. For that reason, the required suspension travel should also be evaluated when evaluating the performance of a suspension system.

The last performance criterium that will be considered in this chapter is the power consumption of the suspension. To get an impression of the power demands, the mechanical power output of the suspensions is compared. Although, there will be additional energy losses in a real setup; the mechanical power is expected to give a good first indication. If there are large power spikes under the given simplified conditions, it will be even worse in practice.

The most commonly used control approach, for an active suspension, is called *skyhook damping*, Karnopp (1983). Herein, a fictive damper is placed between the sky and the suspended mass

$$u = -d_{sky}\dot{z}_c. \quad (4.17)$$

It has been shown that this control performs well for a single suspended mass, and also greatly enhances suspension performance on a 2-DOF quarter car setup, Hrovat (1997). Consequently, it seems logical to adopt a skyhook controller for this concept study.

The Bode magnitude plots of the 4-DOF heave model with active suspension, from the vertical road velocity to the cabin velocity and suspension displacement, are given

in Figure 4.7. Herein, a skyhook damping of $d_{sky} = 10000$ Ns/m is used. It can be seen that the largest reduction of the environmental vibrations can be realized by lowering the passive damping, which especially has a large influence above 1 Hz. However, as a result the required working space also increases significantly. The effect of the added skyhook damping, on the other hand, mainly influences the low frequent suspension characteristics, as well as the 2 Hz resonance.

For the parallel active suspension, see Figure 4.5 (mid), the control strategy as is given in (4.17) is used. However, for the loaded configuration it needs to be slightly modified to compensate for the load of the suspended mass

$$u_{loaded} = -d_{sky}\dot{z}_c + m_c g. \quad (4.18)$$

It is assumed that the mass m_c is known and that the actuator has an internal stiffness c_c , so that all three reference systems have the same stiffness under equilibrium conditions.

Finally, for the variable geometry active suspension, the controller takes the form

$$F_{act} = -\frac{1}{2}d_{sky}\dot{z}_c + \frac{1}{2}m_c g, \quad (4.19)$$

as there are two actuators.

4.4.3 Evaluation

The three reference systems have the same suspension parameters, see Table A.7 in the appendix, and use the controllers as specified in the previous subsection. Furthermore, the variable geometry active suspension (VGAS) is a modification, as depicted in 4.4, with controller (4.19). The actuator parameters are given in Table 4.1, with $c_c^* = c_c - 0.3c_a$.

The normalized accelerations and suspension travel - with respect to the nominal values of the passive system - using the road inputs as depicted in Figure 4.6, are given in Table 4.2. The normalized values are the same for both road inputs, as the only difference between the two consists of a scaling factor, see Figure 4.6.

Under these idealized conditions, the same level of performance can be obtained with all three active suspension systems, when it comes to accelerations and suspension travel. Using the nominal skyhook controller, the peak accelerations are lowered by 32% at a cost of 91% more workingspace. Alternatively, a reduction of the passive damping may be more preferable. With three times the workingspace, the peak accelerations are reduced by 69%.

The power requirements on the other hand show some major differences, see Table 4.3. Overall, the loaded suspension configuration has a strikingly large peak power requirement, making it undesirable. Furthermore, the mean power consumption is higher using an hydraulic actuator than an electro-mechanical actuator, as the latter can regenerate energy. However, for the variable geometry active suspension and parallel configuration, the differences between electro-mechanical and hydraulic actuator are relatively small under these idealized conditions.

Table 4.2: Simulated normalized accelerations and suspension travel.

System	rms \ddot{z}_c	max \ddot{z}_c	rms $z_c - z_f$	max $z_c - z_f$
Passive suspension	1	1	1	1
Nominal damping				
VGAS	0.68	0.64	1.55	1.91
Parallel/Loaded	0.67	0.65	1.54	1.90
Reduced damping				
VGAS	0.35	0.31	2.64	3.03
Parallel/Loaded	0.36	0.32	2.63	2.99
Norm. values	0.20 m/s ²	0.65 m/s ²	0.96 mm	2.88 mm

Table 4.3: Simulated mean(max) mechanical energy requirements in Watt on A-class and C-class road. Variable geometry active suspension (VGAS), parallel and loaded configuration, with electro-mechanical or hydraulic actuator, and nominal passive damping or reduced passive damping.

	VGAS	Parallel	Loaded
A-class road			
Electric	1 (18)	1 (10)	1 (231)
Hydraulic	1 (18)	1 (10)	30 (231)
Elec. red.	-1 (5)	-1 (8)	-1 (401)
Hydr. red.	0 (5)	1 (8)	58 (401)
C-class road			
Electric	44 (1055)	44 (584)	45 (1978)
Hydraulic	62 (1055)	51 (584)	244 (1978)
Elec. red.	-45 (299)	-47 (447)	-45 (2783)
Hydr. red.	13 (299)	18 (447)	422 (2783)

When comparing the variable geometry active suspension and parallel configuration, it can be seen that the differences dependent on the chosen passive suspension components. For the case with nominal passive damping, the peak power consumption of the parallel configuration is the lowest. However, when the amount of passive damping decreases, the actuator has to compensate less for the high frequent vibrations that are transmitted by the damper. As a consequence, the reference force variations become smaller and the peak power consumption drops significantly.

As can also be seen in Figure 4.8, the dynamics that lead to power spikes differs fundamentally between the two concepts. The peak mechanical power consumption

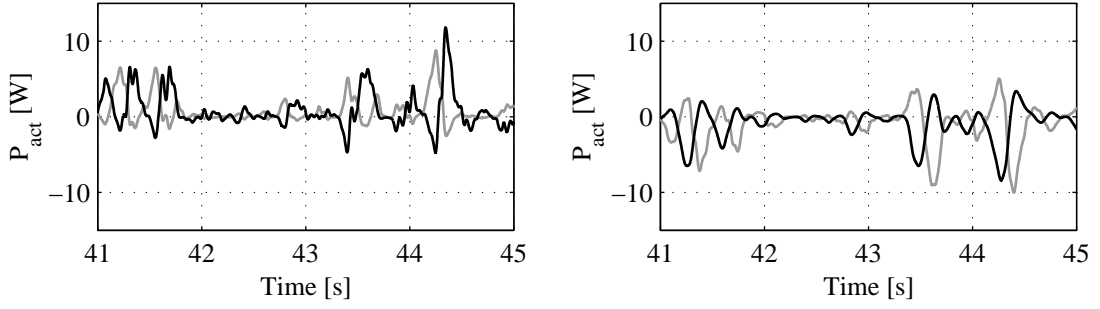


Figure 4.8: Mechanical power required by the electric actuator on A-class road at 30 km/h, with nominal passive damping (left) and reduced passive damping (right), using: parallel configuration (grey); and variable geometry active suspension (black).

depends mainly on the chosen control strategy and suspension parameters. In this case, the power requirements of the variable geometry active suspension (P_{act}^{VGAS}), parallel (P_{act}^{par}), and loaded configuration (P_{act}^{load}), are given by

$$P_{act}^{VGAS} = d_{sky}\ddot{z}_c(z_c - z_f), \quad (4.20)$$

$$P_{act}^{par} = -d_{sky}\dot{z}_c(\dot{z}_c - \dot{z}_f), \quad (4.21)$$

$$P_{act}^{load} = P_{act}^{par} + m_cg(\dot{z}_c - \dot{z}_f). \quad (4.22)$$

Overall it can be concluded that the performance of the three systems is identical. However, the power consumption of the variable geometry active suspension and parallel active suspension are significantly lower than that of the loaded configuration.

4.5 Conclusion

In this chapter various active cabin suspension concepts are considered. Three have been selected for an evaluation under idealized conditions by means of a simulation study. It is shown, that there is no fundamental difference between the obtainable level of performance. However, the peak mechanical power requirements differ significantly. From that perspective, the so-called *loaded active* suspension is undesirable as it has large power spikes. On the other hand, the power requirements of the so-called *parallel active* and variable geometry actuator are considerably lower. They are of the same order of magnitude, but depend on the chosen control strategy and suspension parameters. Still, the variable geometry actuator may be favorable, as there are some practical considerations that need to be taken into account.

First of all, in a vehicle suspension the load of (or down force on) the suspended mass will vary. Therefore, the parallel configuration requires an actuator with a leveling device in parallel (or the power consumption will increase similar to the loaded configuration), while the variable geometry active suspension is capable of performing

the leveling itself. In principle, the power consumption of the leveling device should be added to that of the parallel configuration for a fair comparison.

Secondly, there are few electric motors capable of delivering forces of the magnitude that is required for this application. So the fact, that the variable geometry actuator can suffice with an electro-mechanical motor which is considerably smaller (and lighter) than that of the parallel active suspension, Sharp (1998), makes it very attractive.

On the other hand, when looking at the feasibility of the basic variable geometry actuator concept it should be noted that a translational motor and sliding contact are required. This may introduce problems of its own in “dirty” automotive environments. For that reason, a rotatory variable geometry (3D) actuator design is evaluated in the next chapter. Other (2D) alternatives can be found in Sampaio (2009) and Van der Sanden (2008).

Chapter 5

The electromechanical low-power active suspension

5.1 Introduction

In the previous chapter, the so-called variable geometry actuator (Venhovens and van der Knaap (1995); Watanabe and Sharp (1999)) is shown to be an attractive concept for the design of an active cabin suspension. Using a simple (2D) model representation it is illustrated, that the variable geometry actuator can (theoretically) obtain the same level of performance as other active suspension configurations. Moreover, it can achieve this with a relatively low power consumption. This is a result of the fact that it is electro-mechanical and that the power consumption is related to variations in actuator force (4.11) instead of the absolute value of the actuator force (4.13).

The variable geometry actuator was first presented as a 3D rotary concept called the *Delft Active Suspension*, Venhovens and van der Knaap (1995), see Figure 1.3. Herein, a rotary design was chosen to overcome the practical issues that arise when using a translational motor and translational joint in a dirty automotive environment. Furthermore, the *Delft Active Suspension* has been built in practice. For the experimental validation four actuators were used in a passenger car and the results were very promising.

A similar concept is evaluated in Watanabe and Sharp (1999). Using various controller concepts, it is shown by means of simulations that good performance can be obtained using relatively little energy. “The results reinforce the notion that variable geometry schemes have practical applications potential and are worthy of further research effort.”

The first results with the *Delft Active Suspension* were presented in 1995. However, at present there are still no vehicle manufacturers that have embraced the system. This fact can be contributed to a few negative aspects of the original concept. Firstly, the *Delft Active Suspension* has major packaging issues, due to the large area needed for the moving spring. Secondly, there is also the issue of the nonlinear actuator stiffness. This might be a source of discomfort to the driver, and even lead to instability in the

absence of a secondary spring. Finally, there is the safety issue. In most vehicles, the suspension is a safety critical component. So, it should never fail. This last topic will not be further addressed in this dissertation, but it remains an open question how to achieve this.

Recently, a new design of variable geometry actuator has been introduced, Van der Knaap et al. (2007); Van der Knaap (2006), which may solve the first two problems. It is called *electromechanical Low-Power Active Suspension (eLPAS)* and features a fixed spring and an optimized actuator stiffness characteristic. As a consequence of the fixed spring the packaging options are enhanced and the mass of the moving part is reduced. This last part results in a higher achievable bandwidth compared to previous designs, Venhovens and van der Knaap (1995). However, the characteristics of this design, and its practical feasibility are still unclear.

The aim of this chapter is to analyse and model the characteristics of the new design and evaluate its feasibility as an active suspension device for a commercial vehicle cabin. Hereto, a model of the actuator is derived that includes the electric motor and friction characteristics. Using this model a cascaded controller is developed and the steady-state and dynamic properties are evaluated. The simulation results are validated with real world prototype tests. The results show, that the model gives an accurate representation of the prototype and that a 10 Hz bandwidth can be easily obtained. However, the stiffness of the prototype does vary slightly over the actuator range as a result of manufacturing inaccuracies. Nevertheless, it is concluded that the *eLPAS* design is feasible and that the model gives an accurate representation of both the steady-state and dynamic prototype characteristics.

The chapter is structured as follows. First, a model of the *eLPAS* design is derived and the parameters are optimized to obtain a constant actuator stiffness. Using this, in combination with an electric motor- and friction model, a controller is designed. Finally, the actuator control strategy is implemented on a prototype and the experimental results are evaluated.

5.2 eLPAS design and parameter optimization

In this section the *eLPAS* design, as described in Van der Knaap et al. (2007), is modeled and the geometric parameters are optimized to obtain a constant actuator stiffness.

5.2.1 Geometric design

The *eLPAS* design is depicted in Figure 5.1. It consists of a wishbone with length l , which is connected to a frame using a joint F , that allows a rotation α around the \vec{e}_F^1 -axis. Furthermore, attached to the wishbone at a distance y_m from the joint is an electric motor M , which driven direction (γ) is perpendicular to an arm with length l_b . At the end of this arm, a rod with length l_r is connected through a ball joint S ,

which in turn is connected to another rod through a rotational joint H , which allows rotation around two axis. This second rod is connected to a plate which constraints a spring with stiffness c_a and pre-tension F_s^0 . The force within this spring gives rise to a force F_{act} at the end of the wishbone. This is the actuator force, which varies for different values of α and γ .

The actuator is specifically designed for power efficiency. When the wishbone is horizontal ($\alpha = 0$), the outer end of the rotating arm describes a circle, of which the tangential velocity lies perpendicular to the spring force. As such, a fictitious cone is created with height h_c and radius l_b , similar to that obtained by the *Delft Active Suspension*, Venhovens and van der Knaap (1995). Consequently, the rotating arm can be rotated over any angle γ without changing the spring elongation. So ideally, for $\alpha = 0$, in the absence of friction and inertia effects, any rotation γ (and thus any actuator force F_{act}) can be achieved without power usage. For any $\alpha \neq 0$ a disturbance moment (M_d), induced by the spring force, acts on the electric motor which needs to be compensated to maintain a certain angle γ .

So, with respect to the string design as presented in Van der Knaap (2006) and studied in Evers et al. (2008a,b), two major differences are visible. First of all, the string with length l_s is replaced by the two rods and rotational joint for durability reasons. Secondly, the orientation of the rotational axis of the electric motor (and gearbox) is changed to influence the actuator stiffness characteristics.

For the derivation of the equations of motion, consider the inertial coordinate frame at O ($\underline{\vec{e}}^o$) and the body-fixed coordinate frame at point F ($\underline{\vec{e}}^F$). Assume that both coordinate systems coincide to facilitate the derivation of the equations of motion. Furthermore, at point F there is a second body-fixed coordinate frame that follows any rotation α of the wishbone

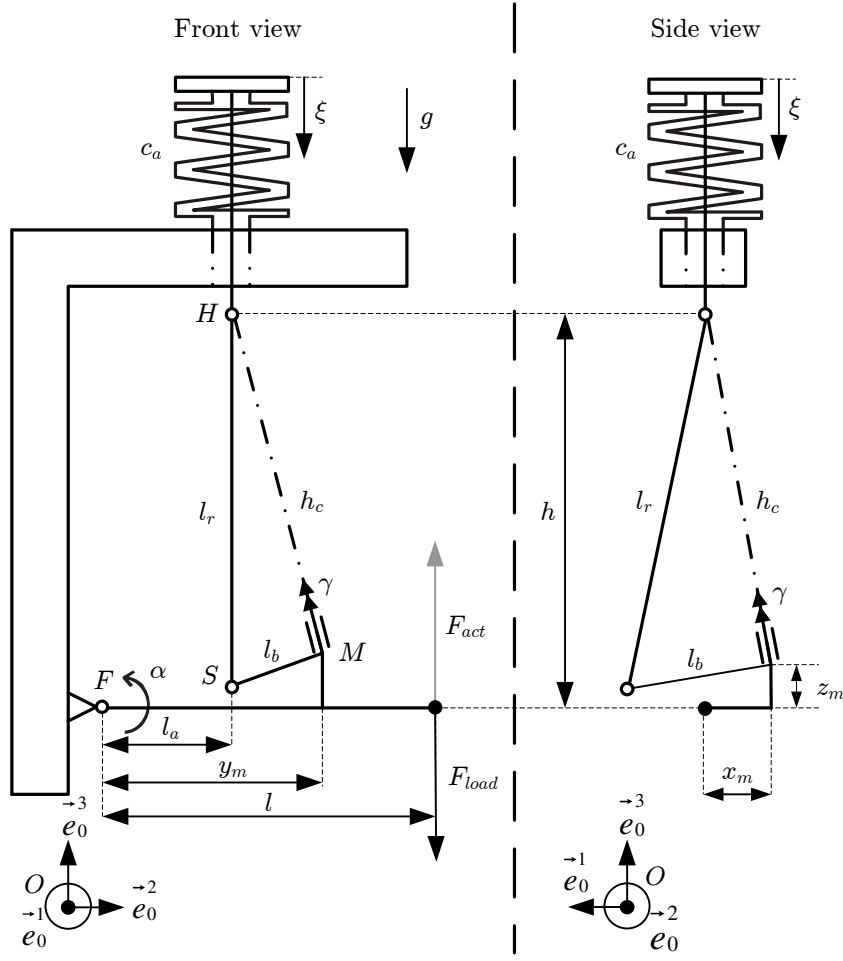
$$\begin{aligned} \underline{\vec{e}}^W &= \underline{A}^{WF} \underline{\vec{e}}^F \\ &= \begin{bmatrix} 1 & 0 & 0 \\ 0 & \cos \alpha & \sin \alpha \\ 0 & -\sin \alpha & \cos \alpha \end{bmatrix}. \end{aligned} \quad (5.1)$$

Consequently, the vector from F to M can be given by

$$\underline{\vec{r}}_m = \begin{bmatrix} -x_m \\ y_m \\ z_m \end{bmatrix}^T \quad \underline{\vec{e}}^W = \begin{bmatrix} -x_m \\ y_m \cos \alpha - z_m \sin \alpha \\ y_m \sin \alpha + z_m \cos \alpha \end{bmatrix}^T \underline{\vec{e}}^F. \quad (5.2)$$

At point M there is another body-fixed coordinate frame ($\underline{\vec{e}}^M$). It is oriented such that $\underline{\vec{e}}_1^M$ is always aligned with the rod with length l_b and that for $\alpha = 0$, $\underline{\vec{e}}_3^M$ goes through point H . The relation between $\underline{\vec{e}}^F$ and $\underline{\vec{e}}^M$ can be given as

$$\begin{aligned} \underline{\vec{e}}^M &= \underline{A}^{M2}(\bar{\gamma}) \underline{A}^{21}(\theta_0) \underline{A}^{1F}(\bar{\alpha}) \underline{\vec{e}}^F = \underline{A}^{MF} \underline{\vec{e}}^F \\ \underline{A}^{MF} &= \begin{bmatrix} C\bar{\gamma}C\theta_0 & S\bar{\gamma}C\bar{\alpha} + C\bar{\gamma}S\theta_0S\bar{\alpha} & S\bar{\gamma}S\bar{\alpha} - C\bar{\gamma}S\theta_0C\bar{\alpha} \\ -S\bar{\gamma}C\theta_0 & C\bar{\gamma}C\bar{\alpha} - S\bar{\gamma}S\theta_0S\bar{\alpha} & C\bar{\gamma}S\bar{\alpha} + S\bar{\gamma}S\theta_0C\bar{\alpha} \\ S\theta_0 & -C\theta_0S\bar{\alpha} & C\theta_0C\bar{\alpha} \end{bmatrix}, \end{aligned} \quad (5.3)$$

Figure 5.1: Kinematics of the *eLPAS* design, front- (left) and side-view (right).

where $C = \cos$, $S = \sin$,

$$\begin{aligned}\bar{\alpha} &= \alpha_0 + \alpha \\ \bar{\gamma} &= \gamma_0 + \gamma,\end{aligned}\tag{5.4}$$

and α_0 , θ_0 , γ_0 are constant design parameters. This rotation matrix is obtained by first rotating over an angle $\bar{\alpha}$ along the $\underline{\bar{e}}_1^{F1}$ -axis. The resulting coordinate frame is then rotated over an angle θ_0 along the $\underline{\bar{e}}_2^{F1}$ -axis. And finally, the resulting coordinate frame is rotated over an angle $\bar{\gamma}$ along the $\underline{\bar{e}}_3^{F2}$ -axis to obtain the $\underline{\bar{e}}^M$ reference frame.

Using this knowledge, the vector from F to S can be given by

$$\begin{aligned}\vec{r}_s &= \vec{r}_m + \begin{bmatrix} l_b \\ 0 \\ 0 \end{bmatrix}^T \underline{\bar{e}}^M \\ &= \begin{bmatrix} -x_m + l_b C \bar{\gamma} C \theta_0 \\ y_m C \alpha - z_m S \alpha + l_b S \bar{\gamma} C \bar{\alpha} + l_b C \bar{\gamma} S \theta_0 S \bar{\alpha} \\ y_m S \alpha + z_m C \alpha + l_b S \bar{\gamma} S \bar{\alpha} - l_b C \bar{\gamma} S \theta_0 C \bar{\alpha} \end{bmatrix}^T \underline{\bar{e}}^F\end{aligned}\tag{5.5}$$

Define $h(\alpha = 0) = h_0$, then the spring compression ξ can be given by

$$\begin{aligned}\xi &= h_0 - h \\ &= h_0 - \left(\vec{r}_s \cdot \vec{e}_3^F + \sqrt{l_r^2 - (\vec{r}_s \cdot \vec{e}_1^F)^2 - (\vec{r}_s \cdot \vec{e}_2^F - l_a)^2} \right) \\ &= a_3^r - a_1^r,\end{aligned}\tag{5.6}$$

where

$$\begin{aligned}a_1^r &= \{l_r^2 - (l_b C \bar{\gamma} C \theta_0 - x_m)^2 \\ &\quad - (y_m C \alpha - l_a + l_b S \bar{\gamma} C \bar{\alpha} + l_b C \bar{\gamma} S \theta_0 S \bar{\alpha} - z_m S \alpha)^2\}^{\frac{1}{2}} \\ a_3^r &= h_0 - z_m C \alpha - y_m S \alpha - l_b S \bar{\gamma} S \bar{\alpha} + l_b C \bar{\gamma} S \theta_0 C \bar{\alpha}.\end{aligned}\tag{5.7}$$

The generalized coordinates are chosen as $\underline{q} = [\alpha, \gamma]$. As such, the kinetic energy is given by

$$T = \frac{1}{2} J_w \dot{\alpha}^2 + \frac{1}{2} J_r \dot{\gamma}^2,\tag{5.8}$$

with J_w and J_r the inertias of the wishbone and electric motor with rotating arm and reductor respectively.

From Figure 5.1 it follows that the nonconservative forces can be written as

$$\underline{Q}_{nc} = \begin{bmatrix} -F_{load} l \cos \alpha - \frac{1}{2} m_w g l \cos \alpha \\ M_r \end{bmatrix},\tag{5.9}$$

with M_r the driving moment, F_{load} the load from the suspended mass acting on the actuator and m_w the mass of the wishbone.

The potential energy on the other hand, is more complicated. It is given by

$$\begin{aligned}V &= \int_0^\epsilon (c_a \xi + F_s^0) d\xi \\ &= \frac{1}{2} c_a \epsilon^2 + F_s^0 \epsilon \\ &= \frac{1}{2} c_a ((a_3^r)^2 - 2a_1^r a_3^r + (a_1^r)^2) + F_s^0 (a_3^r - a_1^r).\end{aligned}\tag{5.10}$$

Lagrange's equation of motion in the absence of constraints are (see for example Huston (1995)) given by

$$\frac{d}{dt} \left(\frac{\delta T}{\delta \dot{\underline{q}}} \right) - \frac{\delta T}{\delta \underline{q}} + \frac{\delta V}{\delta \underline{q}} = \underline{Q}_{nc}^T.\tag{5.11}$$

Herein,

$$\begin{aligned}\frac{\delta V}{\delta \underline{q}} &= \left[\frac{\delta V}{\delta \alpha}, \frac{\delta V}{\delta \gamma} \right] \\ &= \begin{bmatrix} F_s^0 \left(a_4^r - \frac{a_2^r}{a_1^r} \right) + c_a \left(a_4^r (a_3^r - a_1^r) + a_2^r \left(1 - \frac{a_3^r}{a_1^r} \right) \right) \\ F_s^0 \left(a_6^r - \frac{a_5^r}{a_1^r} \right) + c_a \left(a_6^r (a_3^r - a_1^r) + a_5^r \left(1 - \frac{a_3^r}{a_1^r} \right) \right) \end{bmatrix}^T\end{aligned}\tag{5.12}$$

with

$$\begin{aligned} a_2^r &= \frac{\delta a_1^r}{\delta \alpha}, & a_4^r &= \frac{\delta a_3^r}{\delta \alpha}, \\ a_5^r &= \frac{\delta a_1^r}{\delta \gamma}, & a_6^r &= \frac{\delta a_3^r}{\delta \gamma}. \end{aligned} \quad (5.13)$$

Combining (5.10, 5.11, 5.12), it can be found that

$$\begin{aligned} J_w \ddot{\alpha} + F_s^0 \left(a_4^r - \frac{a_2^r}{a_1^r} \right) + c_a \left(a_4^r (a_3^r - a_1^r) + a_2^r \left(1 - \frac{a_3^r}{a_1^r} \right) \right) + \frac{1}{2} m_w g l \cos \alpha &= -F_{load} l \cos \alpha \\ &\quad \underbrace{\hspace{10em}}_{-F_{act} l \cos \alpha} \\ J_r \ddot{\gamma} + F_s^0 \left(a_6^r - \frac{a_5^r}{a_1^r} \right) + c_a \left(a_6^r (a_3^r - a_1^r) + a_5^r \left(1 - \frac{a_3^r}{a_1^r} \right) \right) &= M_r, \\ &\quad \underbrace{\hspace{10em}}_{-M_d} \end{aligned} \quad (5.14)$$

with F_{act} the steady-state actuator force and M_d the steady-state disturbance moment. Using these characteristics, the design parameters are optimized next, in an attempt to minimize the nonlinearity of the actuator stiffness.

5.2.2 Parameter optimization

The design goal is to obtain a constant stiffness for all γ at $\alpha = 0$ as strong nonlinearities in the effective stiffness may result in discomfort or even instability in vehicle applications. First however, it is important to define a (reduced) set of design parameters.

Choice of the design parameters

Looking back at the previous subsection, the model has a lot of parameters. These are used to specify the system in its nominal position, i.e., for $\alpha = \gamma = 0$. However, not all of them are free as there are certain design constraints. Assuming that the gravity constant and the mass of the wishbone are fixed, a reduced set of parameters is given by

$$\begin{aligned} \underline{\zeta}_{in} &= [\underline{\zeta}_1, \underline{\zeta}_2] \\ \underline{\zeta}_1 &= [l, l_a, l_b, F_s^0] \\ \underline{\zeta}_2 &= [c_a, h_0, x_s, z_s, \gamma_0], \end{aligned} \quad (5.15)$$

where x_s and z_s are used in the definition of point S (for $\alpha = 0$ and $\gamma = 0$)

$$\vec{r}_{s0} = [x_s, l_a, z_s]. \quad (5.16)$$

Note that no design flexibility is allowed in $\vec{r}_{s0} \cdot \vec{e}_2^F$ in an attempt to minimize the normal force acting on the bearing in point H . The parameters $\underline{\zeta}_1$ follow directly

from the actuator's force-range and packaging requirements. Which leaves ζ_2 free for stiffness optimization.

In fact, ζ_2 is a minimal set of remaining design parameters. This can be deduced with the knowledge that they are needed to specify the geometric properties of the intersection of a cone. A cone can be specified as two points in space and its bottom radius, so with 7 parameters. Moreover, one additional parameter is needed for the intersection (γ_0). However, the \vec{e}_1^F and \vec{e}_2^F position of the top of the cone, as well as the bottom radius are constraint, leaving a total of 5 design parameters.

Consequently, the set of dependent parameters is given by

$$\zeta_d = [x_m, y_m, z_m, l_r, h_c, \alpha_0, \theta_0]. \quad (5.17)$$

The relation between ζ_d and ζ_{in} needs to be determined if the model is to be used in accordance with the design constraints.

As mentioned, the most important design constraint is the cone for $\alpha = 0$, with center M , height h_c and ground radius l_b . A cone can be parameterized using two points in space and the radius of the ground. For this purpose, the points H and S are considered, where the position coordinates are chosen as (5.16) and

$$\vec{r}_{h0} = [0 \ l_a \ h_0] \vec{e}^F. \quad (5.18)$$

As a result the magnitude of l_r and h_c is determined as

$$\begin{aligned} l_r &= \sqrt{x_s^2 + (h_0 - z_s)^2} \\ h_c &= \sqrt{l_r^2 - l_b^2}. \end{aligned} \quad (5.19)$$

Furthermore, in the nominal position ($\alpha = 0$ and $\gamma = 0$) it is also known that

$$\begin{aligned} \vec{r}_{h0} &= \vec{r}_m + \vec{r}_{mh} = [-x_m \ y_m \ z_m] + \begin{bmatrix} 0 & 0 & \sqrt{l_r^2 - l_b^2} \end{bmatrix} \vec{e}^M \\ &= \begin{bmatrix} -x_m + h_c \sin \theta_0 \\ y_m - h_c \cos \theta_0 \sin \alpha_0 \\ z_m + h_c \cos \theta_0 \cos \alpha_0 \end{bmatrix} \vec{e}^F. \end{aligned} \quad (5.20)$$

Moreover, from (5.5) it follows that in the nominal position

$$\vec{r}_{s0} = \begin{bmatrix} -x_m + l_b \cos \gamma_0 \cos \theta_0 \\ y_m + l_b \sin \gamma_0 \cos \alpha_0 + l_b \cos \gamma_0 \sin \theta_0 \sin \alpha_0 \\ z_m + l_b \sin \gamma_0 \sin \alpha_0 - l_b \cos \gamma_0 \sin \theta_0 \cos \alpha_0 \end{bmatrix}^T \vec{e}^F. \quad (5.21)$$

Combining (5.16, 5.18, 5.20, 5.21), gives

$$\begin{aligned} -h_c \sin \theta_0 + l_b \cos \gamma_0 \cos \theta_0 &= x_s \\ x_m &= h_c \sin \theta_0 \\ \alpha_0 &= \tan^{-1} \left\{ \frac{-l_b \sin \gamma_0}{h_c \cos \theta_0 - l_b \cos \gamma_0 \sin \theta_0} \right\} \\ y_m &= l_a + h_c \cos \theta_0 \sin \alpha_0 \\ h_m &= h_0 - h_c \cos \theta_0 \cos \alpha_0. \end{aligned} \quad (5.22)$$

So, using the constraint equations (5.19) and (5.22) the parameter set $\underline{\zeta}_d$ is determined by the design parameters $\underline{\zeta}_{in}$. In the following subsection the design parameters are optimized.

Optimization criterion

As mentioned before, the design objective is to obtain a steady-state actuator stiffness characteristic that is (reasonably) constant without making concessions with respect to the actuator force range. For that reason, the design variables have been split in two parameter sets in the previous subsection. The actuator force range is tuned using $\underline{\zeta}_1$. This leaves $\underline{\zeta}_2$ to obtain the desired stiffness characteristic. Consequently, the optimization problem can be posed as

$$\begin{aligned} \min_{\underline{\zeta}_2} J = \max & \left\{ \left(\frac{c_{eff}(\gamma, \alpha = 0)}{c_d} - 1 \right)^2 \right\} \\ \text{s.t.:} & \\ & \underline{\zeta}_1 \text{ given} \\ & c_a \in [15, 60] \text{ N/mm} \\ & h_0 \in [0.1, 0.4] \text{ m} \\ & x_s \in [-0.05, 0.05] \text{ m} \\ & z_s \in [-0.05, 0.05] \text{ m} \\ & \gamma_0 = 0. \end{aligned} \tag{5.23}$$

The relatively strict constraint on γ_0 is a choice to simplify the problem.

The posed optimization problem is not convex and therefore a large range of initial conditions were checked. The end result may still not be the global optimum, but gives a sufficiently smooth stiffness characteristic. The parameters for a design with a stiffness c_d of 15 N/mm are given in Table 5.1.

The optimized characteristic, as well as the effect of varying z_s is shown in Figure 5.2 (right). The optimal result is represented by the solid line. As can be seen, the actuator stiffness is nearly equal to c_d over the γ -range of actuation. Furthermore, looking at Figure 5.2 (left), the actuator force characteristics run nearly parallel over the full γ -range for the minimum and maximum α values, indicating that while the optimization aimed for a constant stiffness at $\alpha = 0$, the effective stiffness variations at other α are small as well.

Again considering Figure 5.2 (right), it is interesting to note that z_s can be used to shift the complete stiffness characteristic up and down. In other words, z_s can be used to influence the mean actuator stiffness over all γ . Furthermore, increasing z_s to increase the actuator stiffness has a beneficial effect on the actuator force range, see Figure 5.3 (right). The downside however, is that the maximum disturbance moment is also increased, see Figure 5.3 (left).

Table 5.1: Optimized actuator parameters - constant stiffness design.

Design parameters			Constraint parameters		
parameter	value	unit	parameter	value	unit
l	0.15	m	x_m	0.011	m
l_a	0.059	m	y_m	0.059	m
l_b	0.05	m	z_m	0.039	m
F_s^0	6800	N	l_r	0.193	m
c_a	15	N/mm	h_c	0.186	m
h_0	0.225	m	α_0	0	rad
x_s	0.039	m	θ_0	0.059	rad
z_s	0.036	m	m_w	20	kg
γ_0	0	rad	g	9.81	m/s ²

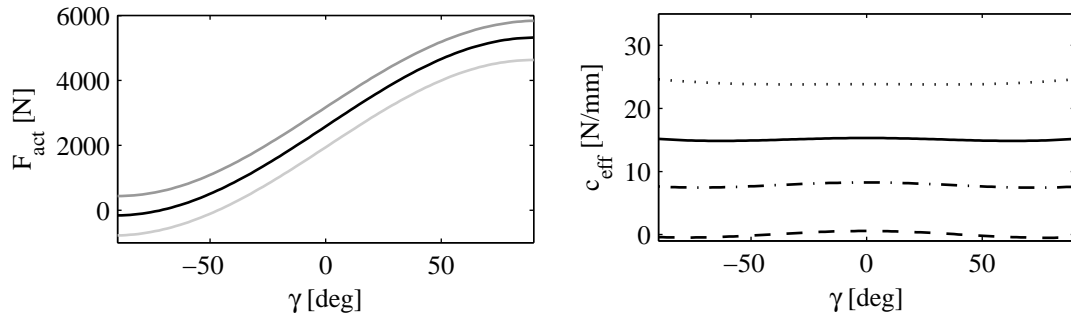


Figure 5.2: Actuator effective stiffness (right) for $\alpha = 0$ and: $z_s = 0.054$ [m] (dotted); optimized $z_s = 0.036$ [m] (solid); $z_s = 0.018$ [m] (dash-dotted); and $z_s = -0.006$ [m] (dashed). Actuator force (left) for the optimized $z_s = 0.036$ [m] and: $\alpha = 0$ (black); $\alpha = -15$ degrees (dark grey); and $\alpha = 15$ degrees (light grey).

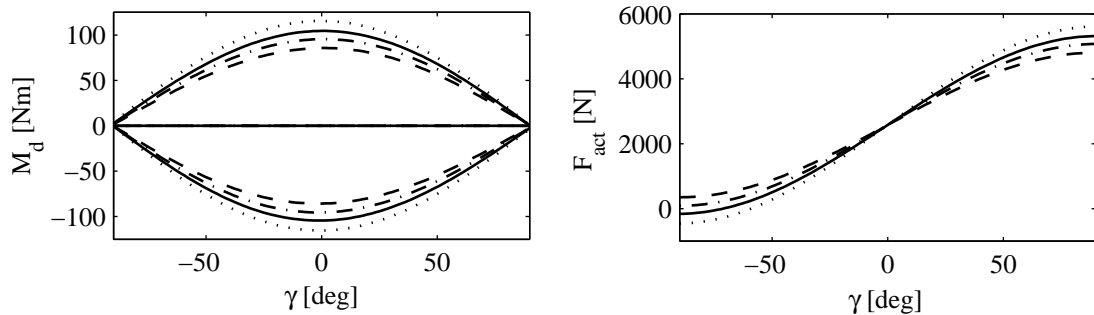


Figure 5.3: Actuator disturbance moment (right) for $\alpha = [-15 \ 0 \ 15]$ degrees and actuator force (left) for $\alpha = 0$, with: $z_s = 0.054$ [m] (dotted); optimal $z_s = 0.036$ [m] (solid); $z_s = 0.018$ [m] (dash-dotted); and $z_s = -0.006$ [m] (dashed).

5.3 Simulation model

In this section the components of the simulation model are discussed. These are used for the controller design later on.

5.3.1 Actuator model

In the previous section a model is derived for the *eLPAS* - variable geometry actuator. However, this model only holds as long as the frame (point F) does not rotate with respect to the inertial frame at point O . This is in vehicle implementations typically not the case, e.g. when cornering. To overcome this limitation a simulation model is also created using *Matlab SimMechanics*, the multibody toolbox of *Matlab Simulink*.

5.3.2 Electric motor model

The *eLPAS* actuator angle is controlled by a three phase brushless permanent magnet (PM) DC motor, where the motor bandwidth is significantly higher than that of the total actuator assembly. For that reason it might be warranted to assume exact tracking of any reference torque ($T_r = T_r^{ref}$). However, a motor model is needed to gain insight in the power consumption of the actuator. Furthermore, under extreme circumstances saturation of current and/or voltage may occur.

The brushless PM DC motor is typically characterized as having a trapezoidal back electromotive force (EMF), driven by rectangular pulse currents. As this mimics the operation of a brush PM DC motor the name “brushless DC” fits even though it is in fact a synchronous AC motor (Hanselman, 2003, Chapter 1).

The brushless PM DC motor differs from the brush PM DC motor in that the brushes, needed for generating a varying magnetic field, have been replaced by an electrical commutation (inverter). Moreover, where the brush PM DC motor has its permanent magnets in the stator and the varying magnetic field is realized in the rotor; it is the other way around in a brushless PM DC motor. As a result, the brushless PM DC motor is a nonlinear machine which is considerably more complex than the brush PM DC motor. Despite these differences the following assumption is adopted.

Assumption 5.3.1. *The equivalent electrical scheme of a brush PM DC motor, given in Figure 5.4, also holds for the brushless PM DC motor.*

In practice the three phase brushless PM DC motor is described by three of these electrical schemes, resulting in a maximum realizable torque which is roughly a factor $3/2$ higher than that of a brush PM DC motor (Hanselman, 2003, Section 8.3). Consequently, an error is introduced by this simplification. Still, the model will suffice to get a reasonable indication of the power requirements. For more reliable and detailed models, the reader is referred to for example Lomonova (1997).

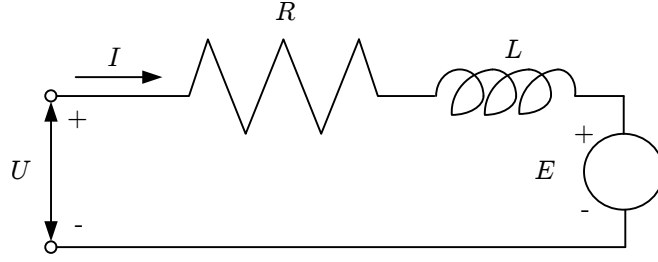


Figure 5.4: Electrical scheme of a DC drive.

Adopting the electrical circuit depicted in Figure 5.4 under Assumption 5.3.1, the motor dynamics is modeled as

$$L \frac{dI}{dt} = U - E - RI, \quad (5.24)$$

where the back electromotive force voltage

$$E = K_E \omega_m, \quad (5.25)$$

K_E is a motor constant, ω_m is the rotational velocity of the motor, I is the current, U is the command voltage, L is the motor inductance and R is the motor resistance. Furthermore, the effective actuation torque is given by

$$T_r = (T_{rel} - M_{fric})N, \quad (5.26)$$

where N is the gearbox (reductor) ratio,

$$T_{rel} = K_T I, \quad (5.27)$$

K_T is a motor constant and M_{fric} is the friction moment of the motor and gearbox, which has to be incorporated in the model as it is an important source of energy dissipation.

5.3.3 Friction model

The friction moment is modeled using a *LuGre* model, Canudas de Wit et al. (1995) and is given by

$$M_{fric} = s_0 z + s_1 \dot{z} + s_2 \omega_m, \quad (5.28)$$

with s_0, s_1, s_2 friction parameters. Furthermore, z can be seen as the deflection of tiny bristles in the contact patch and

$$\dot{z} = \omega_m - \frac{|\omega_m|}{\beta} z. \quad (5.29)$$

Moreover,

$$\beta = \left\{ F_c + (F_s - F_c) e^{-(\omega_m/\omega_s)^2} \right\} / s_0, \quad (5.30)$$

where F_c, F_s and ω_s are parameters that determine the steady-state friction characteristic.

Table 5.2: Friction and motor parameters

Friction parameters			Motor parameters		
parameter	value	unit	parameter	value	unit
s_0	15	Nm	K_E	0.095	Vs/rad
s_1	0.1	Nms	K_T	0.095	Nm/A
s_2	0.0042	Nms	R	0.13	Ω
F_c	0.2	Nm	L	$2.5 \cdot 10^{-4}$	H
F_s	0.555	Nm	N	-59	-
ω_s	11.8	rad/s	J_r	0.70	kgm ²
			I_{max}	75	A
			U_{max}	42	V

5.3.4 Actuator limitations

In practice the dynamic behavior of the electric motor will be limited due to the maximum voltage; maximum current; and the danger of thermal overloading, which could damage the motor. Although important, the thermal behavior is not further evaluated in this thesis given its complexity. The effect of the current and voltage limitations can be visualized by looking at the maximum size of a sine-shaped reference that can be followed, without saturation. The reference is given by

$$\gamma_{ref} = A \sin(2\pi ft). \quad (5.31)$$

The reference and its derivatives are constrained as

$$\begin{aligned}
|\gamma_{ref}| &\leq \gamma_{max} \\
|\dot{\gamma}_{ref}| &\leq \omega_m^{max} = \frac{U_{max}}{K_E N} \\
|\ddot{\gamma}_{ref}| &\leq \frac{T_{max} - |M_d|}{J} = \frac{N(K_T I_{max} - |M_{fric}|) - |M_d|}{J},
\end{aligned} \quad (5.32)$$

by the physical limitations of the actuator with electric motor. So, the actuator's working range is intrinsically limited by three constraints.

Consider the parameters as given in Table 5.2 and $\gamma_{max} = 90$ degrees. The working range of the actuator under these conditions, with $M_{fric} = 0$ and $\alpha = 0$ is represented in Figure 5.5 by the area beneath the solid line. Furthermore, the three constraints are given by the dashed lines.

The first constraint, given by the horizontal line can be increased by increasing γ^{max} . However raising it above 90 degrees will have no beneficial effect on the maximum actuator force. The second constraint, given by the dashed line with -1 slope, is determined by the maximum rotational velocity of the electric motor. It can be increased by increasing the maximum voltage U_{max} . The third constraint, given by the dashed line with -2 slope, is determined by the maximum rotational acceleration of the electric motor. It can be increased by increasing the maximum current I_{max} .

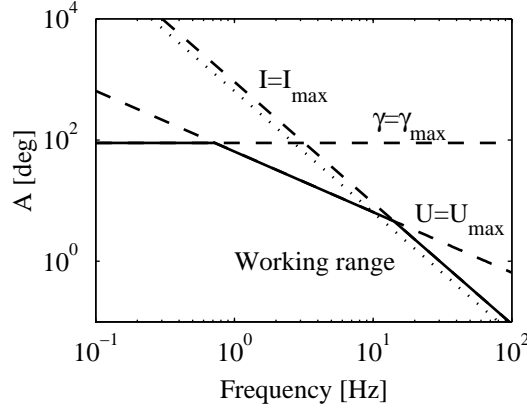


Figure 5.5: Actuator working range (under the solid line). Constraints for $\alpha = 0$ and $M_{fric}^{max} = 0$ (dashed) and third constraint for $M_{fric}^{max} = 0.9$ Nm, $\alpha = 15$ degrees (dotted).

In reality the friction will be nonzero and also typically, there will be some rotation of the wishbone $|\alpha| > 0$. These two conditions will give rise to a shift of the third constraint. For the prototype, the maximum friction moment for high rotational velocities is approximately 0.9 Nm. This is in accordance with the experimental data that will be shown later on. When applying this friction moment and a maximum disturbance moment (for $\alpha = 15$ degrees at $\gamma = 0$), the worst-case working range limitation can be approximated. This approximation is given in Figure 5.5 by the dotted line.

5.4 Controller design

A cascaded control strategy is chosen to control the actuator. As such, there is a motor controller, angle controller and force controller. The reason for choosing this strategy lies within the wish to constraint the reference angle to ± 90 degrees. As a result, it is possible to use linear techniques to generate the reference angle as a function of the reference force and actual force. The three controller modules are shortly discussed in the following sections.

5.4.1 Electric motor control

The inner most control loop is that of the torque controller, see Figure 5.6. It consists of a standard PI-controller with anti-windup,

$$C_m = P_m + \frac{I_m}{s} \bigg|_{I_m^{max}}, \quad (5.33)$$

and a resistance feed forward,

$$U_m^{ff} = RI_{ref}. \quad (5.34)$$

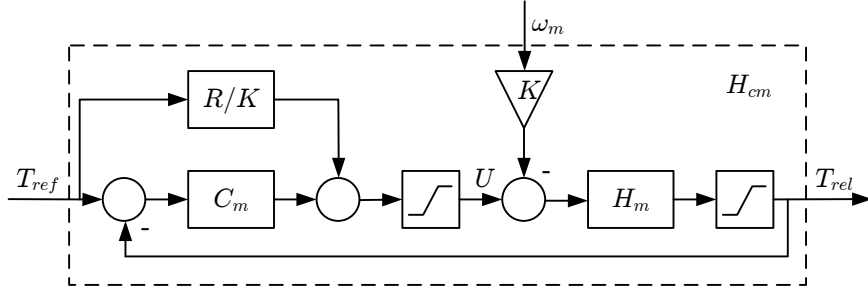


Figure 5.6: Block-scheme of the motor control-loop.

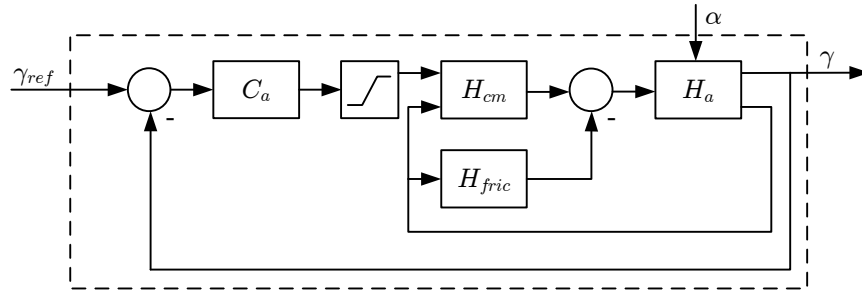


Figure 5.7: Block-scheme of the angle control-loop.

Herein, P_m , I_m are control gains. The transfer function z_m follows from (5.24),

$$H_m = \frac{T_{rel}(s)}{U(s) - E(s)} = \frac{K}{Ls + R}, \quad (5.35)$$

where s is the Laplace variable. The controller brings the actual current close to the reference current and thus the realized moment M_{rel} , see (5.26) and (5.27), close to the reference moment

$$T_{ref} = KI_{ref}. \quad (5.36)$$

Moreover, both the maximum voltage and current are constraint (saturation blocks).

5.4.2 Angle control

The second feedback loop is that of the angle controller, see Figure 5.7. It consists of a lead-lag filter with integral action and anti-windup,

$$C_a = -P_a \left(\frac{s + D_a}{s + L_a} \right) - \frac{I_a}{s} \Big|_{I_a^{max}}. \quad (5.37)$$

Herein, the control gain is negative as a result of the negative gear ratio N . The closed-loop system H_{cm} is shown in Figure 5.6 and H_{fric} is defined by (5.28, 5.29, 5.30).

The actuator hardware dynamics H_a follows from the *SimMechanics* model.

5.4.3 Force control

The highest level control consists of the force controller. Its task is to minimize the difference between the generated actuator force and the reference actuator force. In Evers et al. (2008b) this is done using a feed forward and feedback part. However, as it is desired to obtain an implementation with a minimum number of sensors it is assumed that the modeled $F_{act} - \gamma - \alpha$ relation is exact. The consequences of this assumption are discussed in Section 5.5.

By assuming that the modeled $F_{act} - \gamma - \alpha$ relation is exact, the feedback part can be omitted. Instead, a 3D-lookup table can be used that specifies γ_{ref} for a given reference force F_{ref} and a measured deflection α . As the effective stiffness variation as a function of γ is relatively small $c_{eff}(\alpha, \gamma) \approx c_{eff}$, it is chosen to use a 2D-lookup table instead ($F_{act} - \gamma$ relation for $\alpha = 0$). The uncompensated suspension force $lc_{eff} \sin \alpha$ is considered to be desirable, as it effectively works as a passive spring placed in parallel with the actuator. Furthermore, to limit the power consumption as a result of high frequent reference inputs, see Evers et al. (2008b), a 10 Hz first order low-pass filter is used to filter the reference force. Finally, the total reference angle is bounded

$$\gamma_{ref} \in \left(-\frac{\pi}{2}, \frac{\pi}{2}\right) \text{ [rad]}, \quad (5.38)$$

to prevent the actuator from hitting its bump-stops.

5.4.4 Actuator power consumption

In order to get an idea of the worst case power consumption of the actuator several simulations are performed. First, for $\alpha = 0$ with- and without friction, a number of sine shaped force references are tracked. Herein the amplitude and frequency of the sines is varied. The maximum amplitude A for a certain frequency is obtained from Figure 5.5, and transformed to a reference force. The results, given in Figure 5.8, show that the energy consumption of the *eLPAS* design is very low for low angular velocities ($\dot{\gamma}$). However, it increases as $\dot{\gamma}$ increases. Consequently, high frequent reference signals result in a relatively large power consumption. Furthermore, it can be seen that friction effects account for the major part of the used power below 6 Hz. Above 6 Hz, the motor resistance starts to become important. The significant drop-off above 10 Hz is a result of the decreasing maximum velocity.

From simulations using the maximum amplitude A and various fixed α , it follows that the influence of α on the mean power consumption under extreme circumstances is small, see Figure 5.9 (right). However, the maximum power consumption does vary significantly, see Figure 5.9 (left), as a result of the spring force component that acts on the electric motor for $\alpha \neq 0$.

At this point it is worth remarking that an active suspension with a peak power consumption of 2.5 kW has the potential to be very expensive from an energy perspective. Especially, considering the fact that a typical vehicle suspension requires four *eLPAS* actuators. In that case, the worst-case energy consumption will be similar to that of

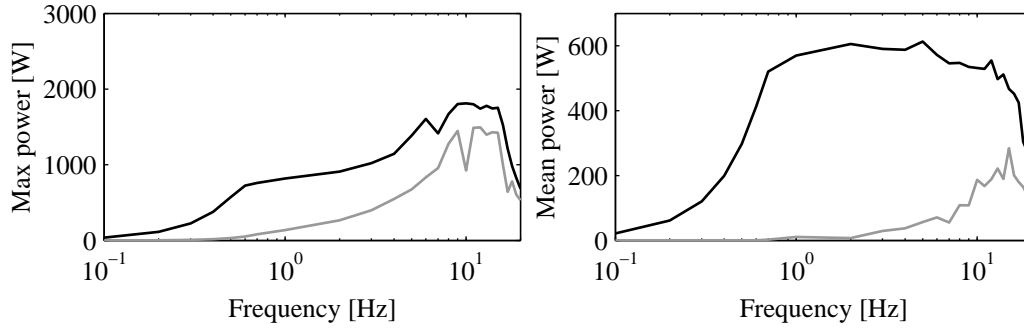


Figure 5.8: Actuator worst-case power consumption. Mean (right) and maximum (left) power consumption for $\alpha = 0$, when tracking sines of varying frequency and maximum amplitude A . Simulations with friction (black) and without friction (grey).

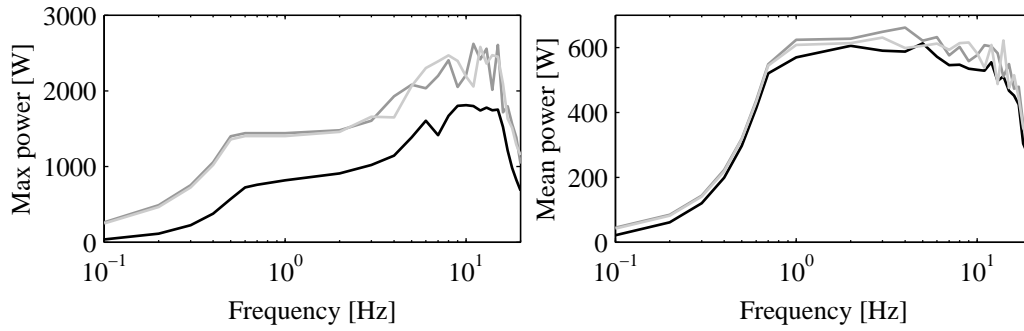


Figure 5.9: Actuator worst-case power consumption. Mean (right) and maximum (left) power consumption, when tracking sines of varying frequency and maximum amplitude A . Simulations with $\alpha = -15$ degrees (dash-dotted), $\alpha = 0$ (black), $\alpha = 15$ degrees (dashed)

known hydraulic solutions. However, once again, these are simulations using worst-case reference inputs. When tracking force references with half or one-fourth of the maximum amplitude, see Figure 5.10, both the maximum and mean power consumption drop significantly.

Under normal working conditions, the reference force variations need to be kept as low as possible, without impairing the suspension performance (too much). When doing so, the energy requirements will remain far below the shown worst-case results. So, this is very important to take into consideration when designing a global suspension controller. Controlled correctly, the *eLPAS* design has the potential to be considerably more energy efficient than other comparative active suspension systems.

5.5 Experimental validation

The question remains whether or not the used *eLPAS* model gives an accurate description of the system characteristics. In this section the steady-state and dynamic

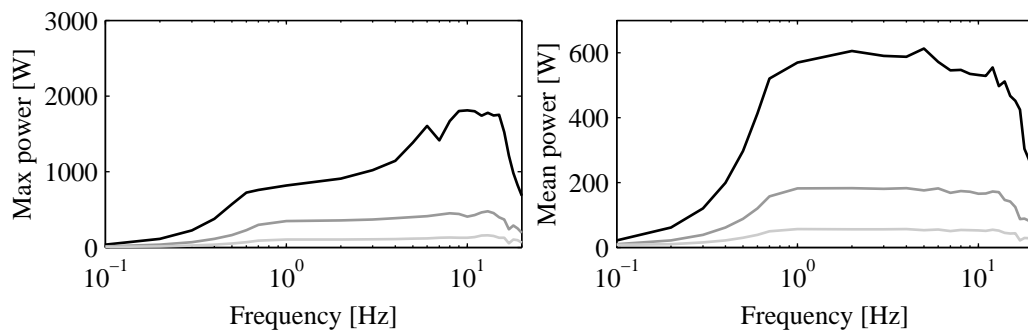


Figure 5.10: Actuator mean (right) and maximum (left) power consumption, when tracking sines of varying frequency for $\alpha = 0$. Simulations with $A_F = A_{max}$ (black), $A_F = A_{max}/2$ (dark grey), and $A_F = A_{max}/4$ (light grey).

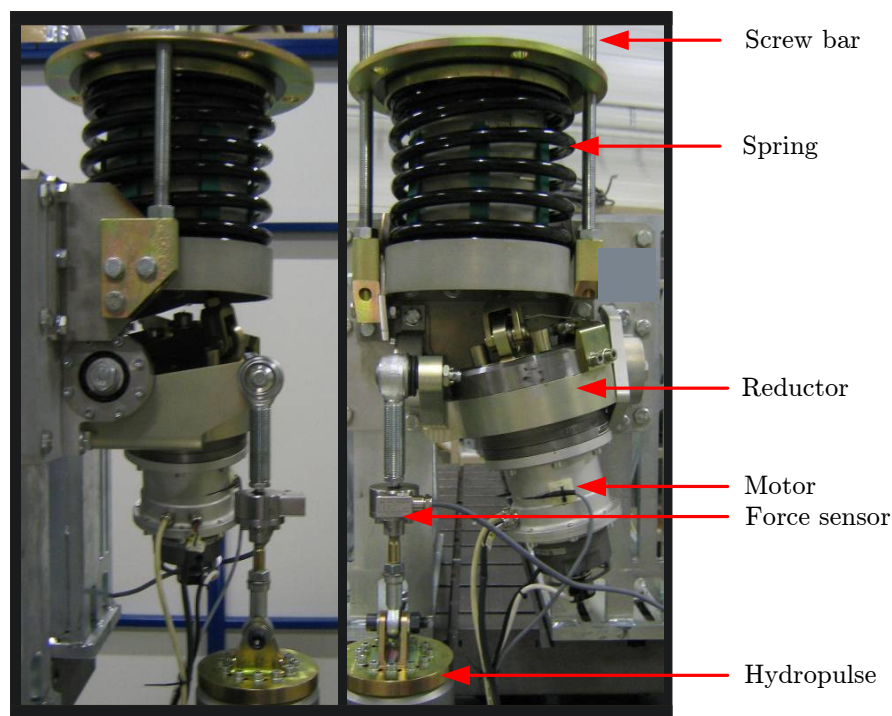


Figure 5.11: Experimental setup, front view (left) and side view (right).

simulation results are compared to measurements obtained from an experimental setup. The test-rig is discussed first.

5.5.1 The prototype

The experimental setup is depicted in Figure 5.11 from similar viewpoints as the model in Figure 5.1. The two elements that dominate the picture are the electric motor with reductor on the one hand and the rather large steel spring on the other hand. A hydropulse is used to control the angle α . The small block between the wishbone and

Table 5.3: Actuator parameters - experimental setup

Design parameters			Constraint parameters		
parameter	value	unit	parameter	value	unit
l	0.15	m	x_m	0.039	m
l_a	0.059	m	y_m	0.061	m
l_b	0.05	m	z_m	0.042	m
F_s^0	6800	N	l_r	0.208	m
c_a	25	N/mm	h_c	0.202	m
h_0	0.24	m	α_0	0.008	rad
x_s	0.01	m	θ_0	0.194	rad
z_s	0.033	m	m_w	20	kg
γ_0	-0.03	rad	g	9.81	m/s ²

Table 5.4: Controller parameters - experimental setup

parameter	value	unit
P_m	0.1	V/(Nm)
I_m	50	Vs/(Nm)
I_m^{max}	28	V
P_a	1500	Nm
D_a	94.2	1/s
L_a	377	1/s
I_a	750	Nms
I_a^{max}	2	Nm

the hydropulse is a force sensor. Furthermore, it can be seen that the rod with length l_r almost completely vanishes within the spring. The parameters of the experimental setup and the controller are given in Table 5.3 and Table 5.4 respectively. Using these parameters, the experimental setup is compared to the model.

5.5.2 Steady-state validation

For the steady-state analysis a sine-shaped reference angle is used, while $\alpha = 0$. The frequency of the sine is chosen sufficiently low to minimize the influence of possible dynamic effects. The resulting actuator force measurements are compared to simulation results obtained with both the analytical model and the *SimMechanics* model, see Figure 5.12 (left).

A couple of things can be concluded from this figure. First of all, it can be seen that the *SimMechanics* model and analytical model show very similar results. Furthermore, the difference between the models and the measurements is relatively small. However,

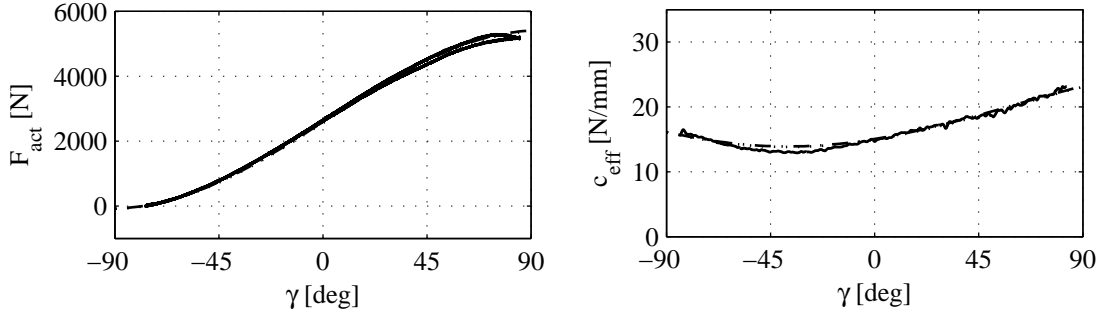


Figure 5.12: Actuator force (left) and effective stiffness (right) for $\alpha = 0$: measurement (solid); Analytic model (dash-dotted); and *SimMechanics* model (dotted).

for $\gamma \rightarrow 90$ degrees there is a small hysteresis effect that is not included in the models. It may be a result of the bending of the wishbone due to the large spring force which acts at an increasing distance from the rotational joint. Changing the frequency of the sine-shaped reference from 0.01 Hz to 0.05 Hz did not change the magnitude of this effect.

The same reference signal is used for $\alpha = -3.4$ degrees and $\alpha = 4.2$ degrees. The difference between these two force measurements is used to determine the effective stiffness around $\alpha = 0$, see Figure 5.12 (right). The effective stiffness for the models is determined in a similar way. It can be seen that the results almost show a perfect match. There is only a small difference around $\gamma = -50$ degrees. Furthermore, the effect of the relatively high spring stiffness is also clearly visible as the effective stiffness does show some variation as a function of γ . In retrospect, the steel spring may not have been the most ideal choice, as its characteristics also changed during the months of testing.

Using the measurements of the motor current and (5.27) it is possible to determine the actuation moment at the reductor M_r . However, this moment consists of both the friction moment and disturbance moment (5.26), so isolating the disturbance moment requires an additional computational step. Assuming that the friction moment is dominated by the coulomb friction for these low speeds, it can be given as

$$M_{fric}^* = \text{sign}(\omega_m)M_c. \quad (5.39)$$

Herein, the coulomb friction is estimated to be $M_c = 0.5$ Nm. Note that this is the moment at the motor, so before the reductor. After the reductor the influence is equal to 29.5 Nm as a result of the gear ratio $i = 59$. After subtraction of the estimated friction moment the disturbance moment can be obtained. This moment, filtered with a 1 Hz second order causal, anti-causal filter, is given in Figure 5.13.

It can again be seen that the difference between the analytical and *SimMechanics* model is negligible. However, the difference between the models and the measurements is substantial. For $\alpha = 4.2$ degrees the results match quite well, but for $\alpha = 0$ degrees it is clear that the measured disturbance moment is unequal to zero. This might be a

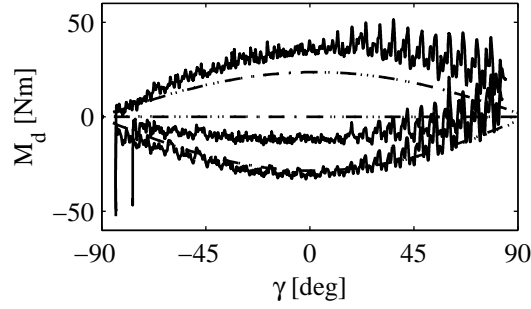


Figure 5.13: Actuator disturbance moment for $\alpha = [-3.4 \ 0 \ 4.2]$ degrees: measurement (solid); Analytic model (dash-dotted); and *SimMechanics* model (dotted).

result of an alignment error of the hydropulse ($\alpha_{meas} = 0 \neq \alpha$) or an indication that the constructed cone is not perfect. Moreover, the friction compensation might also introduce an error. The difference is largest for $\alpha = -3.4$ degrees. Furthermore, for all three γ -sweeps a strange effect occurs for $\gamma \rightarrow 90$ degrees. This effect is probably also the result of the bending of the wishbone. Nevertheless, the size and shape of the modeled and measured disturbance moment as a function of γ and α do show a fair similarity.

5.5.3 Dynamic validation

In this subsection the *SimMechanics* model is compared to the measurement results under dynamic conditions. First the friction model is evaluated. Next, the closed-loop model is evaluated using a step-shaped reference. Finally, the transfer functions $|F_{act}/F_{ref}|$ and $|F_{act}/(l \sin \alpha)|$ are evaluated.

Friction model

The friction modeling is evaluated with two experiments, inspired by Canudas de Wit et al. (1995). In the first test, the friction-velocity characteristic is determined. And in the second test, the friction stiffness is evaluated.

For the first test, the connection rod with length l_r has to be disconnected from the rod with length l_b , see Figure 5.1 and the bump-stops which limit γ need to be removed. Otherwise, the normal operating range, $\gamma \in [-90, 90]$ degrees, will be too small to accurately determine the friction moment given the high acceleration levels. Although the spring force acting on the electric motor may in practice influence the friction characteristic, this effect cannot be determined so easily. In this disconnected configuration a triangular velocity reference is followed, which makes a full sweep ($0 \rightarrow \omega_m^{max} \rightarrow \omega_m^{min} \rightarrow 0$) in 50 seconds.

The same experiment is repeated in simulation with the simulation parameters as given in Table 5.2. The results are given in Figure 5.14 (left). It can be seen that the simulation and experimental data match well. This despite the fact that the friction

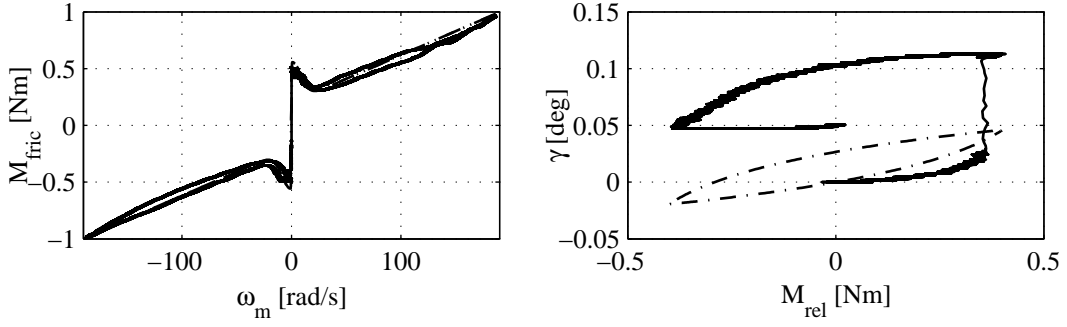


Figure 5.14: Friction characteristics measured (solid) and simulated (dash-dotted): friction moment as a function of the rotational velocity of the motor (left); and γ as a function of the realized motor moment in stiction.

model does not directly include the influence of the spring load on the electric motor.

In the second test, the rods are reconnected and an open-loop test is executed. In this case a triangular reference moment is used (with a period of 50 seconds) to determine the friction stiffness. The maximum reference moment remains below the coulomb friction level. The results are shown in Figure 5.14 (right). The difference between the measurement and the simulation is mainly caused by a slight amount of sliding around $M_{\text{ref}} = 0.4$ [Nm] in the experimental setup. Nevertheless, given the similarities in curvature between measurement and simulation it is concluded that the friction stiffness (tunable with the parameter s_0) is modeled sufficiently accurate.

Step response

In order to check the time response behavior of the model and experimental setup a number of step responses are measured. First, a small force step of ± 100 [N] is performed. The results are given in Figure 5.15 for a positive step (left) and a negative step (right). The force reference and responses are given in the top plots and the power consumption is given in the bottom plots.

From the top plots in Figure 5.15 it can be seen that the responses in simulation and experiment are quite similar when it comes to settling time and overshoot. However there is a small constant offset. This is a result of the open-loop force control structure, small differences between the $F_{\text{act}} - \gamma$ lookup table and the real actuator characteristics, friction, and sensor noise/drift. Furthermore, when looking at the power consumption (bottom plots) it is clear that the peak power consumption of the simulation and measurement are quite similar. However, the measured mean power consumption (33 W for both the positive and negative step) is slightly higher than the simulated mean power consumption (18 W). Still, the differences are relatively small.

The differences increase for larger step responses, see Figure 5.16. When evaluating the maximum size step responses there is a large time period in which the maximum velocity is reached. This maximum velocity determines the slope of the F_{act} response

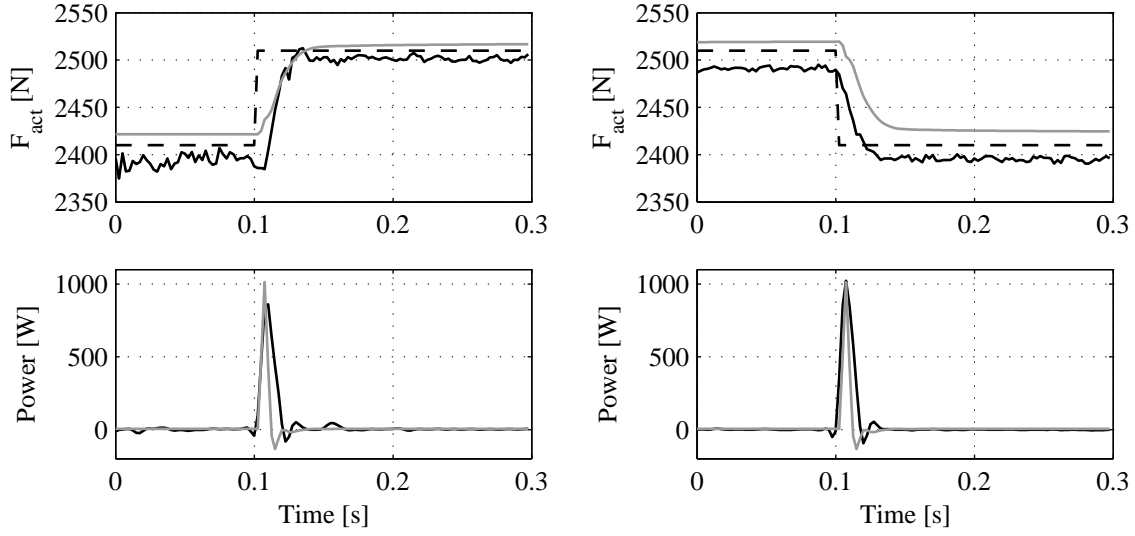


Figure 5.15: Small step: actuator force (top) and power consumption (bottom), for a positive step (left) and negative step (right). The lines represent the reference force (dashed); measurement (solid); and simulation (dash-dotted).

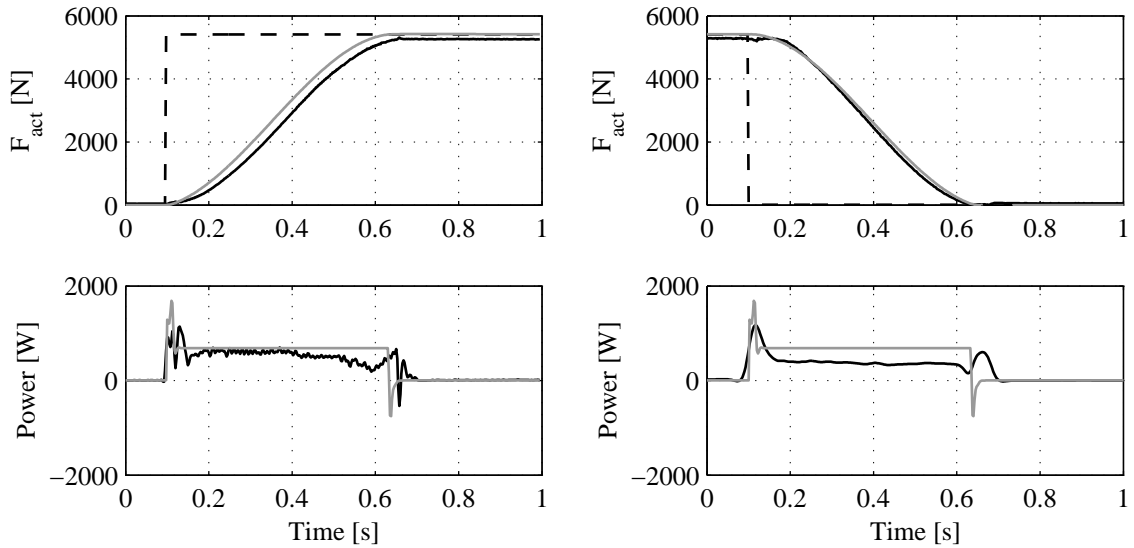


Figure 5.16: Maximum amplitude step: actuator force (top) and power consumption (bottom), for a positive step (left) and negative step (right). The lines represent the reference force (dashed); measurement (solid); and simulation (dash-dotted).

in the top plots of Figure 5.16. It can be seen that there is little difference in maximum velocity and the amount of overshoot between measurement and simulation. However, for the positive step (left) there is a difference in maximum acceleration visible. This might be caused by a difference in the amount of friction for $\gamma = 90$ and $\gamma = -90$ degrees. Moreover, when looking at the power consumption (bottom plots) the difference between the two measurements is striking. This might be an indication that α was not

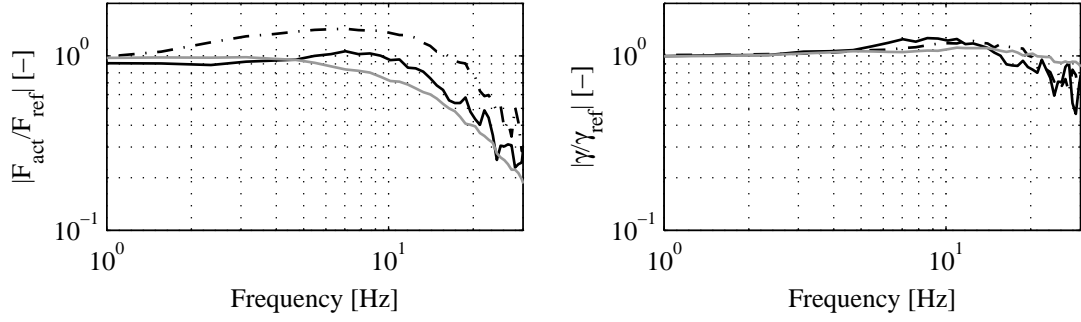


Figure 5.17: Transfer function estimate from F_{ref} to F_{act} (left) and γ_{ref} to γ (right) for $\alpha = 0$ and $\text{mean}(\gamma) = 0$. Measurement with hydropulse (dash-dotted), measurement with hydropulse replaced by a fixed steel rod (solid), and simulation (dashed).

precisely zero during the test. Moreover, the simulated mean power consumption (367 W) is slightly higher than the measured one (315 W for the positive and 255 W for the negative step). It can be seen that the main difference is located in the constant velocity part.

Transfer function estimate

To determine the closed-loop transfer function estimate, a zero mean Gaussian distributed (white noise) signal is used as force reference, filtered with a 15 Hz first order low-pass filter. First, the hydropulse is used to keep $\alpha = 0$. However, the results using this approach show a large mismatch between measurement and simulation for the force loop, see Figure 5.17 (left). This is especially remarkable as the closed-loop transfer from γ_{ref} to γ does not show this difference, see Figure 5.17 (right). Note that the difference between the γ -loop and force loop is due to the 10 Hz first order low-pass filter.

The large difference (in force transfer) between simulation and measurement with hydropulse is most likely a result of a resonance in the transfer function from α to F_{act} around 6 Hz (Figure 5.18). Therefore, the hydropulse is replaced by a solid steel rod and the experiment is repeated (solid line). Clearly, the measurement and simulation results match much better this way.

Dynamic stiffness

The final topic of interest is the influence of α on the actuator force. For that reason a filtered white noise reference for α_{ref} is used and the transfer function from $l \sin \alpha$ to F_{act} is studied, see Figure 5.18 (left). The horizontal line represents the design stiffness. Clearly, both the model and experimental setup follow this stiffness for low frequent disturbances. However, there is an anti-resonance at 6 Hz followed by a strong increase of the transfer magnitude for higher frequencies as a result of the inertia of the wishbone in combination with the spring stiffness. Overall, it can be seen that there is

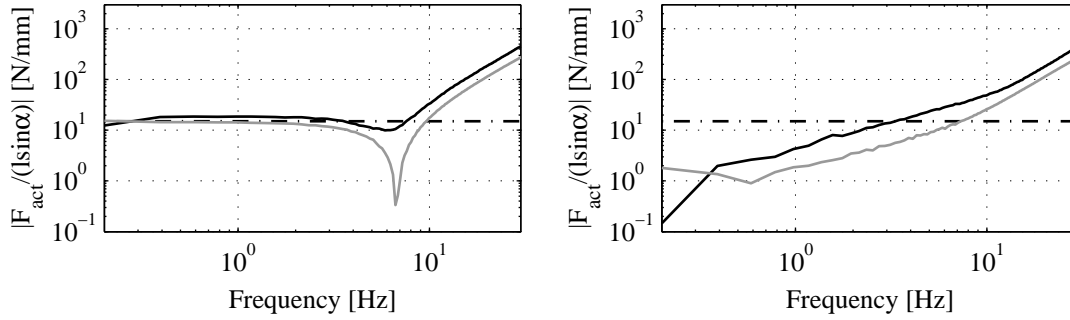


Figure 5.18: Transfer function estimate from $l \sin \alpha$ to F_{act} , for $\gamma = 0$ (left) and $F_{ref} = 0$ (right). The measurement (solid) and simulation (dashed) are given together with the design stiffness (horizontal solid line).

a small offset between measurement and simulation as a result of the difference in the effective stiffness. Furthermore, the resonance seems to be damped more in the actual system than in simulation.

Instead of controlling the angle $\gamma = 0$, it is also possible to demand that $F_{ref} = F_{act}(0, 0) = 2555$ [N], while the hydropulse disturbs the system with filtered white noise. This can be seen as a “flying-carpet” controller, i.e., all “road” disturbances are suppressed without considering suspension travel. So, the actuator is controlled such that the force resulting from the effective *eLPAS* stiffness at various α is compensated. The result is given in Figure 5.18 (right). From this figure it can be concluded that the influence of all disturbances below 8 Hz can be reduced significantly in simulation. On the actual setup this boundary lies around 3 Hz. This difference is most likely a combination of uncompensated variations in the effective stiffness characteristic and inaccuracies in the force measurement.

5.6 Conclusions

In this chapter, an analytical model is presented for the *electromechanical Low-Power Active Suspension (eLPAS)*. It is shown that the orientation of the cone is an important design parameter that can be used to obtain a more or less constant actuator stiffness. The analytical model is implemented in *SimMechanics* for the dynamic evaluation and controller design. The controlled actuator model is validated using measurements from an experimental setup.

The results show, that the model gives an accurate representation of the prototype and that a 10 Hz bandwidth can be easily obtained. However, the stiffness of the prototype does vary slightly over the actuator range as a result of manufacturing inaccuracies. Nevertheless, it can be concluded that the *eLPAS* design is feasible and that the model gives an accurate representation of both the steady-state and dynamic prototype characteristics. Moreover, the *eLPAS* outperforms previous variable geometry actuator designs with respect to stiffness characteristics and achievable bandwidth.

Chapter 6

Optimal vertical cabin control

6.1 Introduction

In the previous chapters, various vehicle models have been introduced and validated. It has been shown, that different active suspension configurations have different power requirements. Furthermore, the *electromechanical Low Power Active Suspension (eLPAS)* has been introduced, modeled and validated. The final questions that remains are: what is the optimal control strategy, given the tractor semi-trailer with an *eLPAS* system at each cabin corner; and what is the achievable performance enhancement with respect to the passive configuration?

The topic of optimal control of active vehicle suspensions has already been covered extensively in literature, see for example Hrovat (1997) for an overview. Still, given the complexity of these systems and the large variety of different control possibilities, the subject remains a topic of interest. Many of the remaining challenges can be studied by first analyzing the vertical vehicle dynamics. This is also the case for the secondary suspension of commercial vehicles. For this reason, the focus in this chapter will be on the quarter truck heave model. The results are used in Chapter 7 to address the more complicated issues associated with the full tractor semi-trailer model.

There is relatively little literature on the analysis, control or state estimation of secondary vehicle suspensions, Cole (2001). The same holds for the vertical secondary suspension dynamics, described by quarter truck models. On the other hand, quarter vehicle models with two degrees of freedom (DOF), that describe the primary suspension behavior, are very often used in literature. Although there are significant differences between the two and four DOF quarter vehicle models, the available literature on the first offers many ideas which are useful when considering the latter.

The simplicity of the quarter vehicle model makes it ideal for analysis purposes. It helps in the understanding of the main control limitations, Karnopp (2008), but also for the comparison of different actuator types, Ballo (2007); Fischer and Isermann (2004). Furthermore, the quarter vehicle model is often used to study the influence of the suspension parameters and for suspension parameter optimization. For example, in Nakhaie Jazar et al. (2006) the parameters are optimized based on the root-mean-

square (rms) values of the suspension travel and suspended mass accelerations. An alternative, elegant, rms based optimization approach is given in Schiehlen (2006). The approach, called covariance analysis, is demonstrated on the quarter vehicle model, but is restricted to systems with a limited complexity. In Verros et al. (2005); Georgiou et al. (2007) the quarter vehicle model is used, with and without semi-active damper, for a multi-objective optimization at various vehicle velocities. As the model is nonlinear and the problem non-convex, Monte-Carlo simulations are used to determine the optimal parameter configurations.

Apart from analysis and parameter optimization, the quarter vehicle model can also be used for controller synthesis. As there are many different ways to solve a control problem, and the problem itself depends on the chosen actuator model, literature on this topic is vast. The performance of the active suspension designs is typically compared to that of a passive suspension only, making it unclear how the various strategies relate. Moreover, although it is well known that suspension configurations should always be compared under identical working space (suspension travel) requirements for practical relevance, Sharp and Crolla (1987), this is often not the case.

Control strategies that have been evaluated on quarter vehicle setups include: preview control, Pilbeam and Sharp (1996); Muijderman (1997); Huisman (1994); cascade control, Purdy and Bulman (1997); nonlinear backstepping, Lin and Kanellakopoulos (1997); fuzzy control, Sie et al. (2006); Boada et al. (2005); LPV/adaptive control, Fialho and Balas (2002, 2000); Chen and Huang (2006); Zhang (2003); Alleyne and Hedrick (1995); Ramsbottom and Crolla (1999); energy neutral control, Kawamoto et al. (2008); LQG control, Hansson (1993); Venhovens (1993); and robust H_∞ control, Hiromatsu et al. (1993). Herein, the last reference is especially interesting as it uses the two DOF quarter vehicle model to describe the chassis-cabin dynamics of a truck. The secondary suspension consists of an air spring in combination with an electric ball screw actuator. It is shown using simulations and experiments on a two DOF setup, that the vertical cabin mode (at 2 Hz) can be suppressed with a relatively modest energy consumption. However, the influence on the required working space remains unclear.

Another noteworthy study, using a quarter truck heave model with three DOF, is presented in Akcay and Türkay (2009). Herein, the model is used as a shape filter for the chassis motions, where the engine and chassis are lumped as a single body. These chassis motions are needed as input for a three DOF heave-roll-pitch cabin model, which uses the parameters of a Ford Cargo truck without payload. An LQG controller is designed for the four idealized actuators, which are placed in parallel with a spring and damper beneath each of the cabin corners. Using this controller, which minimizes cabin heave-, roll-, and pitch accelerations, the low frequent road induced vibrations can be effectively suppressed. However, it remains unclear how the working space requirements are affected. Furthermore, the intrinsic assumption that the chassis motions are not influenced by the active suspension is questionable.

Given the relative novelty of the quarter truck model and variable geometry actua-

tor, there are a large number of questions to be answered. In this chapter the following are addressed. Given the quarter truck heave model, including an idealized variable geometry actuator (no actuator dynamics):

1. Which type of controller/control structure provides the best performance? And how is this affected by the choice of the actuator and passive secondary suspension elements?
2. What is the performance potential when using (road) condition dependent control gains in comparison to a fixed gain setting?
3. How much can the suspension performance be improved with respect to the passive setting? What is the energy cost?

A multi-objective two-norm performance criterion is defined, which depends on driver comfort, working space-, and energy requirements. Although nonlinear controllers may give better results, only linear control strategies are considered to limit the complexity of the problem. It is shown that the full state feedback LQ controllers provide the best performance for the quarter truck heave model. However, near optimal results can be obtained with output feedback controllers, which adopt some of the single mass optimal controller characteristics. Herein, the optimal control strategy is greatly influenced by the chosen actuator type and energy cost criterion. While the performance potential of fixed gain controllers seems to be limited to a 16 – 28% comfort enhancement with respect to the passive design, the potential of road dependent controllers is expected to be significantly larger.

Furthermore, state estimation is needed as not all of the state components, required for the state- or output feedback, are measurable in practice. Using a four sensor setup in combination with a Kalman filter, it is shown that the resulting LQG controller obtains performance levels that are very close to those obtained with the optimal LQ controller. Moreover, it is illustrated that while some passive damping may be desirable in parallel to the variable geometry actuator, from an energy point of view; the passive vertical stiffness should ideally be zero.

The outline of this chapter is as follows. First, the suspension of the single mass cabin model is optimized to obtain some interesting analytic results. Using this as background, the optimal quarter truck LQ and LQG controllers are developed in Section 6.4. Finally, in Section 6.5 the performance potential of gain-scheduled/condition dependent controllers is evaluated.

6.2 One DOF quarter car optimal control

The very first analytic exercises in optimal suspension control date back to the late 1960's and early 1970's. The model of popular choice had a single degree of freedom and was used to obtain interesting insights, some of which are shortly addressed in

this section. This elementary model is also used to evaluate the effect of the frequency dependent comfort weighting (Figure 1.4) on the optimal control solution.

6.2.1 Background

Consider the one DOF model (Figure 3.2), with $c_s = d_s = F_d = 0$. In that case, with $\underline{x} = [x_1, x_2]^T = [z_c - z_r, \dot{z}_c]^T$, the equations of motion can be written as

$$\begin{aligned}\dot{x}_1 &= x_2 - w \\ \dot{x}_2 &= m_c^{-1} F_{act} = u.\end{aligned}\tag{6.1}$$

Herein, $w = \dot{z}_r$ can be assumed to be a zero mean Gaussian distributed (white noise) disturbance, see Section 3.2.2.

In Hrovat (1997), the optimal suspension design problem for this system - taking the rms cabin acceleration and suspension stroke as sole performance criteria - is given by

$$\min J_A = \int_0^\infty (x_1^2 + r u^2) dt,\tag{6.2}$$

with r the control weight. Interestingly, the control effort and suspended mass accelerations are covered by a single term in the objective function. For this case, the Linear Quadratic (LQ) optimal control acceleration can be calculated analytically to be

$$u_{LQ}^A = -r^{-1/2} x_1 - \sqrt{2} r^{-1/4} x_2,\tag{6.3}$$

which corresponds to a combination of a spring and a skyhook damper with dimensionless damping coefficient $\zeta = 0.707$.

Alternatively, in Hrovat and Hubbard (1981) and Hrovat (1997), the case is considered where the jerk of the suspended mass is included in the control problem as an additional comfort measure:

$$\min J_B = \int_0^\infty (x_1^2 + r_1 u^2 + r_2 \dot{u}^2) dt.\tag{6.4}$$

It should however be noted, that when the suspension is controlled by a variable geometry actuator, the energy requirements of the suspension follow the relation $P_{act} \sim \dot{F}_{act}$, see (4.11) and Figure 5.9. Consequently, this control problem can also be considered to be a more appropriate formulation for the system actually under consideration. The analytic solution to this problem takes the form

$$\dot{u}_{LQ}^B = -r_2^{-1/2} x_1 - \sqrt{2f} r_2^{-1/2} x_2 - r_2^{-1/2} f x_3,\tag{6.5}$$

where $x_3 = u$ and

$$f^4 - 2r_1 f^2 - 8r_2 f + r_1^2 = 0.\tag{6.6}$$

Two special cases are of interest. The first is the case where $r_2 \rightarrow 0$, so jerk is not weighted. In this case it can be shown that the optimal control solution of (6.3) is

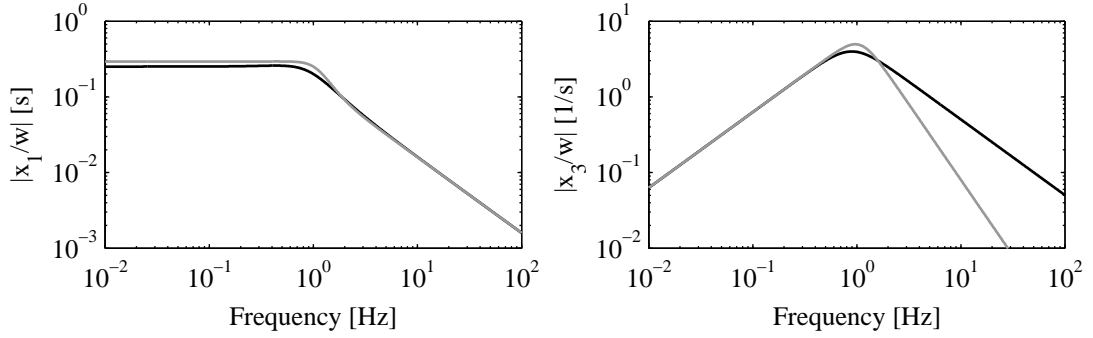


Figure 6.1: Comparison LQ optimal control with (grey) and without (black) jerk weighting. Transfer function from disturbance to suspension displacement (left) and suspended mass acceleration (right).

obtained. For the second case $r_1 = 0$, the acceleration is not weighted. For this case the optimal control acceleration can be shown to be

$$\dot{u}_{LQ}^B = -r_2^{-1/2}x_1 - 2r_2^{-1/2}x_2 - 2r_2^{-1/2}x_3. \quad (6.7)$$

Substitution of either $x_3 = u$ or $x_3 = \dot{x}_2$ shows that

$$\begin{aligned} u_{LQ}^B &= \frac{-r_2^{-1/2}x_1 - 2r_2^{-1/2}x_2}{s + 2r_2^{-1/2}} \\ &= -r_2^{-1/2} \int_0^T x_1 dt - 2r_2^{-1/3} \int_0^T x_2 dt - 2r_2^{-1/6} x_2, \end{aligned} \quad (6.8)$$

where s is the Laplace variable. The latter corresponds to a configuration with a leveling device, a skyhook spring, and a skyhook damper with dimensionless damping coefficient $\zeta = 0.5$, see Hrovat and Hubbard (1981). Note that the top expression in (6.8) is also equivalent to a spring and skyhook damper combined with a low-pass filter. A comparison of the two optimal control strategies where the weights are tuned such that the main part of the characteristics overlap, is given in Figure 6.1.

The jerk optimal control strategy (6.8) significantly improves the rms jerk or, when using a variable geometry actuator, energy requirements. Remarkably, the degeneration in rms working space and acceleration is relatively small with respect to the acceleration optimal control strategy (6.3), see Hrovat and Hubbard (1981). Moreover, the relatively fast load leveling characteristic is desirable as there is no steady-state offset due to external disturbances ($F_d \neq 0$) or weight changes.

However, using this controller a steady-state displacement error does remain for constant $w = \dot{z}_r \neq 0$, see Figure 6.1 (left), which is the result of the skyhook spring. Furthermore, practical implementation may prove problematic as the estimation of the absolute suspended mass movement is, similar to the absolute suspended mass velocity, sensitive to measurement noise in the lower frequency ranges (inducing drift).

There is one more question of interest. That is: how does the optimal control solution change if the road disturbance is known? In the case that the road disturbance is known, the control problem changes from a LQ to a LQ-tracking problem. The model

can be written as

$$\dot{\underline{x}} = A\underline{x} + B\underline{u}, \quad (6.9)$$

with \underline{x} the state vector and \underline{u} the control input. Assuming an infinite control horizon, the performance can be written in the form

$$\min J_k = \int_0^\infty [(C\underline{x} - \underline{r})^T Q (C\underline{x} - \underline{r}) + \underline{u}^T R \underline{u}] dt, \quad (6.10)$$

with $\underline{y} = C\underline{x}$ the performance variables, \underline{r} the known reference, and $Q \geq 0$, $R > 0$ the symmetric weighting matrices. The optimal affine control for this problem is given by, Lewis and Syrmos (1995),

$$\underline{u} = -K\underline{x} + R^{-1}B^T v. \quad (6.11)$$

It consists of a feedback part $-K\underline{x}$, which is independent of the reference \underline{r} , and a feedforward or preview part $R^{-1}B^T v$, which is a function of the reference and is backwards computed in time:

$$-\dot{v} = (A - BK)^T v + C^T Q r. \quad (6.12)$$

It is interesting to observe that as the feedback part is independent of the reference, the optimal feedback controller is the same for the cases with unknown and known road disturbances. Furthermore, as the feedforward part is computed backwards in time, its main effect is an anticipatory motion which lowers the feedback induced accelerations. In Huisman (1994), it is concluded that if the preview time is more than 0.13 seconds, the performance of the primary suspension of a heavy-duty truck can be significantly improved. However, it remains an open question how to obtain this preview information in practice. The inclusion of preview control is not further considered in this thesis.

6.2.2 Effect of the ISO comfort weighting

For the synthesis of optimal suspension controllers in literature, the suspended mass acceleration is often used to determine driver comfort. However, as is discussed in Section 1.4.1, the ISO weighted suspended mass acceleration is a more reliable comfort measure. So, the question arises whether or not this influences the previously obtained optimal control solutions.

To evaluate the effect of the inclusion of the ISO comfort weighting, the LQ controller synthesis is repeated with the cost indices

$$\begin{aligned} \min J_1^* &= \int_0^\infty (x_1^2 + r_1 y_{iso}^2 + r_2 u^2) dt \\ \min J_2^* &= \int_0^\infty (x_1^2 + r_1 y_{iso}^2 + r_2 \dot{u}^2) dt, \end{aligned} \quad (6.13)$$

for the cases with the control input as a function of acceleration and jerk respectively. Herein, $y_{iso} = W_{iso} \dot{x}_2$ is the ISO weighted suspended mass acceleration, with W_{iso} the

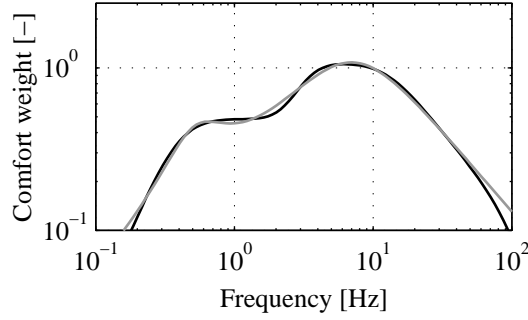


Figure 6.2: ISO 2631 weighting curve for the vertical acceleration (black), ISO 2631-1 (1997), and the fourth order approximation (grey), Zuo and Nayfeh (2007).

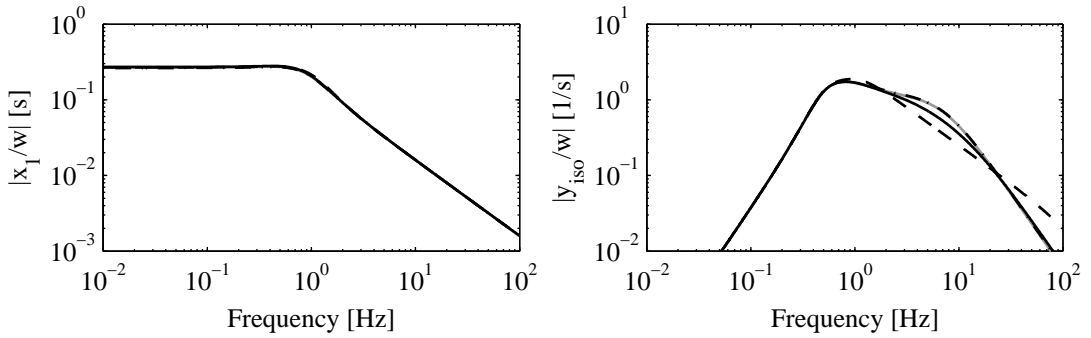


Figure 6.3: LQ optimal controller evaluation for the case without jerk weighting. Comparison without (grey) and with ISO weighted acceleration in the control problem, for: $r_1 = r_2$ (solid black); increased input weighting $r_2 = 100r_1$ (dash-dotted); and decreased input weighting $r_2 = r_1/100$ (dashed). Transfer function from disturbance to suspension displacement (left) and ISO weighted suspended mass acceleration (right).

reduced (fourth) order approximation of the original (ninth order) ISO weighting filter, presented in Zuo and Nayfeh (2007). It is given by

$$W_{iso}(s) = \frac{81.89s^3 + 796.6s^2 + 1937s + 0.1446}{s^4 + 80.00s^3 + 2264s^2 + 7172s + 21196}, \quad (6.14)$$

and depicted in Figure 6.2. The reduced order approximation is chosen to limit the computational complexity.

The case where the control input is governed by the suspended mass acceleration (J_1^*) is considered first. It should be noted that while, in (6.2), comfort and control input are specified in the same criterion, this is no longer the case with the updated comfort measure. Consequently, there are now two weights r_1 and r_2 that need to be specified. Moreover, due to the higher level of complexity, a numerical solution of the control problem is preferable.

The transfer functions, when using the found LQ optimal controller, are given in Figure 6.3 for three different control weights (r_2). For each solution, the comfort weight r_1 is chosen such that the working space requirements remain the same. It can be seen, that when the control weight is much higher than the comfort weight, the classic skyhook controller is recovered. For decreasing control weight, the ISO weighted

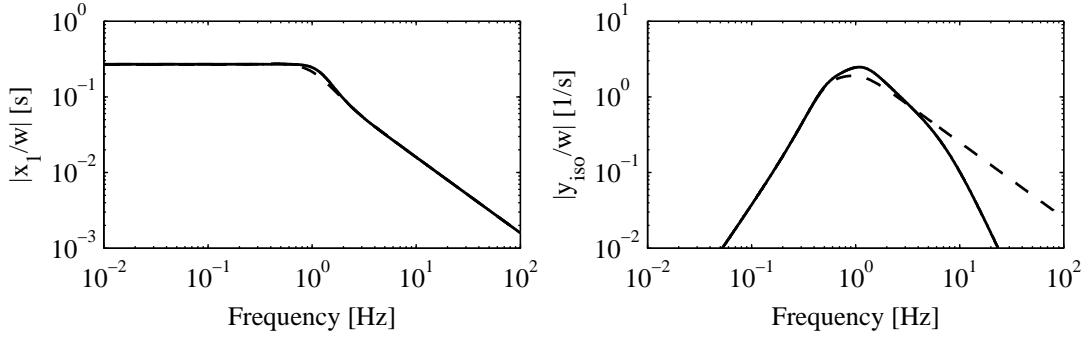


Figure 6.4: LQ optimal controller evaluation for the case with jerk weighting. Comparison without (grey) and with ISO weighted acceleration in the control problem, for: $r_1 = r_2$ (solid black); increased control weighting $r_2 = 1.10^{10}r_1$ (dash-dotted); and decreased control weighting $r_2 = 1.10^{-10}r_1$ (dashed). Transfer function from disturbance to suspension displacement (left) and ISO weighted suspended mass acceleration (right).

accelerations between 2 and 20 Hz are reduced. However, when the control weight is reduced to values significantly lower than the comfort weight, the high frequent ISO weighted accelerations gain influence.

In the second case, the control input is governed by the suspended mass jerk (J_2^*). Again, three different control weights are compared and the comfort weight is used to tune the working space requirements to the same level. The resulting transfer functions are given in Figure 6.4. It can be seen, that the optimal control solution hardly changes for input weights in the range $r_2 \in [1, 1.10^{10}]$, and gives results that greatly resemble that of the problem without the ISO weighting filter (6.8). The optimal solution only changes significantly in the case that the input weighting is chosen to be very small. For this case, the normalized ISO weighted rms acceleration

$$J_c = \sqrt{\int_{\omega_{\min}}^{\omega_{\max}} |H_{y_{iso}/w}(\omega)|^2 d\omega}, \quad (6.15)$$

is reduced by 18% with respect to the other two solutions, but the control jerk is increased.

So, the difference between using either the ISO weighted- or the unweighted suspended mass acceleration as performance measure appears to be relatively small for the one DOF system. Consequently, the use of the unweighted suspended mass acceleration as comfort measure is thought to be a good starting point when synthesizing the optimal quarter truck cabin controller.

6.3 Quarter truck LQ(G) cabin controller design

As is illustrated in section 3.2.3, there are significant differences between the dynamics of 1 and 4 DOF quarter truck models. In this section it is shown that as a consequence, the LQ optimal control solutions for the 1 DOF model, as given in the previous section,

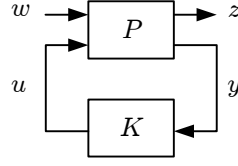


Figure 6.5: General control problem configuration (no model uncertainty).

differ from the LQ optimal control solutions for the 4 DOF model. However, the practical implementation may be problematic, as the LQ optimal control solution for the quarter truck heave model requires full state knowledge. Therefore, the possibilities for reduced order implementations as well as state estimation are also examined.

6.3.1 Quarter truck control problem

The control problem can be written in the generalized or standard plant formulation, see (Skogestad and Postlethwaite, 2005, Chapter 3.8) and Figure 6.5. Herein, w are the (weighted) exogenous inputs, z are the (weighted) performance outputs, u are the control signals and y are the sensed outputs. The exogenous inputs w are assumed to be zero mean, gaussian distributed (white noise), uncorrelated signals. Furthermore, all w, z, u, y are scaled to facilitate the choice of the weights and avoid numeric solver issues. The problem is to find a controller K , which based on y generates a control signal u , that minimizes the influence of w on z .

For the quarter truck model as depicted in Figure 3.1, with no passive secondary suspension elements ($c_s = 0, d_s = 0$) and not considering the disturbance force ($F_d = 0$)

$$w = w_1 = [\dot{z}_r/w_{max}]. \quad (6.16)$$

Furthermore, similar to the one DOF case described in the previous section, the performance outputs are given by

$$\underline{z} = [(z_c - z_f)/s_{max}, u]^T, \quad (6.17)$$

where u can be either the normalized control force or control force variation, depending on the actuator type. For normalization, the maximum values are chosen to be $w_{max} = 0.1$ [m/s], $s_{max} = 0.04$ [m], $a_{max} = 2$ [m/s²] the maximum acceleration, and $j_{max} = 100$ [m/s³] the maximum jerk. Assuming full state knowledge, the standard plant P can be written as

$$P : \begin{cases} \dot{\underline{x}} = A\underline{x} + Bu + Gw \\ \underline{y} = \underline{x} \\ \underline{z} = E\underline{x} + Nu. \end{cases} \quad (6.18)$$

The two special cases of Section 6.2 are again considered: the case with acceleration minimization and the case with jerk minimization.

Control force minimization

In the first case, the normalized control input is given by $u = F_{act}/(m_c a_{max})$. As there are no passive secondary suspension elements, the comfort performance criterion (suspended mass acceleration) is included in the control effort, similar to Section 6.2.1. Choosing $\underline{x} = [z_a - z_r, z_e - z_f, z_f - z_a, z_c - z_f, \dot{z}_a, \dot{z}_e, \dot{z}_f, \dot{z}_c]^T$, the various matrices in (6.18) can be determined to be

$$\begin{aligned} A &= \begin{bmatrix} 0_4 & A_{12} \\ -M_z^{-1}K_z^* & -M_z^{-1}D_z \end{bmatrix} & B &= \begin{bmatrix} \underline{0}_6 \\ -a_{max} \frac{m_c}{m_f} \\ a_{max} \end{bmatrix} & N &= \begin{bmatrix} 0 \\ 1 \end{bmatrix} \\ A_{12} &= \begin{bmatrix} 1 & 0 & 0 & 0 \\ 0 & 1 & -1 & 0 \\ -1 & 0 & 1 & 0 \\ 0 & 0 & -1 & 1 \end{bmatrix} & E &= \begin{bmatrix} 0_{[3 \times 2]} \\ [1/s_{max}, 0] \\ 0_{[4 \times 2]} \end{bmatrix}^T & G &= \begin{bmatrix} -w_{max} \\ \underline{0}_7 \end{bmatrix}, \end{aligned} \quad (6.19)$$

with $\underline{0}_l$ a zero vector with length l , 0_4 a $[4 \times 4]$ zero matrix and D_z, M_z as given in (3.2) where $c_s = d_s = 0$. Furthermore, the modified stiffness matrix is given by

$$K_z^* = \begin{bmatrix} c_t & 0 & -c_p & 0 \\ 0 & c_e & 0 & 0 \\ 0 & -c_e & c_p & -c_s \\ 0 & 0 & 0 & c_s \end{bmatrix}. \quad (6.20)$$

Control force variation minimization

In the second case, the normalized control input is given by $u = \dot{F}_{act}/(m_c j_{max})$, and is therefore directly related to the secondary suspension jerk. Choosing $\underline{x} = [z_a - z_r, z_e - z_f, z_f - z_a, z_c - z_f, \dot{z}_a, \dot{z}_e, \dot{z}_f, \dot{z}_c, F_{act}/m_c]^T$, the matrices in (6.18) are given by

$$\begin{aligned} A &= \begin{bmatrix} 0_4 & A_{12} \\ -M_z^{-1}K_z^* & -M_z^{-1}D_z \end{bmatrix} \begin{bmatrix} \underline{0}_4 \\ \underline{0}_2 \\ -m_c/m_f \\ 1 \\ 0 \end{bmatrix} & B &= \begin{bmatrix} \underline{0}_6 \\ j_{max} \end{bmatrix} & N &= \begin{bmatrix} 0 \\ 1 \end{bmatrix} \\ A_{12} &= \begin{bmatrix} \underline{0}_4^T & \underline{0}_4^T \\ 1 & 0 & 0 & 0 \\ 0 & 1 & -1 & 0 \\ -1 & 0 & 1 & 0 \\ 0 & 0 & -1 & 1 \end{bmatrix} & E &= \begin{bmatrix} 0_{[3 \times 2]} \\ [1/s_{max}, 0] \\ 0_{[4 \times 2]} \end{bmatrix}^T & G &= \begin{bmatrix} -w_{max} \\ \underline{0}_8 \end{bmatrix}. \end{aligned} \quad (6.21)$$

Although the cabin acceleration is not included in the cost function using this problem description, it will be affected in a similar way as is shown for the single mass model. Furthermore, by minimizing the control force variation, the resulting optimal control strategy can be seen as the energy optimal solution for the quarter truck model with variable geometry actuator.

6.3.2 Quarter truck optimal control solution

The two posed control problems are solved numerically using LQ optimization. Herein, the problem can be written as

$$\min J = \int_0^\infty (z_1^2 + ru^2)dt, \quad (6.22)$$

where the choice of the performance weight r remains to be determined. With the knowledge that the power spectral density of the normalized secondary suspension travel is given by

$$\Phi_{z_1}(\omega) = |H_{z_1/w}(\omega)|^2 \Phi_w(\omega), \quad (6.23)$$

with $H_{z_1/w}(\omega)$ the frequency response function from the normalized road disturbance to the normalized secondary suspension travel,

$$J_{ws} = \sqrt{\int_{\omega_{\min}}^{\omega_{\max}} |H_{z_1/w}(\omega)|^2 d\omega} \quad (6.24)$$

can be seen as the normalized rms value of the secondary suspension travel. The LQ performance weight is chosen such that the working space requirements (J_{ws}) resemble those of the validated passive configuration of Chapter 3.

Control force minimization

For the first case, where the control force is minimized, the results are given in Figure 6.6. When considering the working space (left) it can be seen that both the full state feedback and the single mass LQ optimal solution require more working space for low frequency road disturbances and disturbances at the engine/chassis resonance mode (around 15 Hz). Increasing the working space weighting does not change this; it shifts the complete low frequency characteristic down, but does not change the general shape. Nevertheless, the rms working space requirements computed by (6.24) are relatively close to those of the passive configuration, allowing a fair comparison between the resulting accelerations.

Comparing the transfer function from the road disturbance to the cabin accelerations as given in Figure 6.6 (right), the benefit of the full state feedback LQ optimal solution is clear. Apart from the anti-resonance around 10 Hz, the full state feedback controller reduces the transmissibility in the frequency range of 0.5 – 30 Hz, which is the region where road induced vibrations have the highest influence on driver comfort. The normalized rms accelerations are reduced by 17% with respect to the passive setting, but this is without the ISO weighting. With the ISO weighting the reduction will be larger.

The implementation of the single mass LQ optimal control strategy (6.3), with the spring placed between the cabin and the frame, however, seems to be far less effective. Below 10 Hz, it does not significantly lower road induced cabin accelerations. On the other hand, a reduction can be observed above 10 Hz, due to the fact that the passive

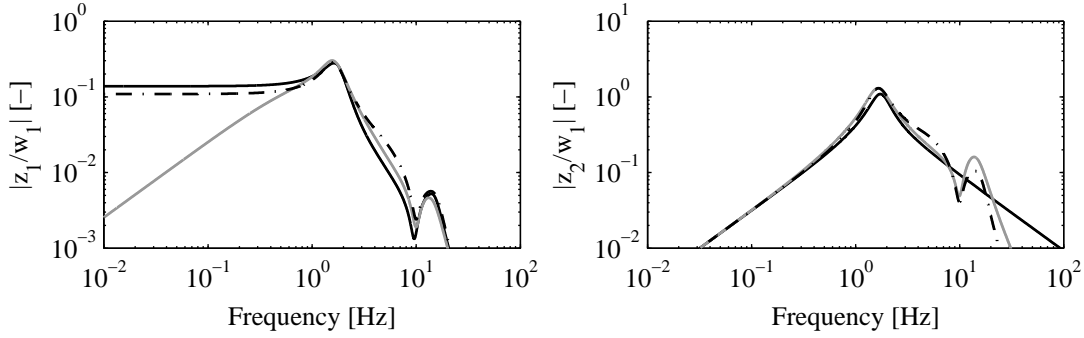


Figure 6.6: LQ optimal controller quarter truck model for control force minimization: validated passive suspension (grey); full state feedback (black); and single mass solution (dash-dotted). Transfer function from normalized road disturbance to normalized suspension displacement (left) and normalized suspended mass acceleration (right).

damper between the chassis and cabin has been removed. Using this configuration, the normalized rms accelerations actually increase by 1%.

On a side note, it is important to realize that this is also an important result for semi-active suspensions. In literature, these are often controlled using a two-state skyhook strategy. This strategy delivers the skyhook force when the passivity constraint is met, and a zero force if this is not the case. For a semi-active cabin suspension, a switched LQ or LPV/LQ controller will give far better performance, see van Iersel (2010) for more information.

Control force variation minimization

For the case where the control force variation is minimized, the resulting transfer functions are shown in Figure 6.7. When considering the working space (left) it can again be seen that both the full state feedback and the single mass LQ optimal solution require more working space for low frequency road disturbances and disturbances at the engine/chassis resonance mode (around 15 Hz). Still, the rms working space requirements are very close to those of the passive configuration, again allowing a fair comparison between the resulting accelerations.

Comparing the transfer function from the road disturbance to the cabin accelerations in Figure 6.7 (right), it can be seen that the full state feedback optimal LQ solution is less sensitive to road induced vibrations above 4 Hz than the passive suspension. Furthermore, its performance above 10 Hz is actually better than that of the full state feedback force optimal LQ solution, see Figure 6.6 (right). This despite the fact, that the cabin acceleration is not explicitly included in the performance criterion. However, the influence of the 2 Hz resonance is suppressed less. Consequently, the normalized rms cabin accelerations are not decreased using this setting with respect to the passive configuration. Still, the ISO weighted accelerations will be reduced more.

On the other hand, the implementation of the single mass LQ optimal control strategy (6.8), with the leveling device placed between the cabin and the frame, just

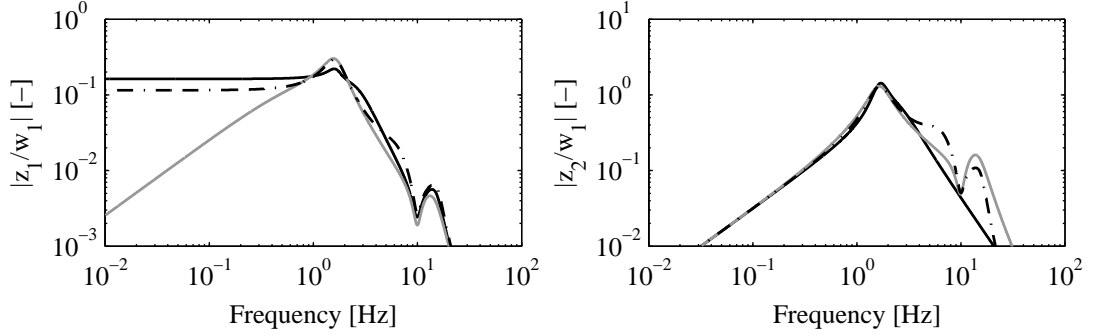


Figure 6.7: LQ optimal controller quarter truck model for control force variation minimization: validated passive suspension (grey); full state feedback (black); and single mass solution (dash-dotted). Transfer function from normalized road disturbance to normalized suspension displacement (left) and normalized suspended mass acceleration (right).

performs poorly. In the frequency range 2 – 7 Hz, the cabin accelerations induced by the road disturbances are higher for the controlled suspension than for the passive suspension. The gain at higher frequencies is not sufficient to warrant this controller implementation.

6.3.3 Quarter truck output feedback

In the previous subsection it is shown that the single mass LQ optimal solutions do not perform significantly better than the validated passive suspension setting. The full state feedback LQ optimal solutions, on the other hand, do show potential. The limiting factor is, however, the requirement that the state \underline{x} needs to be known. In this subsection it is shown that the full state feedback optimal LQ performance characteristics can almost be obtained, using limited state knowledge. Furthermore, it is illustrated that these proposed output feedback controllers show a remarkable resemblance with the single mass LQ optimal solutions.

Control force minimization

The full state feedback LQ force optimal solution, as depicted in Figure 6.6, has feedback control gains

$$\begin{aligned} K_{LQ}^F &= [k_1^F, k_2^F, k_3^F, k_4^F, k_5^F, k_6^F, k_7^F, k_8^F]^T \\ &= [58.3, -8.4, 41.1, 70.1, -0.17, -1.9, -1.3, 7.3]^T. \end{aligned} \quad (6.25)$$

With the knowledge that the state is given by $\underline{x} = [z_a - z_r, z_e - z_f, z_f - z_a, z_c - z_f, \dot{z}_a, \dot{z}_e, \dot{z}_f, \dot{z}_c]$, it becomes clear that not all state components are equally important. When omitting the relatively smaller gains, the controller takes the form

$$u = -k_1^F(z_a - z_r) - k_3^F(z_f - z_a) - k_4^F(z_c - z_f) - k_8^F\dot{z}_c. \quad (6.26)$$

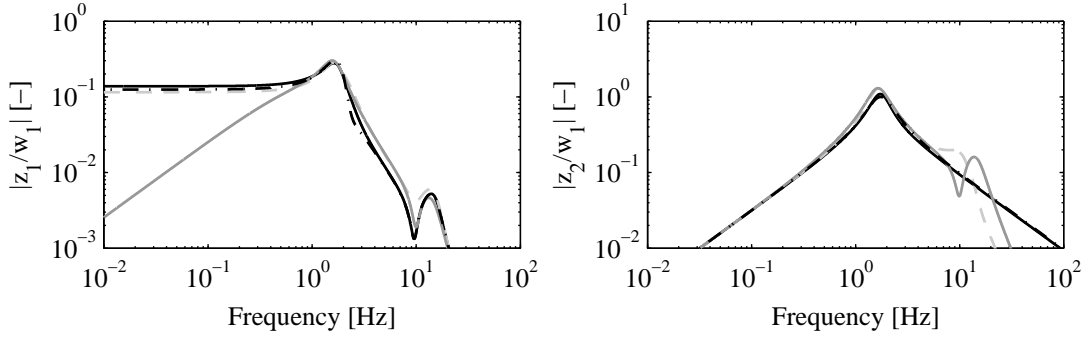


Figure 6.8: LQ optimal controller quarter truck model for control force minimization: validated passive suspension (grey); full state feedback (black); output feedback u_1^F (dash-dotted); and u_2^F (dashed grey). Transfer function from normalized road disturbance to normalized suspension displacement (left) and normalized suspended mass acceleration (right).

Furthermore, seeing that k_1 , k_3 and k_4 are roughly of the same size, the following output feedback structure is proposed

$$u_1^F = -k_{11}^F(z_c - z_r) - k_{81}^F \dot{z}_c, \quad (6.27)$$

where k_{11}^F and k_{81}^F are chosen such that the full state feedback LQ characteristics are best approximated. Remarkably, this controller structure can again be seen as a spring and skyhook damper, just as was the case for the single mass LQ optimal solution. Here however, the spring is placed between the road and the cabin.

If the state components x_1, x_3 and x_4 can be measured, then $z_c - z_r$ can be determined. However, in practice the tyre deflection measurement $x_1 = z_a - z_r$ may be expensive and/or difficult to estimate accurately. For that reason, the following output feedback controller is also evaluated

$$u_2^F = -k_{12}^F(z_c - z_a) - k_{82}^F \dot{z}_c. \quad (6.28)$$

The characteristics, when using either of these two output feedback controllers, are given in Figure 6.8.

It can be observed that the output feedback controller (6.27) can be tuned to closely resemble the optimal full state feedback characteristic. Furthermore, the alternative (6.28) can also closely resemble these characteristics up to approximately 6 Hz. However, as the axle dynamics are not included, the 10 Hz axle resonance deteriorates performance in the region 6 – 15 Hz.

Control force variation minimization

The full state feedback LQ jerk optimal solution, as depicted in Figure 6.7, has feedback control gains

$$\begin{aligned} K_{LQ}^J &= [k_1^J, k_2^J, k_3^J, k_4^J, k_5^J, k_6^J, k_7^J, k_8^J, k_8^J]^T \\ &= [33.9, 1.3, 24.3, 30.6, -0.08, -0.98, -0.68, 3.71, 0.30]^T. \end{aligned} \quad (6.29)$$

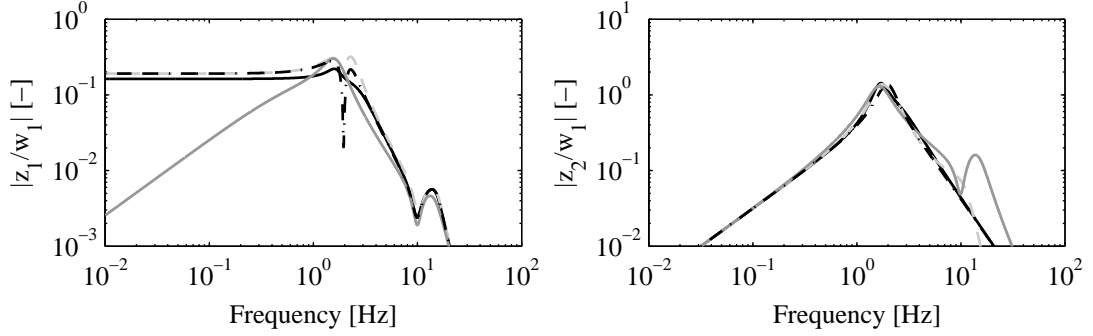


Figure 6.9: LQ optimal controller quarter truck model for control force variation minimization: validated passive suspension (grey); full state feedback (black); output feedback u_1^F (dash-dotted); and u_2^F (dashed grey). Transfer function from normalized road disturbance to normalized suspension displacement (left) and normalized suspended mass acceleration (right).

With the knowledge that the state is given by $\underline{x} = [z_a - z_r, z_e - z_f, z_f - z_a, z_c - z_f, \dot{z}_a, \dot{z}_e, \dot{z}_f, \dot{z}_c, F_{act}/m_c]$, it again becomes clear that not all state components are equally important. When omitting the relatively smaller gains, the controller takes the form

$$u = \frac{\dot{F}_{act}}{m_c j_c^{max}} = -k_1^J(z_a - z_r) - k_3^J(z_f - z_a) - k_4^J(z_c - z_f) - k_8^J \dot{z}_c - k_9^J \frac{F_{act}}{m_c}. \quad (6.30)$$

Furthermore, as k_1 , k_3 and k_4 are roughly of the same size, the following output feedback structure is proposed

$$u_1^J = -k_{11}^J(z_c - z_r) - k_{81}^J \dot{z}_c - k_{91}^J \frac{F_{act}}{m_c}. \quad (6.31)$$

Substituting $F_{act} = m_c \ddot{z}_c$, gives

$$\frac{F_{act}}{m_c j_c^{max}} = -k_{11}^J \int_0^t (z_c - z_r) dt - k_{81}^J \dot{z}_c - k_{91}^J \dot{z}_c, \quad (6.32)$$

which can again be seen as a leveling action with a skyhook spring and skyhook damper. This is similar to the single mass LQ optimal solution, but with the leveling action taking place between the road and the cabin.

As the measurement of $x_1 = z_a - z_r$ may not be available in practice, the output feedback controller

$$u_2^J = -k_{12}^J(z_c - z_a) - k_{82}^J \dot{z}_c - k_{92}^J \frac{F_{act}}{m_c} \quad (6.33)$$

is also evaluated. The characteristics, when using either of these two output feedback controllers, are given in Figure 6.9.

Clearly, the same observations can be made as for the case where the control force is minimized. Both output feedback controllers can be tuned to closely resemble the optimal characteristics, although when applying (6.33) the performance deteriorates somewhat in the frequency range 6 – 20 Hz.

6.3.4 Quarter truck state estimation

As already mentioned, the LQ optimal controller requires full state knowledge, but not all the state components can/will be measured in practice. From the output feedback evaluation given in Section 6.3.3 it is known that especially knowledge of $z_c - z_r$ and \dot{z}_c is required. While this knowledge is useful for sensors placement, it will be difficult to find (cheap) sensors that can directly and accurately measure these signals. However, there is an alternative.

From Chapter 3 it is known that the quarter truck model gives a fairly accurate description of the vertical dynamics. Consequently, in combination with the available measurements, the model can be used to estimate those state components that cannot be sensed directly. The optimal estimator for linear time invariant systems is the Kalman filter. Furthermore, the combination of this estimator and the LQ optimal controller is called a Linear Quadratic Gaussian (LQG) controller, see for example Skogestad and Postlethwaite (2005, section 9.2) or Green and Limebeer (1995, Chapter 5) for more information. It is important to note that while both the LQ optimal controller and Kalman estimator have good robustness characteristics, there are no robustness guarantees for the LQG controller. Therefore, it is always important to evaluate the robustness properties of the designed LQG controllers.

The question arises how the implementation of the Kalman filter with limited sensors influences the performance potential of the active cabin suspension. To investigate this, the system description with the force variation as control input (6.18, 6.21) is considered in the absence of passive suspension elements ($c_s = d_s = 0$).

Two different sensor configurations are used, the first having two and the second having four sensors. More precisely,

$$\begin{aligned} \underline{y}_2 &= [z_c - z_f, \ddot{z}_c]^T \\ &= C_2 \underline{x} + \underline{v}_2 \\ \underline{y}_4 &= [z_c - z_f, \ddot{z}_c, z_f - z_a, \ddot{z}_a]^T \\ &= C_4 \underline{x} + \underline{v}_4, \end{aligned} \tag{6.34}$$

with $\underline{v}_2, \underline{v}_4$ the measurement noise. The sensor choice is based on the observations of Section 6.3.3 and the idea to measure “as closely as possible” to those state components that have the largest influence on the controller.

Kalman filter

The Kalman filter can be designed independently of the controller as a result of the well known separation principle. With the dynamics of the system given by (6.18)

$$\dot{\underline{x}} = A\underline{x} + Bu + Gw,$$

and the measurements (6.34). The noise signals \underline{v} and w are assumed to be independent and gaussian distributed (white noise).

The dynamics of the state estimate \hat{x} can be described by

$$\dot{\hat{x}} = A\hat{x} + Bu + L(\underline{y} - C\hat{x}), \quad (6.35)$$

where $[\underline{y} = \underline{y}_2, C = C_2]$ or $[\underline{y} = \underline{y}_4, C = C_4]$ depending on the sensor configuration. The optimal choice of L , minimizing the variance of $x - \hat{x}$, is given by

$$L = YC^TV^{-1}, \quad (6.36)$$

with $Y = Y^T > 0$ the unique positive semi-definite solution of the algebraic Riccati equation

$$YA^T + AY - YC^TV^{-1}CY + GWG^T = 0. \quad (6.37)$$

Herein, V and W are positive definite weights, for which the covariance of the measurement and process noise is used respectively. A sufficient condition for existence of the optimal estimator gain is that the system is fully observable, i.e.,

$$\text{Rank } O = [C, CA, CA^2, \dots, CA^{n-1}]^T = n, \quad (6.38)$$

with n the number of state components in \underline{x} , Skogestad and Postlethwaite (2005, section 9.2). It can be shown that the quarter truck system as described by (6.18, 6.21, 6.34) is fully observable for both sensor configurations.

Estimator evaluation

From measurements at standstill, Spijkers (2008), of the experimental tractor semi-trailer as described in Chapter 2, it is known that the rms values of the sensor noise are approximately

$$\begin{aligned} \tilde{\underline{v}} &= [\tilde{v}_1, \tilde{v}_2, \tilde{v}_3, \tilde{v}_4]^T \\ &= [1.10^{-4} \text{ m}, 4.10^{-2} \text{ m/s}^2, 2.10^{-4} \text{ m}, 1.10^{-1} \text{ m/s}^2]^T. \end{aligned} \quad (6.39)$$

Choosing,

$$V = \begin{bmatrix} (\tilde{v}_1/s_{max})^2 & 0 & 0 & 0 \\ 0 & (\tilde{v}_2/a_{max})^2 & 0 & 0 \\ 0 & 0 & (\tilde{v}_3/s_{max})^2 & 0 \\ 0 & 0 & 0 & (\tilde{v}_4/a_{max})^2 \end{bmatrix} \quad Q = \begin{bmatrix} q_1^2 & 0 \\ 0 & q_2^2 \end{bmatrix}, \quad (6.40)$$

with $q_1 = 1$ [-], $q_2 = 0.01$ [-] the approximations of the normalized road velocity and control uncertainty respectively, the Kalman filter gains for the two and four sensor configuration can be determined.

To evaluate the characteristics of these two estimators, a special test case is considered for which w is not a white noise signal. The quarter truck model as described in (6.18, 6.21), including the validated passive cabin suspension, with no active elements ($u = 0$) starts with a zero road velocity ($w = 0$). After 1 second the vehicle reaches a

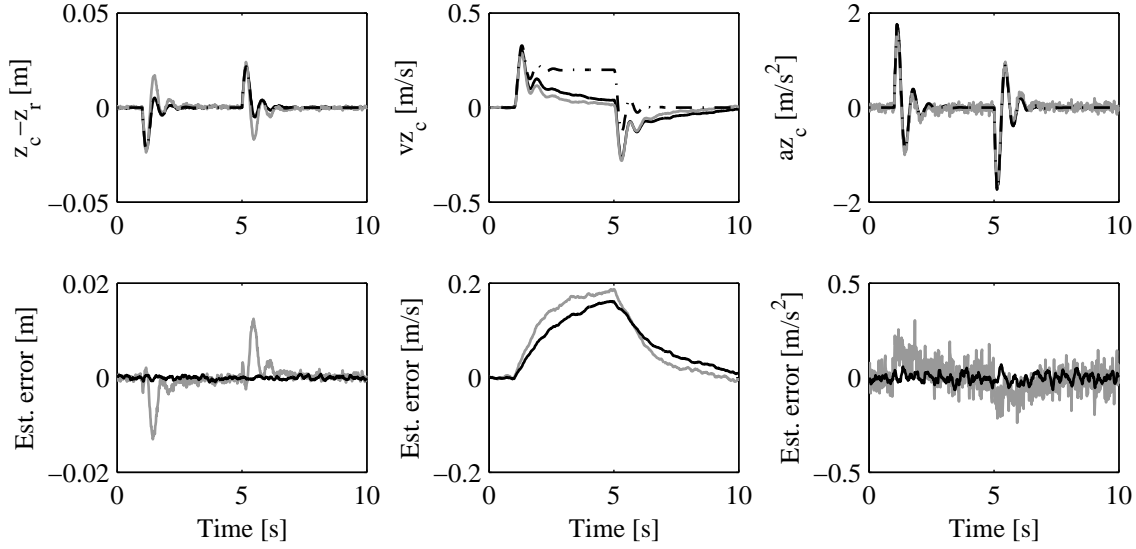


Figure 6.10: Kalman estimator evaluation using the quarter truck model, with validated passive suspension configuration, crossing a road slope: true signals (dash-dotted); four sensors (black); and two sensors (grey). Top: distance between cabin and road (left); cabin velocity (mid); and cabin acceleration (right). Bottom: estimation error of the responses shown in top.

slope and the road position starts to increase with a velocity of 0.2 m/s. Four seconds later the road levels again. The estimated state components that are known to be most critical for the LQ optimal controller implementation are given in Figure 6.10.

It can be seen that, while the cabin acceleration can be estimated accurately for both sensor configurations, the estimation of the cabin velocity is less precise. Effectively, the estimation of the cabin velocity can be seen as the time integral of the high-pass filtered cabin acceleration measurement. Herein, the high pass filter is needed to avoid integrator drift, but also results in an estimation error when driving on graded roads.

The estimation error of the two- and four sensor configuration, for the cabin velocity and acceleration, are similar. For the estimation of the relative displacement between cabin and road, on the other hand, the differences are more distinct. While both provide accurate steady-state estimates, the two-sensor estimation error is significantly larger under dynamic situations. The effects of these estimation errors on the closed-loop performance of the active cabin suspension are evaluated next.

LQG controller evaluation

When combining the quarter truck model (6.18, 6.21), LQ optimal full state feedback (6.29), and the optimal Kalman filter (6.35); the combined dynamics can be written as

$$\begin{bmatrix} \dot{\underline{x}} \\ \dot{\underline{x}} - \hat{\underline{x}} \end{bmatrix} = \begin{bmatrix} A - BK_{LQ}^J & BK_{LQ}^J \\ 0_9 & A - LC \end{bmatrix} \begin{bmatrix} \underline{x} \\ \underline{x} - \hat{\underline{x}} \end{bmatrix} + \begin{bmatrix} G & 0_{9 \times 4} \\ G & -L \end{bmatrix} \begin{bmatrix} w \\ v \end{bmatrix}. \quad (6.41)$$

The resulting transfer functions of the road velocity to the performance variables is given in Figure 6.11.

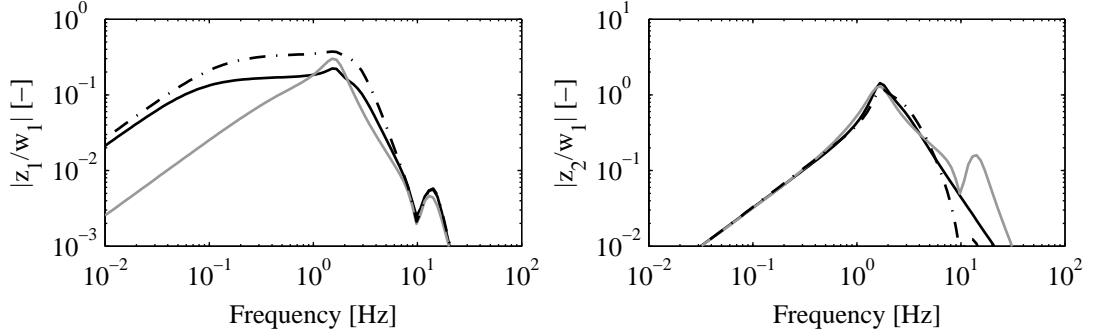


Figure 6.11: LQG optimal controller evaluation, quarter truck model, for the case with jerk weighting. Comparison validated passive suspension (grey), full state feedback LQG optimal solution with four sensors (black); and with two sensors (dash-dotted). Transfer function from normalized road disturbance to normalized suspension displacement (left) and normalized suspended mass acceleration (right).

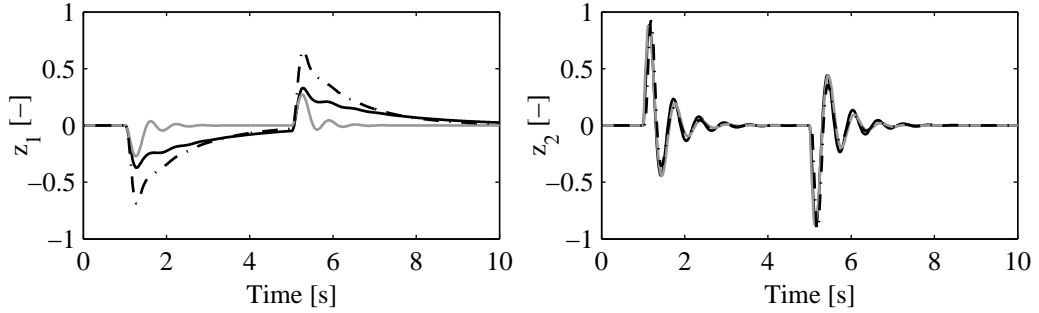


Figure 6.12: LQG optimal controller evaluation, quarter truck model, for the case with jerk weighting. Comparison validated passive suspension (grey), full state feedback LQG optimal solution with four sensors (black); and with two sensors (dash-dotted). Time response when crossing a road slope: normalized suspension displacement (left) and normalized suspended mass acceleration (right).

When comparing Figures 6.9 and 6.11, it can be seen that the performance of the LQG controller with four sensor configuration is relatively close to that of the LQ controller with full state knowledge. One apparent difference is the low frequent working space requirement, which is lower for the LQG controller as a result of the estimation error on the cabin position for low frequent road inputs, see Figure 6.10. The performance of the two sensor configuration, on the other hand, is significantly poorer. Due to the significant error in the cabin - road displacement estimation, the working space requirements increase. Furthermore, the high frequent characteristics of the transfer between the road and cabin accelerations also changes, similar to the case of the output feedback u_2^J where the axle road displacement is unknown, see Figure 6.9.

Finally, both LQG controllers are evaluated in the time-domain for the earlier described special test-case with low-frequent road disturbance: the quarter truck model crosses a four second road slope. The response of the two performance variables is shown in Figure 6.12. As expected from the results of Figure 6.11, the suspended mass accelerations are similar for both LQG controlled systems and the validated passive

Table 6.1: Suspension performance for low frequent road input.

Configuration	$\max y_1$ [m]	a_v [m/s ²]	VDV [m/s ²]
Passive	0.271	0.174	0.334
Four sensor LQG	0.372	0.175	0.335
Two sensor LQG	0.687	0.167	0.337

suspension, while the suspension travel for the three systems differs far more. Especially the maximum suspension displacement for the two sensor configuration is considerable. So, this type of low frequent road disturbance is not favorable for the LQG controllers. The normalized maximum suspension displacements, normalized rms values of the ISO weighted accelerations a_v (1.1), and normalized vibration dose values VDV (1.3), are given in Table 6.1.

Overall, it can be concluded that while the performance degradation from LQ to LQG control using the four sensor configuration is relatively small, this is not the case for the two sensor setup. Furthermore, the overall performance potential using fixed gain LQ(G) controllers does not appear to be extremely large, but it does warrant further research. Although nonlinear optimal controller design, see for example Athans and Falb (1966, Chapters 7 and 8), may lead to better results; it is expected that the largest performance potential lies in the use of road dependent controller gains. This topic is addressed next.

6.4 Quarter truck road dependent control

In this section, the potential of an idealized variable geometry active suspension ($u = \dot{F}_{act}/(m_c j_{max})$) with road dependent LQ control gains is investigated, assuming full state knowledge. The general idea is that the optimal control gains change when the road conditions change, as the optimal controller makes optimal use of the available working space under all conditions.

6.4.1 Reformulation of the control problem

The control problem formulation, as given in Section 6.3.1, suffices when there are no passive suspension elements ($c_s = d_s = 0$) because the minimization of the control input coincides with that of the cabin jerk. However, in this section the influence of passive elements on the optimal control performance is studied. Therefore, the performance outputs for the standard control problem description are changed to

$$\begin{aligned} \underline{z}_c &= [z_1, z_2, z_3]^T \\ &= \left[\frac{z_c - z_f}{s_{max}}, \frac{\ddot{z}_c^{iso}}{a_{max}}, \frac{u}{j_{max}} \right]^T. \end{aligned} \quad (6.42)$$

Herein, \ddot{z}_c^{iso} is the ISO weighted cabin acceleration, using the filter approximation (6.14), and u is used as measure for the power consumption. Consequently, the standard plant changes to

$$P : \begin{cases} \dot{\underline{x}}_c = A_c \underline{x}_c + B_c u + G_c w \\ \underline{y}_c = \underline{x}_c \\ \underline{z}_c = E_c \underline{x}_c + N_c u. \end{cases} \quad (6.43)$$

The state-space equivalent of (6.14) is given by

$$\begin{aligned} \dot{\underline{x}}_{iso} &= A_{iso} \underline{x}_{iso} + B_{iso} \ddot{z}_c \\ y_{iso} &= \ddot{z}_c^{iso} = C_{iso} \underline{x}_{iso}, \end{aligned} \quad (6.44)$$

so the matrices become

$$\begin{aligned} A_c &= \begin{bmatrix} A & 0_{[9 \times 4]} \\ B_{iso} A(8, :) & A_{iso} \end{bmatrix} & N_c &= \begin{bmatrix} 0 \\ 0 \\ 1 \end{bmatrix} \\ B_c &= \begin{bmatrix} B \\ \underline{0}_4 \end{bmatrix} & E_c &= \begin{bmatrix} \underline{0}_3^T & 1/s_{max} & \underline{0}_8^T \\ \underline{0}_9^T & & C_{iso}/a_{max} \\ \underline{0}_9^T & & \underline{0}_4^T \end{bmatrix} & G_c &= \begin{bmatrix} G \\ \underline{0}_4 \end{bmatrix}. \end{aligned} \quad (6.45)$$

6.4.2 LQ optimal control without passive suspension elements

It has been argued that the normalized rms cabin displacement, determined by (6.24), can be used as a performance measure for the required working space. Similarly, the normalized rms driver comfort measure can be defined as

$$J_c = \sqrt{\int_{\omega_{min}}^{\omega_{max}} |H_{z_2/w}(\omega)|^2 d\omega}, \quad (6.46)$$

and the normalized rms energy cost by

$$J_e = \sqrt{\int_{\omega_{min}}^{\omega_{max}} |H_{z_3/w}(\omega)|^2 d\omega}. \quad (6.47)$$

Therefore, the LQ optimization problem can also be written as

$$\begin{aligned} \min_K J_p &= \min_K (J_{ws}^2 + r_1 J_c^2 + r_2 J_e^2) \\ \text{subject to: } &(6.43), \quad u = -K \underline{x}_c, \end{aligned} \quad (6.48)$$

with r_1 , r_2 the comfort and energy weighting respectively.

To evaluate the effectiveness of the proposed control solutions, it is important to determine the obtainable optimal passive suspension performance as a reference value. For the passive case, the first two performance outputs in (6.42) determine the overall performance. Choosing the passive cabin stiffness and damping as optimization

variables ($\underline{p} = [c_s, d_s]$), the optimal passive suspension can be found by solving the optimization problem

$$\begin{aligned} \min_{\underline{p}} \quad & J_p = J_{ws}^2 + r_1 J_c^2 \\ \text{subject to:} \quad & (6.43), \quad u = 0 \\ & 1/2 \leq \frac{c_s}{c_s^0} \leq 100 \\ & 1/100 \leq \frac{d_s}{c_s^0} \leq 100, \end{aligned} \tag{6.49}$$

with c_s^0 , d_s^0 the nominal cabin stiffness and damping of the validated model. The maximum and minimum stiffness and damping are constraint from a practical point of view. It should be noted that the passive suspension is limited to linear spring and damper characteristics. Although it is known that enhanced performance can be obtained using nonlinear characteristics, see (Hansson, 1993, Chapter 4), this topic falls beyond the scope of this thesis.

The optimal comfort and working space performance characteristics of the passive suspension for various r_1 are given in Figure 6.13 (left). The trade-off between comfort and working space is evident. In practice, the maximum suspension deflection will be constraint, so $J_{ws} \leq J_{ws}^{max}$, where J_{ws}^{max} depends on the road conditions and the the cabin disturbance force F_d .

Assumption 6.4.1. *The validated passive setting uses less than 30% of the available working space when driving on smooth, A-class, roads. In other words, on smooth roads the suspension travel can be increased by 70% without hitting the bump stops.*

Measurement data obtained from real world driving tests indicates that this is a reasonable assumption, although this does not account for the incidental severe pothole that may occur on any type of road.

Under Assumption 6.4.1, J_{ws}^{max} may be 0.9 on a smooth road. In this case, the optimal comfort that can be obtained with the passive suspension is $J_c^p|_{J_{ws}^{max}} = 0.43$. On the other hand, on a poor road J_{ws}^{max} may be 0.27, with optimal comfort $J_c^p|_{J_{ws}^{max}} = 0.94$. Still, as the passive suspension cannot adapt, the chosen suspension configuration will need to account for the worst case road condition. So, the best way to improve the comfort obtained with the passive suspension is to increase the total suspension working space. Although, it should be noted that in that case the attitude behavior of the cabin, which is not evaluated in this chapter, will be negatively affected.

The LQ optimal active cabin suspension comfort and working space performance characteristics lie below that of the passive suspension configuration. As such, this idealized active suspension setting outperforms the passive configuration with respect to these two measures. Furthermore, the comfort optimal controllers ($r_2 = 1.10^{-3}$) show a better comfort-working space performance relation than the energy optimal controllers ($r_1 = 1.10^{-6}$). However, the difference is relatively small in comparison to the difference in energy cost, see Figure 6.13 (right). For that reason, adding an energy

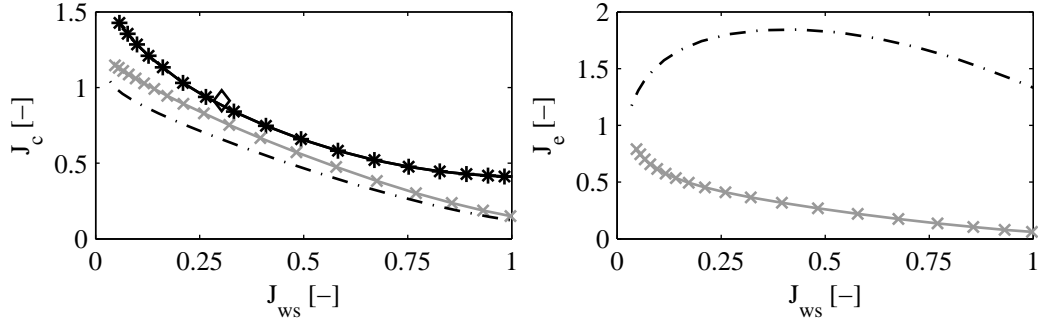


Figure 6.13: Performance diagram: comfort versus working space (left) and energy versus working space (right). Different configurations: passive (stars); validated passive (diamond); optimal LQ controller with $r_1 = 1.10^{-6}$ (grey crosses); and optimal LQ controller with $r_2 = 1.10^{-3}$ (dash-dotted).

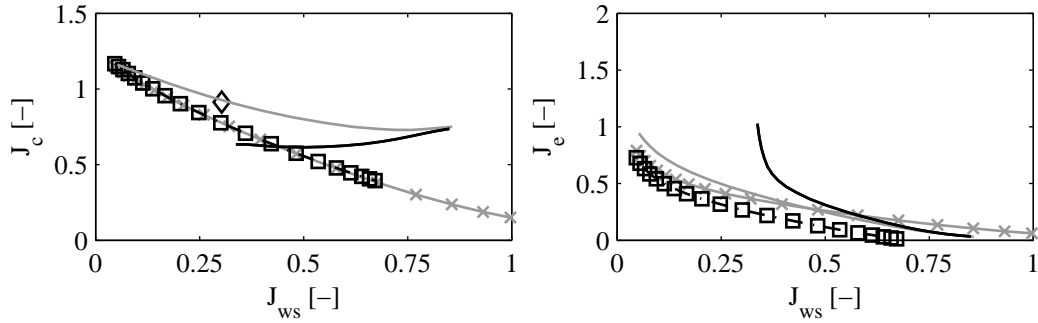


Figure 6.14: Performance diagram: comfort versus working space (left) and energy versus working space (right). Validated passive suspension (diamond), and different optimal LQ controller configurations with: $r_1 = 1.10^{-6}$, $c_s = d_s = 0$ (grey crosses); $r_1 = 1.10^{-6}$, $c_s = 0$, $d_s = 0.25d_s^0$ (squares); $r_1 = 1.10^{-6}$, $c_s = c_s^0$, $d_s = 0.25d_s^0$ (grey line); and $r_1 = 0.5$, $c_s = c_s^0$, $d_s = 0.25d_s^0$ (black line).

weight is considered to be desirable. In the range $0.27 \leq J_{ws}^{max} \leq 0.9$ the energy optimal controller can obtain comfort levels of $0.20 \leq J_c \leq 0.80$, showing that there is potential for a 75% comfort increase with respect to a fixed gain controller. Furthermore, the energy cost can also be lowered by 77%.

6.4.3 LQ optimal control with passive suspension elements

Finally, the influence of adding (linear) passive suspension elements is investigated. Hereto, the LQ optimal controllers for four different settings are evaluated. The performance diagrams are given in Figure 6.14. The effect of the added passive damping is especially noteworthy as it can be used to further lower the energy requirements. The only catch lies in the reduction of the range of optimal solutions. As such, its value should be based on the expectancy of the disturbance levels during the life of the vehicle and the available working space.

The transfer functions of the energy optimal controllers, in the presence of a passive damper, are given in Figure 6.15. For increasing energy weights, the influence of the road disturbance to cabin comfort decreases mainly in the 1 – 10 Hz range. Furthermore, the required working space increases below 10 Hz. Comparing these transfer

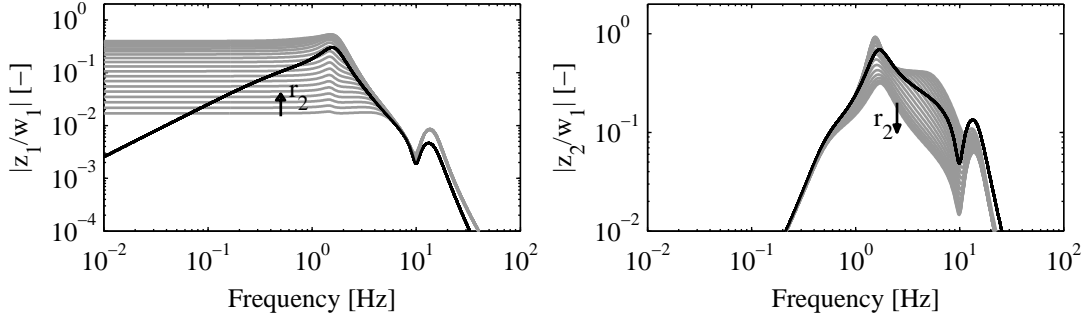


Figure 6.15: LQ optimal controller evaluation, quarter truck model with $c_s = 0$, $d_s = 0.25d_s^0$, for various energy weights r_2 and $r_1 = 1.10^{-6}$. Comparison validated passive suspension (black) and various LQ energy optimal controllers (grey). Transfer function from normalized road disturbance to normalized suspension displacement (left) and normalized ISO weighted suspended mass acceleration (right).

functions with those of the (full state feedback) LQ optimally controlled cabin suspension without passive elements, given in Figure 6.9, it can be seen that the added passive damping mainly influences the high frequency characteristics. The working space requirements are reduced, especially around the 15 Hz resonance, while the cabin accelerations increase.

On the other hand, looking back at Figure 6.14, it can be observed that adding a passive cabin stiffness will result in a degradation of the obtainable comfort and/or energy performance. Though, it is still unclear whether or not it is practically feasible to work without a passive vertical cabin stiffness, these results clearly indicate that any passive vertical stiffness is undesirable from a comfort-energy perspective.

6.5 Conclusions

In this chapter, a multi-objective two-norm performance criterion is defined, which depends on driver comfort, working space-, and energy requirements. It is shown that while, for the quarter truck heave model, the full state feedback LQ controllers provide the best performance; output feedback controllers, which adopt some of the single mass optimal controller characteristics, may provide near optimal results. Herein, the characteristics greatly depend on the chosen actuator type and the corresponding energy cost criterion.

As it cannot be expected that all the state components, required for the state- or output feedback, are measurable in practice; state estimation is required. Using a four sensor setup in combination with a Kalman filter, it is shown that the resulting LQG controller obtains performance levels that are very close to those obtained with the optimal LQ controller. Moreover, it is shown that while some passive damping may be desirable in parallel to the variable geometry actuator from an energy point of view, the passive vertical stiffness should ideally be zero.

Optimizing the passive secondary suspension parameters, a 4% comfort enhance-

ment can be obtained by lowering the passive stiffness and adding damping. However, it is questionable whether this is feasible from a practical point of view. The fixed gain LQ energy optimal controller may provide 16%, and the comfort optimal controller 28% comfort enhancement with respect to the validated passive configuration. On the other hand, the energy requirements of the energy optimal controller are 78% lower than that of the comfort optimal controller, when using a variable geometry actuator; so adding some energy weight is desirable.

Another 75% reduction can be obtained when the disturbance levels drop by 70% or the available suspension working space is increased by 70%. Furthermore, in these cases the energy cost can also be reduced by an additional 77%. So, the expected benefit of condition dependent - in comparison to fixed gain - optimal controllers is huge. However, the main question that remains, is how to effectively and robustly schedule/adapt the control gains. This question is not further addressed in this thesis, but is recommended for future research.

Chapter 7

Modal control of an active cabin suspension

7.1 Introduction

In the previous chapter the suspension performance is defined and it is shown, using the validated quarter truck model, that it is possible to greatly enhance suspension performance using the *electromechanical Low Power Active Suspension (eLPAS)* system, under idealized conditions. However, the design of a cabin controller for a full tractor semi-trailer model is more complicated. In literature it is often chosen to decouple the roll, pitch and heave cabin motions and then adopt various modal control strategies, Holen (2008); Graf et al. (2008). In the latter, the required state transformation is found by optimization. By means of simulation it is shown that the vertical, roll and pitch accelerations can be reduced by 78%, 65% and 40% respectively, which is considerably more than expected based on the findings of Fischer and Isermann (2004) for passenger cars. However, the issue of attitude control is not considered at all.

With or without decoupling, the most popular suspension control method remains LQG control, see for example Hansson (1993). However, the number of full vehicle active cabin suspension studies in literature is fairly limited. Moreover, quite a few of the ones available focus on roll-over prevention, see Yu et al. (2009); Cimba et al. (2006). Consequently, much remains unknown about the performance potential of active secondary suspensions for commercial vehicles.

In this chapter the following problem is addressed. Given the tractor semi-trailer system with four *eLPAS* actuators, one beneath each corner of the cabin; what is the achievable performance using a fixed gain linear control strategy with respect to the passive setting? The restriction to fixed gain linear controllers is imposed to limit the complexity and circumvent adaptation/gain scheduling issues.

To answer this question, the tractor semi-trailer dynamics are decoupled into the roll and pitch-heave dynamics. For each of these, optimal LQG controllers are designed using the validated reduced order models as presented in Chapter 3, and the benefit of adding passive suspension elements is investigated. A fixed gain LQG roll and pitch-

heave controller is selected, with similar working space requirements as the validated passive system, and implemented in the validated 44 DOF tractor semi-trailer model of Chapter 2. Furthermore, assuming that the driver induced longitudinal and lateral accelerations can be accurately estimated, it is possible to include a feedforward disturbance compensation controller which reduces the cabin roll and pitch disturbances when steering, braking or accelerating. The effect of these feedforward terms is evaluated separately.

The overall performance using the selected fixed gain controllers is found to be very poor due to the intrinsic nonlinearities - especially the saturation bounds - which are not included in the controller design, as well as the large uncertainty in the used roll model. Therefore, an alternative single mass energy optimal control strategy (6.8) is adopted for the roll direction and a LQG fixed gain setting that allows more suspension travel is chosen for the pitch-heave directions. The performance of this tuned LQG controller is compared to that of a modal skyhook controller, with low-pass filtered control signals to lower its power requirements, for various conditions. Furthermore, both controllers are evaluated with and without the feedforward disturbance compensation.

Overall it is found, that the tuned LQG controller gives better performance, with respect to comfort and energy at similar suspension travel characteristics, than the modal skyhook controller. That is, as long as the bump-stops are avoided. The achievable performance gain using fixed gain controllers with respect to the validated passive setting is condition dependent. Nevertheless, under some of the simulated conditions with the 44 DOF model, a decrease of the ride comfort index (comfort increase) of 35% is obtained. The mean total power consumption using the tuned LQG controller range from around 300 W on a relatively smooth road up to 1.35 kW under worst-case conditions. However, it should be noted that the designed controllers are not expected to be optimal, due to the nonlinear system characteristics and the control model inaccuracies.

The driver induced disturbance compensation is demonstrated to have great potential for enhancing the cabin attitude behavior. More specifically, the cabin roll and pitch motions accurately follow the driver induced chassis motions when braking, steering, or accelerating, resulting in enhanced feedback to the driver. However, the challenge remains to find suitable estimators, which are sufficiently accurate under all driving conditions. These estimates need to be minimally affected by the various noise sources, as these will otherwise significantly increase the power requirements. Moreover, the assumption that following the driver induced chassis motions is optimal still needs to be validated.

The outline of this chapter is as follows. First the input-output decoupling strategy is presented, followed by an analysis of the optimal LQ(G) roll control strategy. Next, the optimal LQ(G) pitch-heave controller characteristics are evaluated. Finally, in Section 7.5 the various control strategies are evaluated for a number of driving conditions on the 44 DOF tractor semi-trailer model.

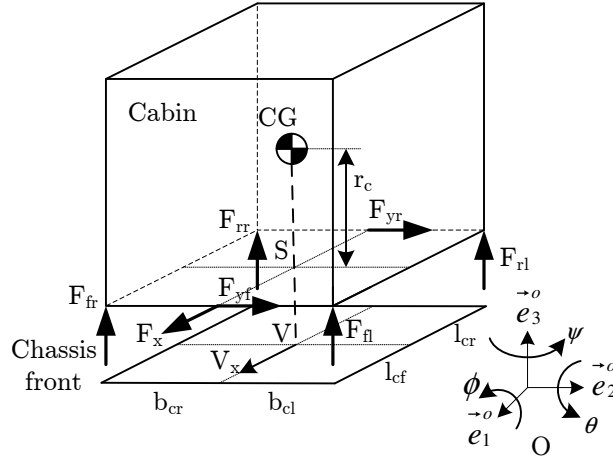


Figure 7.1: Schematic representation of the cabin model.

7.2 Input-output decoupling

The tractor semi-trailer system has three cabin modes that can be controlled by the *eLPAS* actuators: the roll (ϕ_c), the pitch (θ_c), and the heave (z_c). One way to control these, is by decoupling them and designing suitable single-input single-output (SISO) controllers for each mode. However, decoupling may not always lead to the most optimal results, as it imposes additional constraints on the control structure, see Boerlage (2008, Section 2.3).

In this section, two strategies for input-output decoupling are presented. The first separates the roll and the pitch-heave dynamics, facilitating the use of the reduced order models presented in Chapter 3. The second also decouples the pitch-heave dynamics and is used later on to evaluate the performance of a modal skyhook control strategy.

Both decoupling strategies are based on the cabin model as depicted in Figure 7.1. Herein, the cabin is modeled as a rigid body with the center of mass located at a certain height r_c above a point S on the bottom of the cabin. The point S is located at a length l_{cf} from the front of the cabin and l_{cr} from that of the rear. Furthermore, the distances to the left and right side of the cabin are b_{cl} and b_{cr} respectively. The bottom of the cabin is projected on the chassis, where the projection of S is V . V_x is the forward driving direction.

Assumption 7.2.1. *Both chassis and cabin are assumed to behave as rigid bodies.*

Even though the chassis may profoundly twist in reality, these flexibilities are not included in this model.

Assumption 7.2.2. *The motion of the chassis point V with respect to the fixed world point O is given, and is not influenced by the cabin suspension forces.*

Four different coordinate frames are defined, see Figure 7.1: an absolute frame in point O (\vec{e}^O); a relative frame R in point O that follows the chassis rotations around

the \vec{e}_3^O -axis (yaw); and a body-fixed frame in points V and S . The rotations ϕ_s , θ_s , and ψ_s are called the *roll*, *pitch* and *yaw* of S respectively. The subscript (s), which is used here as an example, indicates that the rotations are from the frame R to the relative frame in S .

Assumption 7.2.3. *The longitudinal (\vec{e}_1^R) and lateral (\vec{e}_2^R) movements of point S with respect to point V are negligible due to the high stiffness of the cabin suspension in those directions. Moreover $\psi_v - \psi_s = 0$, so both cabin and chassis follow the yaw-motions of the vehicle (ψ_r) exactly.*

The longitudinal and lateral movements of the vehicle result in suspension forces acting on the cabin. These forces are depicted in Figure 7.1 as F_x , F_{yf} and F_{yr} . Since the chassis motions are determined according to Assumption 7.2.2 and cabin motions according to Assumption 7.2.3, these longitudinal and lateral suspension forces can be deduced.

So, in longitudinal (\vec{e}_1^V) and lateral (\vec{e}_2^V) direction the cabin is suspended to the chassis by means of stiff spring-damper configurations. Additionally, in vertical (\vec{e}_3^V) direction a damper is positioned in parallel with the *eLPAS* actuator, at each of the cabin corners. Therefore, the vertical suspension forces can be split into a force that originates from the passive suspension (F_{ij}^S) and one that is induced by the actuator (F_{ij}^A).

Assumption 7.2.4. $\frac{\delta}{\delta t} \vec{e}^R = 0$.

Assumption 7.2.4 can be used as long as the yaw velocity of the vehicle remains low. Under this assumption, \vec{e}^R can be considered as an absolute frame. In order to derive Lagrange's equations of motion, see for example Huston (1995), position vectors are needed. The position of the center of gravity of the cabin, point S and point V are given by

$$\begin{aligned} \vec{r}_{cg} &= [x_c \ y_c \ z_c] \vec{e}^R \\ \vec{r}_s &= \begin{bmatrix} x_c - r_c \sin \theta_c \\ y_c + r_c \cos \theta_c \sin \phi_c \\ z_c - r_c \cos \theta_c \cos \phi_c \end{bmatrix}^T \vec{e}^R \\ \vec{r}_v &= [x_v \ y_v \ z_v] \vec{e}^R. \end{aligned} \tag{7.1}$$

Assumption 7.2.5. *The suspension forces are all oriented along the principal axis of the frame \vec{e}^R .*

Although this is not entirely in line with reality, this assumption is needed to keep the equations manageable. Moreover, the error that is introduced with this assumption is reasonably small under normal driving conditions.

Assumption 7.2.6. *The angles $\phi_s = \phi_c$, $\theta_s = \theta_c$, ϕ_v and θ_v are small, hence the following approximations can be applied for each of these angles ξ :*

$$\begin{aligned}\cos \xi &\approx 1 \\ \sin \xi &\approx \xi \\ (\sin \xi)^2 &\approx 0.\end{aligned}\tag{7.2}$$

Assumption 7.2.6 holds under normal driving conditions. When driving on graded or strongly banked roads, a more complex (nonlinear) model is required for accurate results.

Assumption 7.2.7. *All cross terms in the inertia matrix are negligible.*

Assumption 7.2.7 holds when the equations of motions are determined for the center of gravity.

Under these assumptions, the following equations of motion are obtained:

$$\begin{bmatrix} m_c \ddot{z}_c \\ J_c^x \ddot{\phi}_c \\ J_c^y \ddot{\theta}_c \end{bmatrix} = \underbrace{T \underline{F}^S}_{\underline{u}^S} + \underbrace{T \underline{F}^A}_{\underline{u}^A} + \underline{w}_c, \tag{7.3}$$

where

$$\begin{aligned}T &= \begin{bmatrix} 1 & 1 & 1 & 1 \\ r_c \phi_c + b_{cl} & r_c \phi_c - b_{cr} & r_c \phi_c + b_{cl} & r_c \phi_c - b_{cr} \\ r_c \theta_c - l_{cf} & r_c \theta_c - l_{cf} & r_c \theta_c + l_{cr} & r_c \theta_c + l_{cr} \end{bmatrix} \\ \underline{w}_c &= \begin{bmatrix} -m_c g \\ l_{cf} \theta_s F_{yf} - l_{cr} \theta_s F_{yr} + r_c (F_{yf} + F_{yr}) - c_{sf}^{\phi} (\phi_c - \phi_v) \\ l_{cf} \phi_s F_{yf} - l_{cr} \phi_s F_{yr} - (l_{cf} \theta_s + r_c) F_x \end{bmatrix}\end{aligned}\tag{7.4}$$

$$\begin{aligned}\underline{F}^S &= [F_{fl}^S \ F_{fr}^S \ F_{rl}^S \ F_{rr}^S]^T \\ \underline{F}^A &= [F_{fl}^A \ F_{fr}^A \ F_{rl}^A \ F_{rr}^A]^T.\end{aligned}$$

Herein, \underline{w}_c is a perturbation vector, c_{sf}^{ϕ} is the cabin roll stabilizer stiffness, \underline{F}^A is a vector containing the actuator forces and \underline{F}^S contains the forces from the vertical passive suspension elements.

Assuming a constant *eLPAS* stiffness c_s and linear dampers with damping constant d_s , the modal passive suspension inputs

$$\underline{u}^S = T \underline{F}^S, \tag{7.5}$$

are given by

$$\underline{u}^S = -c_s G_s \begin{bmatrix} z_c - z_v - r_c \\ \phi_s - \phi_v \\ \theta_s - \theta_v \end{bmatrix} - d_s G_s \begin{bmatrix} \dot{z}_c - \dot{z}_v \\ \dot{\phi}_s - \dot{\phi}_v \\ \dot{\theta}_s - \dot{\theta}_v \end{bmatrix}, \tag{7.6}$$

where

$$G_s = \begin{bmatrix} 4 & 2(b_{cl} - b_{cr}) & 2(l_{cr} - l_{cf}) \\ 2(b_{cl} - b_{cr}) & 2(b_{cl}^2 + b_{cr}^2) & b_{cl}l_{cr} - b_{cl}l_{cf} + b_{cr}l_{cf} - b_{cr}l_{cr} \\ 2(l_{cr} - l_{cf}) & b_{cl}l_{cr} - b_{cl}l_{cf} + b_{cr}l_{cf} - b_{cr}l_{cr} & 2(l_{cr}^2 + l_{cf}^2) \end{bmatrix}. \quad (7.7)$$

A key observation from (7.7) is that the heave, pitch and roll dynamics are coupled through the interaction from the suspension elements. In addition, each actuator force affects all of these modes, see (7.4). Moreover, there are four control inputs and only three remaining degrees of freedom (DOF), hence the system is over-actuated.

Assumption 7.2.8. *The absolute cabin orientation $(\theta_c, \phi_c, \psi_c)$ cannot be measured or estimated accurately and is not available for control. These angles are assumed zero where needed.*

Under these assumptions, using the equations of motions, two input-output decoupling strategies can be determined. The first separates the roll and the pitch-heave dynamics, facilitating the use of the reduced order models presented in Chapter 3. The second also decouples the pitch-heave dynamics and is used later on to evaluate the performance of a modal skyhook control strategy. Each is shortly discussed.

7.2.1 Roll and pitch-heave

When using the roll and pitch-heave models as given in Chapter 3 for controller design, the control inputs of these models need to be transformed to reference forces for each of the *eLPAS* actuators. Furthermore, the roll control and pitch-heave control actions should not interact. So, the control inputs need to be partially decoupled such that $\ddot{\phi}_c$ can be manipulated by M_{act}^x and $(\ddot{z}_c, \ddot{\theta}_c)$ by (F_{act}^F, F_{act}^R) , without interaction between $\ddot{\phi}_c$ and $(\ddot{z}_c, \ddot{\theta}_c)$. It should be noted that (7.3) is not completely applicable as the equations of motion of the roll model are derived for point *S*, giving

$$J_x^s \ddot{\phi}_c = (F_{fl} + F_{rl})b_{cl} - (F_{fr} + F_{rr})b_{cr} + r_c m_c (\ddot{y}_c + g\phi_c) - c_{sf}^\phi (\phi_c - \phi_v), \quad (7.8)$$

with J_x^s the roll inertia in point *S*. However, under Assumption 7.2.8 this does not affect *T* or *G_s*.

In correspondence to the reduced order models, the control inputs are chosen as

$$\begin{bmatrix} F_{act}^F \\ F_{act}^R \\ M_{act}^x \end{bmatrix} = \underline{u}_p = T_p \underline{F}^A, \quad (7.9)$$

where

$$T_p = \begin{bmatrix} \frac{1}{2} & \frac{1}{2} & 0 & 0 \\ 0 & 0 & \frac{1}{2} & \frac{1}{2} \\ b_{cl} & -b_{cl} & b_{cr} & -b_{cr} \end{bmatrix}. \quad (7.10)$$

As T_p is non-square, the relation $\underline{F}^A = T_p^{-1}\underline{u}_p$ cannot be uniquely determined. However, the so-called pseudo-inverse (or *Moore-Penrose inverse*), see Ben-Israel and Greville (1974), which is optimal in a least-square sense, can be used. For (7.10), it is given by

$$\begin{aligned} T_p^\dagger &= T_p^T (T_p T_p^T)^{-1} \\ &= \begin{bmatrix} 1 & 0 & \frac{b_{cl}}{2(b_{cl}^2 + b_{cr}^2)} \\ 1 & 0 & -\frac{b_{cl}}{2(b_{cl}^2 + b_{cr}^2)} \\ 0 & 1 & \frac{b_{cl}}{2(b_{cl}^2 + b_{cr}^2)} \\ 0 & 1 & -\frac{b_{cl}}{2(b_{cl}^2 + b_{cr}^2)} \end{bmatrix}. \end{aligned} \quad (7.11)$$

Moreover, as $b_{cl} = b_{cr}$ the passive suspension elements do not cause interaction between roll and pitch-heave dynamics, i.e., (7.7) reduces to

$$G_s = \begin{bmatrix} 4 & 0 & 2(l_{cr} - l_{cf}) \\ 0 & 2(b_{cl}^2 + b_{cr}^2) & 0 \\ 2(l_{cr} - l_{cf}) & 0 & 2(l_{cr}^2 + l_{cf}^2) \end{bmatrix}. \quad (7.12)$$

Consequently, no passive suspension effects need to be compensated for the partial decoupling, which is beneficial from an energy point of view. The equations of motions are given by

$$\begin{aligned} \begin{bmatrix} m_c \ddot{z}_c \\ J_s^x \ddot{\phi}_c \\ J_c^y \ddot{\theta}_c \end{bmatrix} &= \begin{bmatrix} 2 & 2 & 0 \\ 0 & 0 & 1 \\ -2l_{cf} & 2l_{cr} & 0 \end{bmatrix} \begin{bmatrix} F_{act}^F \\ F_{act}^R \\ M_{act}^x \end{bmatrix} - c_s G_s \begin{bmatrix} z_c - z_v - r_c \\ \phi_c - \phi_v \\ \theta_c - \theta_v \end{bmatrix} \\ &\quad - d_s G_s \begin{bmatrix} \dot{z}_c - \dot{z}_v \\ \dot{\phi}_c - \dot{\phi}_v \\ \dot{\theta}_c - \dot{\theta}_v \end{bmatrix} + \underline{w}_c^*, \end{aligned} \quad (7.13)$$

where

$$\underline{w}_c^* = \begin{bmatrix} -m_c g \\ r_c m_c (\ddot{y}_c + g \phi_c) - c_{sf}^\phi (\phi_c - \phi_v) \\ l_{cf} \phi_s F_{yf} - l_{cr} \phi_s F_{yr} - (l_{cf} \theta_s + r_c) F_x \end{bmatrix}. \quad (7.14)$$

So, the roll and pitch-heave dynamics are decoupled. Furthermore, it is worth noticing that

$$\begin{bmatrix} F_{act}^z \\ M_{act}^y \end{bmatrix} = T_{ph} \begin{bmatrix} F_{act}^F \\ F_{act}^R \end{bmatrix} \quad (7.15)$$

is the input transformation that decouples the pitch and heave inputs, where

$$T_{ph} = 2 \begin{bmatrix} 1 & 1 \\ -l_{cf} & l_{cr} \end{bmatrix}. \quad (7.16)$$

However, this input transformation does not compensate for the pitch-heave interaction caused by the passive suspension elements.

7.2.2 Roll, pitch and heave

By completely decoupling the roll, pitch and heave cabin dynamics, the controller design process can be simplified further. The goal is to find a transformation in which $\ddot{\phi}_c$ is only influenced by M_{act}^x and the passive roll stiffness and damping; $\ddot{\theta}_c$ by M_{act}^y and the passive pitch stiffness and damping; and \ddot{z}_c by F_{act}^z and the passive vertical stiffness and damping. To find this transformation, the vector of modal actuator inputs is defined as

$$\underline{u}^A = T \underline{F}^A. \quad (7.17)$$

Because T is not a square matrix, \underline{F}^A is not uniquely defined for a given \underline{u}^A . One way of finding a unique transformation is by looking for an additional constraint. For this purpose, it makes sense to choose

$$F_{fr}^A + F_{rl}^A - F_{rr}^A - F_{fl}^A = 0, \quad (7.18)$$

as Assumption 7.2.1 will not hold in practice. The cabin floor is flexible to some extent, so if the actuators are used to twist the cabin floor energy is being wasted and cabin fatigue issues may be the result. Using (7.18) this is prevented. Combining (7.3), (7.4) and (7.18) under Assumption 7.2.8 gives

$$\begin{aligned} \underline{F}^A &= \tilde{T}^{-1} \begin{bmatrix} \underline{u}^A \\ 0 \end{bmatrix} \\ \tilde{T}^{-1} &= \begin{bmatrix} 1 & 1 & 1 & 1 \\ b_{cl} & -b_{cr} & b_{cl} & -b_{cr} \\ -l_{cf} & -l_{cf} & l_{cr} & l_{cr} \\ -1 & 1 & 1 & -1 \end{bmatrix}^{-1}, \end{aligned} \quad (7.19)$$

which is an invertible transformation as $(b_{cl}, b_{cr}, l_{cf}, l_{cr}) > 0$. Alternatively, the pseudo-inverse can again be used, which is given by

$$T^\dagger = T^T (T T^T)^{-1}. \quad (7.20)$$

It can be easily checked that

$$\tilde{T}^{-1} = [T^\dagger, \star], \quad (7.21)$$

with \star a vector that does not influence \underline{F}^A . Hence, both approaches give the same unique relation.

The next step is to overcome the interaction that is caused by the passive suspension forces, that is, the forces resulting from the non-diagonal terms in (7.12). Only the stiffness related terms are compensated, as it would be energy inefficient to compensate the fast changing damper related terms using the *eLPAS* system. Consequently, the modal actuator inputs become

$$\underline{u}^A = c_s \tilde{G}_s \begin{bmatrix} z_c - z_v - r_c \\ \phi_s - \phi_v \\ \theta_s - \theta_v \end{bmatrix} + \begin{bmatrix} F_{act}^z \\ M_{act}^x \\ M_{act}^y \end{bmatrix}, \quad (7.22)$$

with $[F_{act}^z, M_{act}^x, M_{act}^y]^T$ the vector of modal controller inputs and ($b_{cl} = b_{cr}$)

$$\tilde{G}_s = \begin{bmatrix} 0 & 0 & 2(l_{cr} - l_{cf}) \\ 0 & 0 & 0 \\ 2(l_{cr} - l_{cf}) & 0 & 0 \end{bmatrix}. \quad (7.23)$$

Consequently, the equations of motion become

$$\begin{bmatrix} m_c \ddot{z}_c \\ J_c^x \ddot{\phi}_s \\ J_c^y \ddot{\theta}_s \end{bmatrix} = \begin{bmatrix} F_{act}^z \\ M_{act}^x \\ M_{act}^y \end{bmatrix} - c_s(\underline{G}_s - \tilde{G}_s) \begin{bmatrix} z_c - z_v - r_c \\ \phi_s - \phi_v \\ \theta_s - \theta_v \end{bmatrix} - d_s \underline{G}_s \begin{bmatrix} \dot{z}_c - \dot{z}_v \\ \dot{\phi}_s - \dot{\phi}_v \\ \dot{\theta}_s - \dot{\theta}_v \end{bmatrix} + \underline{w}_c, \quad (7.24)$$

wherein the roll, pitch and heave input-output behavior is approximately decoupled.

Inspired by the single mass optimal control results presented in the previous chapter, a modal skyhook control strategy can be adopted in combination with (7.22) and (7.19),

$$\begin{aligned} F_{act}^z &= -c_1^z \int_0^t (z_c - z_f) dt - c_2^z (z_c - z_f) - c_3^z \dot{z}_c \\ M_{act}^x &= -c_1^\phi \int_0^t (\phi_c - \phi_f) dt - c_2^\phi (\phi_c - \phi_f) - c_3^\phi \dot{\phi}_c \\ M_{act}^y &= -c_1^\theta \int_0^t (\theta_c - \theta_f) dt - c_2^\theta (\theta_c - \theta_f) - c_3^\theta \dot{\theta}_c, \end{aligned} \quad (7.25)$$

where all c_1, c_2, c_3 are integrator, relative stiffness, and skyhook damping gains, respectively. This controller is used as benchmark setting for the modal LQG controllers that are designed in the next sections.

7.3 Roll control

In this section an LQG controller with disturbance compensation for the roll direction is designed. It is based on the validated half truck roll model shown in Figure 7.2, and a comfort-energy-suspension travel multi-objective performance criterium, see also Section 1.4. First the control problem is formulated, followed by the presentation of the LQ optimal controller and the evaluation of its characteristics. After that, the case of limited state knowledge is considered, wherein the performance degradation using state estimation with various sensor configurations is studied. Finally, an estimator is designed for the lateral cabin acceleration induced by driver steering, which can be used to reduce the influence of the roll disturbance.

7.3.1 Roll control problem

The control problem can again be written in the generalized or standard plant formulation, see Figure 6.5. Herein, \underline{w} are the (weighted) exogenous inputs, \underline{z} are the (weighted) performance outputs, u is the control signal and \underline{y} are the sensed outputs.

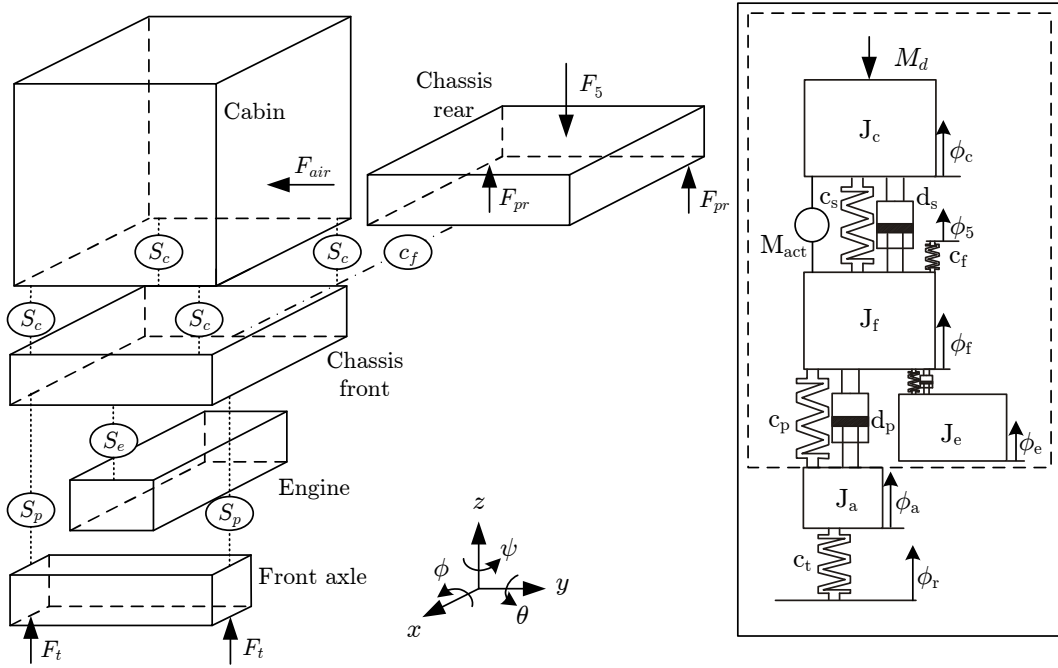


Figure 7.2: Half truck 4-DOF roll model, schematic representation. The part of the model which is validated for road induced vibrations is given in the dashed box.

Furthermore, all $\underline{w}, \underline{z}, \underline{u}, \underline{y}$ are scaled to facilitate the choice of the weights and avoid numeric solver issues. The problem is to find a control K , which based on \underline{y} generates a control signal \underline{u} , that minimizes the influence of \underline{w} on \underline{z} .

For the roll model as depicted in Figure 7.2, the exogenous inputs are given by

$$\underline{w} = [w_1, w_2, w_3]^T = [v_r/\phi_{max}, M_d/(J_c a_\phi^{max}), v_5]^T, \quad (7.26)$$

where w_1 is the frequency weighted normalized road angle, w_2 is the normalized cabin disturbance moment, and w_3 is the normalized frequency weighted chassis angle. Herein, the components of \underline{w} are assumed to be zero mean, gaussian distributed (white noise), uncorrelated signals. In reality w_1 and w_3 will not be completely uncorrelated due to the wheelbase filtering. However, taking this effect into account would result in more complex velocity dependent controllers, which is considered to be undesirable for this study.

Although the vertical road velocity can be described as a white noise signal, see Section 3.2.2, this is not the case for the road roll velocity. The low frequent road input for the latter is significantly lower as wavelengths larger than the lateral wheelbase have little influence on the vehicle roll. For that reason the following road model is adopted

$$\dot{\phi}_r = \beta_r(v_r - \phi_r), \quad (7.27)$$

with ϕ_r the absolute road angle and $\beta_r = 2\pi$ Hz the filter frequency, which is estimated based on Liebrechts (2007). Assuming that the chassis roll is mainly determined by

road disturbances, the rear chassis disturbance is modeled similarly as

$$\dot{\phi}_5 = \beta_r(v_5 - \phi_5). \quad (7.28)$$

Furthermore, the weighted performance variables are given by

$$\underline{z} = [z_1, z_2, z_3]^T = [(\phi_c - \phi_f)/\phi_{max}, \ddot{\phi}_c^{iso}/(a_\phi^{max}), u]^T, \quad (7.29)$$

with control input $u = \dot{M}_{act}^x/(J_c j_\phi^{max})$. The maximum values are chosen as

$$[\phi_{max}, v_\phi^{max}, a_\phi^{max}, j_\phi^{max}]^T = [0.01, 1, 10, 1000]^T, \quad (7.30)$$

where $[v, a, j]$ stand for velocity, acceleration, and jerk respectively.

Assuming full state knowledge, the standard plant P can be written as

$$P : \begin{cases} \dot{\underline{x}} = A\underline{x} + Bu + G\underline{w} \\ \underline{y} = \underline{x} \\ \underline{z} = E\underline{x} + Nu. \end{cases} \quad (7.31)$$

Herein, the state is given by

$$\begin{aligned} \underline{x} &= [\underline{x}_\phi, \frac{M_{act}^x}{J_c}, \underline{x}_{iso}]^T \\ \underline{x}_\phi &= [\phi_r, \phi_5, \phi_a, \phi_e, \phi_f, \phi_c, \dot{\phi}_a, \dot{\phi}_e, \dot{\phi}_f, \dot{\phi}_c]^T, \end{aligned} \quad (7.32)$$

with \underline{x}_{iso} the state belonging to the state space realization of W_{iso}^ϕ ,

$$\begin{aligned} \dot{\underline{x}}_{iso} &= A_{iso}\underline{x}_{iso} + B_{iso}\ddot{\phi}_c \\ \ddot{\phi}_c^{iso} &= C_{iso}\underline{x}_{iso}, \end{aligned} \quad (7.33)$$

which is the reduced (fourth) order approximation of the (seventh order) ISO roll weighting function,

$$W_{iso}^\phi(s) = \frac{6.25s^3 + 42.6s^2}{s^4 + 13.9s^3 + 85.3s^2 + 217s + 269}. \quad (7.34)$$

The approximation is obtained by balanced residualization, see (Skogestad and Postlethwaite, 2005, Section 11.4), using the MATLAB function *balred.m*, and is depicted in Figure 7.3. Furthermore, the matrices in (7.31) are given by

$$\begin{aligned} A &= \begin{bmatrix} A_\phi & B_\phi & 0_{[8 \times 4]} \\ 0_{[1 \times 8]} & 0 & 0_{[1 \times 4]} \\ B_{iso}A_\phi(10, :) & B_{iso} & A_{iso} \end{bmatrix} & B &= \begin{bmatrix} \underline{0}_{10} \\ j_\phi^{max} \\ \underline{0}_4 \end{bmatrix} & N &= \begin{bmatrix} \underline{0}_2 \\ 1 \end{bmatrix} \\ E &= \begin{bmatrix} \underline{0}_4^T & -1/\phi_{max} & 1/\phi_{max} & \underline{0}_5^T & \underline{0}_4^T \\ & \underline{0}_6^T & & \underline{0}_5^T & C_{iso}/a_\phi^{max} \\ & \underline{0}_6^T & & \underline{0}_5^T & \underline{0}_4^T \end{bmatrix} & G &= \begin{bmatrix} \beta_r \phi_{max} & 0 & 0 \\ 0 & 0 & \beta_r \\ \underline{0}_7 & \underline{0}_7 & \underline{0}_7 \\ 0 & a_\phi^{max} & 0 \end{bmatrix}, \end{aligned} \quad (7.35)$$

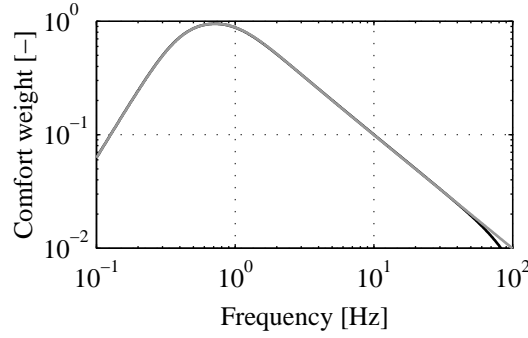


Figure 7.3: ISO 2621 weighting curve for the roll acceleration (black), ISO 2631-1 (1997), and the fourth order approximation (grey).

with

$$A_\phi = \left[\begin{array}{cc|cc|cc} -\beta_r & 0 & & & & \\ 0 & -\beta_r & & & & \\ \hline & & 0_{[2 \times 4]} & & 0_{[2 \times 4]} & \\ & & \hline 0_{[4 \times 2]} & & 0_4 & & I_4 & \\ \hline c_t/J_a & 0 & & & & \\ 0 & 0 & & & & \\ 0 & c_f^\phi/J_f & & & & \\ 0 & 0 & & & & \\ \hline & & -M_\phi^{-1}K_\phi & & -M_\phi^{-1}D_\phi & \end{array} \right] \quad B_\phi = \begin{bmatrix} 0_8 \\ -J_c/J_f \\ 1 \end{bmatrix}. \quad (7.36)$$

It is chosen to look for the controller that minimizes the influence of \underline{w} on \underline{z} in a two-norm sense. In other words, the controller that minimizes

$$J_\phi = \int_0^\infty (z_1^2 + r_1 z_2^2 + r_2 u^2) dt, \quad (7.37)$$

where r_1 is the comfort weighting and r_2 is the energy weighting.

7.3.2 LQ optimal roll control solution

The control problem, as posed in the previous subsection, is solved using LQ optimization. Similar to the previous chapter, the performance obtained with the controller can be split in three parts: suspension travel, comfort, and energy

$$J = J_{ws}^2 + r_1 J_c^2 + r_2 J_e^2. \quad (7.38)$$

However, in this case each of the performance criteria is influenced by all disturbances \underline{w} . These are separated for evaluation purposes, so

$$\begin{aligned} J_{ws}^{wi} &= \sqrt{\int_{\omega_{\min}}^{\omega_{\max}} |H_{z_1/w_i}(\omega)|^2 d\omega} \\ J_c^{wi} &= \sqrt{\int_{\omega_{\min}}^{\omega_{\max}} |H_{z_2/w_i}(\omega)|^2 d\omega} \\ J_e^{wi} &= \sqrt{\int_{\omega_{\min}}^{\omega_{\max}} |H_{z_3/w_i}(\omega)|^2 d\omega}, \end{aligned} \quad (7.39)$$

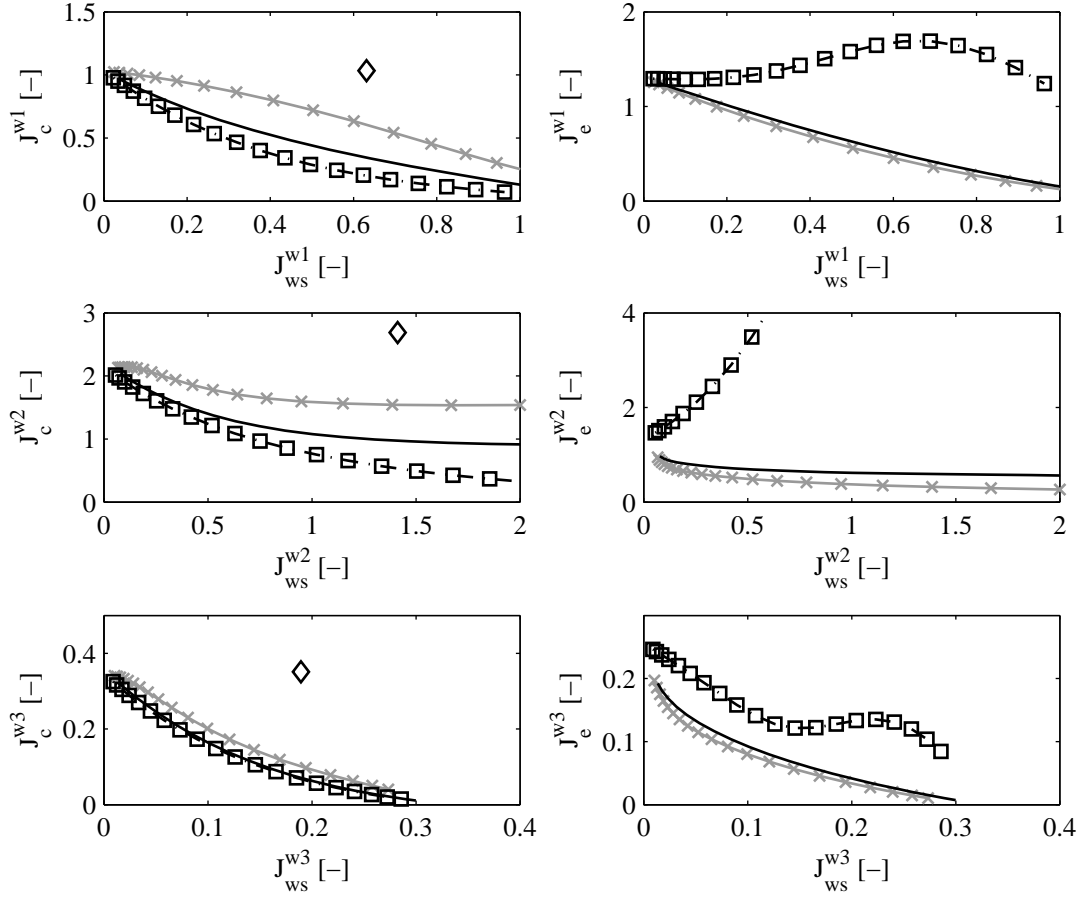


Figure 7.4: Performance diagrams comfort versus working space (left) and energy versus working space (right), resulting from: road disturbance (w_1 , top); cabin disturbance moment (w_2 , mid); and chassis rotations (w_3 , bottom). Different configurations roll model: passive (diamond); energy optimal LQ controller with $r_1 = 1.10^{-6}$ (grey crosses); comfort optimal LQ controller with $r_2 = 1.10^{-3}$ (squares); and optimal LQ controller with $r_1 = r_2$ (solid black).

with $i \in [1, 2, 3]$ and H_{z_j/w_i} the transfer from w_i to z_i . Again note, that z_3 is directly related to \dot{F}_{act} , which in turn can be used as measure for the $eLPAS$ power consumption P_{act} , given the findings in Chapters 4 and 5.

First, the case is considered without additional passive suspension elements ($d_s = 0$ and c_s equal to the $eLPAS$ effective stiffness), and the performance characteristics are evaluated for: very low comfort weighting ($r_1 = 1.10^{-6}$) and various energy weights (energy optimal); low energy weighting ($r_1 = 1.10^{-3}$) and various comfort weights (comfort optimal); and various equal weights ($r_1 = r_2$). The results are given in Figure 7.4. It can be seen that while each configuration outperforms the validated passive setting, the largest comfort gain can be obtained with the comfort optimal setting. However, in that case the energy requirements to suppress disturbances from the cabin disturbance moment w_2 are off the chart. The controllers with the equal weights offer a good compromise: a significant comfort gain with respect to the energy optimal controllers with nearly the same energy requirements.

Next, using the performance characteristics of the controllers with equal weights

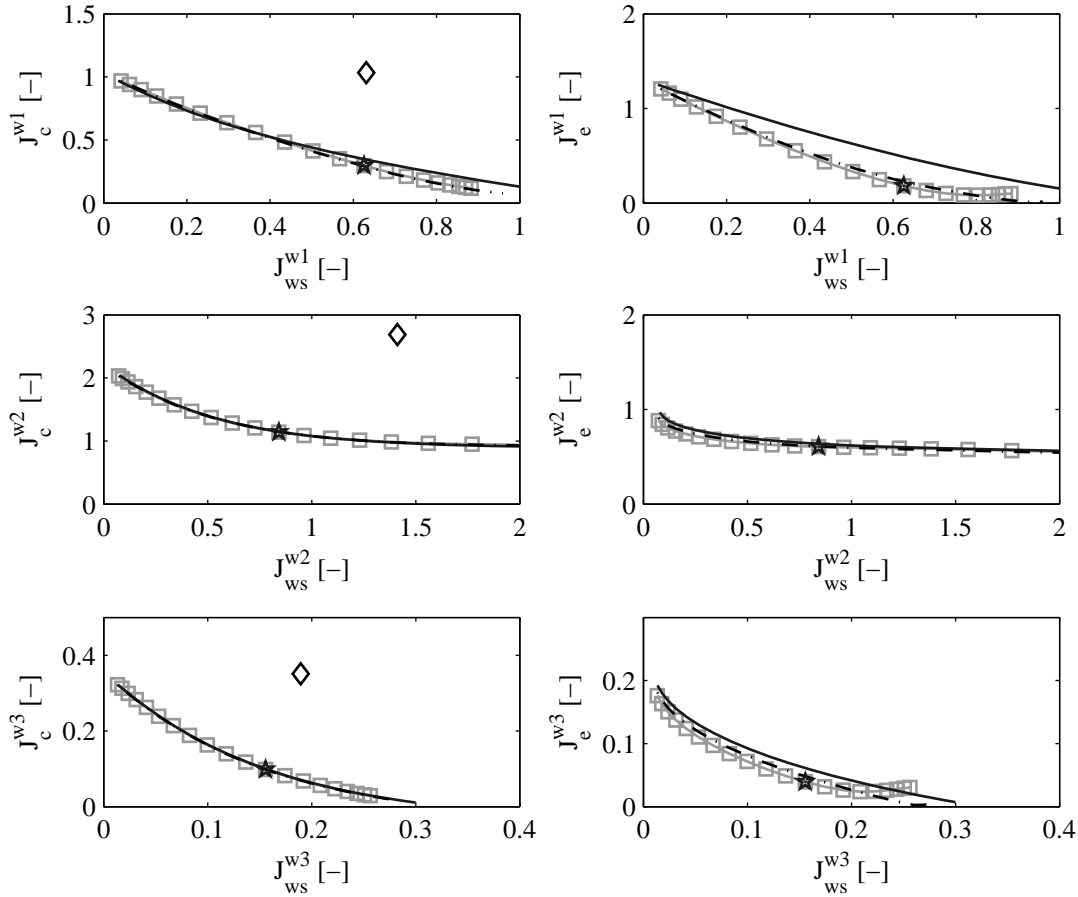


Figure 7.5: Performance diagrams comfort versus working space (left) and energy versus working space (right), resulting from: road disturbance (w_1 , top); cabin disturbance moment (w_2 , mid); and chassis rotations (w_3 , bottom). Different configurations roll model: passive (diamond); optimal LQ controller with $r_1 = r_2$ (solid black); optimal LQ controller with $r_1 = r_2$ and $d_s = d_s^0/2$ (dash-dotted); optimal LQ controller with $r_1 = r_2$, $c_s = c_s^0/4$ and $d_s = d_s^0/2$ (grey squares); and LQ optimal controller with $r_1 = r_2$, $c_s = c_s^0/4$ and $d_s = d_s^0/2$, and passive working space requirement (pentagon).

as reference, the influence of adding passive suspension elements is investigated. The characteristics, as given in Figure 7.5, show that adding some damping seems preferable as it decreases the power requirements. Moreover, for some weights, adding some roll stiffness in addition to the damping further enhances performance. From a practical point of view it is also desirable to add some roll stiffness in case the *eLPAS* actuators are disabled. Especially with respect to road induced vibrations, the realizable comfort enhancement is larger than for the case without passive elements, while the energy requirements are reduced.

In the validated passive suspension, there is a very stiff roll stabilizer in the secondary suspension. Although this roll stabilizer also causes discomfort, it is necessary to lower cabin roll when cornering. The cabin roll when cornering is covered by J_{ws}^{w2} . So, when adopting a fixed gain controller this value should be lower or equal to that of the passive suspension, which is the case for the setting represented by the pentagon for the case with passive elements, in Figure 7.5. It should be noted, that the work-

ing space requirements for road and chassis disturbances, using the selected controller settings, are similar to that of the validated suspension setting.

7.3.3 State estimation

Given the clear performance potential of the selected fixed gain LQ optimal controller, the question arises how this level of performance can be obtained in practice. The LQ optimal controller requires full state knowledge, while only a few measurements will be typically available. In this subsection the performance degradation using two different sensor configurations in combination with a Kalman filter is investigated.

The sensor configurations are given by

$$\begin{aligned}\underline{y}_2 &= [\phi_c - \phi_f, \dot{\phi}_c]^T + \underline{v}_2 \\ \underline{y}_4 &= [\phi_c - \phi_f, \ddot{\phi}_c, \phi_f - \phi_a, \ddot{\phi}_a]^T + \underline{v}_4,\end{aligned}\tag{7.40}$$

with all components of \underline{v}_2 , \underline{v}_4 zero mean, independent, Gaussian distributed, measurement noise. Note that while the two-sensor setup includes the absolute cabin roll velocity measurement, the four-sensor setup gives the absolute accelerations. While acceleration sensors are typically less expensive, it will be shown that the performance degradation without the angular velocity sensor is quite profound.

From measurements at standstill, Spijkers (2008), of the experimental tractor semi-trailer as described in Chapter 2, it is known that the root-mean-square (rms) values of the sensor noise are approximately

$$\begin{aligned}\tilde{v}_2 &= [\tilde{v}_2^1, \tilde{v}_2^2]^T \\ &= [5.10^{-4} \text{ rad}, 23.10^{-3} \text{ rad/s}]^T \\ \tilde{v}_4 &= [\tilde{v}_4^1, \tilde{v}_4^2, \tilde{v}_4^3, \tilde{v}_4^4]^T \\ &= [5.10^{-4} \text{ rad}, 0.07 \text{ rad/s}^2, 11.10^{-2} \text{ rad}, 0.09 \text{ rad/s}^2]^T.\end{aligned}\tag{7.41}$$

Choosing the weighting matrices

$$\begin{aligned}V_4 &= \begin{bmatrix} (\tilde{v}_4^1/\phi_{max})^2 & 0 & 0 & 0 \\ 0 & (\tilde{v}_4^2/a_\phi^{max})^2 & 0 & 0 \\ 0 & 0 & (\tilde{v}_4^3/\phi_{max})^2 & 0 \\ 0 & 0 & 0 & (\tilde{v}_4^4/a_\phi^{max})^2 \end{bmatrix} \\ V_2 &= \begin{bmatrix} (\tilde{v}_2^1/\phi_{max})^2 & 0 \\ 0 & (\tilde{v}_2^2/v_\phi^{max})^2 \end{bmatrix} \\ Q &= \begin{bmatrix} q_1^2 & 0 & 0 & 0 \\ 0 & q_2^2 & 0 & 0 \\ 0 & 0 & q_3^2 & 0 \\ 0 & 0 & 0 & q_4^2 \end{bmatrix},\end{aligned}\tag{7.42}$$

with $q_1 = 0.01$ [-], $q_2 = q_3 = q_4 = 1$ [-] the approximations of the rms value of the control uncertainty and normalized disturbance inputs \underline{w} respectively, the Kalman filter gains for the two and four sensor configuration can be determined, see Section 6.3.4.

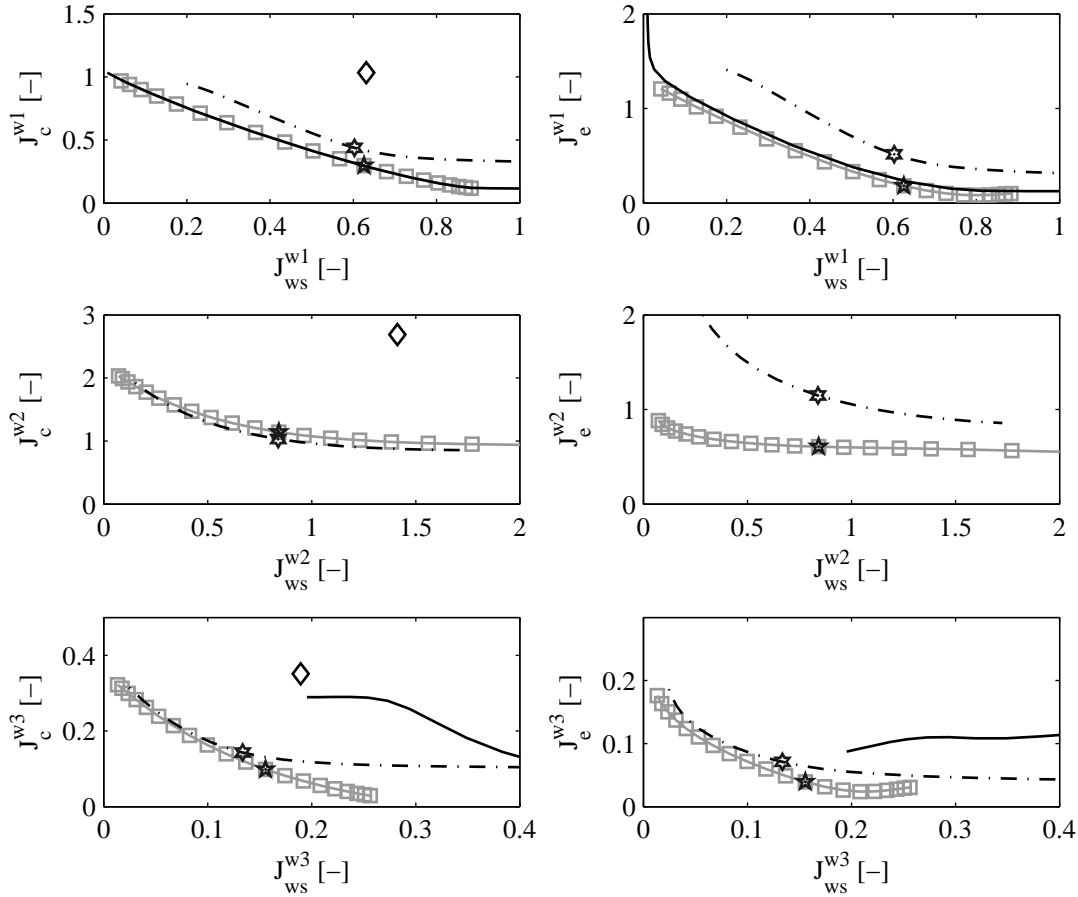


Figure 7.6: Performance diagrams comfort versus working space (left) and energy versus working space (right), resulting from: road disturbance (w_1 , top); cabin disturbance moment (w_2 , mid); and chassis rotations (w_3 , bottom). Passive roll model (diamond) and various active configurations with $c_s = c_s^0/4$, $d_s = d_s^0/2$, $r_1 = r_2$: optimal LQ controller (grey squares) and setting with passive working space requirement (pentagram); 2-sensor optimal LQG controller (dash-dotted) and setting with passive working space requirement (hexagon); 4-sensor optimal LQG controller (solid black).

The performance characteristics using either of the two sensor configurations is given in Figure 7.6. Looking at the performance with respect to road inputs (top), there is some performance degradation visible for the two-sensor setup, while there is none for the four-sensor configuration. On the other hand, when looking at the performance with respect to the other two disturbance sources (mid/bottom), the performance degradation using the four-sensor configuration is huge. However, the two-sensor setup performs much better. This is an indication that the measurement of the cabin roll velocity is truly desirable in a practical setup. Overall, the performance of the two-sensor setup with passive working space requirement (hexagon) is relatively close to that of the LQ controller (pentagram).

Comparing the transfer functions of these fixed gain LQ and two-sensor LQG controllers, as given in Figure 7.7, it can be seen that the main difference occurs at the lower frequencies. This effect can, similar to the case for the vertical dynamics discussed in the previous chapter, be seen as the result of a high-pass filter on the absolute

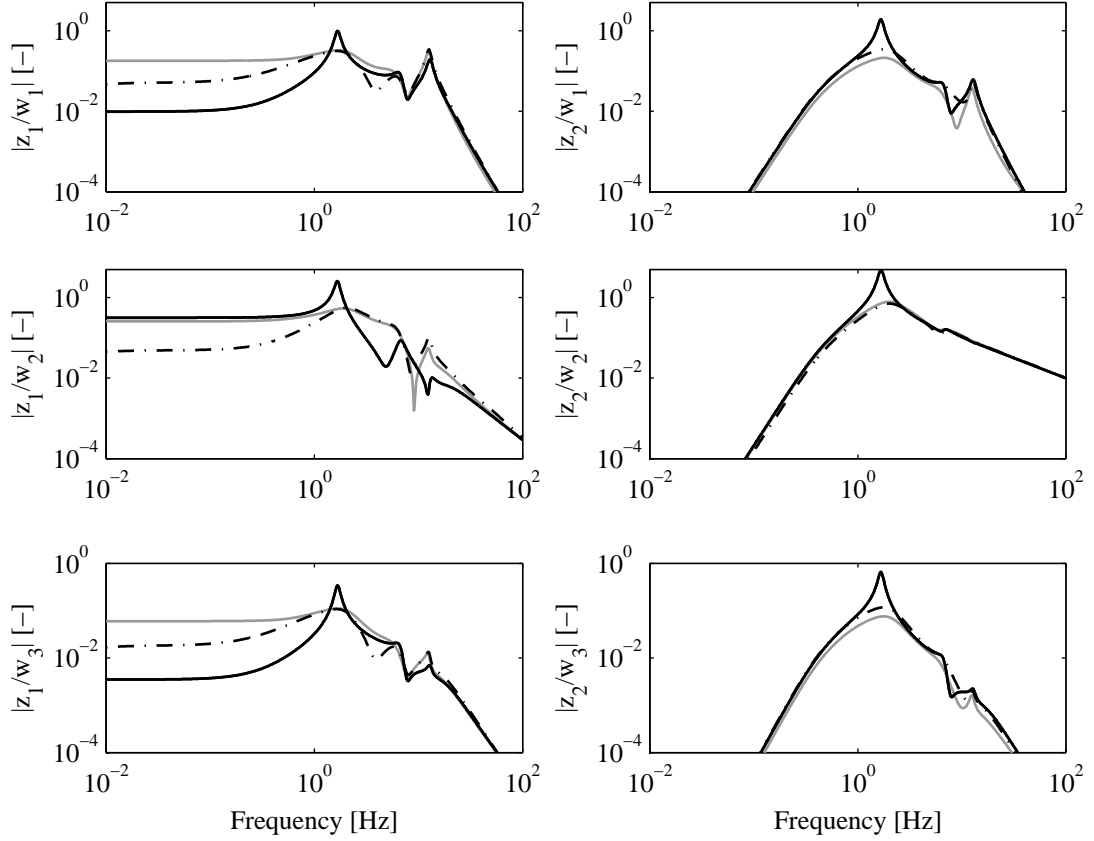


Figure 7.7: Fixed gain controller evaluation quarter truck roll model. Comparison validated passive suspension (black), selected LQ (grey)- and 2-sensor LQG (dash-dotted) optimal controller with $c_s = c_s^0/4$, $d_s = d_s^0/2$. Transfer function from normalized road disturbance to normalized suspension displacement (left) and normalized ISO weighted suspended mass roll acceleration (right).

cabin roll angle estimation. This filter is required to minimize drift, but also results in an estimation error when the steady-state cabin roll angle is unequal to zero. Still, based on these results the selected two-sensor LQG controller is expected to give a level of performance which is close to that obtainable with the selected LQ controller.

7.3.4 Roll disturbance compensation

The roll dynamics are disturbed by the three exogenous inputs given by (7.26). Herein, w_1 depends on the road input which, at present, cannot be predicted accurately without expensive sensors. Similarly, w_3 depends partly on the road input. For the other part, it depends on the drive shaft torque, which is especially noticeable when accelerating or shifting gears. In most modern trucks, the engine moment and gear ratio is available on the CAN-bus, and its influence on the cabin roll can therefore be minimized using a feedforward compensation strategy. However, given the simplicity of the modeled driveline, and the objective to follow the roll and pitch chassis motions caused by driver inputs, this possibility is not further pursued in this dissertation.

The last disturbance input under consideration, w_2 , is a function of the disturbance

moment acting on the cabin. Using (7.4), this moment can be described by

$$M_d^y = l_{cf}\theta_c F_{yf} - l_{cr}\theta_c F_{yr} + r_c(F_{yf} + F_{yr}). \quad (7.43)$$

The first two terms are unknown as θ_c cannot be accurately estimated, see Assumption 7.2.8. However the last term of the disturbance, $r_c(F_{yf} + F_{yr})$, can be estimated. Herein, the driver induced part that causes cabin roll when cornering, $(F_{yf}(\delta_s), F_{yr}(\delta_s))$, is of special interest. If it is possible to separate the driver induced part from the environment induced noise, it should be possible to enforce good chassis roll tracking with a minimal increase in power requirements. However, if the noise is not excluded, the resulting feedforward compensation signal will have a significant high frequent contribution, resulting in an increase in the power requirements when driving on bumpy roads.

Given the relatively slow dynamics when cornering, it can be assumed that

$$\ddot{y}_c(\delta_s) = \ddot{y}_f(\delta_s), \quad (7.44)$$

i.e., the steering induced lateral cabin accelerations equal the steering induced lateral chassis accelerations. Consequently,

$$F_{yf}(\delta_s) + F_{yr}(\delta_s) = m_c \ddot{y}_f(\delta_s), \quad (7.45)$$

and the compensation moment

$$M_{act,ff}^x = -r_c m_c \ddot{y}_f(\delta_s) \quad (7.46)$$

can be used to compensate the additional cabin roll when cornering.

The problem that remains is how to determine $\ddot{y}_f(\delta_s)$. There are two different approaches which can be adopted. These are both shortly discussed.

Model-based estimation

The preferable approach would be to design a model based estimator, which uses the velocity, steer input, yaw-rate and lateral acceleration measurements. For example, a single track vehicle (“bicycle”) model as is given in Figure 7.8 can be adopted to predict the cornering behavior. Herein, δ is the steering angle of the front wheel, α_1 , α_2 are the side slip angles of the front and rear wheel, ψ is the vehicle yaw angle, l_{wb} is the wheel base, V is the vehicle velocity, and F_{y1} , F_{y2} are the front and rear tyre forces respectively.

Assume that: the left and right tyre characteristics can be lumped into a single, equivalent “tyre”; the semi-trailer does not influence the steering dynamics; no body roll; center point steering; constant forward velocity $V_x(\approx V)$; no aerodynamic forces; no slopes, level road surface; small angles δ , α_1 , α_2 ; linear tyre cornering characteristics

$$F_{y1} = C_1 \alpha_1, \quad F_{y2} = C_2 \alpha_2; \quad (7.47)$$

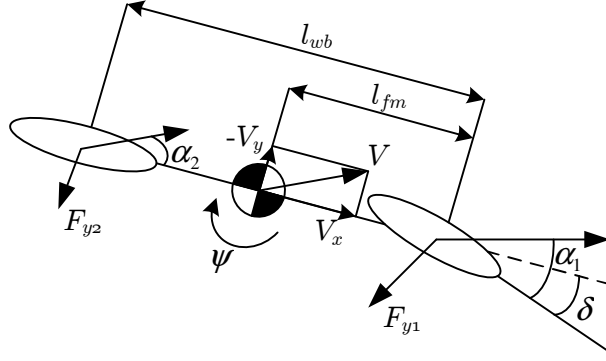


Figure 7.8: Single track vehicle model.

and steady-state cornering, i.e., $\ddot{\psi} = \dot{\delta} = 0$.

In that case, Besselink (2008), the equations of motion can be given by

$$\begin{aligned} m(V_y + V_x \dot{\psi}) &= F_{y1} + F_{y2} \\ J\ddot{\psi} &= l_{fm}F_{y1} - (l_{wb} - l_{fm})F_{y2}, \end{aligned} \quad (7.48)$$

where m is the vehicle mass, J the inertia, and

$$\begin{aligned} \alpha_1 &= \delta - \frac{1}{V_x}(V_y + l_{fm}\dot{\psi}) \\ \alpha_2 &= -\frac{1}{V_x}(V_y - (l_{wb} - l_{fm})\dot{\psi}). \end{aligned} \quad (7.49)$$

After substitution and elimination of V_y ,

$$\begin{aligned} \ddot{\psi} &= \frac{1}{c} \left(\delta - \left(\frac{l_{wb}}{V_x} - mV_x \left(\frac{l_{fm}C_1 - (l_{wb} - l_{fm})C_2}{C_1C_2l_{wb}} \right) \right) \dot{\psi} \right) \\ &= \frac{1}{c} \left(\delta - \frac{l_{wb}}{V_x} \left(1 - \frac{\eta}{gl_{wb}} V_x^2 \right) \dot{\psi} \right), \end{aligned} \quad (7.50)$$

with g the gravity constant, η the understeer coefficient, and

$$\frac{1}{c} = \frac{C_1C_2l_{wb}}{J(C_1 + C_2) + m(l_{fm}^2C_1 + (l_{wb} - l_{fm})^2C_2)}. \quad (7.51)$$

Assuming that the relation between the steering wheel angle δ_s and front wheel steering angle δ is known, the driver induced lateral acceleration at the front wheel can be determined

$$\ddot{y}_f(\delta_s) = l_{fm}\ddot{\psi} + V_x\dot{\psi}. \quad (7.52)$$

This model, combined with velocity; steer input; yaw-rate and lateral acceleration measurements; can be used to estimate the driver induced lateral cabin accelerations. However, its general application is limited due to the assumptions.

For practical use, the estimation model will need to accurately predict the driver induced lateral accelerations under all conditions, so also on banked or low friction road

surfaces. If not, the compensation strategy might actually do more harm than good. As is discussed in Tseng (2001); Best et al. (2000); Gustafsson (1997), it is very difficult to get an accurate prediction under these circumstances. Moreover, the inclusion of play in the steering system may further complicate matters.

Switched low-pass filter

Another approach is to use a switching strategy, which enables the disturbance compensation when an imminent steering maneuver is “sensed”. In that case, it may suffice to simply use a low-pass filtered version of the lateral chassis acceleration as estimate for $\ddot{y}_f(\delta_s)$, assuming that the low-frequent driver induced accelerations dominate the signal. This approach is adopted later on, to demonstrate the potential of the disturbance compensation. The driver steer input is assumed to mainly cover the frequency band up to 5 Hz. Therefore, the lateral chassis accelerations are filtered with a 5 Hz low-pass filter. The resulting compensation signal is only “switched on” when evaluating steering maneuvers. The challenge remains to design either a switching- or an accurate estimation strategy that works in practice.

7.4 Pitch-heave control

In this section an LQG controller with disturbance compensation for the pitch-heave direction is designed. It is based on the half truck pitch-heave model shown in Figure 7.9, and a comfort-energy-suspension travel multi-objective performance criterium, see also Section 1.4. First the control problem is formulated, followed by the presentation of the LQ optimal controller and the evaluation of its characteristics. After that, the case of limited state knowledge is considered, wherein the performance degradation using state estimation is studied. Finally, an estimator is designed for the longitudinal cabin acceleration induced by driver acceleration and braking, which can be used to reduce the influence of the pitch disturbance.

7.4.1 Pitch-heave control problem

Writing the control problem in the generalized or standard plant formulation, see Figure 6.5, the problem is to find a control K , which based on \underline{y} generates a control signal \underline{u} , that minimizes the influence of \underline{w} on \underline{z} . For the pitch-heave model as depicted in Figure 7.9, the exogenous inputs are given by

$$\underline{w} = [w_1, w_2, w_3, w_4]^T = [\dot{z}_{rf}/w_{max}, \dot{z}_{rr}/w_{max}, \dot{x}_T/v_{max}, F_d/(m_c a_{max})]^T, \quad (7.53)$$

where w_1, w_2 is the normalized front and rear vertical road velocity respectively, w_3 is the normalized longitudinal chassis velocity, and w_4 is the normalized disturbance force. Herein, the components of \underline{w} are assumed to be zero mean, gaussian distributed (white noise), uncorrelated signals. The correlation between the front and rear wheels

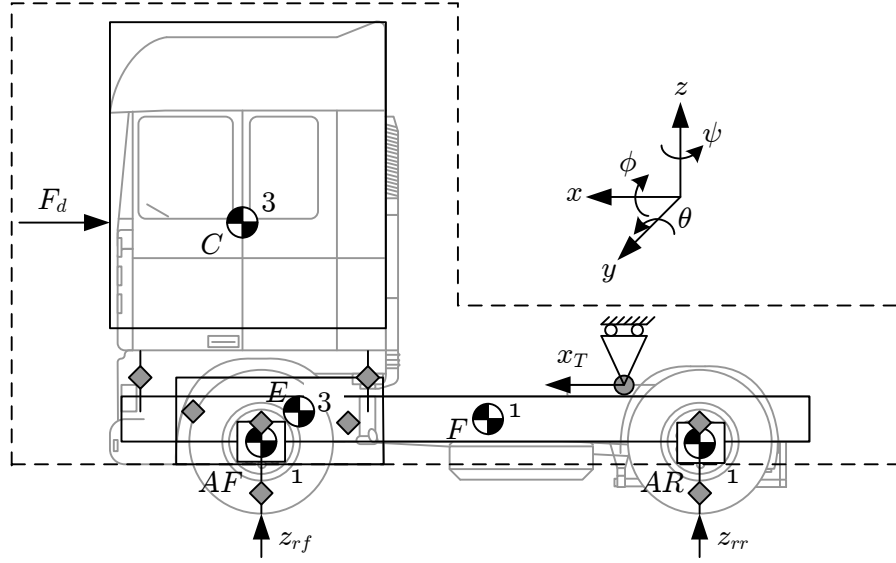


Figure 7.9: Half truck pitch-heave model.

is not included for reasons of simplicity and the desire to obtain a fixed gain controller setting that is independent of the longitudinal velocity of the vehicle.

The weighted performance variables are given by

$$\underline{z} = [z_1, \dots, z_7]^T = \left[\frac{z_c^f - z_f^f}{s_{max}}, \frac{z_c^r - z_f^r}{s_{max}}, \frac{\ddot{x}_c^{iso}}{a_{max}}, \frac{\ddot{z}_c^{iso}}{a_{max}}, \frac{\ddot{\theta}_c^{iso}}{a_{\theta}^{max}}, u_1, u_2 \right]^T, \quad (7.54)$$

with control inputs $\underline{u} = [u_1, u_2] = [\dot{F}_{act}^F / (m_c j_{max}), \dot{F}_{act}^R / (m_c j_{max})]$. The maximum values are chosen as

$$[s_{max}, v_{max}, v_{\theta}^{max}, w_{max}, a_{max}, a_{\theta}^{max}, j_{max}]^T = [0.04, 0.01, 1, 0.1, 2, 10, 100]^T, \quad (7.55)$$

where $s, [v, w], a, j$ stand for suspension displacement, velocity, acceleration, and jerk respectively.

Assuming full state knowledge, the standard plant P can be written as

$$P : \begin{cases} \dot{\underline{x}} = A\underline{x} + B\underline{u} + G\underline{w} \\ \underline{y} = \underline{x} \\ \underline{z} = E\underline{x} + N\underline{u}. \end{cases} \quad (7.56)$$

The state is chosen as

$$\begin{aligned} \underline{x} &= [z_{rf}, z_{rr}, x_T, \underline{x}_h, \dot{\underline{x}}_h, \frac{F_{act}^F}{m_c}, \frac{F_{act}^R}{m_c}, \underline{x}_{iso}^x, \underline{x}_{iso}^z, \underline{x}_{iso}^{\theta}]^T \\ \underline{x}_h &= [z_{af}, z_{ar}, \theta_f, x_e, z_e, \theta_e, x_c, z_c, \theta_c]^T, \end{aligned} \quad (7.57)$$

with \underline{x}_{iso}^z the state belonging to the ISO vertical comfort approximation given in (6.14). The ISO pitch and roll comfort filters are identical, so the state of the ISO pitch comfort

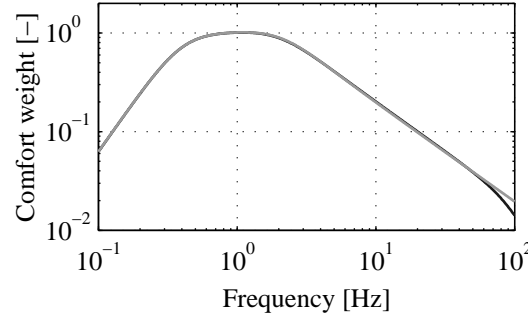


Figure 7.10: ISO 2621 weighting curve for the longitudinal acceleration (black), ISO 2631-1 (1997), and the fourth order approximation (grey).

approximation $\underline{x}_{iso}^\theta$ is also obtained from (7.34). Furthermore, \underline{x}_{iso}^x is the state belonging to the ISO longitudinal comfort approximation given by

$$\begin{aligned}\dot{\underline{x}}_{iso}^x &= A_{iso}\underline{x}_{iso}^x + B_{iso}\ddot{x}_c \\ \ddot{x}_c^{iso} &= C_{iso}\underline{x}_{iso}^x,\end{aligned}\tag{7.58}$$

which is the reduced (fourth) order approximation of the (seventh order) ISO longitudinal acceleration weighting function,

$$W_{iso}^x(s) = \frac{12.3s^3 + 172s^2}{s^4 + 24s^3 + 250s^2 + 740s + 1082}.\tag{7.59}$$

The approximation is obtained by balanced residualization, see (Skogestad and Postlethwaite, 2005, section 11.4), using the MATLAB function *balred.m*, and is depicted in Figure 7.10. Furthermore, the matrices in (7.56) are given by

$$\begin{aligned}A &= \begin{bmatrix} A_h & B_h & 0_{[21 \times 4]} & 0_{[21 \times 4]} & 0_{[21 \times 4]} \\ 0_{[2 \times 21]} & 0_{[2 \times 2]} & 0_{[2 \times 4]} & 0_{[2 \times 4]} & 0_{[2 \times 4]} \\ B_{iso}^x A_h(19, :) & B_{iso}^x B_h(19, :) & A_{iso}^x & 0_{[2 \times 4]} & 0_{[2 \times 4]} \\ B_{iso}^z A_h(20, :) & B_{iso}^z B_h(20, :) & 0_{[2 \times 4]} & A_{iso}^z & 0_{[2 \times 4]} \\ B_{iso}^\theta A_h(21, :) & B_{iso}^\theta B_h(21, :) & 0_{[2 \times 4]} & 0_{[2 \times 4]} & A_{iso}^\theta \end{bmatrix} \\ B &= \begin{bmatrix} 0_{[21 \times 2]} \\ \begin{bmatrix} j_{max} & 0 \\ 0 & j_{max} \end{bmatrix} \\ 0_{[12 \times 2]} \end{bmatrix} \quad G = \begin{bmatrix} G_h \\ 0_{[2 \times 4]} \\ B_{iso}^x G_h(19, :) \\ B_{iso}^z G_h(20, :) \\ B_{iso}^\theta G_h(21, :) \end{bmatrix} \quad N = \begin{bmatrix} 0_{[5 \times 2]} \\ \begin{bmatrix} 1 & 0 \\ 0 & 1 \end{bmatrix} \end{bmatrix} \\ E &= \left[\begin{array}{cc|cc|cc|cc} \underline{0}_5^T & \frac{l_{f5} + l_{am}}{s_{max}} & \underline{0}_4^T & s_{max}^{-1} & -\frac{l_{cf}}{s_{max}} & \underline{0}_{11}^T & \underline{0}_4^T & \underline{0}_4^T & \underline{0}_4^T \\ \underline{0}_5^T & \frac{l_{f5} + l_{am} - l_{cf} - l_{cr}}{s_{max}} & \underline{0}_4^T & s_{max}^{-1} & \frac{l_{cr}}{s_{max}} & \underline{0}_{11}^T & \underline{0}_4^T & \underline{0}_4^T & \underline{0}_4^T \\ & & \underline{0}_{12}^T & & & \underline{0}_{11}^T & \frac{C_{iso}^x}{a_{max}} & \underline{0}_4^T & \underline{0}_4^T \\ & & \underline{0}_{12}^T & & & \underline{0}_{11}^T & \underline{0}_4^T & \frac{C_{iso}^z}{a_{max}} & \underline{0}_4^T \\ & & \underline{0}_{12}^T & & & \underline{0}_{11}^T & \underline{0}_4^T & \underline{0}_4^T & \frac{C_{iso}^\theta}{a_\theta^{max}} \\ & 0_{[2 \times 12]} & & & & 0_{[2 \times 11]} & 0_{[2 \times 4]} & 0_{[2 \times 4]} & 0_{[2 \times 4]} \end{array} \right],\end{aligned}\tag{7.60}$$

with K_h , D_h , M_h as given in (3.10) and

$$A_h = \begin{bmatrix} \begin{bmatrix} -\beta_r & 0 & 0 \\ 0 & -\beta_r & 0 \\ 0 & 0 & -\beta_T \end{bmatrix} & 0_{[3 \times 9]} & 0_{[3 \times 9]} \\ 0_{[9 \times 3]} & 0_9 & I_9 \\ A_h^{13} & -M_h^{-1}K_h & -M_h^{-1}D_h \end{bmatrix}. \quad (7.61)$$

Herein, β_r and β_T are the filter frequencies of the first order low-pass filters describing the first three disturbance inputs. Ideally these filters would not be needed and the road vertical velocity would be modeled as white noise. However, in that case the system is not feedback stabilizable, as the road filter is not influenced by the controller. Using stable road filters, i.e. $(\beta_r, \beta_T) > 0$, this problem is overcome. Therefore small values are chosen: $\beta_T = \beta_r = 0.2\pi$ rad/s. Furthermore,

$$A_h^{13} = \begin{bmatrix} \frac{c_{tf}}{m_{af}} & 0 & 0 & 0 & \underline{0}_2^T & 0 & 0 & 0 \\ 0 & \frac{c_{tr}}{m_{ar}} & 0 & 0 & \underline{0}_2^T & 0 & 0 & 0 \\ 0 & 0 & \frac{z_{f5}}{J_f^*}(c_{ef}^x + c_{er}^x + c_{sf}^x) & \frac{c_{ef}^x + c_{er}^x}{m_e} & \underline{0}_2^T & \frac{c_{sf}^x}{m_c} & 0 & -\frac{z_{cf}}{J_c}c_{sf}^x \end{bmatrix}^T, \quad (7.62)$$

$$B_h = \begin{bmatrix} 0_{[14 \times 2]} \\ \begin{bmatrix} \frac{m_c}{J_f^*}(l_{f5} + l_{am}) & \frac{m_c}{J_f^*}(l_{f5} + l_{am} - l_{cf} - l_{cr}) \end{bmatrix} \\ 0_{[4 \times 2]} \\ \begin{bmatrix} 1 & 1 \\ -\frac{m_c}{J_c}l_{cf} & \frac{m_c}{J_c}l_{cr} \end{bmatrix} \end{bmatrix}, \quad (7.63)$$

and

$$G_h = \begin{bmatrix} w_{max}\beta_r & 0 & 0 & \left| \underline{0}_9^T \right| \\ 0 & w_{max}\beta_r & 0 & \left| \underline{0}_9^T \right| \\ 0 & 0 & v_{max}\beta_T & \left| \underline{0}_9^T \right| \\ 0 & 0 & 0 & \left| \underline{0}_9^T \right| \end{bmatrix}^T G_h^B$$

$$G_h^B = \begin{bmatrix} \underline{0}_2^T & 0 & 0 & \underline{0}_2^T & 0 & 0 & 0 & 0 \\ \underline{0}_2^T & 0 & 0 & \underline{0}_2^T & 0 & 0 & 0 & 0 \\ \underline{0}_2^T & \frac{z_{f5}v_{max}}{J_f^*}(d_{ef}^x + d_{er}^x + d_{sf}^x) & \frac{c_{ef}^x + c_{er}^x}{m_e}v_{max} & \underline{0}_2^T & \frac{v_{max}}{m_c}d_{sf}^x & 0 & -\frac{v_{max}z_{cf}}{J_c}d_{sf}^x \\ \underline{0}_2^T & 0 & 0 & \underline{0}_2^T & -a_{max} & 0 & 0 \end{bmatrix}. \quad (7.64)$$

It is chosen to look for the controller that minimizes the influence of \underline{w} on \underline{z} in a two-norm sense. More specifically, the controller that minimizes

$$J_h = \int_0^\infty (z_1^2 + z_2^2 + r_1(z_3^2 + z_4^2 + \left(\frac{a_\theta^{max}}{a_{max}}k_\theta\right)^2 z_5^2) + r_2(z_6^2 + z_7^2))dt, \quad (7.65)$$

where r_1 is the comfort weighting, r_2 is the energy weighting and k_θ is the pitch comfort multiplying factor used in (1.1).

7.4.2 Pitch-heave optimal solution

The control problem, as posed in the previous subsection, is solved using LQ optimization. Furthermore, the performance evaluation criteria, which are influenced by all disturbances \underline{w} , are determined as

$$\begin{aligned} J_{ws}^{wi} &= \sqrt{\int_{\omega_{\min}}^{\omega_{\max}} (|H_{z_1/w_i}(\omega)|^2 + |H_{z_2/w_i}(\omega)|^2) d\omega} \\ J_c^{wi} &= \sqrt{\int_{\omega_{\min}}^{\omega_{\max}} (|H_{z_3/w_i}(\omega)|^2 + |H_{z_4/w_i}(\omega)|^2 + \left(\frac{a_{\theta}^{max}}{a_{max}} k_{\theta}\right)^2 |H_{z_5/w_i}(\omega)|^2) d\omega} \quad (7.66) \\ J_e^{wi} &= \sqrt{\int_{\omega_{\min}}^{\omega_{\max}} (|H_{z_6/w_i}(\omega)|^2 + |H_{z_7/w_i}(\omega)|^2) d\omega}, \end{aligned}$$

with $i \in [1, \dots, 4]$, ws working space, c comfort, e energy, and H_{z_j/w_i} the transfer from w_i to z_i . So, it is assumed that the rms allowable suspension travel at the front and rear is equal, which holds for the chosen *eLPAS* configuration.

First, the case is considered without additional passive suspension elements ($d_s = 0$ and $c_s = 0$) in which case the *eLPAS* effective stiffness is also assumed to be zero. The performance characteristics are evaluated for: very low comfort weighting and various energy weights (energy optimal); low energy weighting and various comfort weights (comfort optimal); and various equal weights ($r_1 = r_2$). The main focus will be on the influence of the disturbances w_1 and w_3 . The characteristics for w_2 and w_4 are somewhat similar to those of w_1 and w_3 respectively.

The results are given in Figure 7.11. It can be seen that while each configuration outperforms the validated passive setting, the largest comfort gain can be obtained with the comfort optimal setting. However, in that case the energy requirements to suppress disturbances w_2 are very large. The controllers with equal weights $r_1 = r_2$ offer a good compromise: a significant comfort gain with respect to the energy optimal controllers with nearly the same energy requirements.

Next, using the performance characteristics of the controllers with equal weights as reference, the influence of adding passive suspension elements is investigated. The characteristics as given in Figure 7.12 show that, while adding the *eLPAS* effective stiffness seems to have little influence, also adding some damping seems again to be desirable from an energy point of view. Herein, the ratio of the front and rear passive damping is an important variable. When crossing a bump, the chassis mainly pitches around the trailer hitch point. Consequently, the secondary suspension velocity is larger at the front than at the rear. Taking this into account, the cabin pitch resulting from road bumps and potholes can be decreased. Choosing

$$d_{sf} = d_{sr} \left(1 - \frac{l_{cr} + l_{cf}}{l_{f5} + l_{am}} \right), \quad (7.67)$$

with the lengths as specified in Figure A.4, the damping forces at the front and rear of the cabin are equal when excited by any θ_f .

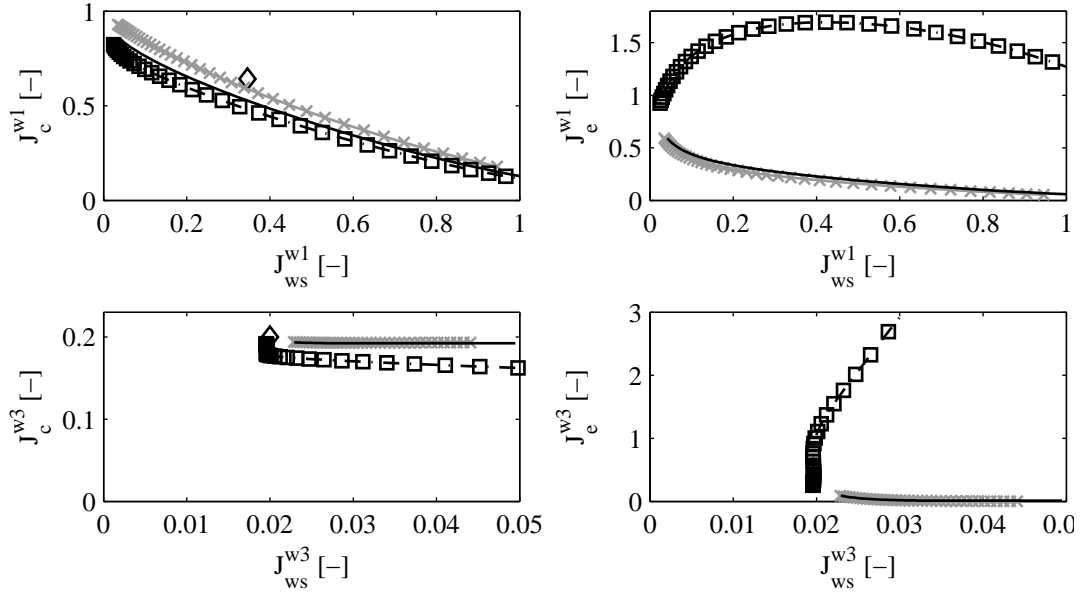


Figure 7.11: Performance diagrams comfort versus working space (left) and energy versus working space (right), resulting from: road disturbance (w_1 , top); and longitudinal tractor motions (w_3 , bottom). Different configurations pitch-heave model: passive (diamond); energy optimal LQ controller with $r_1 = 1.10^{-6}$ (grey crosses); comfort optimal LQ controller with $r_2 = 1.10^{-3}$ (dashed-dotted, squares); and optimal LQ controller with $r_1 = r_2$ (solid black).

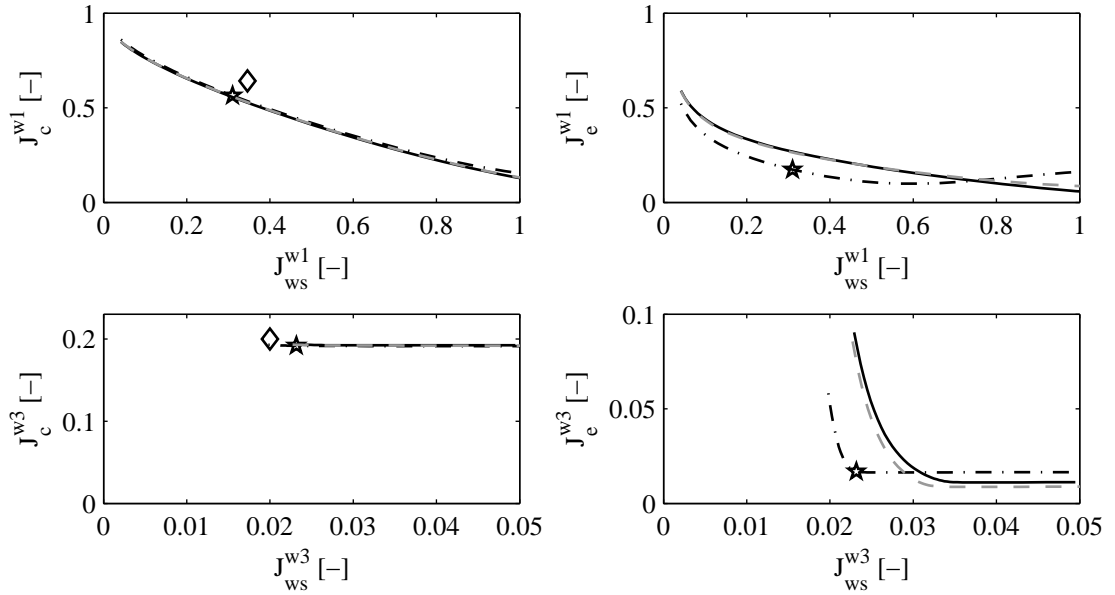


Figure 7.12: Performance diagrams comfort versus working space (left) and energy versus working space (right), resulting from: road disturbance (w_1 , top); and longitudinal tractor motions (w_3 , bottom). Different configurations pitch-heave model: validated passive (diamond); optimal LQ controller with $r_1 = r_2$ (solid black); optimal LQ controller with $r_1 = r_2$ and $c_s = c_s^{eLPAS}$ (dashed grey); optimal LQ controller with $r_1 = r_2$ and $c_s = c_s^{eLPAS}$, $[d_s^F, d_s^R] = [2261, 4327]$ Ns/m (dash-dotted), and setting with passive working space requirement (pentagon).

7.4.3 State estimation for pitch-heave control

The LQ optimal controller requires full state knowledge, while only partial state measurements will be typically available. The performance degradation using various sensor configurations in combination with a Kalman filter has been studied. One particularly promising configuration, with a relatively low number of sensors and offering good results, is presented in this subsection. This five sensor configuration is given by

$$\underline{y}_5 = [z_c^f - z_f^f, z_c^r - z_f^r, \dot{\theta}_c, \ddot{z}_{af}, \ddot{z}_c]^T + \underline{v}_5, \quad (7.68)$$

with \underline{v}_5 a vector with zero mean, independent, Gaussian distributed, measurement noise. While acceleration sensors are typically less expensive, the performance degradation without the angular velocity sensor was again found to be quite profound.

From measurements at standstill, Spijkers (2008), of the experimental tractor semi-trailer as described in Chapter 2, it is known that the rms values of the sensor noise are approximately

$$\begin{aligned} \underline{v}_5 &= [v_5^1, v_5^2, v_5^3, v_5^4, v_5^5]^T \\ &= [1.10^{-4} \text{ m}, 1.10^{-4} \text{ m}, 25.10^{-4} \text{ rad/s}, 0.1 \text{ m/s}^2, 0.04 \text{ m/s}^2]^T. \end{aligned} \quad (7.69)$$

Although these values may be larger when using cheaper commercially viable sensors, they are used here to evaluate the concept. Choosing the weighting matrices

$$V_5 = \begin{bmatrix} (v_5^1/s_{max})^2 & 0 & 0 & 0 & 0 \\ 0 & (v_5^2/s_{max})^2 & 0 & 0 & 0 \\ 0 & 0 & (v_5^3/v\theta_{max})^2 & 0 & 0 \\ 0 & 0 & 0 & (v_5^4/a_{max})^2 & 0 \\ 0 & 0 & 0 & 0 & (v_5^5/a_{max})^2 \end{bmatrix}, \quad (7.70)$$

and

$$Q = \begin{bmatrix} q_1^2 & 0 & 0 & 0 & 0 \\ 0 & q_2^2 & 0 & 0 & 0 \\ 0 & 0 & q_3^2 & 0 & 0 \\ 0 & 0 & 0 & q_4^2 & 0 \\ 0 & 0 & 0 & 0 & q_5^2 \end{bmatrix}, \quad (7.71)$$

with $q_1 = 0.01$ [-], $q_2 = q_3 = q_4 = q_5 = 1$ [-] the approximations of the rms values of the control uncertainty and normalized disturbance inputs w respectively, the Kalman filter gain can be determined.

The performance characteristics using the five sensor configurations is given in Figure 7.13. Looking at the performance with respect to road inputs (top), there is little performance degradation visible. On the other hand, when looking at the performance with respect to the longitudinal disturbance, the performance degradation is more substantial with respect to the energy requirements. Still, overall this LQG controller promises good results with a limited number of sensors.

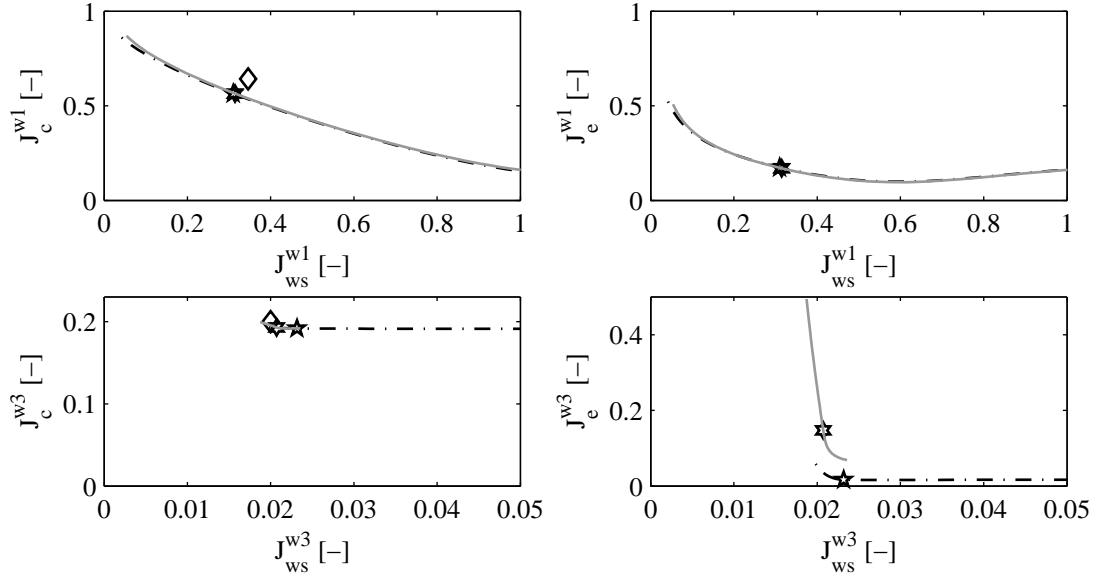


Figure 7.13: Performance diagrams comfort versus working space (left) and energy versus working space (right), resulting from: road disturbance (w_1 , top); and longitudinal tractor motions (w_3 , bottom). Different configurations pitch-heave model: passive (diamond); optimal LQ controller with $r_1 = r_2$ and $c_s = c_s^{eLPAS}$, $[d_s^F, d_s^R] = [2261, 4327]$ Ns/m (dash-dotted), and setting with passive working space requirement (pentagon); 5-sensor optimal LQG controller with $r_1 = r_2$ and $c_s = c_s^{eLPAS}$, $[d_s^F, d_s^R] = [2261, 4327]$ Ns/m (dashed grey), and setting with passive working space requirement (hexagon).

The transfer functions for the LQ and LQG selected fixed gain controller settings, the pentagram and hexagram respectively in Figure 7.13, are shown in Figure 7.14. Clearly, the main differences between the two are with respect to longitudinal disturbances w_3 . Not surprisingly, the differences between the longitudinal accelerations z_3 for the validated and LQG setting are marginal. The largest comfort enhancement can be found in the ISO weighted pitch acceleration z_5 , which is significantly reduced with the LQG controller in comparison to the validated setting.

7.4.4 Disturbance compensation

The pitch-heave dynamics are disturbed by the four exogenous inputs given in (7.53). Herein, w_1 , w_2 , and w_3 depend on the road input and cannot be accurately predicted without additional expensive sensors. Therefore, the compensation of these is not further investigated, although there is clear potential, see for example Huisman (1994); Jones (2005).

On the other hand, w_4 is a function of the longitudinal disturbance force acting on the cabin. Using (7.4), the resulting disturbance moment in pitch can be described by

$$M_d^y = -(l_{cf}\theta_s + r_c)F_x. \quad (7.72)$$

Herein, under Assumption 7.2.8, θ_s is considered to be unknown. The other term, $-r_c F_x$ can be estimated. Again, the driver induced part, which causes cabin pitch when

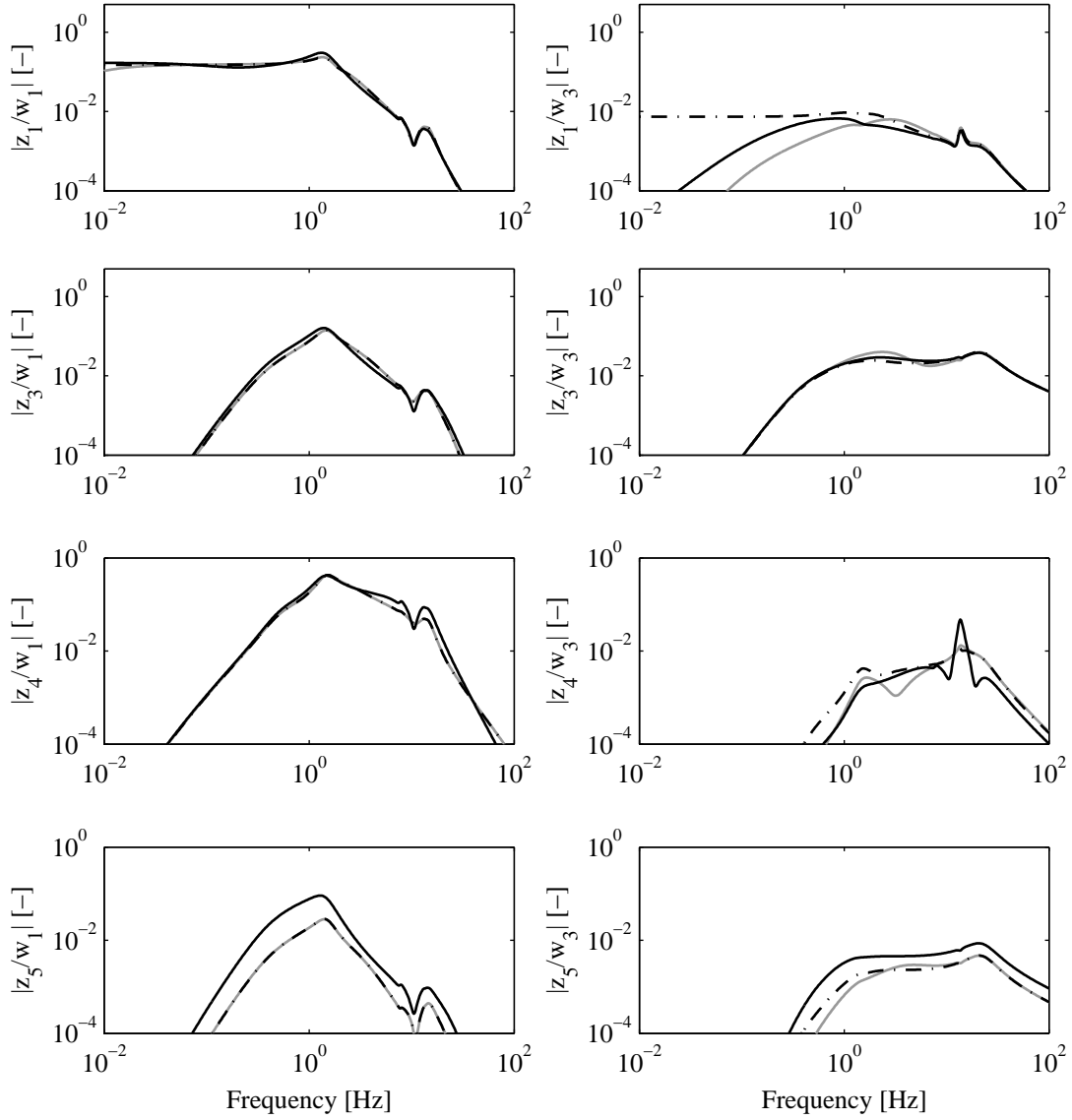


Figure 7.14: Fixed gain controller evaluation quarter truck pitch-heave model. Comparison passive suspension (black), selected LQ (dash-dotted)-, and 5-sensor LQG (grey) optimal controller with $c_s = c_s^{eLPAS}$, $[d_s^F, d_s^R] = [2261, 4327]$ Ns/m. Transfer functions from normalized road disturbance (left) and normalized longitudinal tractor motions (right) to: normalized front suspension displacement (z_1 , top); normalized ISO weighted longitudinal cabin acceleration (z_3 , second from top); normalized ISO weighted vertical cabin acceleration (z_4 , third from top); and normalized ISO weighted cabin pitch acceleration (z_5 , bottom).

braking or accelerating ($F_x(\delta_{ab})$), is of special interest. If it can be separated from the environmental noise contribution, it should be possible to enforce good chassis pitch tracking with a minimal increase in power requirements.

Under steady-state conditions

$$\ddot{x}_c(\delta_{ab}) = \ddot{x}_f(\delta_{ab}), \quad (7.73)$$

with δ_{ab} the driver induced acceleration and brake input. In other words, the driver induced longitudinal cabin accelerations equal the driver induced chassis accelerations.

Consequently,

$$F_x(\delta_{ab}) = F_{aero}^x(\delta_{ab}) + m_c \ddot{x}_f(\delta_{ab}), \quad (7.74)$$

where $F_{aero}^x(\delta_{ab})$ is the driver induced aerodynamic disturbance force, recall (2.2), given by

$$F_{aero}^x(\delta_{ab}) = \frac{1}{2} \rho A C_d \dot{x}_f(\delta_{ab}). \quad (7.75)$$

Therefore, the compensation moment

$$M_{act,ff}^y = r_c \left(m_c \ddot{x}_f(\delta_{ab}) + \frac{1}{2} \rho A C_d \dot{x}_f(\delta_{ab}) \right) \quad (7.76)$$

can be used to compensate the additional cabin pitch when the longitudinal velocity changes.

The problem that remains is how to determine $\ddot{x}_f(\delta_{ab})$ and $\dot{x}_f(\delta_{ab})$. The preferable approach would be to design a model based estimator, which accurately predicts the driver induced longitudinal velocity and acceleration under all conditions, even on graded or low friction road surfaces. However, similar to the case for the roll compensation, and as is discussed in Vahidi et al. (2005), it is very difficult to get an accurate prediction under these circumstances.

The alternative is to use a switching strategy, which enables the disturbance compensation when an imminent braking or accelerating maneuver is “sensed”. In that case, it may suffice to simply use a low-pass filtered version of the longitudinal chassis velocity and acceleration as estimates for $\dot{x}_f(\delta_{ab})$ and $\ddot{x}_f(\delta_{ab})$ respectively, assuming that the low-frequent driver induced accelerations dominate the signal. This approach is adopted to demonstrate the potential of the disturbance compensation. The driver inputs are assumed to be limited to 5 Hz and the signals are filtered with a 5 low-pass filter. The resulting compensation signal is only “switched on” when evaluating accelerating or braking maneuvers. The challenge remains to design either a good switching- or an accurate estimation strategy that works in practice.

7.5 Full vehicle modal controller evaluation

In this section, the *eLPAS* actuators are implemented in the 44 DOF tractor semi-trailer model. Using these combined models various modal control strategies are evaluated for the range of driving conditions discussed in Chapter 2. First, the implementation is discussed, followed by the performance evaluation when driving over a bump. Secondly, the comfort and power requirements are evaluated on a relatively smooth and a very rough road. Finally, the performance is evaluated when braking, steering, and accelerating; and the performance potential using disturbance compensation is illustrated.

7.5.1 Implementation

From the analysis in the previous sections, it follows that it is desirable to have some passive stiffness and damping in parallel to the *eLPAS* system. More specifically, it is suggested to include a roll stabilizer with a stiffness equal to 25% of the passive vehicle; and dampers at the front and rear with damping coefficients 2261 and 4327 Ns/m respectively. These elements have been added to the simulation model.

The various controllers that are evaluated require various measurements. In the case of the LQG controllers, assumptions on the magnitude of the measurement noise are included. However, no measurement noise is added in the following simulations to facilitate understanding of the observed responses. Furthermore, the 10 Hz first order low-pass filters in the *eLPAS* force control loops, see Section 5.4.3, are not included.

Implementation of the LQG controllers presents a challenge as these generate a control signal related to \dot{F}_{act}^{ref} , while the *eLPAS* actuators require F_{act}^{ref} . Simple integration will result in large estimation errors when the actuators reach their maximum force variation bounds. Therefore, the LQ control input needs to be bounded, and this bounded value is fed back to the state estimator. Moreover, for the pitch-heave loop, if \dot{F}_{act}^F is saturated while \dot{F}_{act}^R is not - which frequently happens when crossing bumps - the cabin may experience excessive pitching.

For that reason, it is decided to bound the modal inputs \dot{F}_{act}^z , \dot{M}_{act}^y , and \dot{M}_{act}^x , using (7.15) and (7.16). The saturation bounds are chosen as

$$\begin{aligned} \max \dot{F}_{act}^z &= 12000 \text{ N/s} \\ \max \dot{M}_{act}^x &= 8000 \text{ Nm/s} \\ \max \dot{M}_{act}^y &= 12000 \text{ Nm/s}, \end{aligned} \tag{7.77}$$

which enforces that all $\dot{F}_{act}^{ref} \leq 10000 \text{ N/s}$. Furthermore, the integrated control input ($\int_0^t \dot{F}_{act}^{ref} dt$) is bounded to the *eLPAS* force range, such that for each actuator $0 \leq F_{act}^{ref} \leq 6500 \text{ N}$. The alternative, of bounding the modal integrated control inputs F_{act}^z , M_{act}^y , and M_{act}^x such that $0 \leq F_{act}^{ref} \leq 6500 \text{ N}$, is not adopted as the resulting modal input ranges would be too restrictive during extreme maneuvers.

In the previous sections, LQG control gains are selected which have the same working space requirements as the validated passive setting. However, implementation of these control gains in combination with the roll, pitch-heave decoupling (7.11) does not provide good performance in the 44 DOF model. In case of a road obstacle, the cabin starts an oscillatory roll motion after hitting a bump, and the pitch-heave accelerations are also significantly larger than those of the passive vehicle. The poor performance of the roll controller is expected to be mainly the effect of the model inaccuracies. On the other hand, for the pitch-heave performance, the nonlinear actuator characteristics when the control inputs saturate may be to blame. So, although informative, this result is disappointing.

To obtain a control configuration that does enhance performance for the considered conditions, the LQG pitch-heave setting is selected with $J_c^{w1} = 0.9$, which is approxi-

mately three times larger than the validated passive setting. Furthermore, the single mass energy optimal control structure

$$\frac{M_{act}^y}{J_c} = -c_1 \int_0^t (\phi_c - \phi_f) dt - c_2 \int_0^t \dot{\phi}_c|_{hpf} dt - c_3 \dot{\phi}_c, \quad (7.78)$$

is adopted as roll controller, with the control gains tuned manually as $c_1 = 20 \text{ s}^{-3}$, $c_2 = 20 \text{ s}^{-2}$, $c_3 = 10 \text{ s}^{-1}$ and $\dot{\phi}_c|_{hpf}$ the high-pass filtered cabin roll velocity, where the filter pole is located at 0.2 Hz. This combination of single mass energy optimal roll controller and LQG pitch-heave controller is labeled as “tuned LQG” controller. In the following evaluation its performance is compared to that of the modal skyhook controller (7.25), where the control gains have been tuned to mimic the tuned LQG suspension travel requirements as

$$\begin{array}{lll} c_1^z & = 200.000 & c_2^z = 240.000 & c_3^z = 35000 \\ c_1^\phi & = 40.000 & c_2^\phi = 0 & c_3^\phi = 40000 \\ c_1^\theta & = 100.000 & c_2^\theta = 140.000 & c_3^\theta = 50000 \end{array} \quad (7.79)$$

This modal skyhook controller is inspired by the single mass comfort optimal control results of the previous chapter and serves as a benchmark setting. Furthermore, a second order 10 Hz Butterworth filter has been added to each of the modal control inputs to limit the energy requirements.

Finally, for the attitude tests the two control strategies are also evaluated when including the driver induced disturbance compensation. Herein, the disturbance compensation is embedded in the decoupling procedure.

7.5.2 Road obstacles

The first event under consideration is the case when driving over a one-sided pyramid shaped bump, at 15 km/h. The response for the various suspension configurations is given in Figure 7.15. The bump is hit at $t = 5$ seconds. The response before that time is related to the fact that the simulation uses the measured velocity and steering inputs, as discussed in Chapter 2.

Comparing the responses, it can be seen that both active configurations significantly reduce the ISO weighted accelerations. While the ISO weighted roll and pitch accelerations with the tuned LQG are somewhat larger, the vertical accelerations are lower than with the modal skyhook controller. Consequently, the comfort increase is relatively similar: the RCI (1.1) is reduced with 37% with respect to the passive setting for both; and the VDV (1.3) is reduced by 17% and 18% for the tuned LQG and modal skyhook controller respectively. The crest factors are between 3 and 5, indicating that the RCI can be used.

It should be noted that the vertical cabin position and orientation, which are given to clarify the overall response, do not directly influence the performance criteria for this event. They are, however, related to the suspension travel, which is depicted in Figure

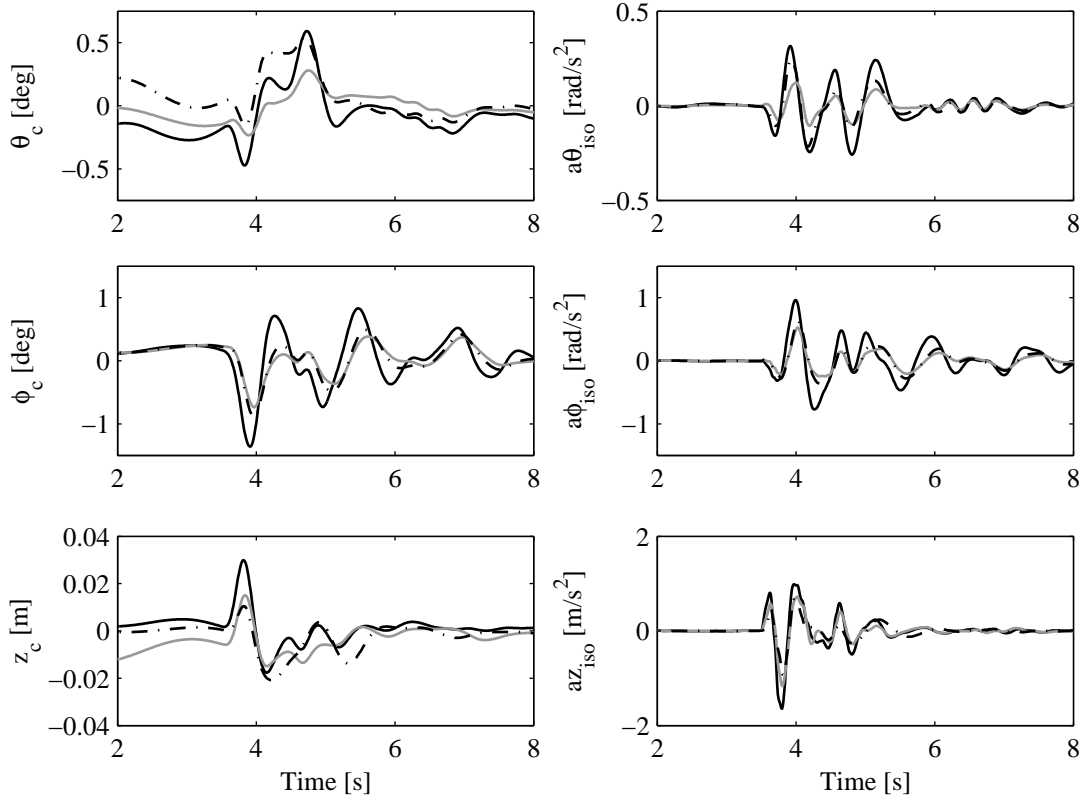


Figure 7.15: Fixed gain controller evaluation tractor semi-trailer model when driving over a pyramid obstacle at 15 km/h. Comparison passive suspension (grey), tuned LQG (dash-dotted) controller, and modal skyhook controller (solid black). Absolute cabin pitch angle (top-left), ISO weighted pitch acceleration (top-right), absolute roll angle (mid-left), ISO weighted roll acceleration (mid-right), absolute vertical position (bottom left), and ISO weighted vertical acceleration (bottom-right).

7.16. It can be seen that, while the suspension travel for both active settings is of a similar magnitude, the validated passive suspension requires significantly less working space. Nevertheless, with all configurations the bump-stops are avoided.

Finally, although the differences between the two active configurations are small with respect to comfort and working space requirements, there is a profound difference in power consumption. The mean total power consumption over the 8 seconds simulation is 187 W for the modal skyhook controller versus 140 W (25% lower) for the tuned LQG setting.

7.5.3 Comfort evaluation

Given the impressive performance when crossing the pyramid obstacle, the question arises what level of comfort can be obtained when driving on a “real” road. Therefore, two types of simulations are run. In the first type, the vehicle drives on a relatively smooth stretch of asphalt - the same as in Section 2.7 - with a constant velocity of 80 km/h. There is however, one severe pothole in this road.

The power spectral density (PSD) of the ISO weighted roll, pitch and heave accel-

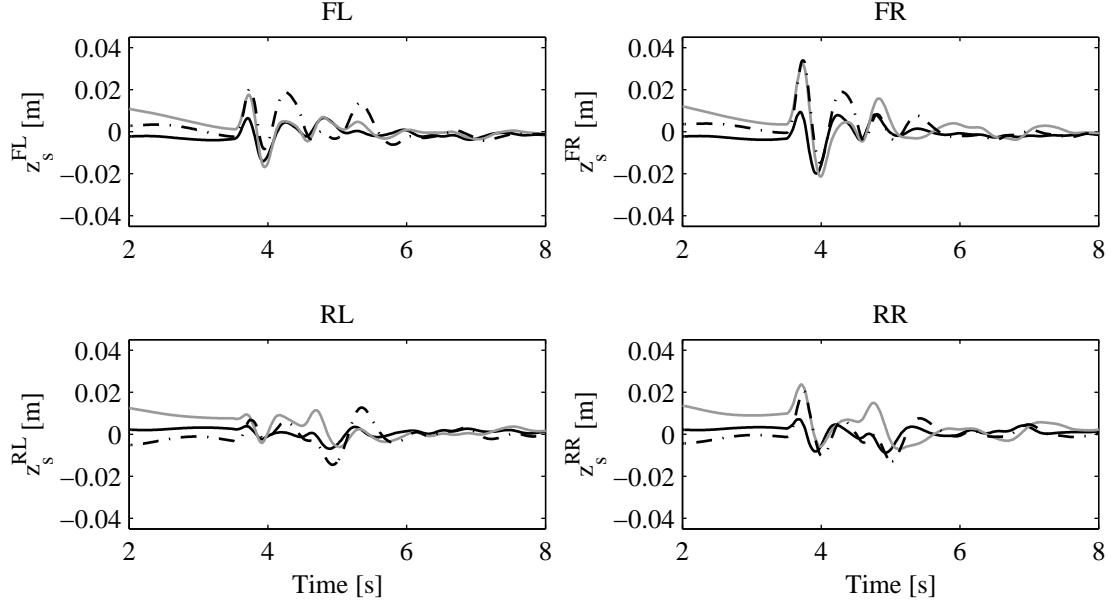


Figure 7.16: Fixed gain controller evaluation tractor semi-trailer model when driving over a pyramid obstacle at 15 km/h. Comparison validated passive suspension (grey), tuned LQG (dash-dotted) controller, and modal skyhook controller (solid black). Secondary suspension travel: front left (top-left), front right (top-right), rear left (bottom-left), and rear right (bottom-right). Positive displacements correspond to compression.

erations as well as the RCI (1.1), VDV (1.3), and mean total power consumption is given in Figure 7.17. Again it can be observed that the modal skyhook controller gives the largest reduction in pitch and roll accelerations, while the tuned LQG controller gives the largest reduction in ISO weighted heave accelerations. However, the latter hits the bump-stops when crossing that relatively nasty bump in the road, while the former does not. As a result, the VDV of the latter is much higher. Moreover, the crest factors of the former are in the range of 5 to 6, while those of the latter go up to 16. So, it can be concluded that hitting the bump-stops - even a single time - on a relatively smooth road is highly undesirable from a comfort point of view.

In the second simulation type, the vehicle drives on a rough clinker brick road, at 40 km/h. The results are given in Figure 7.18. It can be seen, that while the magnitude is different, the shape of the PSD's resembles that of those given in Figure 7.17. In this case all the configurations stay clear of the bump-stops, although the rms suspension travel is significantly higher than on the smooth road. The crest factors are all in the range of 3 to 6. Clearly, the tuned LQG controller gives the best performance for this test, with a 45% reduction in RCI with respect to the passive setting. However the mean total power consumption of 1.35 kW is considerable, and significantly higher than that on the smooth road. Therefore it would be worth investigating how much performance would be lost with more energy efficient control strategies on poor roads.

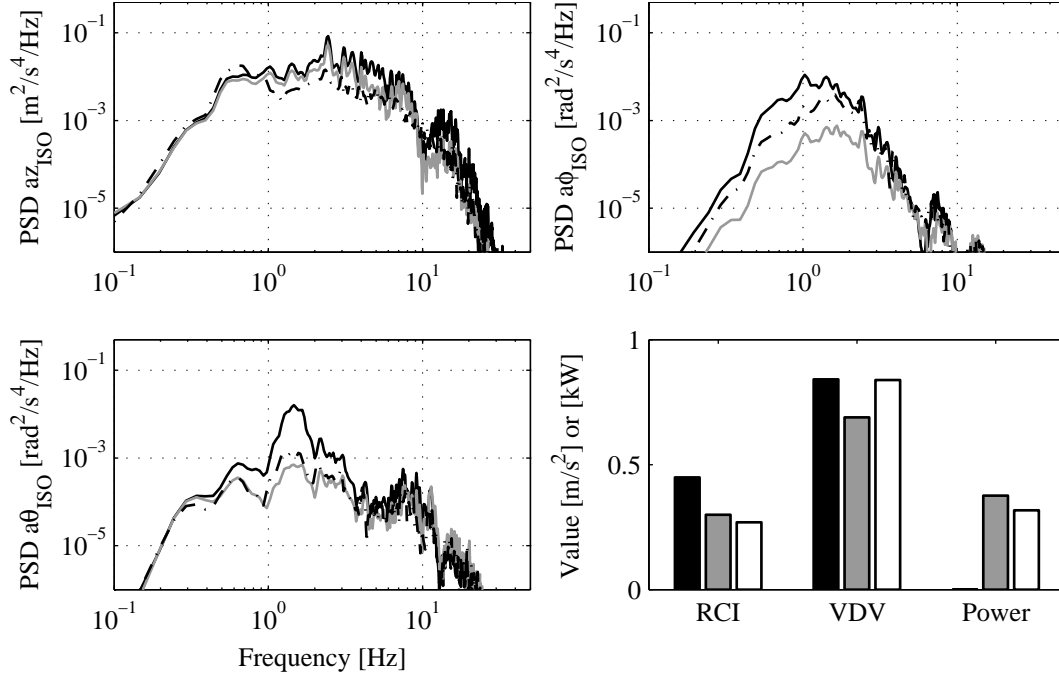


Figure 7.17: Fixed gain controller evaluation tractor semi-trailer model when driving on a smooth asphalt road at 80 km/h. Comparison passive suspension (black), tuned LQG (dash-dotted / white box) controller, and modal skyhook controller (grey). Power spectral density of: ISO weighted vertical acceleration (top-left); ISO weighted roll acceleration (top-right); and ISO weighted pitch acceleration (bottom-left). Bottom-right: Ride Comfort Index, Vibration Dose Value, and total mean power consumption.

7.5.4 Braking

In the previous subsections the achievable comfort improvement is evaluated. Another important performance characteristic of the suspension is the attitude behavior as is discussed in Section 1.4.2. To evaluate the performance when braking, the vehicle is simulated at an initial velocity of 60 km/h. After 3.5 seconds the driver starts to brake, following the same measured deceleration profile as is used in Section 2.6.2. The maximum deceleration is 4.6 m/s^2 . The cabin pitch and heave response, using the tuned LQG and modal skyhook controller with and without disturbance compensation, is shown in Figure 7.19.

For the case without compensation, it can be observed that the cabin pitch using the active configurations does not resemble that of the chassis. Furthermore, when coming to a standstill ($t > 8$) it takes quite some time for the cabin to level. The fact that the cabin pitch with the modal skyhook controller increases for $t > 8$, which may look curious, is a result of the combination of the change in aerodynamic force, the relatively slow integral part and high skyhook damping.

The attitude behavior with compensation is far more desirable, as the cabin pitch accurately follows the chassis pitch more accurately, and the undesirable characteristics when coming to a standstill disappear. Furthermore, the fact that the vertical cabin motion is reduced with respect to that of the chassis is also considered to be favorable.

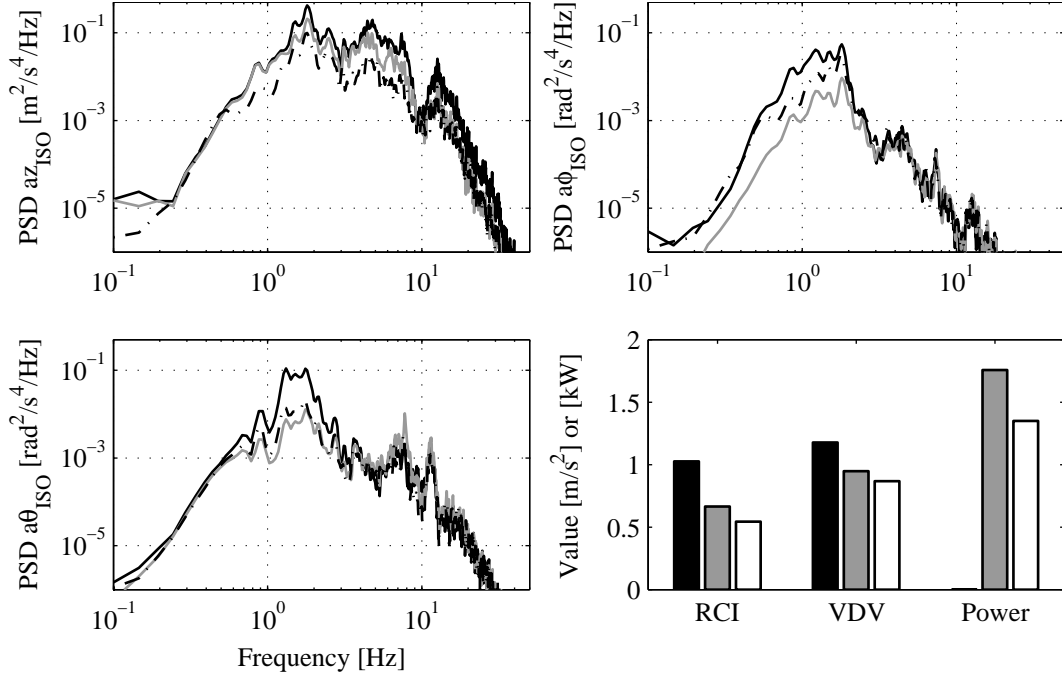


Figure 7.18: Fixed gain controller evaluation tractor semi-trailer model when driving on a rough clinker brick road at 40 km/h. Comparison passive suspension (black), tuned LQG (dash-dotted / white box) controller, and modal skyhook controller (grey). Power spectral density of: ISO weighted vertical acceleration (top-left); ISO weighted roll acceleration (top-right); and ISO weighted pitch acceleration (bottom-left). Bottom-right: Ride Comfort Index, Vibration Dose Value, and total mean power consumption.

7.5.5 Double lane change

To evaluate the attitude performance when steering, the simulation model is taken through a double lane-change maneuver at 55 km/h. The velocity and steering inputs are again obtained from the real world measurements, as discussed in Section 2.6.4. The cabin roll and heave response for the case with and without compensation is given in Figure 7.20.

For the case without compensation, it can be observed that the cabin rolls more than the chassis. However, as there is a passive roll stiffness added, even though smaller than in the validated setting, the cabin roll response does somewhat resemble that of the chassis. For the case with compensation, the cabin roll with the active suspensions accurately follows that of the chassis. There is, however, an additional effect that requires attention.

The lateral accelerations, during the double lane change, rise up to $\pm 3.8 \text{ m/s}^2$. As a result, the roll disturbance compensation (7.46) reaches values up to 4800 Nm, which is enough to saturate the two *eLPAS* actuators that are required to give the highest actuation forces. However, the actuator force of the other two actuators does not saturate, leading to a discrepancy in the input transformation (7.19), i.e., besides the roll moment a negative vertical force is realized. This is the cause of the dips in the vertical cabin position in Figure 7.20 (bottom).

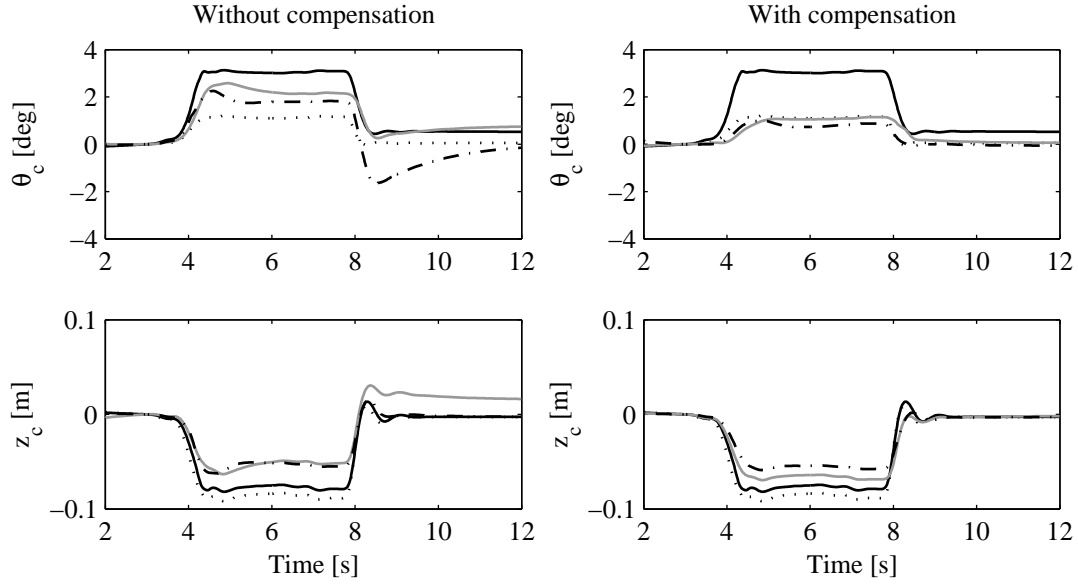


Figure 7.19: Fixed gain controller evaluation tractor semi-trailer model when performing an emergency brake at 60 km/h. Comparison passive suspension (black) and its chassis response (dotted), tuned LQG (dash-dotted) controller, and modal skyhook controller (grey): with- (right) and without disturbance compensation (left). Cabin absolute pitch angle (top), and absolute vertical position (bottom).

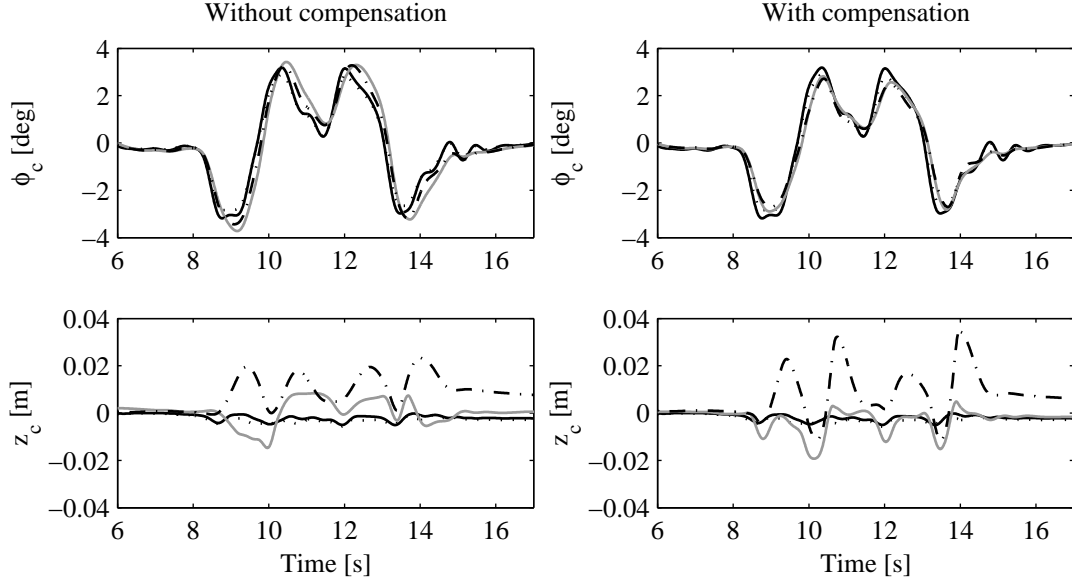


Figure 7.20: Fixed gain controller evaluation tractor semi-trailer model when performing a double lane change at 53 km/h. Comparison passive suspension (black) and its chassis response (dotted), tuned LQG (dash-dotted) controller, and modal skyhook controller (grey): with- (right) and without disturbance compensation (left). Cabin pitch angle (top), and vertical position (bottom).

Moreover, for the tuned LQG controller the vertical cabin position increases significantly on several occasions (at Time 9.3, 10.8, 12.6, and 14.0 seconds). Just before each of these occasions the references, of the two *eLPAS* actuators that are required

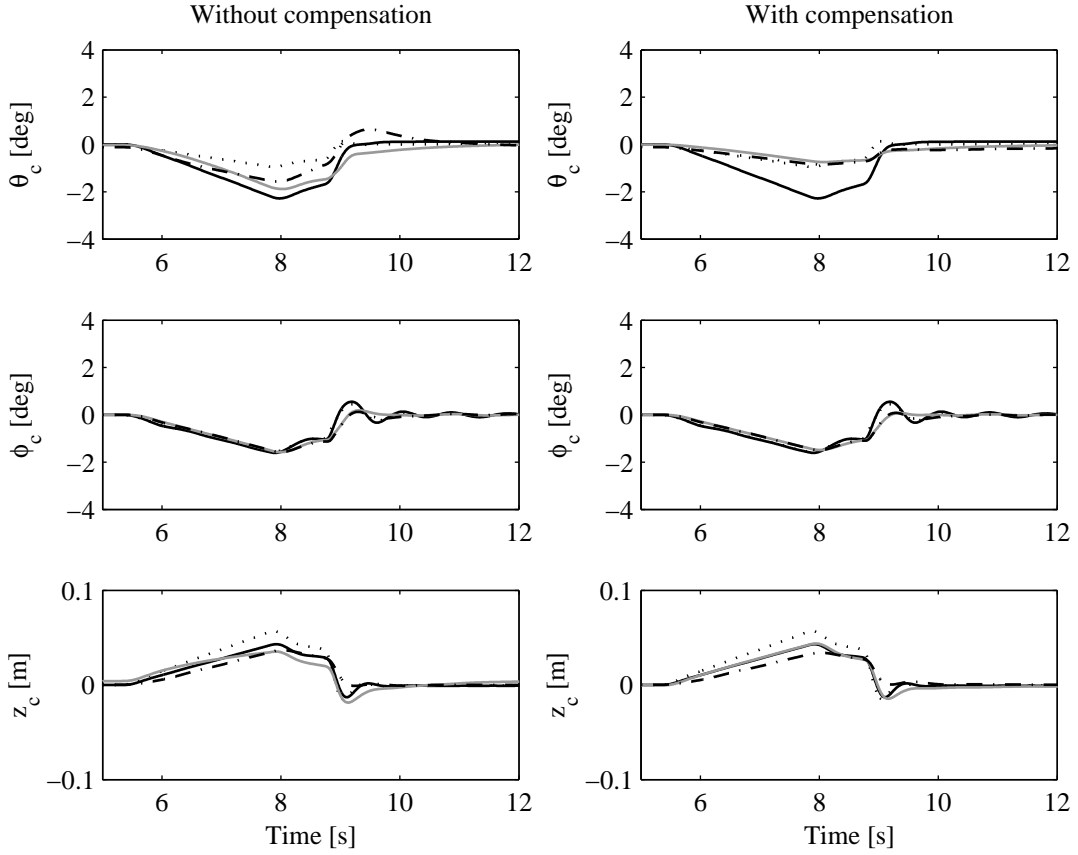


Figure 7.21: Fixed gain controller evaluation tractor semi-trailer model when accelerating from stand-still in first gear. Comparison passive suspension (black) and its chassis response (dotted), tuned LQG (dash-dotted) controller, and modal skyhook controller (grey): with- (right) and without disturbance compensation (left). Cabin pitch angle (top), and vertical position (bottom).

to give the highest actuation force, change too quickly for the actuators to follow. The resulting tracking error $\gamma_{ref} - \gamma$ induces a positive vertical force.

So, the observed vertical cabin motions during this maneuver are mainly due to the actuator limitations and the chosen control strategy, which does not take them into account. Bounding the modal control inputs would reduce the vertical cabin movement during this maneuver, but as mentioned in Section 7.5.1, it would also reduce the chassis tracking accuracy as the roll moment requirement cannot be met. Bounding the modal disturbance compensation gains, under the assumption that there is no braking or accelerating during aggressive cornering maneuvers, is for this event the best solution, because it reduces the vertical oscillation while maintaining roll attitude performance. Still, in the end, this maneuver serves as one more example why the actuator dynamics and constraints need to be taken into account explicitly when designing cabin controllers.

7.5.6 Acceleration

The final test under consideration starts with the simulation model at standstill. After five seconds, the driver quickly accelerates in first gear up to a speed of 10 km/h, without excessive wheel spin, at which point he/she declutches. The acceleration profile is obtained from measurements on the real tractor semi-trailer configuration, as is discussed in Section 2.6.1.

The cabin attitude behavior is depicted in Figure 7.21 for the case with and without disturbance compensation. Clearly, the benefit of the compensation is primarily visible in the pitch dynamics. In roll direction, the cabin also follows the chassis motions without compensation. However, in this case it is seriously questionable whether this is actually desirable. It is imaginable that most drivers would prefer the absence of cabin roll when accelerating. Similarly, it might be desirable to reduce the cabin heave motion further. However, this remains a topic for future research. Overall, the potential of driver induced disturbance compensation has been clearly established.

7.6 Conclusion

In this chapter the achievable performance using a fixed gain linear control strategy is investigated for the tractor semi-trailer system with four *eLPAS* actuators. Hereto, a tuned LQG controller and a modal skyhook control strategy are designed and evaluated in simulation for a number of driving conditions on the validated 44 DOF model. Furthermore, the potential of a driver induced disturbance compensation strategy is investigated.

Overall it is found, that the tuned LQG controller gives better performance, with respect to comfort and energy at similar suspension travel characteristics, than the modal skyhook controller. That is, as long as the bump-stops are avoided. The achievable performance gain using fixed gain controllers with respect to the validated passive setting is condition dependent. Nevertheless, under some of the simulated conditions with the 44 DOF model, a decrease of the ride comfort index (comfort increase) of 45% is obtained. Herein, the mean total power consumption using the tuned LQG controller range from around 300 W on a relatively smooth road up to 1.35 kW under worst-case conditions. However, it should be noted that the designed controllers are not expected to be optimal, due to the nonlinear system characteristics and the control model inaccuracies.

The driver induced disturbance compensation is demonstrated to have great potential for enhancing the cabin attitude behavior. Using this feedforward strategy, the cabin roll and pitch will follow the chassis motions when braking, steering, or accelerating, resulting in enhanced feedback to the driver. Here, the challenge remains to find suitable estimators, which are sufficiently accurate under all driving conditions. Furthermore, these estimates need to be minimally affected by the various noise sources, as these will otherwise significantly increase the power requirements.

Chapter 8

Conclusions and recommendations

There is an apparent need to further improve the driver comfort in heavy-duty vehicles. As the open literature on secondary suspension design and controllable suspensions for these vehicles is limited, there are many interesting challenges that require research. With that in mind, the following question is studied in this thesis:

In which manner, using a low-power active secondary suspension, is it possible to further enhance the cabin comfort and attitude behavior of commercial vehicles?

In view of this problem, the research objectives have been defined as:

1. Develop and validate a tractor semi-trailer model, which is suitable for comfort and attitude studies;
2. Develop a model for a new design variable geometry actuator and use it to evaluate the actuator's characteristics;
3. Design a cabin controller, for the tractor semi-trailer model equipped with variable geometry active suspension, that significantly enhances cabin comfort and attitude behavior at a low energy cost.

Overall, it is concluded that a configuration with four *electromechanical Low-Power Active Suspension (eLPAS)* actuators, in combination with a modal control strategy including disturbance compensation, has great potential. The conclusions and recommendations corresponding to each of the research objectives are discussed in more detail in the following sections.

8.1 Vehicle models and validation

8.1.1 Conclusions

A simulation model of a tractor semi-trailer combination is developed. Due to the modular design structure, it can be used for a wide range of research, also outside the

field of cabin suspension design. Furthermore, as it is constructed in *SimMechanics* which is the multi-body toolbox of *MATLAB/Simulink*, the model can be used conveniently for controller evaluation and implementation of active components. Especially this last feature makes it very valuable.

The model is validated in the time-domain using measurement data from a variety of tests obtained with a real tractor with semi-trailer combination. More specifically, the following are considered: an acceleration test, a braking test, driving over a pyramid-shaped road obstacle, and a double lane change (DLC). It is concluded that the model can be used to evaluate the dynamic behavior of the vehicle for the validated driving conditions. However, there are a few points of attention. First of all, the rear axle accelerations show a significant mismatch in the majority of the road obstacle tests. Secondly, the deflections of the rear cabin suspension during the double lane change also show a large mismatch. Finally, a static offset is visible in the front cabin suspension displacement at the end of the brake test.

The high level of complexity of the the 44 DOF model, as well as the difficulty to linearize, are expected to be problematic for controller design studies. Therefore, a 4 degrees of freedom (DOF) quarter truck heave model, a 4 DOF roll model, and a 9 DOF half truck pitch-heave model are developed. These models use the parameters of the 44 DOF model and, as such, can be seen as reduced order models. To validate their accuracy in the comfort relevant frequency range, as well as that of the 44 DOF tractor semi-trailer model, a new model validation technique is proposed. The technique is suited for asynchronous repeated measurements with noise contributions on both inputs and outputs and separates noise- and model uncertainty. It is concluded that the developed model validation technique is very useful when developing reliable vehicle models.

Overall, the 44 DOF model has the highest level of accuracy and is also deemed suitable for driver comfort evaluation. However, there remains a significant mismatch above 4 Hz for the transfers to the longitudinal- and pitch cabin acceleration. Furthermore, the 4 DOF heave and 9 DOF pitch-heave model also have a relatively high level of accuracy in the comfort relevant frequency ranges. The 4 DOF roll model on the other hand, is significantly less accurate and is considered to be unreliable when designing cabin roll controllers for practical application.

8.1.2 Recommendations

In light of these findings, the following is recommended. First of all, to further increase the general applicability of the 44 DOF model, its accuracy needs to be improved. Hereto, it is recommended to adopt an objective model quality criterion. Furthermore, it may prove beneficial to do component tests and measurements with a deterministic road input. It may also be possible to link with more detailed *NASTAN* models to include more of the frame flexibilities. A detailed drive-line model would be desirable to simulate start-stop and gear shifting behavior. Moreover, for reliability the model

should also be validated for more driving conditions. Examples include maneuvers on banked roads, road slopes, and low friction surfaces.

Secondly, as the accuracy of the 4 DOF roll model around the 1.7 Hz resonance frequency is relative disappointing, it is recommended to look for alternative low order models which may give better results. Herein, it is important that the model parameters have a clear relation with the real world system. Otherwise, suspension changes cannot be effectively incorporated. Similarly, it may also be desirable to investigate alternatives for the pitch-heave model that more accurately describe the longitudinal and pitching dynamics.

Finally, it may be worthwhile to further develop the proposed model validation procedure. In its present form there are quite some limitations and assumptions that add conservatism to the found uncertainty models. Especially the step from single-input single-output to multiple-input multiple-output validation would be valuable.

8.2 The variable geometry actuator

8.2.1 Conclusions

The potential of various active cabin suspension concepts is investigated. Three have been selected for an evaluation under idealized conditions by means of a simulation study. It is concluded that there is no fundamental difference between the obtainable level of performance with respect to working space requirements and suspended mass accelerations. However, the power requirements differ significantly. From that perspective, energy regenerative systems have the preference. Furthermore, the so-called *loaded active* suspension structure is undesirable as it experiences large power spikes. On the other hand, the power requirements of the so-called *parallel active* and variable geometry actuator are considerably lower.

Under the chosen conditions, the power consumption of these last two are of the same order of magnitude. However, the nature of the power requirements is fundamentally different. The power consumption of the parallel active configuration is related to the control force ($P_{act} \sim F_{act}\dot{z}$), while that of the variable geometry actuator is related to the control force variations ($P_{act} \sim \dot{F}_{act}z$). Consequently, the power requirements of each strongly depends on the chosen control strategy and suspension parameters.

In a vehicle suspension the load of (or down force on) the suspended mass will vary. Therefore, the parallel configuration requires an actuator with a leveling device in parallel. Otherwise the power consumption will increase similar to the loaded configuration, while the variable geometry active suspension is capable of performing the leveling itself. Furthermore, there are few electric motors capable of delivering forces of the magnitude that are required for this application. So, the fact that the variable geometry actuator can suffice with an electric motor which is considerably smaller (and lighter) than that of the parallel active suspension makes it very attractive.

A hardware prototype is presented of a special design of variable geometry active suspension: the *electromechanical Low-Power Active Suspension (eLPAS)*. An analytical model is derived and it is concluded that the orientation of the cone can be used to obtain a more or less constant actuator stiffness. A force controller is designed and the model with controller is validated using the experimental setup. It is concluded that the *eLPAS* design is feasible and that the model gives an accurate representation of both the steady-state and dynamic characteristics of the prototype. For the validation the actuator bandwidth is limited to 10 Hz as high frequent control inputs have a relatively high energy cost. Still, the *eLPAS* outperforms previous variable geometry actuator designs with respect to size, stiffness characteristics and achievable bandwidth.

8.2.2 Recommendations

The main questions that remain, concern the durability and packaging (design) of the *eLPAS* system. Therefore it is recommended that more research is focussed on these two aspects of the system. For instance, it may be beneficial to replace the steel spring with an air spring. Furthermore, when considering design changes it is recommended to look for ways to minimize the friction in the electric motor and gearbox, as this is the main source of energy dissipation.

The analytical *eLPAS* model is used to analyse the actuator power requirements. However, the included electric motor model is rather basic. Therefore, it is also recommended to investigate the (worst case) power requirements using a more detailed and accurate brushless permanent magnet DC motor model. Moreover, given the very real dangers of thermal overloading, a thorough thermal evaluation is also recommended.

8.3 Cabin control

8.3.1 Conclusions

The quarter truck heave model is used to gain more insight in the control problem. A multi-objective two-norm performance criterium is defined, which depends on driver comfort, working space, and energy requirements. It is concluded that, while the full state feedback LQ controllers provide the best performance; output feedback controllers, which adopt some of the single mass optimal controller characteristics, can provide near optimal results. Herein, the characteristics depend on the chosen actuator type and the corresponding energy cost criterium. More specifically, the difference in optimal control structure between a conventional and an idealized variable geometry actuator, is basically an additional low-pass filter on the actuator force reference.

As it cannot be expected that all the state components of the quarter truck heave model, required for the state- or output feedback, are measurable in practice; state estimation is required. Using a four sensor setup, consisting of the primary and secondary

suspension displacement and the cabin and axle accelerations, in combination with a Kalman filter; it is concluded that the resulting LQG controller obtains performance levels that are very close to those obtained with the optimal LQ controller. Moreover, it is concluded that while some passive damping may be desirable in parallel to the variable geometry actuator, from an energy point of view; the passive vertical stiffness should ideally be zero.

Optimizing the passive secondary suspension parameters, a 4% comfort enhancement can be obtained by lowering the passive stiffness and adding damping. However, it is questionable whether this is feasible from a practical point of view. The fixed gain LQ energy optimal controller achieves 16%- and the comfort optimal controller 28% comfort enhancement with respect to the validated passive configuration. On the other hand, the energy requirements of the energy optimal controller are 78% lower than that of the comfort optimal controller, when using a variable geometry actuator; so adding some energy weight is desirable.

Using energy optimal controllers, another 75% comfort improvement can be realized when the disturbance levels drop by 70% or the available suspension working space is increased by 70%. Furthermore, in these cases the energy cost can also be reduced by an additional 77%. So, the benefit of condition dependent - in comparison to fixed gain - optimal controllers is huge. However, it remains unclear how to effectively and robustly schedule/adapt the control gains.

Using this knowledge as background, the more complicated issues embedded in the full tractor semi-trailer controller design problem are addressed. Herein, the achievable performance using a fixed gain linear control strategy is investigated when using four *eLPAS* actuators, one beneath each corner of the cabin. A tuned LQG controller and a modal skyhook control strategy are designed and evaluated in simulation for a number of driving conditions using the validated 44 DOF model. Furthermore, the potential of a driver induced disturbance compensation strategy is investigated.

Overall it is concluded, that the tuned LQG controller gives better performance, with respect to comfort and energy at similar suspension travel characteristics, than the modal skyhook controller. The main exception is the case where the tuned LQG controller hits the bump stops while the modal skyhook controller does not. So, the achievable performance gain using fixed gain controllers with respect to the validated passive setting is condition dependent. Nevertheless, under some of the simulated conditions with the 44 DOF model, a decrease of the ride comfort index (comfort increase) of 45% is realized. The mean total power consumption using the tuned LQG controller ranges from around 300 W on a relatively smooth road up to 1.35 kW on a clinker brick road.

The driver induced disturbance compensation is demonstrated to have great potential for enhancing the cabin attitude behavior. Using this feedforward strategy, the cabin roll and pitch will follow the chassis motions when braking, steering, or accelerating, resulting in enhanced feedback to the driver.

8.3.2 Recommendations

When it comes to the design of suitable low-power controllers for the tractor semi-trailer system, many questions remain. It is essential to note that the implemented controllers are not expected to be optimal. As such, it is recommended to further study the topic of optimal (robust) controller design, including the cabin comfort and attitude requirements, nonlinear bump-stops and actuator characteristics. Doing so, the suspension travel criterion can be omitted and the challenge will become to find a compromise in the trade-off between comfort and energy requirements, subject to the working space limitations, i.e., the absolute suspension travel constraints. Herein, the optimal cabin attitude behavior remains to be determined. It is also recommended to investigate the controller sensitivity to parameter (load) variations.

It may be possible to further increase the suspension performance by adding nonlinear passive suspension elements. Herein, the nonlinear stiffness characteristics can potentially be obtained by geometric design of the *eLPAS* actuators. It may also prove beneficial to include the correlation between the front and rear road disturbance in the pitch-heave model, and design velocity dependent controllers.

Besides the challenge to find the optimal fixed gain active suspension configuration, it is recommended to further investigate the huge potential of condition dependent control gains. Especially the control gain selection mechanism deserves special attention. Moreover, there is a potential pitfall that should be kept in mind: if, on a smooth road, the bump-stops are hit a single time, the driver is likely to complain.

Another remaining challenge is to find suitable estimators for the disturbance compensation algorithm. These need to be sufficiently accurate under all driving conditions and minimally affected by the various noise sources, as these will otherwise significantly increase the power requirements. Particularly the case of low friction surfaces and banked or graded roads need to be included. Still, the nonlinear steering dynamics, steering friction, and drift of the acceleration sensors may also prove to be influential.

Finally, it is recommended to evaluate the performance of the *eLPAS* system on a real test vehicle and compare it to the performance of a conventional passive; passive interconnected; and a semi-active configuration. On the short term, (interconnected) semi-active cabin suspension designs, using for example a switched LQG control strategy, may be a safe bet for truck manufacturers. However, on the long term, energy efficient active cabin suspensions are expected to come out on top of the competition.

Appendix A

Model specification

The majority of the parameter names is structured as $x_{i_1|i_2|i_3}^j$, where $x \in [z, l, b, m, J, c, d]$ depending on the type of parameter: vertical-, longitudinal-, lateral geometric, mass, inertia, stiffness, or damping respectively. Furthermore, $i_1 \in [w, a, f, e, c, T, p, s]$ specifies the body the parameter relates to: wheels, axle, chassis (frame), engine, cabin, trailer, primary-, or secondary suspension. The identifiers i_2 and i_3 are used to further specify the location: front (f), rear (r), hitch point (5), or center of gravity (m). Finally, $j \in [c, d, z, \phi]$ is used to clarify whether the parameters are related to the springs, dampers, vertical- or roll model.

A.1 44-DOF tractor semi-trailer model

The system is depicted in Figures A.2 and A.3, and the parameters are given in Tables A.1, A.2, A.4 and A.5. The parameter values marked by \square are company confidential.

A.2 2-mass quarter car heave model

The system is depicted in Figure 3.2 and the parameters, for a (normal) passenger car (Liebregts (2007)), are given in Table A.6.

A.3 4-mass quarter truck heave model

The system is depicted in Figure 3.1 and the parameters are given in Table A.7. These parameters have been derived from the 44-DOF tractor semi-trailer model, of which the parameters are given in Section A.1.

A.4 4-mass quarter truck roll model

The system is depicted in Figure 3.4 and the parameters are given in Table A.8. These parameters have been derived from the 44-DOF tractor semi-trailer model, of which

Table A.1: Geometric parameters 44-DOF tractor semi-trailer model, vertical.

Parameter	Value	Dimension	Description
z_{am}	0.52	m	position front axle CoG w.r.t. road
z_{fm}	0.90	m	position chassis CoGs w.r.t. road
z_{em}	\square	m	position engine CoG w.r.t. road
z_{ef}	\square	m	position engine front mount w.r.t. below CoG
z_{er}	\square	m	position engine rear mount w.r.t. below CoG
z_{cm}	2.17	m	position cabin CoG w.r.t. road
z_{Tam}	\square	m	position trailer axle CoG w.r.t. road
z_{Tm}	\square	m	position trailer CoG w.r.t. road
z_{f5}	0.25	m	position 5 th wheel w.r.t. chassis CoG
z_{T5}	\square	m	position 5 th wheel w.r.t. trailer CoG
z_p	0.38	m	primary suspension steady-state length
z_s	0.30	m	secondary suspension steady-state length

Table A.2: Geometric parameters 44-DOF tractor semi-trailer model, longitudinal.

Parameter	Value	Dimension	Description
l_{am}	\square	m	position front axle CoG w.r.t. cabin front susp.
l_{ffm}	\square	m	position front chassis CoG w.r.t. front axle.
l_{frm}	\square	m	position rear chassis CoG w.r.t. front axle.
l_{fs}	\square	m	position chassis torsion joint w.r.t. axle CoG
l_{f5}	3.28	m	position 5 th wheel w.r.t. front axle.
l_{em}	1.53	m	position engine CoG w.r.t. cabin front susp.
l_{ef}	0.81	m	position engine CoG w.r.t. engine front susp.
l_{er}	0.32	m	position engine CoG w.r.t. engine rear susp.
l_{cf}	0.94	m	position cabin CoG w.r.t. cabin front susp.
l_{cr}	1.14	m	position cabin CoG w.r.t. cabin rear susp.
l_{wb}	3.8	m	wheel distance tractor
l_{Tw}	\square	m	position trailer front wheel w.r.t. 5 th wheel
l_{Ta}	\square	m	wheel distance trailer
l_{Tm}	\square	m	position trailer front CoG w.r.t. 5 th wheel
l_{Ts}	\square	m	pos. trailer CoG w.r.t. torsion joint

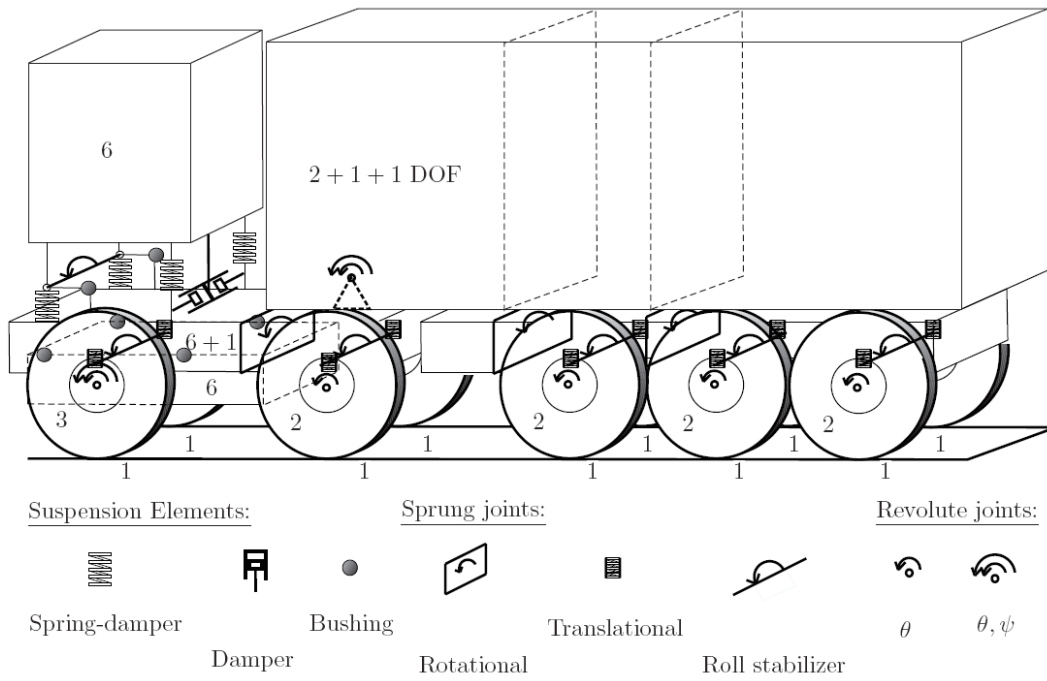


Figure A.1: Tractor semi-trailer model elements.

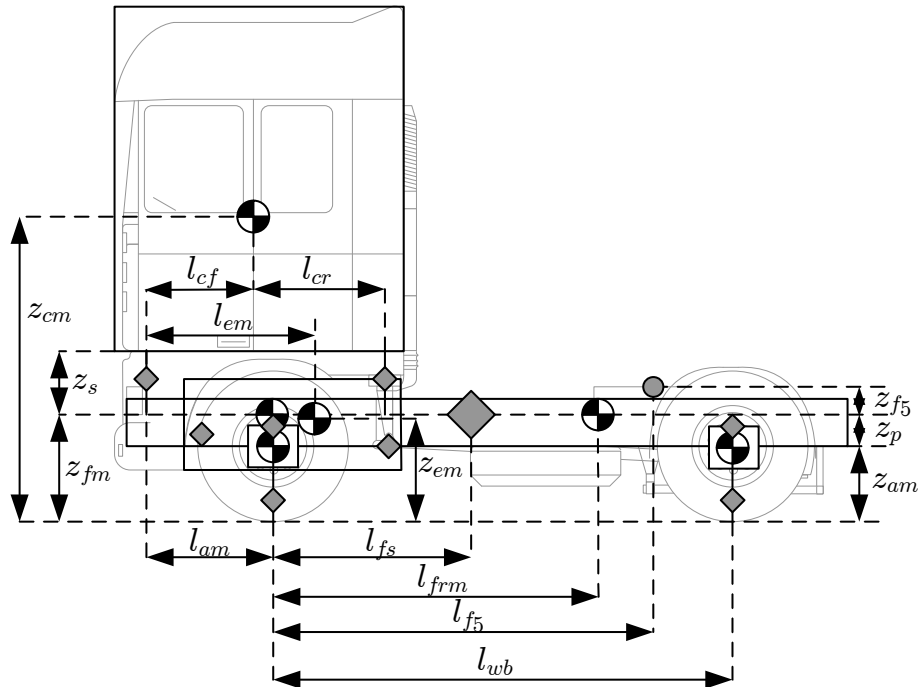


Figure A.2: Tractor model, side-view.

the parameters are given in Section A.1.

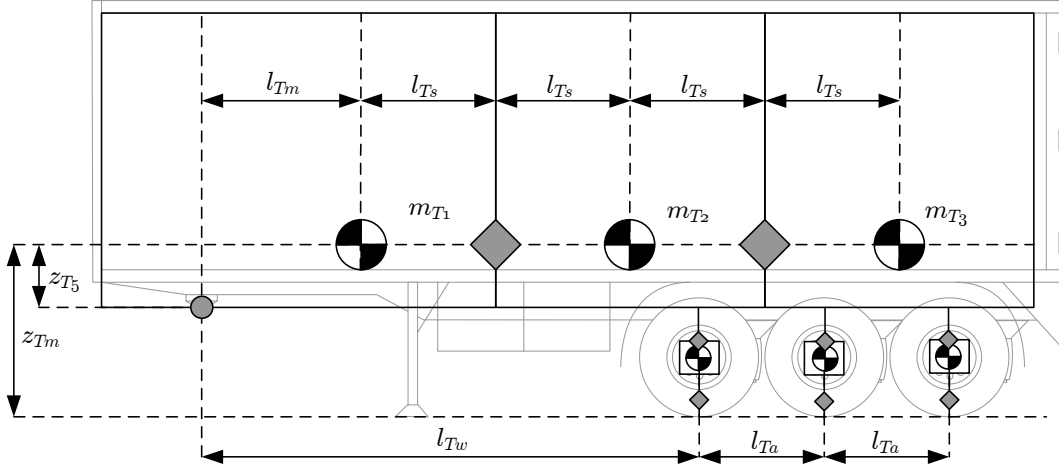


Figure A.3: Semi-trailer model, side-view.

Table A.3: Geometric parameters 44-DOF tractor semi-trailer model, lateral.

Parameter	Value	Dimension	Description
b_{wf}	2.00	m	wheel distance tractor front
b_{wr}	\square	m	wheel distance tractor rear
b_{pf}^c	0.85	m	distance front primary susp. springs
b_{pf}^d	1.05	m	distance front primary susp. dampers
b_{pr}^c	\square	m	distance rear primary susp. springs
b_{pr}^d	\square	m	distance rear primary susp. dampers
b_{pT}	\square	m	distance springs and dampers trailer
b_{ef}	\square	m	position front engine susp. w.r.t CoG axle
b_{er}	\square	m	position rear axle susp. w.r.t CoG axle
b_{sf}	0.56	m	position front secondary susp. w.r.t CoG cabin
b_{sr}	0.56	m	position rear secondary susp. w.r.t CoG cabin
b_{Tw}	2.10	m	wheel distance trailer

A.5 9-DOF pitch-heave model

The system is depicted in Figure A.4. The parameters are given in Tables A.9, A.10, and A.11. These parameters have been derived from the 44-DOF tractor semi-trailer model, of which the parameters are given in Section A.1.

The nonlinear equations of motion are determined using the Newton-Euler ap-

Table A.4: Mass parameters 44-DOF tractor semi-trailer model.

Parameter	Value	Dimension	Description
m_{wf}	160	kg	front wheel mass
m_{wr}	160	kg	drive wheel mass
m_{wT}	\square	kg	trailer wheel mass
m_{af}	475	kg	front axle mass (no tyres)
m_{ar}	740	kg	drive axle mass (no tyres)
m_{ff}	\square	kg	chassis front mass
m_{fr}	\square	kg	chassis rear mass
m_e	1785	kg	engine mass
m_c	1300	kg	cabin mass
$m_{Ta1,2,3}$	\square	kg	trailer axle mass (no tyres)
$m_{T1,2,3}$	\square	kg	trailer segment mass
\underline{J}_{wf}	\square	kgm ²	front wheel inertia
\underline{J}_{wr}	\square	kgm ²	drive wheel inertia
\underline{J}_{wT}	\square	kgm ²	trailer wheel inertia
\underline{J}_{af}	\square	kgm ²	front axle inertia (no tyres)
\underline{J}_{ar}	\square	kgm ²	drive axle inertia (no tyres)
\underline{J}_{ff}	\square	kgm ²	chassis front inertia
\underline{J}_{fr}	\square	kgm ²	chassis rear inertia
\underline{J}_e	\square	kgm ²	engine inertia
\underline{J}_c	\square	kgm ²	cabin [xx,yy,zz] inertia
$\underline{J}_{Ta1,2,3}$	\square	kgm ²	trailer axle inertia (no tyres)
$\underline{J}_{T1,2,3}$	\square	kgm ²	trailer segment inertia

proach, and are given by

$$\begin{aligned}
m_{af}\ddot{z}_{af} &= F_{tf} - F_{af} - m_{af}g \\
m_{ar}\ddot{z}_{ar} &= F_{tr} - F_{ar} - m_{ar}g \\
J_f^*\ddot{\theta}_f &= F_{cf}^z \cos \theta_f l_5 - F_{cf}^z \sin \theta_f z_{f5} + F_{cf}^x \cos \theta_f z_{f5} + F_{cf}^x \sin \theta_f l_5 + F_{cr}^z \cos \theta_f l_6 \\
&\quad - F_{cr}^z \sin \theta_f z_{f5} + F_{cr}^x \cos \theta_f z_{f5} + F_{ef}^z \cos \theta_f l_3 - F_{ef}^z \sin \theta_f z_{f5} + F_{ef}^x \cos \theta_f z_{f5} \\
&\quad + F_{er}^z \cos \theta_f l_4 - F_{er}^z \sin \theta_f z_{f5} + m_f g (l_{f5} - l_{fm}) \cos \theta_f - m_f g z_{f5} \sin \theta_f \\
&\quad + F_{er}^x \cos \theta_f z_{f5} - F_{af}^z \cos \theta_f l_1 + F_{ar}^z \cos \theta_f l_2 + (F_{af}^z + F_{ar}^z) z_{f5} \sin \theta_f \\
m_e \ddot{x}_e &= F_{ef}^x + F_{er}^x \\
m_e \ddot{z}_e &= F_{ef}^z + F_{er}^z - m_e g \\
J_e \ddot{\theta}_e &= F_{er}^z \cos \theta_e l_{er} - F_{ef}^z \cos \theta_e l_{ef} + F_{er}^x l_{er} \sin \theta_e - F_{ef}^x l_{ef} \sin \theta_e \\
&\quad - F_{er}^x \cos \theta_f z_{er} - F_{ef}^x \cos \theta_f z_{ef} + F_{er}^z \sin \theta_e z_{er} + F_{ef}^z \sin \theta_e z_{ef} \\
m_c \ddot{x}_c &= F_{cf}^x + F_{cr}^x - F_d \\
m_c \ddot{z}_c &= F_{cf}^z + F_{cr}^z - m_c g \\
J_c \ddot{\theta}_c &= F_{cr}^z \cos \theta_c l_{cr} + F_{cr}^z \sin \theta_c z_{cr} - F_{cf}^z \cos \theta_c l_{cf} + F_{cf}^z \sin \theta_c z_{cf} - F_{cf}^x \cos \theta_c z_{cf},
\end{aligned} \tag{A.1}$$

Table A.5: Suspension parameters 44-DOF tractor semi-trailer model.

Parameter	Value	Dimension	Description
c_{tf}	$1.2 \cdot 10^6$	N/m	tyre stiffness front
c_{tr}	$1.1 \cdot 10^6$	N/m	tyre stiffness rear
c_{tT}	\square	N/m	tyre stiffness trailer
c_f^ϕ	\square	Nm/rad	tractor chassis torsion stiffness
c_T^ϕ	\square	Nm/rad	trailer chassis torsion stiffness
c_{pf}	$3 \cdot 10^5$	N/m	prim. susp. stiffness front
c_{pr}	$3 \cdot 10^5$	N/m	prim. susp. stiffness rear
c_{pT}	$4 \cdot 10^5$	N/m	prim. susp. stiffness trailer
c_{pf}^ϕ	$2.1 \cdot 10^5$	Nm/rad	prim. susp. roll stiffness front
c_{pr}^ϕ	\square	Nm/rad	prim. susp. roll stiffness rear
c_{pT}^ϕ	\square	Nm/rad	prim. susp. roll stiffness trailer
c_{ef}	\square	N/m	eng. susp. [x,y,z] stiffness front
c_{er}	\square	N/m	eng. susp. [x,y,z] stiffness rear
c_{sf}	$[60, 20, 0.2] \cdot 10^5$	N/m	sec. susp. [x,y,z] stiffness front
c_{sr}	$[0, 0, 2] \cdot 10^4$	N/m	sec. susp. [x,y,z] stiffness rear
c_{sf}^ϕ	$8.6 \cdot 10^5$	Nm/rad	sec. susp. roll stiffness front
d_{pf}	\star	Ns/m	prim. susp. damping front
d_{pr}	\star	Ns/m	Prim. susp. damping rear
d_{pT}	\square	Ns/m	prim. susp. damping trailer
d_{ef}	\square	Ns/m	eng. susp. [x,y,z] damping front
d_{er}	\square	Ns/m	eng. susp. [x,y,z] damping rear
d_{sf}	$[25, 25, 7.4] \cdot 10^3$	Ns/m	sec. susp. [x,y,z] damping front
d_{sr}	$[0, 9.6, 5.9] \cdot 10^3$	Ns/m	sec. susp. [x,y,z] damping rear
I_{front}	200	kg/s ²	leveling control gain front
I_{rear}	200	kg/s ²	leveling control gain rear
C_d	0.8		Drag coefficient
A	6	m ²	Frontal surface
ρ	1.3	kg/m ³	Air density
\star	Nonlinear function		

Table A.6: Parameters 2-mass quarter car heave model.

Parameter	Value	Dimension	Description
m_s	400	kg	suspended mass
m_{us}	40	kg	axle mass
c_1	200.000	N/m	tyre stiffness
c_2	20.000	N/m	primary suspension stiffness
d_2	700	Ns/m	primary suspension damping

Table A.7: Parameters 4-mass quarter truck heave model.

Parameter	Value	Dimension	Description
m_a	700/2	kg	axle mass
m_f	1286/2	kg	front chassis mass
m_e	1785/2	kg	engine mass
m_c	1300/2	kg	cabin mass
c_t	$1.2 \cdot 10^6$	N/m	tyre stiffness
c_p	$3 \cdot 10^5$	N/m	primary suspension stiffness
c_e	$35 \cdot 10^5$	N/m	engine suspension stiffness
c_c	$40 \cdot 10^3$	N/m	cabin front+rear suspension stiffness
d_p	$11 \cdot 10^3$	Ns/m	primary suspension damping
d_e	8000	Ns/m	engine damping
d_c	13300	Ns/m	cabin damping

with l_1, l_2, \dots, l_6 the distance in longitudinal direction of the hitch-point (5th wheel) to each of the numbered points indicated in Figure A.4. Furthermore, the tyre and axle forces are

$$\begin{aligned}
F_{tf} &= c_{tf}^z(z_{rf} - z_{af} + z_{am} + F_{tf}^0) \\
F_{tr} &= c_{tr}^z(z_{rr} - z_{ar} + z_{am} + F_{tr}^0) \\
F_{af} &= c_{pf}(z_{af} - z_1) + d_{pf}^z(\dot{z}_{af} - \dot{z}_1) + F_{af}^0 \\
F_{ar} &= c_{pr}(z_{ar} - z_2) + d_{pr}^z(\dot{z}_{ar} - \dot{z}_2) + F_{ar}^0,
\end{aligned} \tag{A.2}$$

where z_{af}, z_{ar}, z_1 and z_2 are the vertical displacement of the front axle, rear axle, point 1 and 2, respectively, with respect to the equilibrium position at standstill; and $F_{tf}^0, F_{tr}^0, F_{af}^0, F_{ar}^0$ are the steady-state spring forces. The forces acting on the engine are

$$\begin{aligned}
F_{ef}^x &= c_{ef}^x(x_3 - x_e - l_{ef} \cos \theta_e) + d_{ef}^x(\dot{x}_3 - \dot{x}_e + l_{ef} \dot{\theta}_e \sin \theta_e) \\
F_{er}^x &= c_{er}^x(x_4 - x_e + l_{er} \cos \theta_e) + d_{er}^x(\dot{x}_4 - \dot{x}_e - l_{er} \dot{\theta}_e \sin \theta_e) \\
F_{ef}^z &= c_{ef}^z(z_3 - z_e + l_{ef} \sin \theta_e) + d_{ef}^z(\dot{z}_3 - \dot{z}_e + l_{ef} \dot{\theta}_e \cos \theta_e) + F_{ef}^0 \\
F_{er}^z &= c_{er}^z(z_4 - z_e - l_{er} \sin \theta_e) + d_{er}^z(\dot{z}_4 - \dot{z}_e - l_{er} \dot{\theta}_e \cos \theta_e) + F_{er}^0,
\end{aligned} \tag{A.3}$$

Table A.8: Parameters 4-mass roll model.

Parameter	Value	Interpretation
r_c [m]	1	height of the cabin CoG above the roll center
J_a [kgm ²]	400	front axle inertia, at roll center
J_f [kgm ²]	145	front chassis inertia, at roll center
J_e [kgm ²]	190	engine inertia, at roll center
J_c [kgm ²]	2323	cabin inertia, at roll center
c_t [Nm/rad]	$24 \cdot 10^5$	tyre stiffness
c_p [Nm/rad]	$32 \cdot 10^4$	primary suspension stiffness
c_e [Nm/rad]	$45 \cdot 10^4$	engine suspension stiffness
c_f [Nm/rad]	$14 \cdot 10^4$	chassis internal stiffness
c_s [Nm/rad]	$88 \cdot 10^4$	secondary suspension stiffness
d_p [Nms/rad]	6064	primary suspension damping
d_e [Nms/rad]	1161	engine suspension damping
d_s [Nms/rad]	8047	secondary suspension damping

and the forces acting on the cabin are given by

$$\begin{aligned}
F_{cf}^x &= c_{sf}^x(x_5 - x_c - l_{cf} \cos \theta_c + z_{cf} \sin \theta_c) + d_{sf}^x(\dot{x}_5 - \dot{x}_c + l_{cf} \dot{\theta} \sin \theta_c + z_{cf} \dot{\theta}_c \cos \theta_c) \\
F_{cf}^z &= c_{sf}^z(z_5 - z_c + z_{cf} \cos \theta_c + l_{cf} \sin \theta_c) + d_{sf}^z(\dot{z}_5 - \dot{z}_c + z_{cf} \dot{\theta}_c \sin \theta_c + l_{cf} \dot{\theta}_c \cos \theta_c) \\
&\quad + F_{cf}^0 + F_{act}^F \\
F_{cr}^x &= 0 \\
F_{cr}^z &= c_{sr}^z(z_6 - z_c + z_{cr} \cos \theta_c - l_{cr} \sin \theta_c) + d_{sr}^z(\dot{z}_6 - \dot{z}_c + z_{cr} \dot{\theta}_c \sin \theta_c - l_{cr} \dot{\theta}_c \cos \theta_c) \\
&\quad + F_{cr}^0 + F_{act}^R.
\end{aligned} \tag{A.4}$$

At standstill, the equilibrium conditions are given by $\underline{x}_h = \dot{\underline{x}}_h = \ddot{\underline{x}}_h = 0$, with $\underline{x}_h = [z_{af}, z_{ar}, \theta_f, x_e, z_e, \theta_e, x_c, z_c, \theta_c]^T$.

Table A.9: Geometric parameters 9-DOF pitch-heave model.

Parameter	Value	Dimension	Description
z_{f5}	0.25	m	vert. pos. 5 th wheel w.r.t. chassis CoG
z_{cf}	0.97	m	vert. pos. cabin front mount w.r.t. CoG
z_{cr}	0.97	m	vert. pos. cabin rear mount w.r.t. CoG
z_{ef}	0.13	m	position engine front mount w.r.t. below CoG
z_{er}	0.18	m	position engine rear mount w.r.t. below CoG
l_{am}	1.11	m	long. pos. front axle CoG w.r.t. cabin front susp.
l_{fm}	1.46	m	long. pos. chassis CoG w.r.t. front axle.
l_{f5}	3.28	m	long. pos. 5 th wheel w.r.t. front axle.
l_{em}	1.53	m	long. pos. engine CoG w.r.t. cabin front susp.
l_{ef}	0.81	m	long. pos. engine CoG w.r.t. engine front susp.
l_{er}	0.32	m	long. pos. engine CoG w.r.t. engine rear susp.
l_{cf}	0.94	m	long. pos. cabin CoG w.r.t. cabin front susp.
l_{cr}	1.14	m	long. pos. cabin CoG w.r.t. cabin rear susp.
l_{wb}	3.8	m	wheel distance tractor

Table A.10: Mass parameters 9-DOF pitch-heave model.

Parameter	Value	Dimension	Description
m_{af}	700/2	kg	Front axle mass (with tyres)
m_{ar}	1240/2	kg	Drive axle mass (with tyres)
m_f	2503/2	kg	Engine mass
m_e	1785/2	kg	Engine mass
m_c	1300/2	kg	Cabin mass
m_{tot}	19567/2	kg	Combined load on tractor tyres
\underline{J}_f^*	7735/2	kgm ²	Chassis inertia at hitch-point
\underline{J}_e	1000/2	kgm ²	Engine inertia
\underline{J}_c	1100/2	kgm ²	Cabin inertia

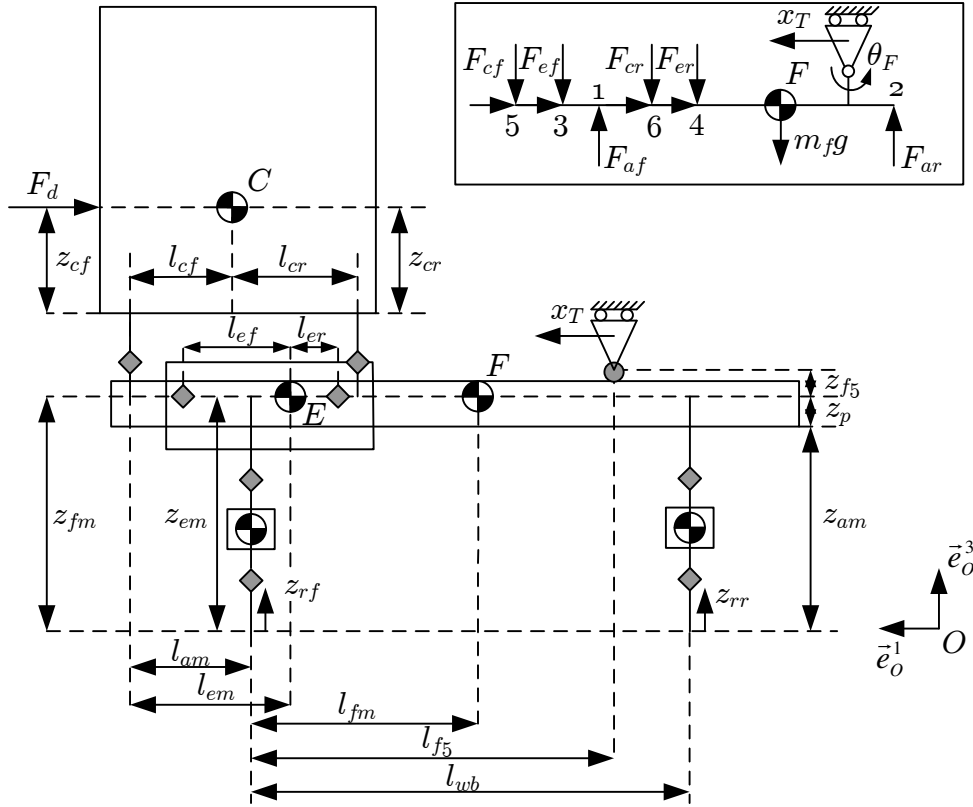


Figure A.4: Half truck pitch-heave model, schematic representation (left) and free-body diagram chassis (top right).

Table A.11: Suspension parameters 9-DOF pitch-heave model.

Parameter	Value	Dimension	Description
c_{tf}	$1.2 \cdot 10^6$	N/m	tyre stiffness front
c_{tr}	$1.1 \cdot 10^6$	N/m	tyre stiffness rear
c_{pf}	$3 \cdot 10^5$	N/m	prim. susp. stiffness front
c_{pr}	$3 \cdot 10^5$	N/m	prim. susp. stiffness rear
c_{ef}	$[5, 15] \cdot 10^5$	N/m	eng. susp. [x,z] stiffness front
c_{er}	$[6, 2] \cdot 10^6$	N/m	eng. susp. [x,z] stiffness rear
c_{sf}	$[60, 0.2] \cdot 10^5$	N/m	sec. susp. [x,z] stiffness front
c_{sr}	$[0, 2] \cdot 10^4$	N/m	sec. susp. [x,z] stiffness rear
d_{pf}	$11 \cdot 10^3$	N/m	prim. susp. damping front
d_{pr}	$22 \cdot 10^3$	N/m	prim. susp. damping rear
d_{pT}	$1 \cdot 10^4$	N/m	prim. susp. damping trailer
d_{ef}	$[2, 2] \cdot 10^3$	Ns/m	eng. susp. [x,z] damping front
d_{er}	$[6, 6] \cdot 10^3$	Ns/m	eng. susp. [x,z] damping rear
d_{sf}	$[25, 7.4] \cdot 10^3$	Ns/m	sec. susp. [x,z] damping front
d_{sr}	$[0, 5.9] \cdot 10^3$	Ns/m	sec. susp. [x,z] damping rear

Appendix B

Control invariant points

It is well known that the quarter car model has a control invariant point around the wheel hop resonance, Karnopp (2008). In this appendix it is shown that the quarter truck heave model does not have this limitation. First however, the origin of the control invariant point of the quarter car model is analyzed to illustrate the differences. The equations of motion for the quarter car model are given by

$$\begin{aligned} m_1 \ddot{z}_1 &= c_1(z_r - z_1) + c_2(z_2 - z_1) + d_2(\dot{z}_2 - \dot{z}_1) - F_{act} \\ m_2 \ddot{z}_2 &= c_2(z_1 - z_2) + c_2(z_2 - z_1) + d_2(\dot{z}_1 - \dot{z}_2) + F_{act}, \end{aligned} \quad (\text{B.1})$$

with m_1, z_1, c_1 the mass, vertical position and stiffness of the unsuspended mass and m_2, z_2, c_2, d_2 the mass, vertical position, stiffness and damping of the suspended mass. Furthermore, F_{act} is the actuator force. After substitution, Laplace transform, and rearranging, the motion of the suspended mass can be written as

$$z_2 \{ (m_2 s^2 + d_2 s + c_2)(m_1 s^2 + c_1) + m_2 s^2 (d_2 s + c_2) \} = (m_1 s^2 + c_1) F_{act} + z_r c_1 (c_2 + d_2 s). \quad (\text{B.2})$$

The control invariant points are defined as

$$\left| \frac{z_2}{F_{act}} \right|_{s=j\omega} = 0. \quad (\text{B.3})$$

So, there exists a control invariant point at

$$\left| m_1 s^2 + c_1 \right|_{s=j\omega} = 0 \rightarrow \omega_{ip} = \sqrt{\frac{c_1}{m_1}}. \quad (\text{B.4})$$

Furthermore, the dynamics at the invariant point are given by

$$\left. \frac{z_2}{z_r} \right|_{s=j\omega_{ip}} = \left. \frac{c_1(c_2 + d_2 s)}{m_2 s^2(c_2 + d_2 s)} \right|_{s=j\omega_{ip}} = -\frac{m_1}{m_2}. \quad (\text{B.5})$$

For the quarter truck model, the engine and frame masses are lumped and the cabin damping is set to zero to simplify the equations. The resulting system, with the states

as defined in section 3.2.3, is given by

$$\begin{aligned} m_c \ddot{z}_c + c_c z_c &= c_c z_f + F_{act} \\ m_f \ddot{z}_f + d_a \dot{z}_f + (c_a + c_c) z_f &= c_c z_c + c_a z_a + d_a \dot{z}_a - F_{act} \\ m_a \ddot{z}_a + d_a \dot{z}_f + (c_a + c_t) z_a &= c_a z_f + c_t z_r + d_a \dot{z}_f. \end{aligned} \quad (\text{B.6})$$

After Laplace transformation the frequency domain description is given by

$$\begin{aligned} D_c z_c &= c_c z_f + F_{act} \\ D_f z_f &= c_c z_c + z_a (d_a s + c_a) - F_{act} \\ D_a z_a &= z_f (d_a s + c_a) + c_t z_r. \end{aligned} \quad (\text{B.7})$$

Substitution gives

$$\underbrace{(D_f - D_a^{-1}(d_a s + c_a)^2)}_{\bar{D}_f} z_f = c_c z_c + \underbrace{D_a^{-1} c_t (d_a s + c_a)}_{D_r} z_r - F_{act}, \quad (\text{B.8})$$

and

$$D_c z_c = c_c \bar{D}_f^{-1} (c_c z_c + D_r z_r - F_{act}) + F_{act}. \quad (\text{B.9})$$

After rearranging, the cabin vertical dynamics are given by

$$z_c (D_c - c_c^2 \bar{D}_f^{-1}) = c_c \bar{D}_f^{-1} D_r z_r + F_{act} (1 - c_c \bar{D}_f^{-1}). \quad (\text{B.10})$$

If a control invariant point exists, it must hold that

$$\begin{aligned} 0 &= \left| 1 - c_c \bar{D}_f^{-1} \right|_{s=j\omega} \\ &= \left| \frac{D_a (m_f s^2 + d_a + c_a) - (d_a s + c_a)^2}{D_a} \right|_{s=j\omega}. \end{aligned} \quad (\text{B.11})$$

Consequently, the nominator of the last equation needs to equal zero. However,

$$\begin{aligned} &\left| D_a (m_f s^2 + d_a + c_a) - (d_a s + c_a)^2 \right|_{s=j\omega} = \\ &\left| m_f m_a \omega^4 - (m_f (c_a + c_t) + c_a m_a) \omega^2 + c_a c_t - (m_f d_a + m_a d_a) j \omega^3 + d_a c_t j \omega \right| = \\ &\sqrt{\underbrace{(m_f m_a \omega^4 - (m_f (c_a + c_t) + c_a m_a) \omega^2 + c_a c_t)^2}_{\geq c_a^2 c_t^2} + \underbrace{(d_a c_t \omega - (m_f d_a + m_a d_a) \omega^3)^2}_{\geq 0}} \geq c_a c_t. \end{aligned} \quad (\text{B.12})$$

So, as the tyre and axle stiffness have positive values, there cannot be a control invariant point for the quarter truck heave model with active cabin suspension, under these lumped conditions.

Bibliography

- Acarman, T. and Özgüner, U. Rollover prevention for heavy trucks using frequency shaped sliding mode control. *Vehicle System Dynamics*, 44(10):737–762, 2006.
- Ahmed, S., Gawthorpe, R., and Mackrodt, P.-A. Aerodynamics of road and rail vehicles. *Vehicle System Dynamics*, 14(4):319–392, 1985.
- Akcay, H. and Türkay, S. Active suspension design for an idealized truck cabin. *Proc. of the European Control Conference*, 2009.
- Alleyne, A. and Hedrick, J. Nonlinear adaptive control of active suspensions. *IEEE Transactions on Control Systems Technology*, 3(1):94–101, 1995.
- Athans, M. and Falb, P. *Optimal Control: An Introduction to the Theory and Its Applications*. McGraw-Hill Book Company, 1966.
- Baek, S., Cho, S., and Joo, W. Fatigue life prediction based on the rainflow cycle counting method for the end beam of a freight car bogie. *International Journal of Automotive Technology*, 9(1):95–101, 2008.
- Ballo, I. Properties of air spring as a force generator in active vibration control systems. *Vehicle System Dynamics*, 35(1):67–72, 2001.
- Ballo, I. Comparison of the properties of active and semiactive suspension. *Vehicle System Dynamics*, 45(11):1065–1073, 2007.
- Ben-Israel, A. and Greville, T. *Generalized Inverses: Theory and Applications*. Wiley-Interscience, 1974. ISBN 978-0-387-00293-4.
- Besselink, I. Vehicle dynamics analysis using SimMechanics and TNO Delft-Tyre. *Proc. of the IAC 2006 The Mathworks International Automotive Conference*, 2006.
- Besselink, I. Vehicle dynamics. *Lecture notes 4L150*, 2008. Department of Mechanical Engineering, Eindhoven University of Technology.
- Besselink, I. and van Asperen, F. Numerical optimization of the linear dynamic behavior of commercial vehicles. *Vehicle System Dynamics*, 23:53–70, 1994.
- Best, M., Gordon, T., and Dixon, P. An extended adaptive kalman filter for real-time

- state estimation of vehicle handling dynamics. *Vehicle System Dynamics*, 34(1):57–75, 2000.
- Boada, M., Boada, B., Castejon, C., and Diaz, V. A fuzzy-based suspension vehicle depending on terrain. *International Journal of Vehicle Design*, 37(4):311–326, 2005.
- Boerlage, M. *Rejection of disturbances in multivariable motion systems*. Ph.D. thesis, Eindhoven University of Technology, 2008.
- Bose. http://www.bose.com/learning/project_sound/bose_suspension.jsp, 2007.
- BS 6841, . Measurement and evaluation of human exposure to whole-body mechanical vibration and repeated shock. *British Standards Institution*, 1987.
- Canudas de Wit, C., Olsson, K., Aström, K., and Lischinsky, P. A new model for control of systems with friction. *IEEE Transactions on Automatic Control*, 40(3):419–425, 1995.
- Cao, D., Rakheja, S., and Su, C.-Y. Heavy vehicle pitch dynamics and suspension tuning. part i: unconnected suspension. *Vehicle System Dynamics*, 46(10):931–953, 2008.
- Carbibles. http://www.carbibles.com/suspension_bible.html, 2007.
- Chantranuwathana, S. and Peng, H. Force tracking control for active suspensions -theory and experiments. *Proceedings of the 1999 IEEE Conference on Control Applications*, pages 442–447, 1999.
- Chen, P.-C. and Huang, A.-C. Adaptive sliding control of active suspension systems with uncertain hydraulic actuator dynamics. *Vehicle System Dynamics*, 44(5):357–368, 2006.
- Cimba, D., Wagner, J., and Baviskar, A. Investigation of active torsion bar actuator configurations to reduce vehicle body roll. *Vehicle System Dynamics*, 44(9):719–736, 2006.
- Cole, D. Fundamental issues in suspension design for heavy road vehicles. *Vehicle System Dynamics*, 35(4-5):319–360, 2001.
- DAF. <http://www.daf.com>, 2009.
- Davis, R. *Model Validation for Robust Control*. Ph.D. thesis, Churchill College, Cambridge, 1995.
- Deprez, K., Dimitrios, D., Anthonis, J., de Baerdemaeker, J., and Ramon, H. Improvement of vibrational comfort on agricultural vehicles by passive and semi-active cabin suspensions. *Computers and Electronics in Agriculture*, 49(3):431–440, 2005.
- Donati, P. Survey of technical preventative measures to reduce whole-body vibration effects when designing mobile machinery. *Journal of Sound and Vibration*, 253(1):169–183, 2002.
- Dortland, A. *Integration, validation and control of a powertrain and multibody truck*

- vehicle model*. Master's thesis, Eindhoven University of Technology, 2009. DCT report number 2009.040.
- Dressler, K., Speckert, M., and Bitsch, G. Virtual durability test rigs for automotive engineering. *Vehicle System Dynamics*, 47(4):387–401, 2008.
- Elmadany, M., Dokainish, M., and Allan, B. Ride dynamics of articulated vehicles - a literature survey. *Vehicle System Dynamics*, 8(4):287–316, 1979.
- Encică, L. *Space-mapping optimization applied to the design of a novel electromagnetic actuator for active suspension*. Ph.D. thesis, Eindhoven University of Technology, 2008.
- Evers, W.-J., Besselink, I., Teerhuis, A., and Nijmeijer, H. Experimental validation of a quarter truck model using asynchronous measurements with low signal-to-noise ratio's. *International Symposium on Advanced Vehicle Control (AVEC)*, (accepted), 2010a.
- Evers, W.-J., Besselink, I., Teerhuis, A., and Nijmeijer, H. Experimental validation of a truck roll model using asynchronous measurements with low signal-to-noise ratio's. *Proceedings of the American Control Conference*, (accepted), 2010b.
- Evers, W.-J., Besselink, I., Teerhuis, A., van der Knaap, A., and Nijmeijer, H. Controlling active cabin suspensions in commercial vehicles. *Proceedings of the American Control Conference, St. Louis, USA*, pages 683–688, 2009a.
- Evers, W.-J., Besselink, I., van der Knaap, A., and Nijmeijer, H. Analysis of a variable geometry active suspension. *International Symposium on Advanced Vehicle Control (AVEC), Kobe, Japan*, pages 350–355, 2008a.
- Evers, W.-J., Besselink, I., van der Knaap, A., and Nijmeijer, H. Modeling, analysis and control of a variable geometry actuator. *IEEE Intelligent Vehicles Symposium, Eindhoven, The Netherlands*, pages 251–256, 2008b.
- Evers, W.-J., Besselink, I., van der Knaap, A., and Nijmeijer, H. Development and validation of a modular simulation model for commercial vehicles. *Int. Journal of Heavy Vehicle Systems*, 16(1-2):132–153, 2009b.
- Fancher, P. and Winkler, C. Directional performance issues in evaluation and design of articulated heavy vehicles. *Vehicle System Dynamics*, 45(7-8):607–647, 2007.
- Fialho, I. and Balas, G. Design of nonlinear controllers for active vehicle suspensions using parameter-varying control synthesis. *Vehicle System Dynamics*, 33(5):351–370, 2000.
- Fialho, I. and Balas, G. Road adaptive active suspension design using linear parameter-varying gain-scheduling. *IEEE Transactions on Control Systems Technology*, 10(1):43–54, 2002.
- Fischer, D. and Isermann, R. Mechatronic semi-active and active vehicle suspensions. *Control Engineering Practice*, 12(11):1353–1367, 2004.
- Ford. <http://www.fordtranscontinental.nl>, 2009.

- Franklin, F., Powell, J., and Emani-Naeini, A. *Feedback control of dynamic systems*. Addison-Wesley Publishing Company, third edition, 1994. ISBN 0-201-53487-8.
- Georgiou, G., Verros, G., and Natsiavas, S. Multi-objective optimization of quarter-car models with a passive or semi-active suspension. *Vehicle System Dynamics*, 45(1):77–92, 2007.
- Gillespie, T. Heavy truck ride. *SAE Special Publication SP 607*, 1985.
- Gillespie, T. and Karamihas, S. Simplified models for truck dynamic response to road inputs. *International Journal of Heavy Vehicle Systems*, 7(1):52–63, 2000.
- Graf, C., Maas, J., and Pflug, H.-C. Konzept für eine aktive lkw-fahrerhauslagerung. *AUTOREG 2008 Conference, Baden-Baden, Germany*, 2008. (Written in German).
- Green, M. and Limebeer, D. *Linear robust control*. Pearson Education, Inc., 1995. ISBN 0-13-102278-4.
- Griffin, M. Discomfort from feeling vehicle vibration. *Vehicle System Dynamics*, 45(7):679–698, 2007.
- Guillaume, P., Pintelon, R., and Schoukens, J. Nonparametric frequency response function estimators based on nonlinear averaging techniques. *IEEE Transactions on instrumentation and measurement*, 41(6):739–746, 1992.
- Gustafsson, F. Slip-based tire-road friction estimation. *Automatica*, 33(6), 1997.
- Gysen, B., Janssen, J., Paulides, J., and Lomonova, E. Design aspects of an active electromagnetic suspension system for automotive applications. *IEEE Transactions on Industry Applications*, 45(5):1589–1597, 2009.
- H. Inoue, H. and Kondo, T. Suspension device for vehicle. *European patent application number 05803908.2*, (serial number EP1829718A1), 2007.
- Hakvoort, R. and van den Hof, P. Identification of probabilistic system uncertainty regions by explicit evaluation of bias and variance errors. *IEEE Transactions on automatic control*, 42(11):1516–1528, 1997.
- Hanselman, D. *Brushless permanent magnet motor design*. Writers' Collective Cranston, Rhode Island, second edition, 2003.
- Hansson, P. *Modelling and Optimization of Passive and Adaptively Controlled Active Cab Suspensions on Terrain Vehicles, especially Agricultural Tractors*. Ph.D. thesis, Swedish University of Agricultural Sciences, Uppsala, 1993.
- Heath, W. The variation of non-parametric estimates in closed-loop. *Automatica*, 39(11):1849–1863, 2003.
- Heißing, B. and Ersoy, M. *Fahrwerkhandbuch*. Friedr. Vieweg & Sohn Verlag, 2007. ISBN 3834801054. (Written in German).
- Hiromatsu, T., Inaba, T., and Matsuo, Y. Development of an electromechanical active-cab-suspension. *Proc. of the Int. Conf. on Industrial Electronics, Control, and Instrumentation*, pages 2132–2137, 1993.

- Holen, P. Experimental evaluation of modally distributed damping in heavy vehicles. *Vehicle System Dynamics*, 46(6):521–539, 2008.
- Houben, L. *Analysis of truck steering behaviour using a multi-body model*. Master’s thesis, Eindhoven University of Technology, 2008. DCT report number 2008.139.
- Howe, J., Chrstos, J., Allen, R., Myers, T., Lee, D., Liang, C.-Y., Gorsich, D., and Reid, A. Quarter car model stress analysis for terrain/road profile ratings. *International Journal of Vehicle Design*, 36(2-3):248–269, 2004.
- Hrovat, D. Survey of advanced suspension developments and related optimal control applications. *Automatica*, 33(10):1781–1817, 1997.
- Hrovat, D. and Hubbard, M. Optimum vehicle suspension minimizing rms rattlespace, sprung-mass acceleration and jerk. *ASME Journal of Dynamic Systems, Measurement and Control*, 103(3):228–236, 1981.
- Huisman, R. *A controller and observer for active suspensions with preview*. Ph.D. thesis, Eindhoven University of Technology, 1994.
- Huston, R. *Multibody dynamics*. Butterworth-Heinemann, 1995. ISBN 0409900419.
- van Iersel, S. *unknown title*. Master’s thesis, Eindhoven University of Technology, 2010. To be published.
- ISO 2631-1, . Mechanical vibration and shock - evaluation of human exposure to whole-body vibration: Part 1. *International Organisation for Standardization, second edition*, 1997.
- ISO 8608, . Mechanical vibration - road surface profiles - reporting of measured data. *International Organisation for Standardization*, 1995.
- Jiang, Z., Streit, D., and El-Gindy, M. Heavy vehicle comfort: Literature survey. *International Journal of Heavy Vehicle Systems*, 8(3/4):258–284, 2001.
- Jones, W. Easy ride: Bose corp. uses speaker technology to give cars adaptive suspension. *IEEE Spectrum*, 42(5):12–14, 2005.
- Karnopp, D. Active damping in road vehicle suspension systems. *Vehicle System Dynamics*, 12(6):291–311, 1983.
- Karnopp, D. How significant are transfer function relations and invariant points for a quarter car suspension model? *Vehicle System Dynamics*, 47(4):457–464, 2008.
- Kawamoto, Y., Suda, Y., Inoue, H., and Kondo, T. Electro-mechanical suspension system considering energy consumption and vehicle manoeuvre. *Vehicle System Dynamics*, 46(1):1053–1063, 2008.
- van der Knaap, A. *Design of a low power anti-roll/pitch system for a passenger car*. Master’s thesis, Delft University of Technology, 1989.
- van der Knaap, A. Anti-roll/pitch system for use in a vehicle and vehicle equipped with such system. *International patent application number PCT/NL2005/000604*, (serial number WO 2006/019298 A1), 2006.

- van der Knaap, A. and Pacejka, H. Mass spring system with roll/pitch stabilization for use in vehicles. *International patent application number PCT/NL93/00094*, (serial number WO 93/22150), 1993.
- van der Knaap, A., Teerhuis, A., Tinsel, R., and Verschuren, R. Active suspension assembly for a vehicle. *International patent application number PCT/EP2007/061366*, (serial number WO 2008/049845 A1), 2007.
- van der Knaap, A., Venhovens, P., and Pacejka, H. Evaluation and practical implementation of a low power attitude and vibration control system. *International Symposium on Advanced Vehicle Control (AVEC)*, pages 318–324, 1994.
- Ksiazek, M. and Luczko, J. Optimal vibration isolation of a tractor-semi-trailer system. *Vehicle System Dynamics*, 45(3):277–289, 2007.
- Lewis, F. and Syrmos, V. *Optimal control*. John Wiley & Sons, 1995. ISBN 0471033782.
- Liebrechts, R. Vibrations, comfort & fatigue. *Course sheets advanced vehicle dynamics, 4J570*, 2007. Department of mechanical engineering, Eindhoven University of Technology.
- Lin, J.-S. and Kanellakopoulos, I. Nonlinear design of active suspensions. *IEEE Control System Magazine*, 17(3):45–59, 1997.
- Lomonova, E. *A System Look at Electromechanical Actuation for Primary Flight Control*. Number 2 in 3. Delft University Press, 1997. ISBN 90-407-1582-3.
- Mazzaro, M. and Sznaier, M. Convex necessary and sufficient conditions for frequency domain model (in)validation under sltv structured uncertainty. *IEEE Transactions on automatic control*, 49(10):1683–1692, 2004.
- Miege, A. and Cebon, D. Optimal roll control of an articulated vehicle: theory and model validation. *Vehicle System Dynamics*, 43(12):867–893, 2005.
- Muijderman, J. *Flexible objective controllers for semi-active suspensions with preview*. Ph.D. thesis, Eindhoven University of Technology, 1997.
- Nakano, K. and Suda, Y. Combined type self-powered active vibration control of truck cabins. *Vehicle System Dynamics*, 41(6):449–473, 2004.
- Nakano, K., Suda, Y., Nakadai, S., and Tsunashima, H. Self-powered active control applied to a truck cab suspension. *JSAE Review*, 20(4):511–516, 1999.
- Nakhaie Jazar, G., Alkhatib, R., and Golnaraghi, M. F. Root mean square optimization criterion for vibration behaviour of linear quarter car using analytical methods. *Vehicle System Dynamics*, 44(6):477–512, 2006.
- Nelles, O. *Nonlinear System Identification*. Springer-Verlag, 2001. ISBN 3-540-67369-5.
- Oomen, T. and Bosgra, O. Estimating disturbances and model uncertainty in model validation for robust control. *Proceedings of the 47th Conference on Decision and Control*, pages 5513–5518, 2008.

- Oomen, T. and Bosgra, O. Well-posed model quality estimation by design of validation experiments. *Proceedings of the 15th IFAC Symposium on System Identification*, pages 1199–1204, 2009.
- Ozay, N. and Sznaier, M. A pessimistic approach to frequency domain model (in)validation. *Proceedings of the 46th Conference on Decision and Control*, pages 4895–4900, 2007.
- Pacejka, H. *Tyre and Vehicle Dynamics*. Butterworth-Heinemann, 2002. ISBN 0750651415.
- Philipson, N., Andreasson, J., Gäfvert, M., and Woodruff, A. Heavy vehicle modeling with the vehicle dynamics library. *Proc. of the 6th Int. Modelica Conference, Bielefeld, Germany*, pages 629–634, 2008.
- Phillips, D. Truck drivers and lower back pain. <http://www.suite101.com>, 2009.
- Pilbeam, C. and Sharp, R. Performance potential and power consumption of slow-active suspension systems with preview. *Vehicle System Dynamics*, 25(3):169–183, 1996.
- Pintelon, R. and Schoukens, J. *System identification: a frequency domain approach*. IEEE Press, 2001. ISBN 0-7803-6000-1.
- Pinxteren, M. *Brake and Roll-over performance of LZV combinations*. Master’s thesis, Eindhoven University of Technology, 2009.
- Poolla, K., Khargonekar, P., Tikku, A., and Krause, J. A time-domain approach to model validation. *IEEE Transactions on automatic control*, 39(5):951–959, 1994.
- Purdy, D. and Bulman, D. An experimental and theoretical investigation into the design of an active suspension system for a racing car. *Proc. Instn. Mech. Engrs.*, 211(D):161–173, 1997.
- Ramsbottom, M. and Crolla, D. Simulation of an adaptive controller for a limited-bandwidth active suspension. *International Journal of Vehicle Design*, 21(4-5):355–371, 1999.
- Sampaio, J. Design of a low power active truck cab suspension. Technical report, Eindhoven University of Technology, 2009. DCT report number 2009.119.
- Sampson, D. and Cebon, D. Achievable roll stability of heavy road vehicles. *Proc. Instn. Mech. Engrs, Part D, Journal of Automobile Engineering*, 210(1):45–55, 2003.
- van der Sanden, M. Actuatorontwerp voor een actieve ophanging. Technical report, Eindhoven University of Technology, 2008. DCT report number 2008.122 (written in dutch).
- Schiehlen, W. White noise excitation of road vehicle structures. *Sadhana*, 31(4):487–503, 2006.
- Schilperoord, P. Intelligente systemen moeten chauffeurs bijsturen. *De Ingenieur*, (5):22–29, 2007. (Written in Dutch).

- Sharp, R. Variable geometry active suspension for cars. *Computing & Control Engineering Journal*, 9(5):217–222, 1998.
- Sharp, R. and Crolla, D. Road vehicle suspension system design - a review. *Vehicle System Dynamics*, 16(3):167–192, 1987.
- Sie, W.-T., Lian, R.-J., and Lin, B.-F. Enhancing grey prediction fuzzy controller for active suspension systems. *Vehicle System Dynamics*, 44(5):407–430, 2006.
- Skogestad, S. and Postlethwaite, I. *Multivariable feedback control: analysis and design*. John Wiley & Sons, West Sussex, United Kingdom, second edition, 2005. ISBN 0-470-01168-8.
- Smith, R. and Doyle, J. Model validation: A connection between robust control and identification. *IEEE Transactions on automatic control*, 37(7):942–952, 1992.
- Smith, R. and Dullerud, G. Continuous-time control model validation using finite experimental data. *IEEE Transactions on automatic control*, 41(8):1094–1105, 1996.
- Söderström, T. Errors-in-variables methods in system identification. *Automatica*, 43(6):939–958, 2007.
- Spijkers, T. *Validation and enhancement of a tractor semi-trailer multibody simulation model*. Master’s thesis, Eindhoven University of Technology, 2008. DCT report number 2008.068.
- Strandemar, K. *On objective measures for ride comfort evaluation*. Ph.D. thesis, Royal Institute of Technology (KTH) Sweden, 2005.
- Tseng, H. Dynamic estimation of road bank angle. *Vehicle System Dynamics*, 36(4-5):307–328, 2001.
- Uffelmann, F. and Wiesmeijer, A. Active cab suspension for trucks: technical realization and achievable ride comfort. *24th FISITA Congress, London, England*, pages 75–85, 1992.
- Vahidi, A., Stefanopoulou, A., and Peng, H. Recursive least squares with forgetting for online estimation of vehicle mass and road grade: theory and experiments. *Vehicle System Dynamics*, 43(1):31–55, 2005.
- Venhovens, P. *Optimal control of vehicle suspensions*. Ph.D. thesis, Delft University of Technology, 1993.
- Venhovens, P. and van der Knaap, A. Delft active suspension (DAS). Background theory and physical realization. In J. Pauwelussen and H. Pacejka, editors, *Smart Vehicles*, pages 139–165. Swets & Zeitlinger Publishers, 1995.
- Venhovens, P., van der Knaap, A., and Pacejka, H. Semi-active vibration and attitude control. *International Symposium on Advanced Vehicle Control (AVEC)*, pages 170–175, 1992.
- Verros, G., Natsiavas, S., and Papadimitriou, C. Design optimization of quarter-car

- models with passive and semi-active suspensions under random road excitation. *Journal of Vibration and Control*, 11(5):581–606, 2005.
- Verver, M. *Numerical tools for comfort analysis of automotive seating*. Ph.D. thesis, Eindhoven University of Technology, 2004.
- Vissers, J. Real-time implementation of a preview-based control strategy for a semi-active truck suspension. Technical Report WFW 97.078, Eindhoven University of Technology, 1997.
- Volvo. <http://www.volvo.com/trucks/global/en-gb/company/history>, 2009.
- Watanabe, Y. and Sharp, R. Mechanical and control design of a variable geometry active suspension system. *Vehicle System Dynamics*, 32:217–235, 1999.
- Wiesmeijer, A. and Uffelmann, F. Vibration isolated cabin by active suspension—requirements, concept, and first results. *Fifth Autotechnologies Conference and Exposition, Monte-Carlo, Monaco*, pages 197–210, 1991.
- Williams, D. and Haddad, D. Nonlinear control of roll moment distribution to influence vehicle yaw characteristics. *IEEE Transactions on Control Systems Technology*, 3(1):110–116, 1995.
- Wouw, N. Multibody dynamics: lecture notes. *Course sheets Multibody Dynamics*, 2005. Department of Mechanical Engineering, Eindhoven University of Technology.
- Wright, P. and Williams, D. The application of active suspension to high performance road vehicles. *IMechE C239/84*, 1984.
- Yu, H., Güvenc, L., and Özgüner, U. Heavy duty vehicle rollover detection and active roll control. *Vehicle System Dynamics*, 46(6):451–470, 2009.
- Zalm, G. v. d., Huisman, R., Steinbuch, M., and Veldpaus, F. Frequency domain approach for the design of heavy-duty vehicle speed controllers. *International Journal of Heavy Vehicle Systems*, 15(1):107–123, 2008.
- van Zanten, A. Bosch ESP systems: 5 years of experience. *SAE 2000-01-1633*, 2000.
- Zhang, N., Smith, W., and Jeyakumaran, J. Hydraulically interconnected vehicle suspension: background and modelling. *Vehicle System Dynamics*, 48(1):17–40, 2010.
- Zhang, Y. *A hybrid adaptive and robust control methodology with application to active vibration isolation*. Ph.D. thesis, University of Illinois at Urbana-Champaign, 2003.
- Zhou, K., Doyle, J., and Glover, K. *Robust and optimal control*. Prentice Hall, New Jersey, USA, 1996. ISBN 0-13-456567-3.
- Zuo, L. and Nayfeh, S. H2 optimal control of disturbance-delayed systems with application to vehicle suspensions. *Vehicle System Dynamics*, 45(3):233–247, 2007.

Summary

Improving driver comfort in commercial vehicles

Modeling and control of a low-power active cabin suspension system

Comfort enhancement of commercial vehicles has been an engineering topic ever since the first trucks emerged around 1900. Since then, significant improvements have been made by implementing cabin (secondary) and seat suspensions. Moreover, the invention of the air spring and its application to the various vehicle's suspension systems also greatly enhanced driver comfort. However, despite these improvements many truck drivers have health related problems, which are expected to be caused by their exposure to the environmental vibrations over longer periods of time.

The most recent suspension improvements in commercial vehicles date back more than a decade and the possibilities for further improvements using passive devices (springs and dampers) seem nearly exhausted. Consequently, in line with developments in passenger cars, truck manufacturers are now investigating semi-active and active suspension systems. Herein, active suspensions are expected to give the best performance, but also come at the highest cost. Especially the high power consumption of market-ready devices is problematic in a branch where all costs need to be minimized.

In this dissertation the field of secondary suspension design and controllable suspensions for heavy vehicles is addressed. More specifically, the possibilities for a low-power active cabin suspension design are investigated. The open literature on this topic is very limited in comparison to that of passenger cars. However, as heavy vehicle systems are dynamically more challenging, with many vibration modes below 20 Hz, there is great research potential.

The dynamic complexity becomes clear when considering the developed 44 degrees of freedom (DOF) tractor semi-trailer simulation model. This model is a vital tool for suspension analysis and evaluation of various control strategies. Moreover, as it is modular it can also be easily adapted for other related research. The main vehicle components all have their own modules. So, for example, when evaluating a new cabin suspension design, only the cabin module needs to be replaced. The model has been validated using extensive tests on a real tractor semi-trailer test-rig.

The control strategy is a key aspect of any active suspension system. However, the 44 DOF tractor semi-trailer model is too complex for controller design. Therefore,

reduced order models are required which describe the main dynamic properties. A quarter truck heave-, half truck roll-, and half truck pitch-heave model are developed and validated using a frequency-domain validation technique and the test-rig measurements. The technique is based on a recently developed frequency domain validation method for robust control and adapted for non-synchronous inputs, with noise on the input and output measurements. The models are shown to give a fair representation of the complex truck dynamics. Furthermore, the proposed validation method may be a valuable tool to obtain high quality vehicle models.

As a first step, in search of a low power active cabin suspension system, various suspension concepts are evaluated under idealized conditions. From this evaluation, it follows that the variable geometry active suspension has great potential. However, the only known physical realization - the *Delft Active Suspension* - suffers from packaging issues, nonlinear stiffness characteristics, fail-safe issues and high production cost. Recently, a redesign - the *electromechanical Low-Power Active Suspension (eLPAS)* - was presented, which is expected to overcome most of these issues. This design is modeled, analyzed and a controller is designed, which can be used to manipulate the suspension force. Feasibility of the design is demonstrated using tests on a hardware prototype.

Finally, the validated reduced order models are used to design suitable roll and pitch-heave control strategies. These are evaluated using a combination of the 44 DOF tractor semi-trailer and *eLPAS* models. Four *eLPAS* devices are placed at the lower corners of the cabin and modal input-output decoupling is applied for the controller implementation. It is shown, that driver comfort and cabin attitude behavior (roll, pitch and heave when braking, accelerating or steering) can be greatly improved without consuming excessive amounts of energy.

So, overall these results enforce the notion that the variable geometry active suspension can be effectively used as low power active cabin suspension. However, there are still some open questions that need to be addressed before this design can be implemented in the next generation commercial vehicles. Durability and failsafe behavior of the *eLPAS* system, as well as controller robustness to variations in the vehicle parameters and environmental conditions, are some of the topics that require further study.

Samenvatting

Het verbeteren van het comfort in commerciële voertuigen is al een punt van onderzoek sinds het ontstaan van de eerste vrachtwagens rond 1900. Sinds die tijd zijn er significante verbeteringen gemaakt door de implementatie van cabine (secundaire) en stoelvering. Verder heeft de uitvinding van de luchtveer en diens applicatie in elk van de voertuig veersystemen het comfort ook aanzienlijk verbeterd. Desalniettemin hebben een groot aantal vrachtwagen bestuurders gezondheidsklachten die zijn terug te leiden tot hun dagelijkse blootstelling aan cabine trillingen.

De meest recente verbeteringen in de veersystemen van commerciële voertuigen dateren al van meer dan een tiental jaar geleden en de mogelijkheden voor verdere verbetering met behulp van passieve elementen (veren en dempers) lijken redelijk uitgeput. Daarom, geïnspireerd door de ontwikkelingen voor personenauto's, richten vrachtwagen fabrikanten hun onderzoek nu op de mogelijkheden van semi-actieve en actieve veersystemen. Hierbij is de verwachting dat actieve systemen de beste performance leveren, maar ook het duurste zijn. Vooral het hoge energie verbruik van de systemen die op dit moment op de markt zijn is problematisch in een branche waar alles draait om de minimalisatie van de kosten.

In deze thesis ligt de focus op het gebied van het ontwerp en regelen van secundaire veringen voor vrachtwagens. Specifieker, de mogelijkheden voor een actieve cabine vering met een laag energieverbruik zijn onderzocht. De open literatuur op dit onderwerp is erg beperkt in vergelijking met die voor personenauto's. De onderzoeksmogelijkheden zijn echter geweldig, gezien het feit dat de dynamica van vrachtwagens veel uitdagender is, met veel dynamische modes onder de twintig hertz.

De dynamische complexiteit wordt duidelijk bij de beschouwing van het ontwikkelde tractor semi-trailer simulatie model met 44 graden van vrijheid (DOF). Dit model is een essentieel gereedschapsmiddel voor de analyse en evaluatie van verschillende veer systemen en regelstrategieën. Het is modulaair opgebouwd zodat het ook makkelijk gebruik kan worden voor ander gerelateerd onderzoek. Elk van de belangrijkste voertuig componenten is beschreven door één module. Als zodanig hoeft, bijvoorbeeld, alleen de cabine module vervangen te worden voor de evaluatie van verschillende cabine veersystemen. Het model is gevalideerd met behulp van uitgebreide test-data, verkregen met een werkelijk tractor semi-trailer test voertuig.

De regelstrategie is één van de belangrijkste elementen van een actieve vering. Het 44 DOF model is echter te complex voor regelaar ontwerp. Daarom zijn vereenvoudigde

modellen nodig die de belangrijkste dynamische eigenschappen beschrijven. Een kwart voertuig model voor de vertikaal dynamica, een half voertuig model voor de rol dynamica, en een half voertuig model voor de damp en vertikaal dynamica zijn ontwikkeld en gevalideerd. Voor de validatie is een frequentie domein methode ontwikkeld die is gebaseerd op een recent ontwikkelde techniek voor robuust regelaar ontwerp. Deze techniek is aangepast voor niet-synchrone ingangen met ruis op de in- en uitgangsmetingen. De modellen blijken een redelijke representatie te geven van de complexe vrachtwagen dynamica. Verder wordt de ontwikkelde validatie methode gezien als een waardevol hulpmiddel voor het verkrijgen van kwalitatief hoogwaardige voertuig modellen.

Als eerste stap bij de zoektocht naar een actieve cabine vering met een laag energie verbruik zijn verschillende veerconcepten geëvalueerd onder geïdealiseerde condities. Uit deze evaluatie volgt dat vooral de zogenaamde actieve vering met variable geometrie veelbelovend is. De enige fysische realisatie - de *Delft Active Suspension* - heeft echter een aantal nadelen: hij is groot; heeft een niet-lineaire stijfheidskarakteristiek; heeft problematisch faal gedrag; en hoge productie kosten. Recentelijk is er echter een nieuw ontwerp gepresenteerd - de *electromechanical Low Power Actieve Suspension (eLPAS)* - die hiervan naar verwachting minder last heeft. Dit ontwerp is geanalyseerd en een regelstrategie is ontwikkeld waarmee de kracht die het veersysteem uitoefent kan worden gemanipuleerd. De praktische haalbaarheid van het ontwerp is aangetoond middels tests met een hardware prototype.

Als laatste stap zijn de gevalideerde modellen gebruikt voor het ontwerp van geschikte rol en damp-vertikaal regelstrategieën. Deze zijn geëvalueerd met behulp van een combinatie van de 44 DOF en *eLPAS* modellen. Vier *eLPAS* mechanismen zijn geplaatst onder de hoeken van de cabine en modale ingangs-uitgangs ontkoppeling is toegepast voor de regelaar implementatie. Het is aangetoond dat het comfort, en het cabine gedrag bij remmen, accelereren en sturen aanzienlijk kan worden verbeterd zonder dat daar gigantische hoeveelheden energie voor nodig zijn.

Deze resultaten ondersteunen dus het idee dat een actieve vering met variable geometrie kan worden gebruikt als actieve vrachtwagen cabine vering met een laag energie verbruik. Er zijn echter nog wel een aantal open vragen die beantwoord moeten worden voordat dit ontwerp kan worden geïmplementeerd in de volgende generatie commerciële voertuigen. Duurzaamheid en faalgedrag van het *eLPAS* systeem, als ook regelaar robuustheid voor variaties van de voertuig parameters en omgevingscondities, zijn een aantal van de onderwerpen die verder onderzoek verlangen.

Acknowledgements

I can still clearly recall the windy November morning in 2005, when we had the official kick-off meeting of the project named *Active Cabin Suspension* at TNO Automotive in Helmond. There was cake, a merry atmosphere, a lot of plans, expectations and open questions. Now four years later, on a sunny but chilly afternoon, the project has come to an end, and I am enriched with the recollections of this interesting period. In my opinion, the project has been quite successful, and for that I want to acknowledge the contributions of a number of people.

First of all, I would like to thank my promotor Henk Nijmeijer, for offering me the opportunity to work on such an interesting project as a Ph.D. student. I greatly enjoyed your supervising approach: efficient, direct, and honest. Furthermore, you could always free some time for a quick chat if needed, which I experienced as very motivating. For the daily supervision, I would like to thank my copromotor Igo Besselink. Despite your often hectic agenda, you remained enthusiastic, positive, and critical. I also greatly enjoyed our cooperation and discussions during the various teaching tasks.

Part of this research project has been financed by TNO Automotive. Besides the financial contribution there has also been a lot of interaction, especially during the experimental work and the thirteen quarterly (QRT) meetings. Herein, the efforts of Albert van der Knaap as project leader during the first two and a half years are greatly acknowledged. Your knowledge of the *DAS* system, experiences with suspension and vehicle dynamics, and critical questions have forced me to reconsider proposed ideas on more than one occasion. I would also like to thank Jeroen Vandenhoude, who was promoted to project leader after Albert switched jobs, and Arjan Teerhuis. Both of you have been extremely involved in this project, assisting me with experimental challenges and reviewing the various publications. Furthermore, I would like to thank all the TNO members who contributed to this project. In particular, I would like to thank Edwin Stierman, Raymond Tinsel, Robert Verschuren, and Friedes Lameris.

This project originally started within the framework of CCAR (Competence Center for Automotive Research) and, as such, members of DAF Trucks N.V. have often provided valuable feedback during the QRT meetings. Here, I would like to acknowledge the contributions of Victor Raue, Rene Liebrechts, Willem-Jan Lamers, and in particular Theo de Ruijter.

I also want to thank all the students who contributed to my research: Thijs Spijkers for his work on truck modeling and validation; Sven van Iersel for his research on semi-

active cabin suspension control; and Michiel van der Sanden and Joao Vitor Sampaio for investigating the possibilities for alternative 2D variable geometry actuator designs. Furthermore, I want to thank Rob Mestrom, for checking the equations of motion of the *eLPAS* model. I would also like to thank the members of the reading committee, Elena Lomonova, Daniel Rixen, and David Limebeer, for their efforts. This work has been significantly enhanced thanks to your valuable feedback. Furthermore, I want to thank Paul van den Bosch and Albert van der Knaap for taking part in the defense committee.

Despite the fact that my experience is limited to what I learned on conferences; I think that the working environment at the department of Dynamics and Control Systems Technology ranks among the best in the world. Naturally, this is mainly the result of the people that work there and their social interaction. First of all, I would like to thank my roommates Stan van der Meulen and Tom Oomen, who I've known since our freshmen introduction at the University over ten years ago, for the many interesting and often fruitful discussions. Furthermore, I would also like to thank all my colleagues - in particular the MTB, Snowboard, Hora Est, Friday Afternoon, and Friday Night associates - for the great times we shared.

Finally, I would like to thank my parents, brothers, 'sisters', friends, and relatives for their love and support. A Ph.D. signifies a period of ups and downs, and although their contributions may not be directly visible, it was invaluable for finishing it.

Willem-Jan Evers

Eindhoven, March 2010

Curriculum Vitae

Willem-Jan Evers graduated from secondary school at the Odulphus Lyceum, Tilburg, The Netherlands, in 1999. He received his M.Sc. degree (With Great Appreciation) in Mechanical Engineering from the Eindhoven University of Technology (TU/e), Eindhoven, The Netherlands, in September 2005. During his external traineeship he went to ESA/ESTEC, where he worked on the “Dynamical analysis and controller design for the Gravity and Ocean Circulation Explorer (GOCE)”, a satellite launched in 2009. His M.Sc. project was entitled “Practical stabilization of a mobile robot with n trailers using saturated control” and was carried out at the TU/e.

In November 2005 he started as a Ph.D. student in the Dynamics and Control group at the TU/e and participated in a research project, lead by the Dutch Organization for Applied Scientific Research (TNO), which focussed on the development of a low-power active truck cabin suspension. He was responsible for vehicle modeling, dynamic analysis and controller design. The results are presented in this thesis.

Stellingen

behorende bij het proefschrift

Improving driver comfort in commercial vehicles Modeling and control of a low-power active cabin suspension system

1. Onder geïdealiseerde condities verschilt het energieverbruik van de *variabele geometrie actieve vering* fundamenteel van het verbruik van conventionele actieve veringsconcepten. Voor een goed onderbouwde afweging is het echter belangrijk dat deze concepten worden vergeleken gebruikmakend van gedetailleerde modellen, verschillende geoptimaliseerde regelstrategieën en een eenduidig prestatie criterium.

Hoofdstuk 4 van dit proefschrift.

2. De comfort-optimale vering voor een personenauto is verre van optimaal indien deze gebruikt wordt als cabinevering voor een vrachtwagen. Het regelmatig voorkomende gebruik hiervan in de cabinevering kan derhalve ten onrechte leiden tot een pessimistische inschatting van de haalbare prestaties.

Hoofdstuk 6 van dit proefschrift.

3. Voor een energie-efficiënte actieve cabinevering is de stap van prototype naar commercieel product een langzaam traject. Gegeven de beschikbaarheid van regelbare dempers is een semi-actieve cabinevering, zoals bestudeerd in [1], echter goedkoper en op kortere termijn te introduceren.

[1] *S.S. van Iersel. Master's thesis, te verschijnen in 2010.*

4. Elektrische voertuigen zijn na een tweetal historische tegenslagen momenteel bezig aan een hernieuwde wereldwijde intrede [2]. Hierbij lijkt Nederland, gezien de relatief korte afstanden, ideaal te zijn voor een pioniersrol op het gebied van de grootschalige introductie van elektrisch vervoer. Echter, een snelle omschakeling naar volledig elektrisch rijden is, hoofdzakelijk door de lage brandstof prijzen, niet mogelijk zonder substantiële financiële prikkels.

[2] *A. Hoekstra. Elektrisch rijden. Rijkswaterstaat, 2009.*

5. Mensen veranderen pas als ze van de noodzaak daartoe zijn doordrongen. Dit inzicht moet ter harte worden genomen door hen die onderwijzen, want het biedt mogelijkheden om de moderne zesjescultuur te doorbreken en zodoende de kwaliteit van het genoten onderwijs te verhogen.

6. Gegeven de superieure kwaliteit van de Nederlandse wegen zal de actieve cabinevering van grotere waarde zijn in Tweede en Derde Wereld landen, alsook dichterbij huis in België.

7. Promovendi zijn voor de industrie een financieel aantrekkelijke optie om te investeren in hoogwaardig onderzoek. Bedrijven moeten er echter voor waken dat er voldoende afstand blijft tussen deze promotieprojecten en de eigen commerciële ontwikkelingslijn, zodat tegenstrijdige belangen de opbrengsten van beiden niet beperken.
8. Goed, slecht en lelijk [3] zijn relatieve culturele begrippen die door sommigen tot beangstigende dogma's worden verheven om aan te zetten tot de gedachteloze veroordeling van anderen.
[3] *The Good, the Bad, and the Ugly, directed by Sergio Leone, 1966.*
9. “Een grote meester streeft ernaar dat de leerling hem overtreft.” Als deze kabbalistische opvatting van begin af aan het uitgangspunt zou zijn geweest bij het verstrekken van ontwikkelingshulp, dan zouden er nu veel minder mensen honger lijden.
10. “Soms is *verdwaald* precies waar je moet zijn. Het feit dat je niet weet wat je richting is, betekent niet dat je geen richting hebt” [4]. Een promovendus die dit niet onderkent, zij het door culturele dan wel industriële of projectmatige restricties, heeft onvoldoende zeggenschap over zijn of haar promotieproject.
[4] *Battlestar Galactica, seizoen 4, aflevering 17, 2009.*

Propositions

belonging to the thesis

Improving driver comfort in commercial vehicles Modeling and control of a low-power active cabin suspension system

1. Under idealized conditions the energy requirements of the *variable geometry active suspension* differ fundamentally from that of conventional active suspension concepts. However, for a well founded assesment it is important that these concepts are compared using detailed models, different optimized control strategies, and a clear performance criterion.

Chapter 4 of this thesis

2. The comfort optimal suspension of a passenger car is far from optimal if used as truck cabin suspension. The regular use of this in cabin suspension systems can, consequently, incorrectly lead to a pessimistic assessment of the achievable performance.

Chapter 6 of this thesis

3. The step from prototype to commercial product is a slow proces for an energy-efficient active cabin suspension. However, a semi-active cabin suspension as studied in [1] can, given the availability of controllable dampers, be introduced more quickly and relatively inexpensively.

[1] *S.S. van Iersel. Master's thesis, to appear in 2010.*

4. After two historic setbacks we are presently witnessing a renewed worldwide entry of electric vehicles [2]. Given the relatively short distances the Netherlands seems to be ideal for pioneering the large scale implementation of electric transportation. However, mainly due to the low fuel prices, there cannot be a quick transition to full electric driving without substantial financial incentives.

[2] *A. Hoekstra. Elektrisch rijden. Rijkswaterstaat (Dutch), 2009.*

5. People only change when they are truly convinced of the necessity to change. This insight has to be taken to heart by those that teach, for it presents options to counter the modern *zesjescultuur* (“culture of mediocrity”) and thereby enhance the quality of education.

6. Given the excellent quality of the Dutch roads the active cabin suspension will be of more value in Second and Third World countries, as well as closer to home in Belgium.

7. Doctoral students are, for the industry, a financially attractive option to invest in high-end research. However, companies have to remain vigilant that there remains sufficient distance between these PhD projects and their own commercial development activities, such that conflicts of interest do not limit the yield of both.
8. Good, bad, and ugly [3] are relative cultural notions, which are elevated by some to frightening dogmas, to instigate the mindless prosecution of others.
[3] *The Good, the Bad, and the Ugly*, directed by Sergio Leone, 1966.
9. “A great master strives to be exceeded by his apprentice.” If this cabbalistic view would have been adopted from the start as a basis for development aid, there would be significantly less people starving these days.
10. “Sometimes *lost* is where you need to be. The fact that you don’t know your heading does not mean you don’t have one” [4]. A PhD student who does not recognize this, be it as a result of cultural, industrial, or project restrictions, does not have sufficient control of his or her project.
[4] *Battlestar Galactica*, season 4, episode 17, 2009.

Willem-Jan Evers
Eindhoven, May 2010

